SISTEMA AQUA
"ADVANCED QUALITY ASSURANCE"
PER IL
CENTRO NAZIONALE DI ADROTERAPIA ONCOLOGICA

Radiografia per assorbimento di protoni
(Proton Range Radiography – PRR)

Tomografia per Diffusione Nucleare e Ricostruzione dei Vertici di Interazione
(Nuclear Scattering Tomography – NST
Interaction Vertex Imaging - IVI)

PET-sul-fascio con Rivelatori Gassosi
(in-beam-PET with Gas Detectors)

PET-sul-fascio con Rivelatori a Cristalli
(in-beam-PET with Crystal Detectors)

Documento preparato dalla Fondazione TERA

15 febbraio 2008

RIASSUNTO OPERATIVO

Nel maggio del 2006 la Fondazione CNAO ha affidato a TERA lo studio preliminare di un sistema di PET-sul fascio di cui dotare eventualmente una o più sale di trattamento del Centro di Pavia in modo da poter controllare sessione per sessione la localizzazione della dose depositata dal fascio di ioni carbonio. Lo studio prevedeva la stesura di un rapporto intermedio, che è stato distribuito il 15 novembre 2006. Questo documento descrive il lavoro fatto sino ad allora ed illustra le scelte tecniche a cui si era giunti.

Nel corso di questo primo studio, oltre alla prevista ***in-beam-PET (PET-sul-fascio***) furono esaminate due altre possibili metodiche di diagnostica sul fascio che, per quello che si sa, non sono utilizzate dai gruppi che si occupano di adroterapia:

A) la "radiografia a diffusione nucleare" (oggi ribattezzata ***NST = Nuclear Scattering Tomography***)la cui fattibilità fu dimostrata da G. Charpak, F. Sauli e collaboratori molti anni fa; in questo caso si utilizza un fascio di protoni da 1000 MeV, che può essere prodotto dal sincrotrone del CNAO e che, attraversando il corpo del paziente, permette di ricostruire dai protoni diffusi una immagine accurata e tridimensionale degli organi del paziente disteso sul lettino prima del trattamento;

B) un nuovo approccio alla determinazione del percorso degli ioni carbonio nel tessuto irradiato basato sulla rivelazione delle particelle che, strappate dagli ioni e dai loro secondari ai nuclei della materia, fuoriescono dal corpo del paziente; questa tecnica è stata chiamata ***IVI = Interaction Vertex Imaging***. Come previsto nella Convenzione firmata da CNAO e TERA, i risultati ottenuti hanno permesso di individuare i prototipi di rivelatori che è necessario costruire e provare nei prossimi sei mesi per giungere, se i risultati saranno positivi, a una scelta del sistema definitivo da sottoporre alla CNAO per l'approvazione, il finanziamento, la costruzione e l'installazione in una delle sala di trattamento.

Il documento fu esaminato dal Consiglio Tecnico Scientifico della CNAO nella seduta del 21 dicembre 2006, che accettò la proposta di proseguire nell'approfondimento dello studio non soltanto della PET-sul-fascio, ma anche delle altre due tecniche.

All'inizio del 2007 TERA ha stretto una collaborazione scientifica con il gruppo del Prof. George Chen del Massachusset General Hospital, che ha come scopo la progettazione e la realizzazione di un sistema di *radiografia con protoni*, da utilizzare possibilmente prima di ogni sessione di adroterapia per fare una proto-radiografia del paziente già allineato sul fascio di ioni carbonio o di protoni. e ricostruire con precisione, prima del trattamento, la posizione e la dimensione degli organi bersaglio e degli organi a rischio

Nel progetto TERA sono usate due camere GEM e un telescopio di range di 1-2 mm di risoluzione spaziale, che costituiscono il PRT (Proton Range Telescope). A questo technica è stato dato il nome ***PRR = Proton Range Radiography***.

Il PRT è fatto di scintillatori di circa 10x10 cm^2 registrati singolarmente che hanno uno spessore compreso tra circa 3 mm. Si vuole ottenere una risoluzione sul percorso dell'1% circa. La lettura delle due camere GEM da 10x10 cm^2 deve essere molto rapida se la proto-radiografia deve essere fatta *in situ* in una frazione di minuto. Attualmente non esistono circuiti elettronici in grado di far questo, e la proposta avanzata da TERA alla CNAO nel rapporto del 24 aprile 2007 indicava le possibili linee di sviluppo.

Nello stesso rapporto si metteva in luce che, durante la fase di messa in funzione del sincrotrone e dei sistemi di distribuzione della dose, un sistema costituito da un telescopio di percorso e due camere GEM sarà molto utile per avere informazioni *on-line* sulle caratteristiche dei fasci di protoni e di ioni carbonio prodotti dall'acceleratore. Può trattarsi di un sistema elettronicamente più lento, in quanto l'intensità del fascio può essere ridotta senza perdere la possibilità di ricostruire in tempo reale l'immagine della distribuzione di dose tridimensionale e vedere come si comporta non soltanto l'acceleratore, quando si cambia energia, ma anche il sistema di magneti di "scanning" che deflettono trasversalmente il fascetto.

La Fondazione CNAO ha accettato la proposta, tenuto anche conto del fatto che non comporta costi superiori a quelli previsti dall'accordo iniziale. Si sono invece allungati i tempi, dato che tre altri progetti si sono aggiunti alla PET-sul-fascio.

* * *

La figura rappresenta schematicamente la disposizione, nel piano verticale che passa per il fascio, degli strumenti discussi in questo rapporto.

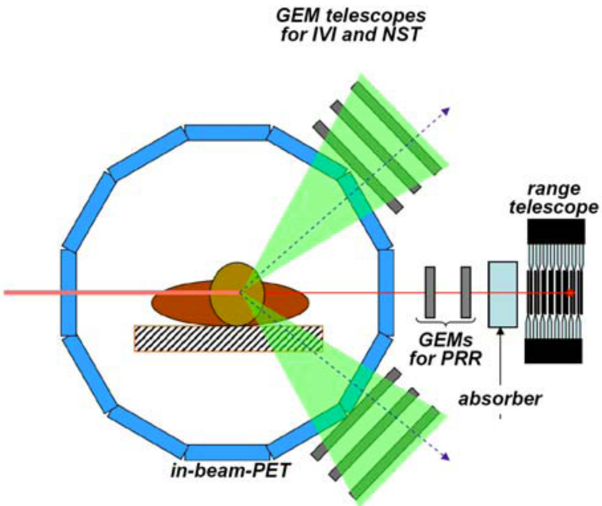

Qui di seguito sono riassunti i principali argomenti trattati e le conclusioni raggiunte.

1) Il **Capitolo 1** è dedicato alla **PRR**, il cui interesse clinico è discusso sulla base della vasta esperienza di George Chen e del suo gruppo, che propone l'uso di un blocco di scintillatore. La tecnica scelta da TERA è più moderna, in quanto basata su due (o tre) camere a gas di tipo GEM (un rivelatore rapido e preciso inventato da Fabio Sauli) e su un insieme di scintillatori sottili visti da nuovissimi Silicon Photo-Multipliers (SiPM). L'insieme costituisce un Proton Range Telecoppe (PRT).

   Dopo aver verificato i risultati ottenibili facendo uso di una simulazione Monte Carlo basata sul codice standard CERN detto Geant4, si è passati alla realizzazione del sistema. Le foto mostrano la prima GEM costruita e gli elementi del telescopio di percorso: uno scintillatore di 3 mm di spessore, una barretta di Wave Light Shifter e un SiPM).

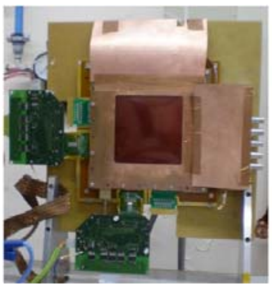

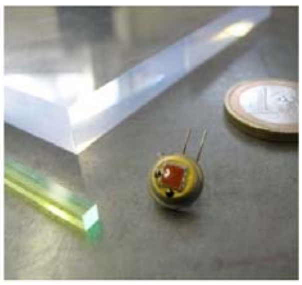

Il telescopio di percorso sarà completato entro l'estate e **portato a Pavia in tempo** per la prima estrazione dei fasci di protoni e ioni carbonio dal sincrotrone del CNAO.

2) Nel **Capitolo 2** è discusso lo strumento utilizzato per la simulazione dei processi fisici che sono alla base delle tecniche discusse nel seguito. Dopo una breve descrizione di Geant4 e dei suoi modelli, i risultati ottenuti sono confrontati con dati sperimentali in modo da validare i modelli stessi. La seconda parte del Capitolo è dedicata agli strumenti informatici sviluppati per la tecnica della in-beam-PET. In particolare sono descritti i risultati ottenuti simulando la produzione di emettitori di positoni da parte di ioni carbonio. Dal confronto dei risultati ottenuti con i dati sperimentali riportati in letteratura si può concludere che i codici ora a disposizione sono non soltanto sufficientemente accurati ma, in alcuni casi, più vicini alla realtà di quelli impiegati dal gruppo del GSI di Darmstadt, che nel campo della PET-sul-fascio ha un'esperienza decennale.
3) Le tecniche **IVI** ed **NST** sono discusse nel **Capitolo 3.** Esse sono trattate insieme in quanto utilizzano la stessa strumentazione: due telescopi costituiti di camere GEM di 30x30 cm2, scintillatori e assorbitori. La differenza è che per NST i due telescopi sono usati in coincidenza, mentre per IVI funzionano in singola. Se i calcoli qui presentati saranno confermati dai risultati che si conta di ottenere nel 2009 utilizzando un sistema prototipo NST nell'area sperimenentale del CNAO a Pavia, inviando prima di un trattamento con ioni carbonio un fascio di protoni da 700-800 MeV sarà possibile rivelare gli eventi di diffusione elastica dei protoni sui nuclei di idrogeno dei tessuti. Si otterranno, in qualche decina di secondi e *prima* che inizi il trattamento, informazioni analoghe a quelle che si hanno con una Risonanza Magnetica, informazioni che sono diverse e complementari di quelle ottenute con i raggi X.
4) Il **Capitolo 4** è dedicato al disegno e alle proprietà che deve avere il **rivelatore per la in-beam-PET** che TERA intende realizzare per la Fondazione CNAO. La geometria del rivelatore è discussa con particolare attenzione al problema delle 'collisioni' tra le teste del rivelatore, il sistema di monitoraggio del fascio e il lettino del paziente. Poi il sistema di acquisizione dei dati, che è particolare per la CNAO per via l'estrazione lenta fatta con il metodo del "betatron core", è analizzato sulla base di un piano di trattamento preparato da F. Bourhaleb.
5) Il **rivelatore a cristalli di tipo LYSO** proposto è descritto nel **Capitolo 5**. I calcoli e le misure effettuate su cristalli di questo tipo sono riportate dopo la descrizione dell'utilizzazione fatta del codice LITRANI, che è stato utilizzato per la simulazione del trasporto della luce in questo nuovo tipo di rivelatore. Si è scelto di simulare con un Monte Carlo apposito e poi provare sperimentalmente un blocco di cristallo di 12x30x60 mm^3, letto analogicamente dal fotomoltiplicatore multianodo mostrato in figura.

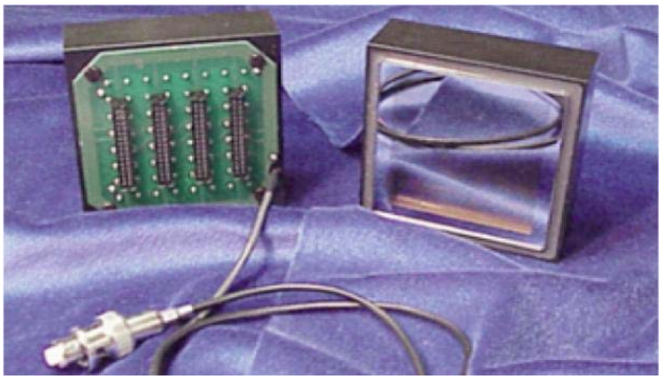

In futuro si pensa di utilizzare gli stessi Silicon PhtoMultiplies (SiPM) impiegati nel telescopio di percorso per la PRR.

Questa tecnica non permette risoluzioni spaziali molto spinte, ma ciò in questo caso non è necessario perché l'attività indotta dal fascio di ioni carbonio nel corpo del paziente è bassa (circa 200 becquerel per cm3 per gray); le fluttuazioni statistiche quindi dominano e risoluzioni spaziali dell'ordine di 5 mm sono sufficienti quando si tratta di una in-beam-PET, una situazione molto diversa da quella che si ha in una PET per animali, che richiede risoluzioni dell'ordine del millimetro. La dettagliata simulazione ha dato risultati più che soddisfacenti e i risultati sperimentali li hanno sostanzialmente confermati, pur con alcuni peggioramenti che sono fisiologici quando si passa dal mondo della simulazione alla realtà..

6) Il **Capitolo 6** è dedicato all'utilizzazione di **rivelatori a gas del tipo RPC** (Resistive Plate Chambers) per la in-beam-PET della CNAO. Vi si descrive l'originale soluzione proposta, che si basa sull'uso di elettrodi di vetro sui quali è depositato un sottile strato di diamante artificiale che ha una resistività controllata a evitare il caricamento degli elettrici quando i flussi di particelle sono elevati. La soluzione GEM è anche discussa ed attualmente è seguita dal gruppo Gas Detector Developments (GDD) del CERN, con cui TERA collabora.

* * *

Il compito affidato a TERA dalla CNAO nel 2006 concerneva un sistema in-beam-PET utile per la verifica della localizzazione della dose nei trattamenti con fascetti di ioni carbonio. Nel corso dello studio sono state individuate altre possibilità di controllo della posizione degli organi interni del paziente allineato sul fascio e della distribuzione della dose impartita.

Nasce quindi spontanea l'idea di proporre la progettazione e la prova sul fascio di prototipi di un sistema integrato di rivelatori nel quadro di un programma di controllo della qualità dei trattamenti, a cui è stato dato il nome di **AQUA = Advanced QUality Assurance**. Come primo passo, si tratta di realizzare i prototipi di tutti i rivelatori necessari per applicare le tecniche PRR, IVI, NST, in-beam-PET rappresentate nella prima figura.

Se le possibilità di controllo della localizzazione degli organi da irradiare e della dose impartite, descritte in questo rapporto, saranno confermate da dati sperimentali raccolti sul fascio sperimentale del CNAO, sarà poi possibile decidere quali e quanti di questi strumenti andranno costruiti.

La proposta AQUA è contenuta in un altro documento preparato per la Fondazione CNAO.

TABLE OF CONTENT

INTRODUCTION

In May 2006 the CNAO Foundation gave to TERA the responsibility of studying a in-beam-PET device to be eventually built and used in one of the treatment areas of the Pavia centre. This technique allows the in situ determination of the spatial distribution of the positron emitting isotopes produced in the patient body by the carbon ion beam, and can also be applied when protons are used. It has been pioneered by the Dresden group of W. Enghardt, who built for the GSI project a device based on conventional PET detectors. The results obtained on many hundreds patients are very encouraging: few minutes after the end of a carbon ion treatment the localization of the delivered dose can be determined with an accuracy of about 1 mm.

During the first part of this study, described in the intermediate report presented on 21 December 2006 to the CNAO Technical and Scientific Committee (CTS), TERA came to the conclusion that two other techniques were worth investigating. They have been called IMI (Interaction Vertex Imaging) and NST (Nuclear Scattering Tomography). They use gas detectors of the GEM type placed at about 45° with respect to the beam and determine the direction of the charged particles coming out of the patient body.

In IVI, during a carbon irradiation the on-line reconstructed points of interactions of the outgoing tracks with the incoming pencil beams allows a continuous check of the irradiation conditions. In NST a 700-800 MeV proton beam is sent, for a short time before the treatment, along the path of the carbon beam employed for the irradiation and the proton-proton scattering events are used to image the hydrogen distribution in the patient body. It has to be remarked that new very fast electronics has to be developed for this device.

These ideas, only sketched in the intermediate report, have been further developed and are the subject of **Chapter 3** of this final report.

At the beginning of 2007 TERA decided o collaborate with G. Cheng of Massachusetts General Hospital on another diagnostic technique, which is here called PRR (Proton Range Radiography). In this case, before or after a treatment, a Proton Range Telescope (PRT) measures the residual range of the protons having enough energy large enough to cross the patient body. The reconstructed “radiograph” gives direct information on the integral of the electron density along the protons path.

In April 2007 TERA proposed to CNAO to build a prototype of such a device underlining that it will be extremely useful in the commissioning phase of the Pavia centre since, placed at the end of a beam transport line, will allow the operator to “see” the build-up of the dose distribution obtained with the raster technique. Also in this case new very fast electronics has to be designed and built for the final device.

CNAO agreed with the proposal of constructing the proton telescope. The status of the prototype, which will be ready in summer 2008 and brought to Pavia, and the plans for the implementation of the PRR technique are described in **Chapter 1**.

If CNAO accepts the continuation of the TERA study and the construction of the prototypes, these three devices could complement the information provided by the in-beam-PET system.

Four Chapters of this report concentrate of the in-beam-PET technique.

Chapter 2 is devoted to the description of the tests and the modifications made to the CERN Monte Carlo code Geant4, which has been used to compute backgrounds and performances of all the devices, including the in-beam-PET systems.

In **Chapter 4** the geometry of the CNAO in-beam-PET system and its utilization with the peculiar very stable hadron beam are discussed.

Finally **Chapter 5** and **Chapter 6** describe in detail the status of the computational and experimental work which has been done on PET systems since the intermediate report. The first one is devoted to the development of a new crystal detector and the second one discusses the use of gas chambers.

* * *

As a consequence of the work done till now, TERA will propose to CNAO the launching of a project of **Advanced QUality Assurance = AQUA**, which will built prototypes of the instruments needed for the four techniques PRR, IVI, NST and PRR. These prototypes will be tested in the CNAO experimental area starting form fall 2008.

The proposal is described in another document submitted to the CNAO Foundation.

1. PROTON RANGE RADIOGRAPHY

1.1 Introduction

Pioneered in the eighties[1] proton radiography, which exploits the information of energy loss in the target, has been subject of many studies of diagnostic tools in hadrontherapy[2,3,4]

The basic principle of the method is to measure the residual energy of the beam traversing an absorber, and build a two-dimensional map of the integral density in the target. The precision in the measurement of the residual range (or energy) determines the sensitivity to density variations in the target.

Most systems described in previous work use position-sensitive detectors before the target, followed by a scintillator providing a signal proportional to the residual proton energy. For best performances, fast inorganic scintillating crystals have been used (NaI, BGO, LYSO, LSO,YAP); to achieve the desirable image contrast, energy resolutions of a few percent are needed, a non-trivial requirement. Despite its simplicity, the method suffers from a major drawback: very large scintillators are needed to cover the required areas (up to 30x30 cm^2), with consequent problems of cost, response uniformity and laborious calibrations needed to achieve the required energy resolution.

In the present study we propose a different approach that appears to be cheaper, more flexible and capable of covering larger areas.

Before presenting the chosen solution and describing the prototype work, the clinical advantages of such a technique are discussed by using detailed information provided by Prof. George Chen of Massachusetts General Hospital, with whom a collaboration has been established.

1.2 Clinical aspects

The primary advantage of proton radiotherapy over conventional radiotherapy is its finite range in tissues. In principle, a therapeutic beam, under precise control, can be directed at a tumour and spare normal tissues distal to the beam's end of range. A relevant example involves irradiating a lung tumour while avoiding unnecessary irradiation to distal lung and other critical structures (e.g. spinal cord). This is achieved by construction of a compensating bolus that is designed based on a CT scan taken during patient workup. The ability to achieve precise targeting at the time of treatment delivery is dependent upon accurate patient setup, and reproducibility of the geometry and radiological path length in fractionated radiotherapy.

Range control in treatment of lung tumours is challenging for a number of physiological reasons. Lung anatomy is fundamentally dynamic, and both intrafractional and interfractional anatomical variations can alter beam penetration. Factors affecting range include:

- Tumour shrinkage: Fig. 1.1 shows a treatment-planning scan acquired before initiation of therapy. The CT scan on the right, at essentially the same anatomical level, shows substantial (70cc) shrinkage of the tumour after 5 weeks of radiotherapy. Clearly a

---

1 Hanson K.M. et al, Phys. Med. Biol. 26 (1981) 965.
2 Sadrozinski H.et al. Nucl. Instr. and Meth. A511 (2003) 275.
3 Schulte R. et al, Med. Phys. 32 (2005) 1035.
4 Cirrone G. et al, Nucl. Instr. and Meth. A576 (2007) 194.

compensating bolus designed for the larger tumour results in overshoot when applied to the midcourse scan.

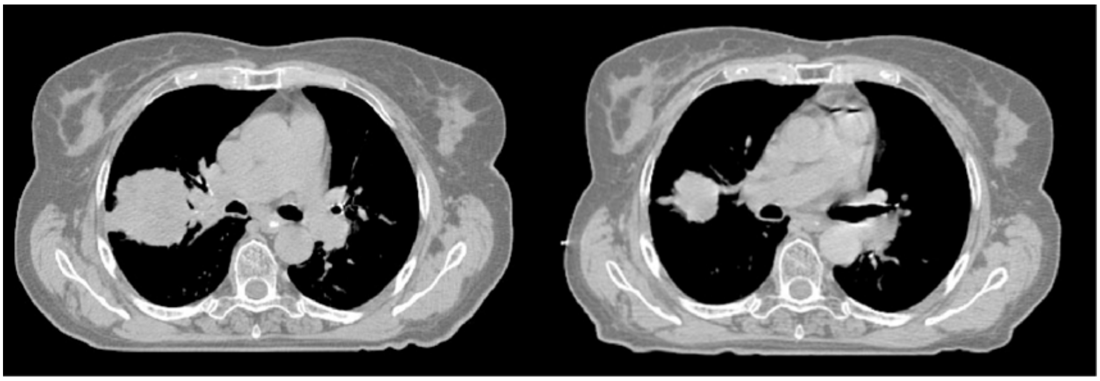

Figure 1.1 *Left: planning scan; right: scan at same level 5 weeks later. Note decrease in gross tumour volume post initial irradiation.*

- In addition to the gross shrinkage of the tumour, other more subtle effects are seen in the scans above. The shape and position of the breast is slightly different, as well as the location of the mainstem bronchi. These changes will affect the penetration of a charged particle beam.

- Respiratory motion: 4DCT provides a view of radiological pathlength changes during respiration. Appreciation of the effects of respiration and cardiac motion on range is important. Fig. 1.2 below is a difference image (colourwash) that quantifies variation of range through the patient (as in a transmission proton radiograph) relative to exhale. The mottled regions in the lung parynchema represent range changes due to movement of the larger vessels during breathing. The bright yellow region adjacent to the left ventricle of the heart is due to the contraction of the heart; regions in this interface area are replaced by lower density lung, resulting in beam overshoot, hence the intense colour change representing range perturbations. Finally, the obvious motion of the diaphragm during respiration is shown in blue, and represents motion of the diaphragm inferiorly, with subsequent replacement of the diaphragm / liver with lung tissue.

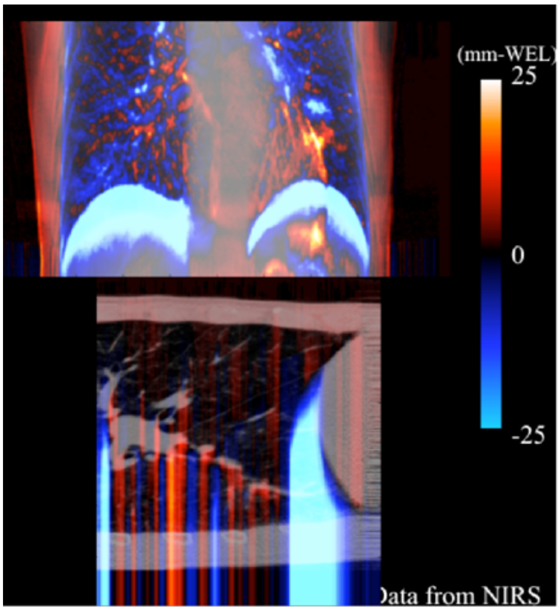

Figure 1.2 *Upper: AP difference image of radiograph map between exhale and inhale. The colour wash scale indicates range differences for various rays.*

- Trajectory changes: A tumour's initial position and trajectory from day to day may change. The MDAH has studied this using serial 4D CT, where a 4D scan is performed once per week over the six weeks of radiotherapy. The results of such a study are shown in Fig. 1.3.

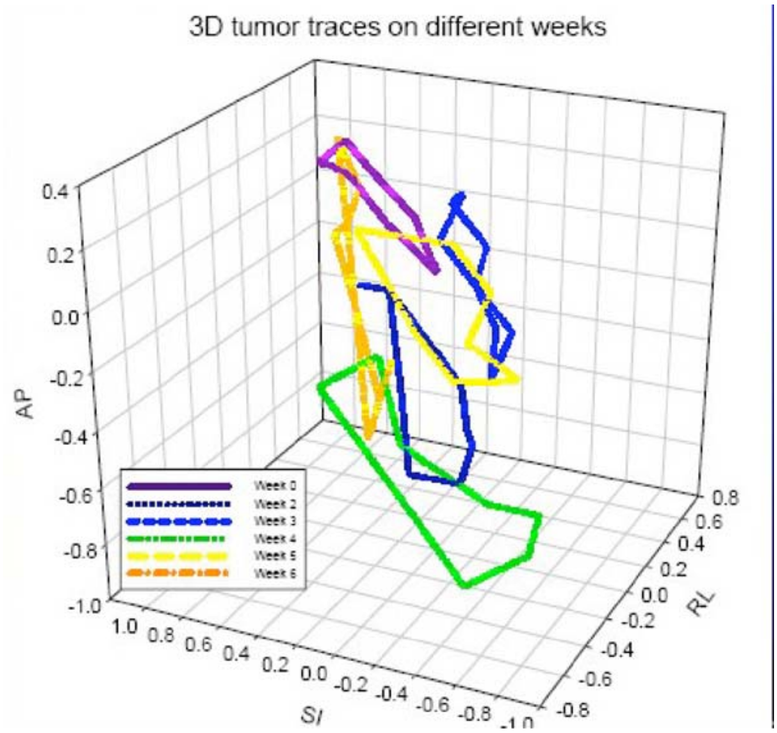

Fig. 1.3 *Each coloured curve represents the three-dimensional trajectory of a lung tumour centre of mass from serial 4D CT scans performed on a weekly basis. The common coordinate system is the vertebral column. The spine is aligned in each scan to the planning scan (courtesy Lei Dong Mdah).*

Note that on different serial CT scans, the initial position of the centre of mass of the tumour is different, relative to bony anatomy. Furthermore, the trajectory varies in both amplitude and position.

Setup in presence of variations of position, shape, and density changes is difficult; Physicians are reluctant to use radio-opaque markers (clips) because of the risk of complications (pneumothorax). Radio-opaque clips only show clip positions, not soft tissue changes in anatomy; cone beam CT may help but only documents tumour position prior to treatment. Cone-beam cannot be performed continuously during treatment. A Proton Range Telescope can provide several important insights:

- Produce a radiograph that visualizes the location of the tumour on a daily basis;
- Produce a proton fluoroscopic video clip that documents tumour motion on a daily basis and a minimal dose;
- Verify changes in tissue density or detect thickness changes in tissue thickness.

A range map can be generated from 4D CT data. At MGH tools have been developed, (S. Mori, PhD) to calculate radiographic pathlength maps based on CT data. The Hounsfield units of a CT scan are converted to relative stopping power. The image in Fig. 1.4 appears to be a radiograph, but each element in the image is a measure of the water equivalent thickness of the patient from anterior skin surface to a plane just anterior to the vertebral body (shown in the picture within the picture). A large spherical tumour is seen in the right mid lung.

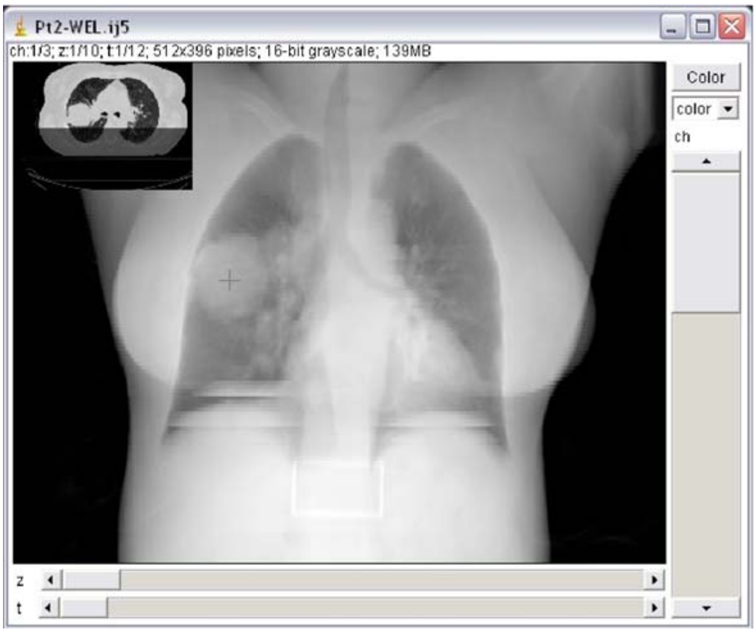

Figure 1.4 *WEL map generated from CT scan. The grey level values of each pixel in this image encode the WEL (gm/cm2) from entrance surface to the plane indicated in the inset. Crosshairs in the centre of the tumour show a WEL of 11.3 cm water. The slider bars are used to select 1) the WEL as a function of respiratory phase and 2) the beam entry angle for different possible radiation portals.*

One can calculate the range difference map from two such range maps. This is shown in Fig. 1.5. In the colour image, the initial range map and the subsequent range map generated from the initial planning CT scan and the follow-up scan after 5 weeks of treatment is shown. Several regions have changed "thickness" as shown in the difference map. Because the spherical tumour has shrunken, there is a dark rim where the tumour is located (right lung). In addition, there is a blue region above the tumour.

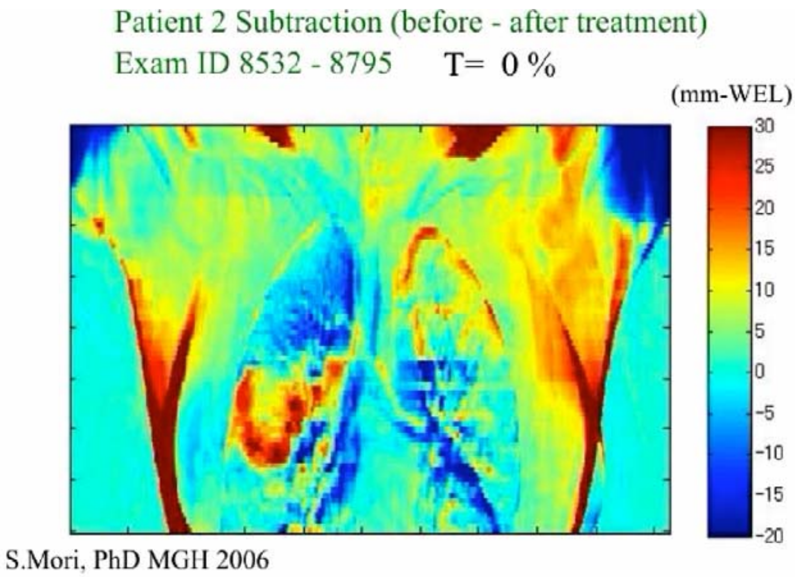

Figure 1.5 *Difference range map between planning and follow-up scan.*

Closer investigation of the HU of this region (Fig. 1.6) shows that the lung electron density has changed from 0.2 g/cc to 0.3 g/cc, which over a 10 cm path, can result in a 1 cm water equivalent length radiological pathlength change. Because the typical lung density is 0.3 g/cc, this leads to a geometric overshoot of approximately 3 cm of lung volume.

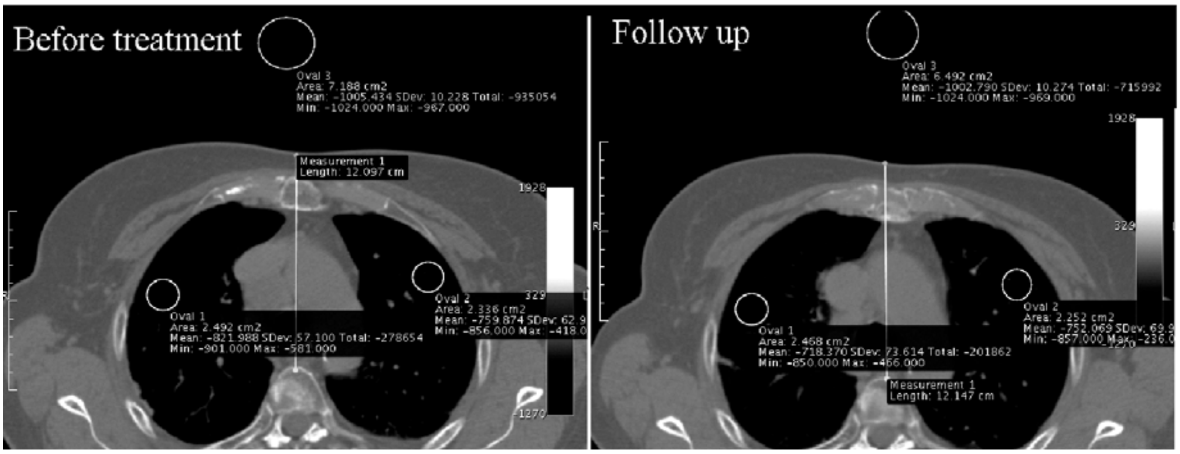

Figure 1.6 *Sampling of HU of lung, documenting change in density of the ipsilateral lung over time, while the HU of soft tissue, air, and contralateral lung remain stable.*

The simulated coronal image below (Figure 1.7) shows the tumour in the right lung (posterior view). A white circle indicates the ROI over which the MC calculation was performed. The location and energy of each proton passing from the anterior skin surface was tracked through the lung and chest wall, and into the plane just posterior to the back skin surface. Approximately 1 million protons were used in the simulation.

Figure 1.7*: Image of radiograph (proton) under calculation.*

1.3 Proton Range Telescope

The Proton Range Telescope, PRT, chosen to apply the technique PRR, consists of a set of position-sensitive detectors for tracking and a stack of plastic scintillator plates with individual pulse height recording to determine the residual range of the particles after the absorber (see Fig. 1.8). In view of their very high rate capability and excellent position resolution, we have selected the Gas Electron Multiplier (GEM)[5] as tracking detector; GEM1

[5] Sauli F., Nucl. Instr. and Meth. A386 (1997) 531.

and GEM2 measure the incident proton trajectory, and GEM3 can be used optionally to reject tracks with too large deviation from a straight line due to multiple scattering.

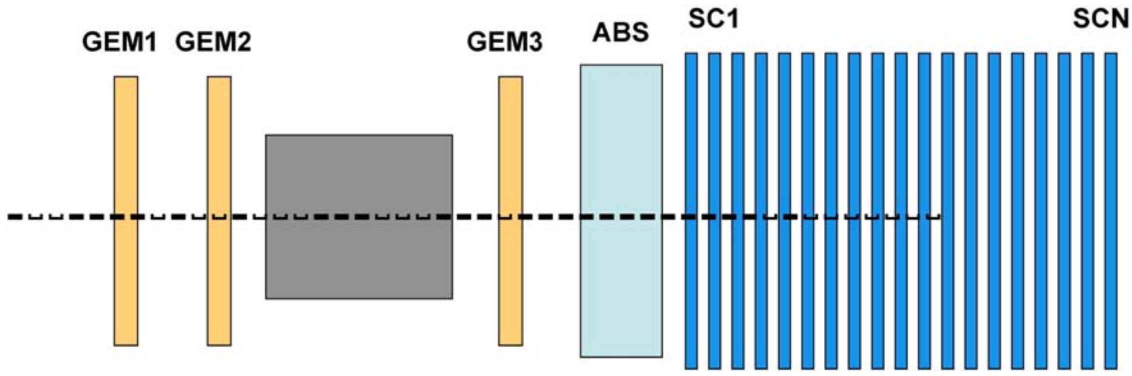

Figure 1.8*: Schematics of the Proton Range Telescope*

Detection of the last fired plate provides a rough measurement of the residual range; a fit of the measured differential energy loss in each plate to the (known) Bragg curve should provide, according the simulation (see below), an accuracy in the residual range comparable to the measurement of the energy loss. To extend the range of energy covered, passive absorbers can be inserted in front of the stack or in the gaps between scintillators.

1.4 Performance studies

Using a Monte Carlo code (Geant4) we have simulated various properties of the PRT. Fig. 1.9 shows the integral energy loss profile as a function of penetration (Bragg curve) for protons at two initial energies in plastic scintillator. The slow drop of the distribution at the end is due to range straggling.

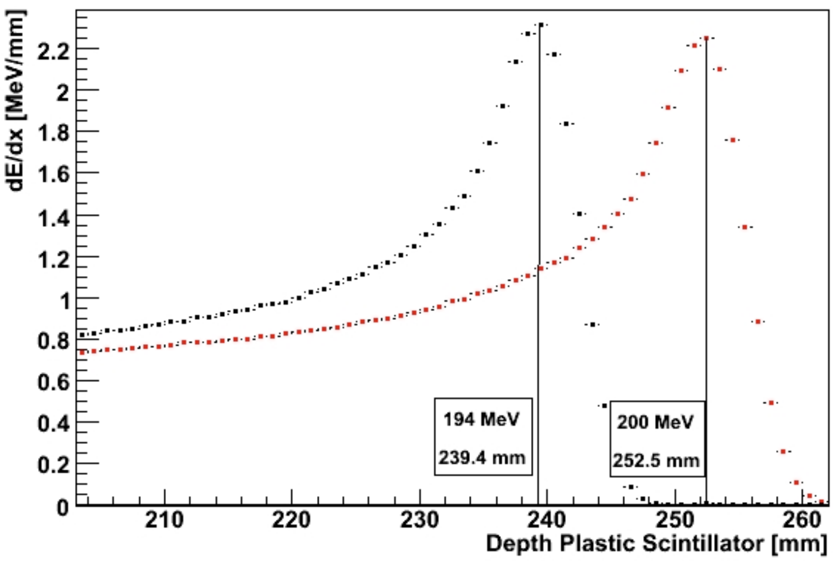

Figure 1.9 *Energy loss profile (Bragg peak) for protons at 194 and 200 MeV in plastic scintillator. The inset provides the corresponding average range.*

This is shown also in Fig. 1.10 that provides, for three values of energy, the computed spread in penetration, before the particle comes to stop, due to multiple scattering. As one can see, at the highest energy the range straggling is 1% rms, corresponding to about 3 mm; this has defined the initial choice of the scintillator thickness.

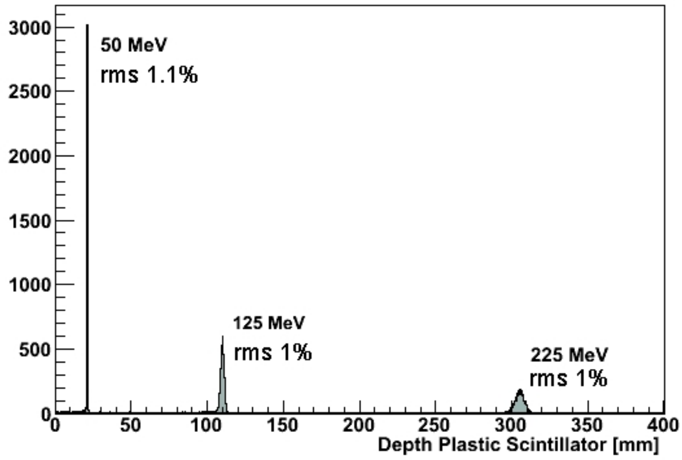

Figure 1.10 *Range straggling of protons in plastic scintillator.*

A thin segmentation of the range telescope and a simple digital count of the scintillators with a pulse above a pre-determined threshold should allow reaching the quoted resolution. However, recording the pulse height profile with a fit to the Bragg distribution can substantially improve the residual range determination accuracy.

Fig. 1.11 shows the energy loss profile of a single proton track.

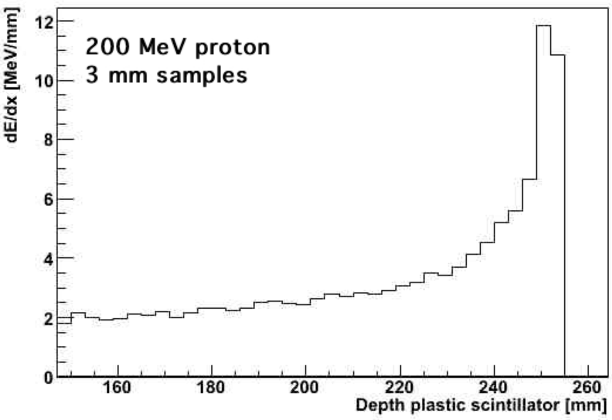

Figure 1.11 *Single 200 MeV proton differential energy loss (in MeV/mm) computed for 3 mm thick samples.*

The energy distributions towards the end of the range are shown in Fig. 1.12.

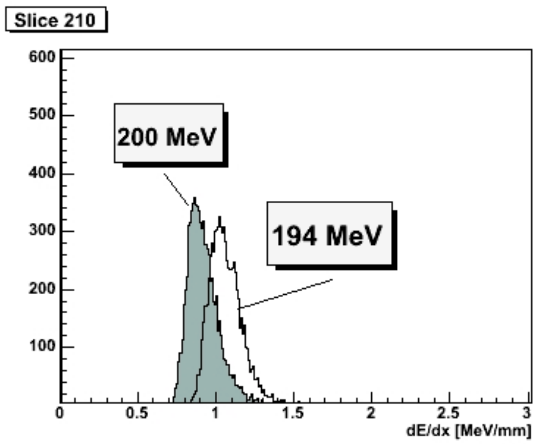

Figure 1.12 *Differential energy loss spectrum for protons near the end of range*

As seen in the figure, the energy loss resolution at the end of range, computed for one mm scintillator, has a FWHM of about 20%, well below to the difference between two adjacent, the energy loss resolution at the end of range, computed for one mm scintillator, has a FWHM of about 20%, well below to the difference between two adjacent

Pending a more accurate simulation, it seems intuitive that a sampling of energy loss in a number of adjacent slabs, even with moderate accuracy and taking into account straggling and statistical dispersions should allow reconstructing the end point of the track with sub-mm accuracy. The fit can be done taking the initial energy loss as normalization, resulting in a moderate dependence of the result from a detailed calibration of response over the scintillator area, assuming yield variations in different slabs to follow similar patterns.

1.5 Prototypes and tests

As indicated above, beam tracks are recorded with a pair of GEM chambers with 10x10 cm^2 active area. Based on a well-proven design[6] the detector assembly includes three multiplier foils, a drift electrode and the readout board within a dismountable gas box (Fig. 1.13).

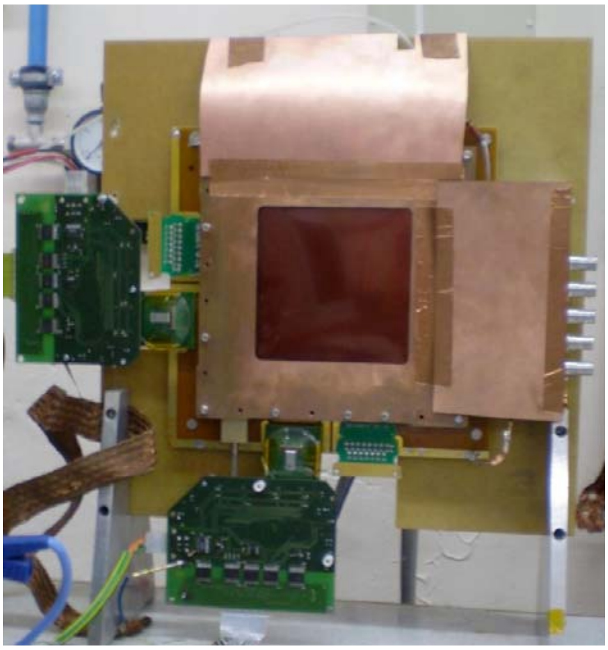

Figure 1.13 *Small size GEM detector*

Coordinates are read out recording signals on two sets of 256 perpendicular strips at 400 μm pitch. For the readout, we are comparing the performances of two high-density electronics design, one based on the VFAT chip [7]providing the digital strip address for each hit as well as a fast global event trigger, and an analogue making use of the VATA GP5 chip[8]. For laboratory tests, we use a portable Data Acquisition system with USB interface to a PC; future development of the project calls however for a dedicated faster DAQ.

Based on the simulation discussed above, we have chosen as scintillators standard NE-102 polystyrene plates, 12x12 cm in area ad 3 mm thick; the readout is made coupling on one edge a wavelength shifter fiber to a solid state silicon photomultiplier (Fig 1.14).

---

[6] Bressan A.et al, Nucl. Instr. and Meth. A435 (1999) 262.
[7] Szczygiel R. and Kaplon J., The VFAT-128 (CERN 2000).
[8] http://www.ideas.no/

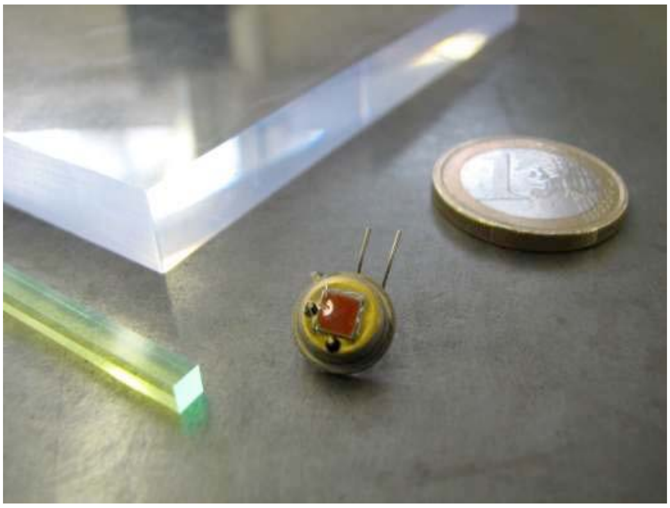

Figure 1.14 *Scintillator, WLS and SiPM*

The scintillator and readout assembly are schematically shown in Fig. 1.15: a light support plate, emptied in the active area, is used both to support the components of each module and to assembly the modules. Depending on the thickness of the active components and connectivity, the modules can be assembled coherently or rotated in pairs.

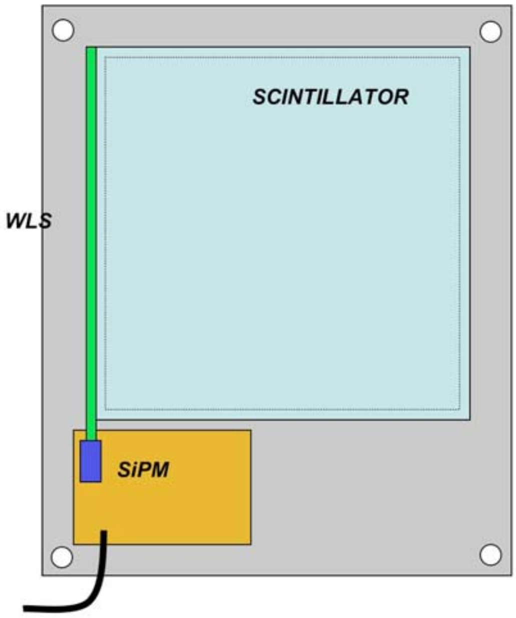

Figure 1.15 *Schematics of a scintillator and sensor module.*

For best performance, the WLS bar should be square in cross section, matching the size of the SiPM; while 3x3 mm^2 devices are expected to be available in the near future, we have made preliminary tests using a smaller area sensor, the Hamamatsu Multi-Pixel Photon Counter (MPPC S10362) with 1 mm^2 active area, and a 1 mm diameter WLS fiber. The pulse height distribution recorded for minimum ionizing electrons from a ^{106}Ru source in coincidence with a second scintillator is shown in Fig. 1.16; one can clearly distinguish the single and multi-photoelectron peaks. The average value of the signal, about 8 photoelectrons, will increase by an order of magnitude when using a larger area sensor. Moreover, protons of 200 MeV are already about four times above minimum ionizing, so we expect a rather good resolution for each sample.

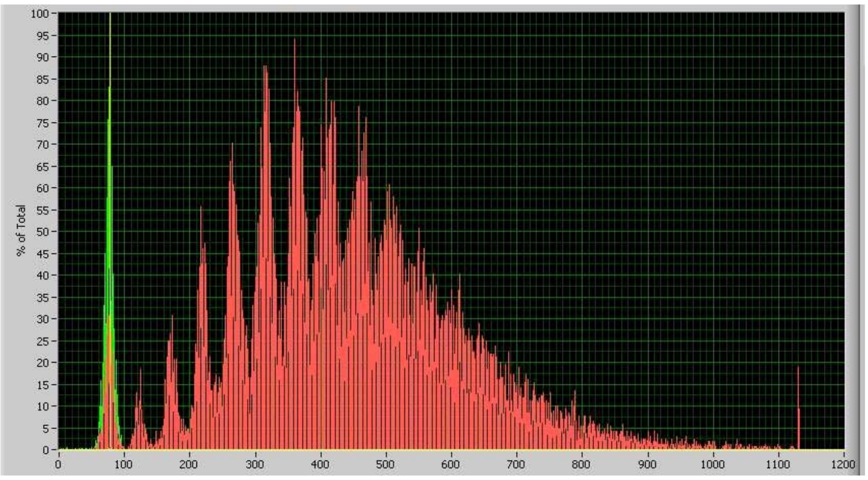

Figure 1.16 *Pulse height spectrum for minimum ionizing electrons in the prototype scintillator-WLS-SiPM module.*

At present the scintillators have been ordered and the electronics is being designed. It is expected to have the PRT ready by summer 2008, in time to be used for checking the performance of the first beams extracted from the CNAO synchrotron.

2. VALIDATION OF THE GEANT4 CODE AND IN-BEAM-PET CALCULATIONS

2.1 Introduction

Modern particle and nuclear physics experiments pose enormous challenges in the creation of complex software frameworks and applications. Many codes have been developed in order to satisfy the wide range of requirements of the physics community and hadrontherapy can of course benefit of the progress made in this field. For the description of the interactions of particles in matter many Monte Carlo tools have been developed and widely validated in the high energy physics domain but a lack of information on the behaviour of these softwares at the intermediate energies, of interest for hadrontherapy applications, still remains. Among them, Geant4 [9] [10] has been selected for its flexibility in geometry and physics modelling.

In this Chapter, after a review of the interactions of hadrons beams in matter, the capabilities of Geant4 to reproduce experimental data in the energy range of interest are discussed.

2.2 Interactions of charged hadrons in matter

Charged hadrons when passing through the matter release their energy mainly via interaction with the electrons of the target material. Since the energy dissipated in each electronic collision is very small, the energy loss of the projectile is practically continuous. The mean energy loss (also called "stopping power" and "Unrestricted Linear Energy Transfer", LET) is described by the Bethe-Bloch formula:

$$-\frac{dE}{dx} = Kz_{eff}^2 \frac{Z}{A}\frac{1}{\beta^2}\left[\frac{1}{2} ln \frac{2m_e c^2 \beta^2 \gamma^2 T_{max}}{I^2} - \beta^2 - \frac{\delta}{2}\right], \tag{2.1}$$

where:

- $\frac{dE}{dx}$ is the energy loss [$MeVg^{-1}cm^2$]
- β is the ratio between the particle velocity and the velocity of light c
- z_{eff} is the effective charge of the incident particle
- A is the atomic mass of the medium [$g\ mol^{-1}$]
- Z is the atomic number of the medium
- K / A is equal to $4\pi N_A r_e^2 m_e c^2 / A$ whose value is 0.307075 $MeVg^{-1}cm^2$
- I is the mean ionization potential of the atoms of the medium [eV]
- T_{max} is the maximum kinetic energy transferred to a free electron in a single collision
- δ is the density correction to the ionization energy loss.

Since the trajectory is practically straight, the range can be computed by integrating the inverse of the stopping power from the initial energy of the projectile down to zero:

---

[9] Agostinelli S. et al., "GEANT4-a simulation toolkit", Nucl. Instrum. Meth. A506 (2003) 250-303
[10] GEANT4 Web page: http://geant4.cern.ch/

$$R = \int_{E_0}^{0} (\frac{dE}{dx})^{-1} dE. \tag{2.2}$$

At lower energies, some corrections to the Bethe-Bloch formula are required. The first one is the shell correction, which takes into account the binding of the electrons in the target nuclei. The Barkas effect, instead, explains why the energy loss of positive charged particles, e.g. proton, is higher in respect to their antiparticle, e.g. $\overline{p}$. This behaviour is due to the polarization of target electrons toward (away) by positive (negative) projectile.
Another important effect occurring at low energies is the decreasing of the effective charge of the projectile, z_{eff}, because when it slowly passes close to a target atom, it can collect some of the electrons. This effect is described by the Barkas formula:

$$z_{eff} = z(1 - e^{-125\beta z^{2/3}}), \tag{2.3}$$

that underlines the dependence on the projectile velocity. Within the range of therapeutic energies, the Bethe-Bloch formula is to a good approximation dominated by the z_{eff} term and by $1/\beta^2$. The latter determines the increase of the stopping power with decreasing projectile energy.

The subscript ∞ in the symbol LET reminds the fact that in the atomic collisions all energy losses are considered without restriction. In practice the subscription is forgotten and the symbol used is simply LET. Plotted as a function of the residual range, the resulting curve is the well known Bragg curve.

The LET values of light ions are summarized in Table 2.1 for particle energies corresponding to the same range of 200 MeV protons, i.e. 262 mm.

Table 2.1. *The energies in column 2 correspond to a range of 262 mm in water. The other columns give the LET values at different depths in the target* [11]..

Charged particle $^{A}\mathbf{N}^{Z}$	E **MeV/u** R **=262 mm**	**LET [keV/ μ m] at various depth in water [mm]**				
		0 mm	**112**	**192**	**232**	**261**
$^{1}H^{+1}$	200.0	0.5	0.6	0.8	1.1	4.8
$^{2}He^{+2}$	202.0	1.8	2.2	3.1	4.4	20.0
$^{7}Li^{+3}$	243.3	3.7	4.6	6.2	8.9	40.0
$^{11}Be^{+5}$	329.5	8.5	10.0	13.5	19.0	87.5
$^{12}C^{+6}$	390.7	11.0	13.5	17.5	24.5	112.0
$^{14}N^{+7}$	430.5	14.5	17.5	22.5	31.5	142.0
$^{16}O^{+8}$	468.0	18.0	21.5	28.0	39.0	175.0

Since the energy loss is a stochastic process, a spread in energy always occurs after a mono-energetic beam has passed through a given target thickness. The energy spread leads to the range straggling, defined as the fluctuation in path length for individual particles of the same initial energy. The range straggling, despite mainly dominated by the stochastic nature of the energy loss, is also affected by the scattering experienced by the particles traversing a

[11] Amaldi U. and Kraft G., "Radiotherapy with beams of carbon ions", Rep. Prog. Phys. 68 (2005) 1861-1882.

material. The range spread amounts to about 1% of the mean range of protons and it is only 0.3% for carbon ions, because of the dependence on the mass as $1/\sqrt{m}$.

Multiple scattering

A charged hadron passing through matter is deflected by several small angles in the electromagnetic interactions with target nuclei. The Multiple Coulomb Scattering (MCS) can be described at small angles by a Gaussian, according to the Molière theory, with a standard deviation given by:

$$\sigma_\theta = \frac{13.6MeV}{\beta pc} z\sqrt{x/X_0}\left[1+0.038ln\left(\frac{x}{X_0}\right)\right], \tag{2.4}$$

where x is the thickness of the material traversed, X_0 is the radiation length and p is the particle momentum. At large depths the lateral definition of well collimated photon beams is better than the one of protons.

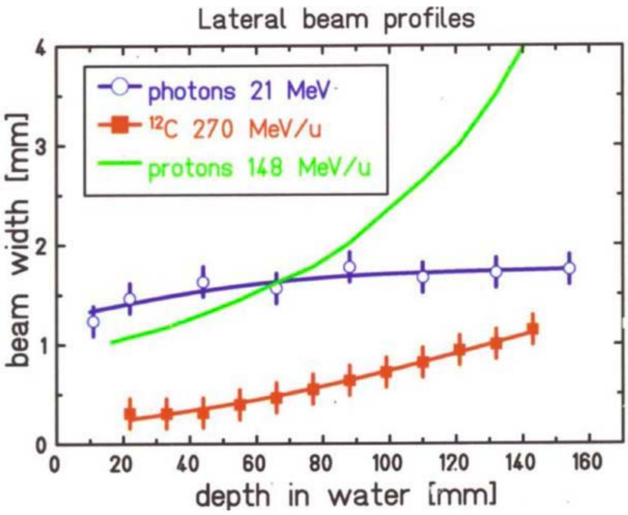

Figure 2.1 *Beam width at different depths in water of photons, protons and carbon ions (courtesy of GSI).*

Figure 2.1 shows also that carbon ion treatments are laterally more conformal than proton and photon treatments.

Fragmentation processes

The biological effect in the target volume is reduced because only a fraction of the primary particles reaches the end of the range without fragmentation and the fragments have, for the same energy, lower biological efficacy.

The physical parameter capable to describe the attenuation of primary particles in the target is the total reaction cross section σ_R, defined as the difference between the total and the elastic cross sections. At high energies (higher than 20 MeV/u), σ_R is dominated by geometrical factors, with an almost constant value. For the range region from the entrance point to a few centimeters before the Bragg peak, the attenuation of the primary particles can be described by the exponential law:

$$N(x) = N_0 \cdot e^{-\lambda x}. \tag{2.5}$$

The linear attenuation coefficient λ is related to σ_R by the equation:

$$\sigma_R(barn) = (10^{24} \cdot \lambda \cdot \rho \cdot A_t) \cdot \frac{1}{N_A}, \tag{2.6}$$

where A_t is the material molecular weight of the target and N_A is the Avogadro's number.

A general model capable to describe fragmentation processes is the abrasion-ablation model [12]; a schematic representation is shown in Fig. 2.2

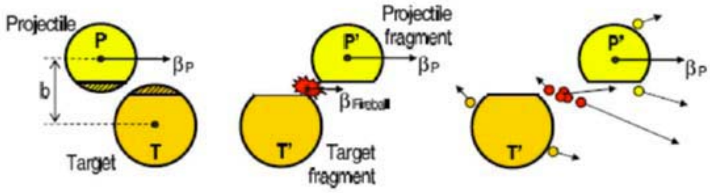

Figure 2.2 *Schematic drawing of a peripheral collision as described by the abrasion-ablation model [13].*

This model describes the more peripheral collisions. In fact, central and near central collisions represent only 10% of all nuclear events.

The interactions result in a wide spread production of fragments. In peripheral collisions, the target and the projectile overlap partially, depending on the impact parameter, and a fireball is formed between overlapping nucleons (participants). Since the fireball is formed on time scale of the order of 10^{-23} s, the target and the projectile nuclei do not take part in the process and for this reason are called "spectators". The fireball has the same direction as the projectile, but a lower energy per nucleon. The excited fireball, as well as the spectator nuclei, de-excite by emitting nucleons (evaporation) until the energy drops under the nucleon barrier potential. This last process can be up to 10^{-16} s long. The fragments of the projectile, resulting from peripheral collision, due to the dynamics of the interaction are mainly forward directed; they can be isotopes of the spectator nuclei as well as lower Z ions.

Assuming that the reaction cross sections are energy independent, the build up of fragments as a function of the depth x can be described by a homogeneous system of differential equations of first order:

$$\frac{d}{dx} N(x) = L \cdot N(x), \tag{2.7}$$

where $N(x)$ denotes the vector $(N_Z, N_{Z-1}, ..., ..., N_{Z-n})$ and the element of the matrix L are proportional to the partial charge-changing cross sections for the production of lower Z fragments, while the elements of the diagonal of L are the total charge changing cross-sections. The result is a linear combination of exponential functions [14].

The final effect of the fragmentation process is a less sharp distal fall-off of the deposited dose, with a long tail beyond the Bragg peak. This is due to the production of lower Z fragments that, having the same velocity and thus energy per nucleon ofthe primary beam, can travel more in the target because of the dependence of the range on A/Z^2. The production of fragments increases with increasing the projectile A, the main parameter on

[12] Oliveira L.F. et al., "Abrasion-ablation calculations of large fragment yields from relativistic heavy ion reactions", Phys. Rev. C19 (1979) 826-833.

[13] Crespo P., "Optimization of In-Beam Positron Emission Tomography for Monitoring Heavy Ion Tumor Therapy", PhD thesis, Technischen Universitat Dresden, Germany (2005)

[14] Schardt D. et al., "Nuclear Fragmentation of High-energy Heavy-Ion beams in water" Adv. Space Res. 17 (1996) 287-204.

which σ_R depends. Carbon ions have been chosen at the beginning of the 90s as the best compromise between (i) low/high LET in the entrance/final part of the range and (ii) limited fragmentation with respect to lower/higher Z fragments. One of the advantages of nuclear fragmentation is the production of positron emitting nuclei. These nuclei, as explained below, allow the monitoring of primary particle range by means of a PET acquisition system.

2.3 Review of Monte Carlo codes available for medical applications

The Monte Carlo technique has become ubiquitous in medical physics in the last fifty years. The range of applications is very broad: commercial treatment planning systems for external beam radiotherapy, brachitherapy, dosimetry, diagnostic x-ray applications and radioprotection are only some of the major examples. One of the most important tasks in conventional radiotherapy, as well as light ion therapy, is the determination of the dose distribution expected in patients. Monte Carlo techniques have always been understood to be the most accurate way to perform this task, but the time required for the calculations was considered as prohibitive. However, as computing power continues to decrease in cost while increasing in speed, it becomes increasingly feasible to use Monte Carlo for treatment planning.

Up to now, Monte Carlo applications in the medical field have involved mainly electron and photon interaction and transport in matter. The most widely applied codes to conventional radiotherapy are EGS (Electron Gamma Shower) [15] and PENELOPE (PEnetration and Energy Loss Of Positrons and Electrons). In 2000 Kawrakow [16]introduced new significant improvements to EGS which led to the development and release of the EGSnrc code. The ensuing software package handled the most difficult of the simulation problems, namely the calculation of the response of ion chambers. The PENELOPE package [17] contains a detailed treatment of cross sections for low-energy transport and a flexible geometry package which allows the simulation of accelerator transport lines. However these tools are not intended to manage hadronic interactions.

Other tools have higher potentials for light ions therapy applications. FLUKA [18] is one of the existing simulations of transport and interaction of particles in matter which is a complete multipurpose tool. In fact, it can treat hadron-hadron, hadron-nucleus, neutrino, electromagnetic and muon interactions up to 1000 TeV. It also manages interaction and transport of neutrons down to thermal energies. With the increasing interest of applications to dosimetry and therapy, a supporting software has been developed to allow the direct conversion of the output files from standard CT-scans directly into a voxel geometry for transport within FLUKA. In such a way the modelling of the human body is feasible. This tool has been successfully used in [19] for the calculation of dose and positron emitters' distributions in proton therapy. The reported agreement in range is 1 mm while the mean agreement between Monte Carlo and treatment planning dose calculations is within 3**%**, though local deviations up to 10**%** can occur. The accuracy of FLUKA to transport ion beam

[15] Bielajew A. F. et al., "History, overview and recent improvements of EGS4" , Technical Report PIRS-0436 (1994)
[16] Kawrakow I., "Accurate condensed history Monte Carlo simulation of electron transport: EGSnrc, the new EGS4 version", Med. Phys. 27 (2000) 485-498.
[17] Baro J. et al., "PENELOPE: an algorithm for Monte Carlo simulation of the penetration and energy loss of electrons and positrons in matter", Nucl. Instrum. Methods B100 (1995) 31-46
[18] Fassò A. et al., "FLUKA: a multi-purpose transport code", CERN Yellow Report 2005-10 (2005)
[19] Parodi K. et al., "Clinical CT-based calculations of dose and positron emitter distributions in proton therapy using the FLUKA Monte Carlo code", Phys. Med. Biol. 52 (2007) 3369-3387.

in matter has been investigated in [20], with an overall satisfactory agreement in both depth dose distribution and fragmentation processes.

The MCNP (Monte Carlo N-Particle) system is a highly stable code tracking neutrons, photons and electrons, by using evaluated data libraries for low-energy interaction probabilities. It is maintained by a large group of scientists of the Los Alamos National Laboratory. This code contains a very powerful geometry package, for example its lattice geometry combined with the "fully specified fill" capability is of great relevance in dosimetry applications. Thanks to the accurate modelling of neutron interactions, MCNP was widely used for reactor simulation and neutron dosimetry, especially related to BNCT (Boron Neutron Capture Therapy). In 1994 the development of the extended MCNP (MCNPX) was started, with an extension to a comprehensive set of particles and light ions [21].

Another multi-purpose particle and heavy ion transport Monte Carlo tool is PHITS (Particle and Heavy Ion Transport code System) [22]. It is capable to simulate hadron-nucleus reactions up to 200 GeV, nucleus-nucleus collisions from 10 MeV/u up to 100 GeV/u, transport heavy ions and all hadrons including low energy neutrons down to 10^{-5} eV, as well as leptons. The energy range of electrons and photons is restricted to 1 keV-1 GeV. Some new functionalities have been added to improve the analysis of the dose distribution in carbon therapy systems. The carbon ion depth-dose distribution shows a good agreement with experimental data, as reported in [23], where the carbon therapy aperture of the HIMAC beam line has been modeled and simulated by means of PHITS.

A dedicated Monte Carlo code for the simulation of the transport of protons and heavier ions in tissue-like media is SHIELD-HIT, a spin-off of SHIELD [24]. The original tool simulates the interactions of hadrons and atomic nuclei with complex extended targets in an energy range from 1 TeV/u down to 1 MeV/u, or to thermal energies in case of neutrons. Since the developments of SHIELD-HIT (Heavy Ion Transport) were driven by applications to ion radiation therapy, the most essential improvements refer to the inclusion of the fluctuations of ionization energy losses and multiple Coulomb scattering of heavy charged particles. Energy depositions up to and well beyond the Bragg Peak due to nuclear fragmentations are well predicted [25]. Satisfactory agreement is also found with experimental determinations of the number of fragments of a given type, as a function of depth in water, produced by 670 MeV/u ^{12}**C** and ^{14}N.

The Monte Carlo chosen for the present work is Geant4 (GEometry ANd Tracking) [26] [27], a general purpose tool developed for particle physics applications. Geant4 has been used for various applications in radiotherapy and it is the basis of the GATE simulation toolkit (see later) for nuclear medicine applications in PET and SPECT.

---

[20] Sommerer F.et al., "Investigating the accuracy of the FLUKA code for transport of therapeutic ion beams in matter", Phys. Med. Biol. ,51 (2006) 4385-4398.

[21] Waters L. S. et al., "The MCNPX Monte Carlo radiation transport code", AIP Conference Proceeding 896 (2007) 81-90

[22] Niita K. et al., "PHITS overview", AIP Conference Proceeding 896 (2007) 61-70

[23] Nose H. et al., "Improvement of three-dimensional Monte Carlo code PHITS for heavy ion therapy", J. Nucl. Sci. Tech.42 (2005) 250-255.

[24] Dementyev A. V. et al., "SHIELD-universal Monte Carlo hadron transport code: scope and applications", Rad. Meas. 30 (1999) 553-557.

[25] Gudowska I.et al., "Ion beam transport in tissue-like media using the Monte Carlo code SHIELD-HIT", Phys. Med. Biol. 49 (2004) 1933-1958.

[26] GEANT4 Web page: http://geant4.cern.ch

[27] Agostinelli S. et al., "GEANT4-a simulation toolkit", Nucl. Instr. and Meth. A 506 (2003) 250-303.

2.4 The Geant4 toolkit

Geant4 is driven by the software requirements of the high energy physics community. It's an object-oriented based software for particle transport; it is flexible thanks to its architecture, implemented so that the description of the physics processes is visible. The user requirements lead to a modular and hierarchical structure where sub-domains are linked by uni-directional dependencies as shown in Fig. 2.3. The main domains (categories) of the simulation are:

- geometry and materials;
- particle interaction in matter;
- tracking management;
- digitization and hit management;
- event and track management;
- visualization;
- user interface.

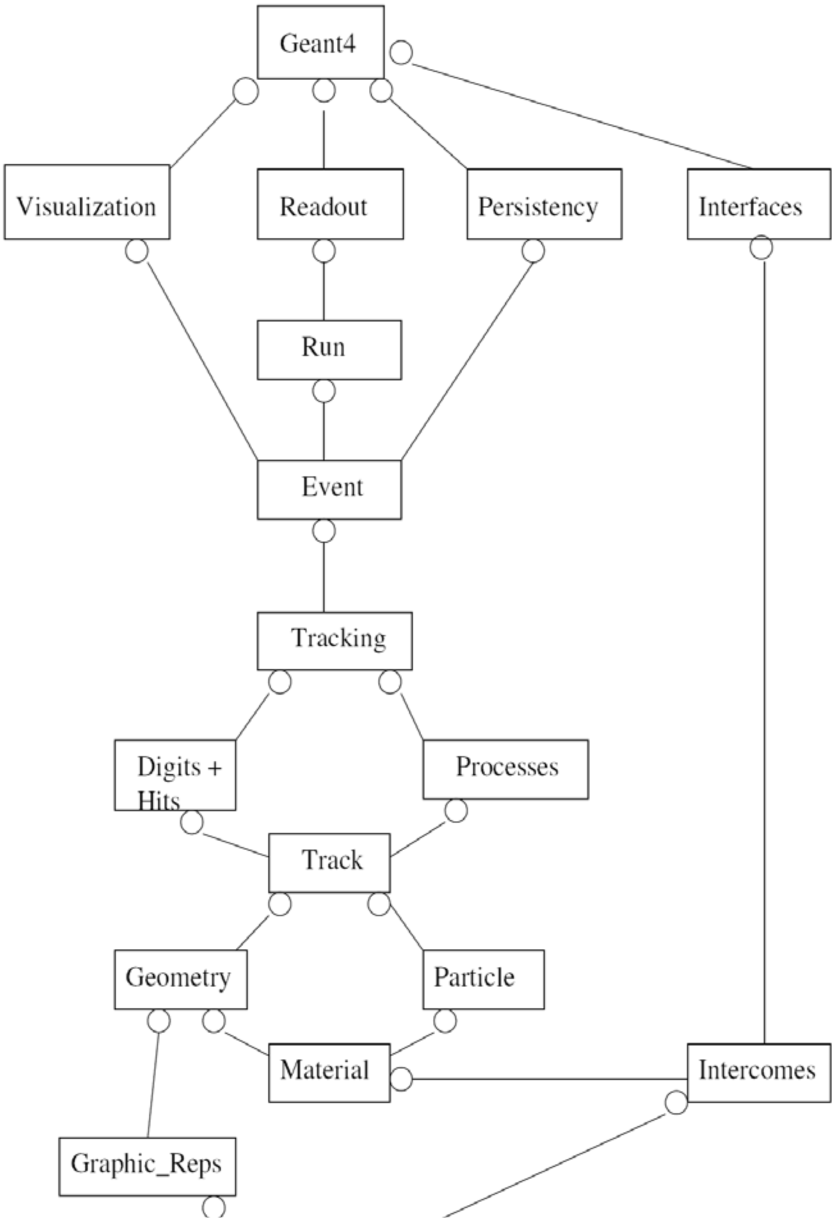

Figure 2.3 *The Geant4 toolkit modular diagram.*

The user has the ability to create a geometry with a large number of components of different shapes and materials, as well as to define sensitive components that record information (hits) to simulate the detector response [28]. To model the behaviour of particles in matter a wide and complete set of physics processes is implemented. In the flexible scheme of Geant4, the management of these categories is performed by the *track* category, which contains classes for tracks and steps (the Geant4 unit of length in the processing), used by *processes*, which handle models of physical interactions.

One of the main processes is *transportation*, that controls the transport of particles in the geometry model. The three main domains of physics processes are particle decay, electromagnetic physics and hadronic physics. The class G4Decay implements a decay mode according to branching ratios contained in the decay table for the particle. Geant4 provides some default decay tables and models to determine the distribution of secondary particles. A comprehensive description of the physics models implemented in Geant4 can be found in Ref. [29]. In the next Section a detailed description of the physics chosen to simulate light ion transport and interactions is given.

Physics models of the electromagnetic processes

In Geant4 many physics models, for electromagnetic and hadronic physics, are available. Electromagnetic physics is divided in two categories: the standard and the Low Energy (LE) physics. The development of the Low Energy (LE) package has been driven by the requirements coming from medicine and space research.

Low energy physics for photons and electrons is available in two flavours: one based on the Livermore Data Library and a second one based on the Penelope code, re-engineered in Geant4. These packages provide a set of processes extending the coverage of the standard electromagnetic physics down to 250 eV (Livermore) or to 100 eV (Penelope) for electrons and photons. The Livermore LE physics is based on Data libraries from Loma Linda National Laboratory that have been especially formatted for Geant4 distribution: EADL (Evaluated Atomic Data Library), EPDL (Evaluated Photon Data Library) and EEDL (Evaluated Electron Data Library). In principle the validity range of the libraries extends down to 10 eV, but some unstable behaviour has been encountered. A detailed atomic modelling is described in EADL for elements with $1 \leq Z \leq 100$, and atomic relaxation is also included for atoms with $Z>5$. In Ref. [30] the behaviour of LE electromagnetic physics was compared to the reference data provided by NIST for different materials , focusing on:

- the total photon attenuation coefficients;
- the cross sections of the individual processes of photons;
- the stopping power and the range of electrons in the Continuous Slowing Down Approximation (CSDA).

The Livermore LE model exhibits the best overall agreement with reference data with respect to the standard electromagnetic physics, deviating less than 3% from the data.

These arguments led to the choice of the Livermore LE physics to be implemented in the code used in the present study and the processes activated are:

---

[28] "User's guide", GEANT4 Web Page
[29] "Physics Reference Manual", GEANT4 Web Page: http://geant4.cern.ch/
[30] Amako K. et al., "Comparison of GEANT4 Electromagnetic Physics Models Against the NIST Reference Data", IEEE Trans. Nucl. Sci. 52 (2005) 250-303.

- γ: `G4LowEnergyPhotoElectric`, `G4LowEnergyCompton`, `G4LowEnergyGammaConversion` and `G4LowEnergyRayleigh`;
- e^- : `G4MultipleScattering`, `G4LowEnergyIonisation` and `G4LowEnergyBremsstrahlung`;
- e^+: `G4MultipleScattering`, `G4eIonisation`, `G4eBremsstrahlung` and `G4eplusAnnihilation`.

Low energy processes are also available to model the electromagnetic interaction of hadrons and ions. Different models are available, depending on the energy range, the particle type and the charge and their validity extends down to approximately the ionization potential of the interacting material. For energies larger than 2 MeV, the Bethe-Bloch formula is applied; below 1 keV the free electron gas model is used. At intermediate energies various models are available based on experimental data from Ziegler and on the ICRU reviews. Also in this case, the Geant4 stopping power and range of protons and alfa particles in the CSDA approximation have been compared to the NIST reference data, pointing out some discrepancies between standard electromagnetic physics and reference data for low energy alfa particles. Preliminary results [31] show an optimal agreement between the proton energy deposition curve and the ICRU49 LE based simulation. On the basis of these results, the LE electromagnetic physics with the ICRU49 parameterization has been adopted in the present application.

In treating electromagnetic processes it is possible to apply cuts (in range and in energy) on the production of secondaries. A range cut is converted, for each particle and for each interacting material, in an energy cut. In this way, if the energy deposited in a step is lower than this limit, the energy is supposed to be continuously deposited along the step instead of being released to secondaries. The energy production cuts give the possibility to produce only secondaries with energy larger than the indicated threshold. Depending on the purpose of the simulation performed, the two values can be tuned in order to achieve a good balance between the accuracy required (for example in Bragg curves computation) and the needed computational time (since the higher the number of secondaries, the higher is the number of particles to be tracked). For electromagnetic physics studies, the applied range cut is of 0.1 mm while the energy production cut has been set to 250 eV.

Physics models of the hadronic processes

The most critical part of the physics choice concerns hadronic processes. As already said, many models are available but few have been tested with experimental data for the energy range of interest in hadrontherapy (from few MeV up to few GeV).

The Bertini Cascade model has been selected to describe proton and neutron inelastic interactions [32]. It is a classical cascade in nuclear medium: the target nucleus is modelled in 3-D and the incident particle is propagated in a density-dependent nuclear potential. The interactions between the hadron and the nucleons are based on free-space cross sections. Each secondary produced by an initial interaction is propagated in the nucleus until it interacts again or leaves the nucleus. During the cascade exciton states are created and at the end, by means of nuclear break up, in evaporation or fission processes, fragments are produced. The validity range of the Bertini Cascade extends from 0 to 10 GeV. The Bertini

[31] CHEP 2007 Web Page: www.chep2007.com

[32] Heikkinen A and Stepanov N., "Bertini intra-nuclear cascade implementation in Geant4", CHEP conference proceeding (2003).

cascade has been implemented in this work by using proton and neutron inelastic cross sections provided by Geant4. The proton inelastic cross-section has been extrapolated from Geant4 and compared to experimental data in Fig. 2.4 [33].

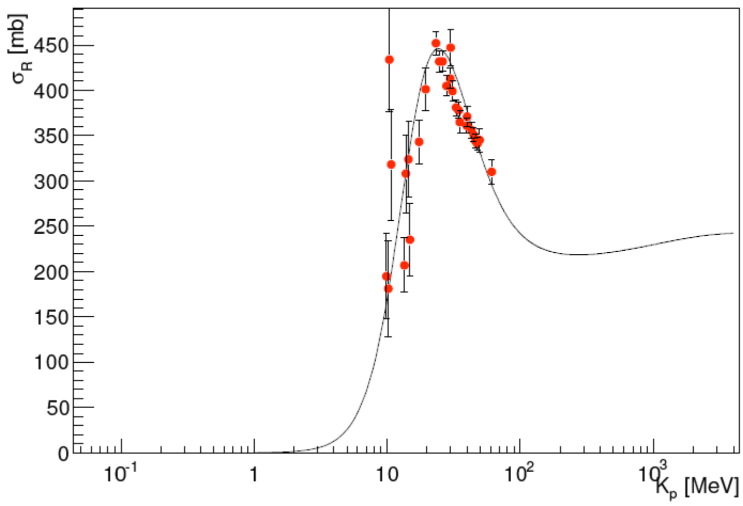

Figure 2.4 *Proton inelastic reaction cross-section on ^{12}C target, as implemented in Geant4, compared to experimental data.*

The elastic interactions of neutrons is handled by the Low Energy neutron elastic model. Low Energy models have also been used for capture and fission processes. Despite the validity of these models extends down to 0 MeV, in the very low energy range (0-20 MeV) the Geant4 High Precision (HP) model has been chosen. HP makes use of a very accurate database including both cross sections and final states.

In Geant4 for light ions (deuterons, tritons, ^3H, ^4H and generic ions) two models are available to simulate inelastic interactions: the Wilson Abrasion-Ablation model and the Binary Light Ion Cascade [34]. For this study, some preliminary investigations of the differences between the two models have been carried out. They do not exhibit marked differences, as confirmed by the proton and neutron production yield in a water target shown in Fig. 2.5.

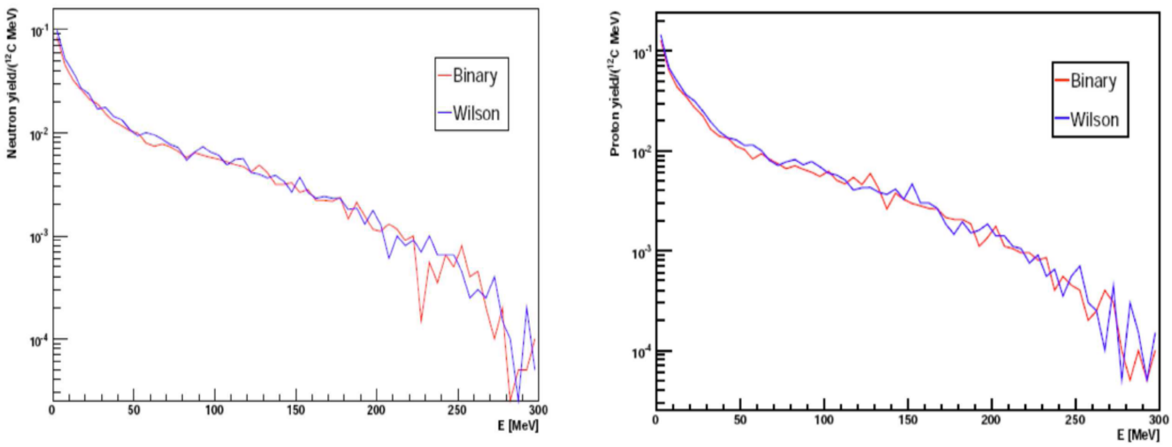

Figure 2.5 *Neutron (left panel) and proton (right panel) production yield for a 200 MeV/u carbon ion beam interacting in a water target.*

---

[33] Bauhoff W., "Tables of reaction and total reaction cross sections for proton-nucleus scattering below 1 GeV", Atomic Data and Nuclear Data Tables 35 (1986) 429-447.

[34] "Physics Reference Manual", GEANT4 Web Page: http://geant4.cern.ch/

Since the Binary Cascade model is thought to describe better the underlying physics and many other groups using Geant4 for medical applications have chosen it, it has been decided to concentrate on this model for the rest of the work presented in this thesis. The Binary Cascade modelling sequence is very similar to the Bertini Cascade, except that hadron-nucleon interactions create resonances that decay according to their quantum numbers. The model is valid for light ions with $A \leq 12$, or higher if the target has $A<12$. The lower energy limit of this model is 80 MeV but, since a model at very low energies for generic ions (so for carbon ions too) is lacking, the validity has been forced down to zero energy.

The Binary Cascade needs to be completed with nucleus-nucleus total reaction cross sections. Several models are available in Geant4 and in this study the Shen cross sections have been selected; Fig. 2.6 shows the comparison of the ^{12}C-^{12}C reaction cross section with experimental data [35].

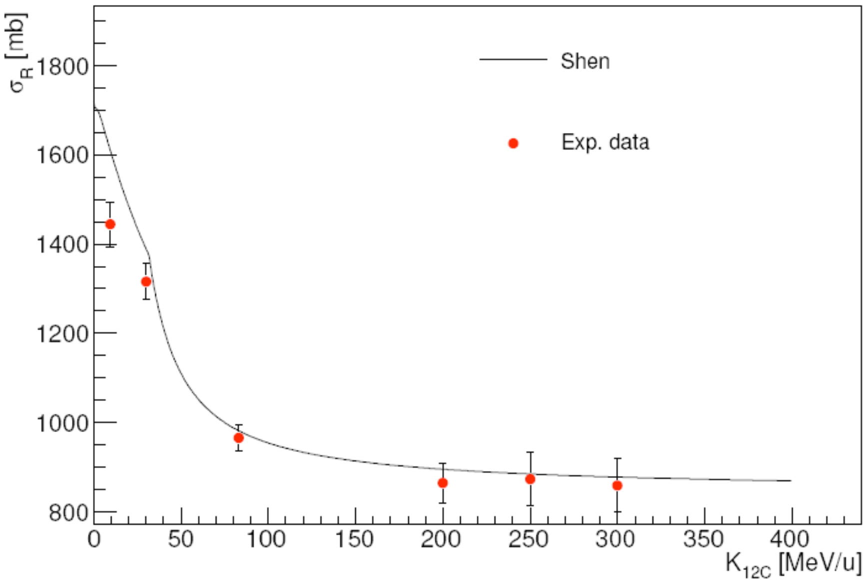

Figure 2.6 *^{12}C-^{12}C reaction cross-section extrapolated from Geant4 are compared with experimental data.*

For deuteron, triton and alphas in the energy range between 0 and 100 MeV, the Low Energy Parameterized (LEP) models have been implemented. They are based on fits of data and theoretical models, and are faster than cascade models even if less accurate. For π^+ and π^- the LEP model has also been used. The Low Energy Elastic scattering model has been applied to all particles (except neutrons). This is a classical scattering description, based on parameterizations of the cross sections and angular distributions. It can be in principle used for all long-lived hadrons at all energies.

The decay of radioactive nuclei is simulated in Geant4 by means of data driven models. The decays implemented are α, β^+, β^- and Electron Capture (EC). Data are derived from Evaluated Nuclear Structure Data File (ENSDF) where half-lives, nuclear level structure for the parent and daughter nuclide, branching ratios and energy of the decay process are reported. If the daughter of a nuclear decay is an excited isomer, its prompt nuclear de-excitation is treated by the `G4PhotonEvaporation` model.

All simulations of this study were performed by means of the release 8.2 of Geant4.

[35] Shen W. et al., "Total reaction cross section for heavy ion collisions and its relation to the neutron excess degree of freedom.", Nucl. Phys. A 491 (1989) 130-146.

2.5 Physics validation of the electromagnetic processes

In hadrontherapy applications, the first requirement for a Monte Carlo code is to reproduce with sub-millimetric precision the range of light ions in tissue equivalent material. The Bragg curve is mainly dominated by electromagnetic interactions, but the higher the energy and the *Z* of the projectile, the larger is the contribution to the dose by secondary fragments, both in the peak region and in the distal fragmentation "tail". In order to reproduce with high accuracy the Bragg curves of carbon ions, it is possible to operate a fine tuning by changing the value of the ionization potential (symbol *W*) of the target material. This approach is reasonable since it has been recently pointed out [36] that the mean ionization potential of water has a certain degree of uncertainty.

The simulation set-up consisted of a 30 cm water phantom divided in 100 μm thick slices, such a small thickness being chosen in order to locate the peak with high accuracy. The energy deposited by the primary mono-energetic pencil-like beam in the phantom was collected in each slice. The simulated curves were compared to experimental data acquired at GSI in water by means of an ionization chamber [37] at four primary beam energies: 100, 200, 300 and 400 MeV/u.

In order to find the optimal ionization potential of water, the difference between the experimental peak position and the simulated one at a certain energy was computed for different values of *W*: 72, 74, 76 and 78 eV.

Fig. 2.7 shows the behaviour of range difference when the *W* value is varied.

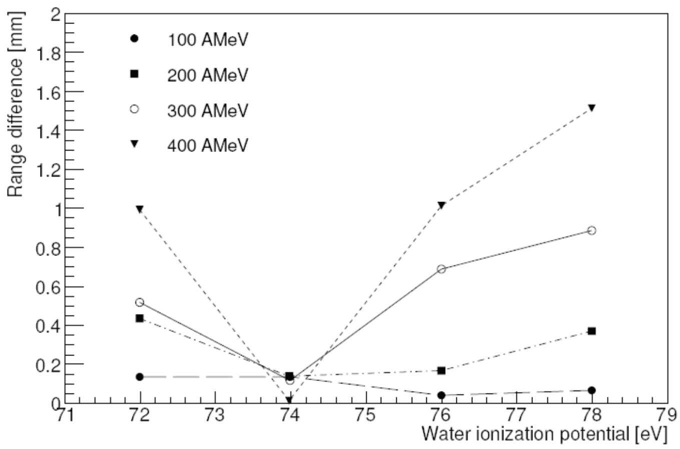

Figure 2.7 *Range difference between experimental and simulated Bragg curves of ^{12}C ions of 100 (filled circle), 200 (filled square), 300 (open circle) and 400 (filled triangle) MeV/u.*

The best agreement with the experimental data is obtained for a potential *W* =74 eV.

Note that the difference is less pronounced at low energies: at both 100 MeV/u and 200 MeV/u the computation agrees with the data better than 0.5 mm for all *W* values. The disagreement increases at higher beam energies. At 400 MeV/u energy, with *W*= 78 eV, the measured and computed ranges differ by 1.6 mm.

A more detailed insight in the dependence of Bragg curves on ionization potential is given by Fig. 2.8. It is seen that, with the choice *W*=74 eV, the measured and computed peak values agree within -6%and +15%.

---

[36] Helmut P., "The mean ionization potential of water, and its connection to the range of energetic carbon ions in water", Nucl. Instr. and Meth. B 255 (2007) 435-437.

[37] Bourhaleb F., personal communication.

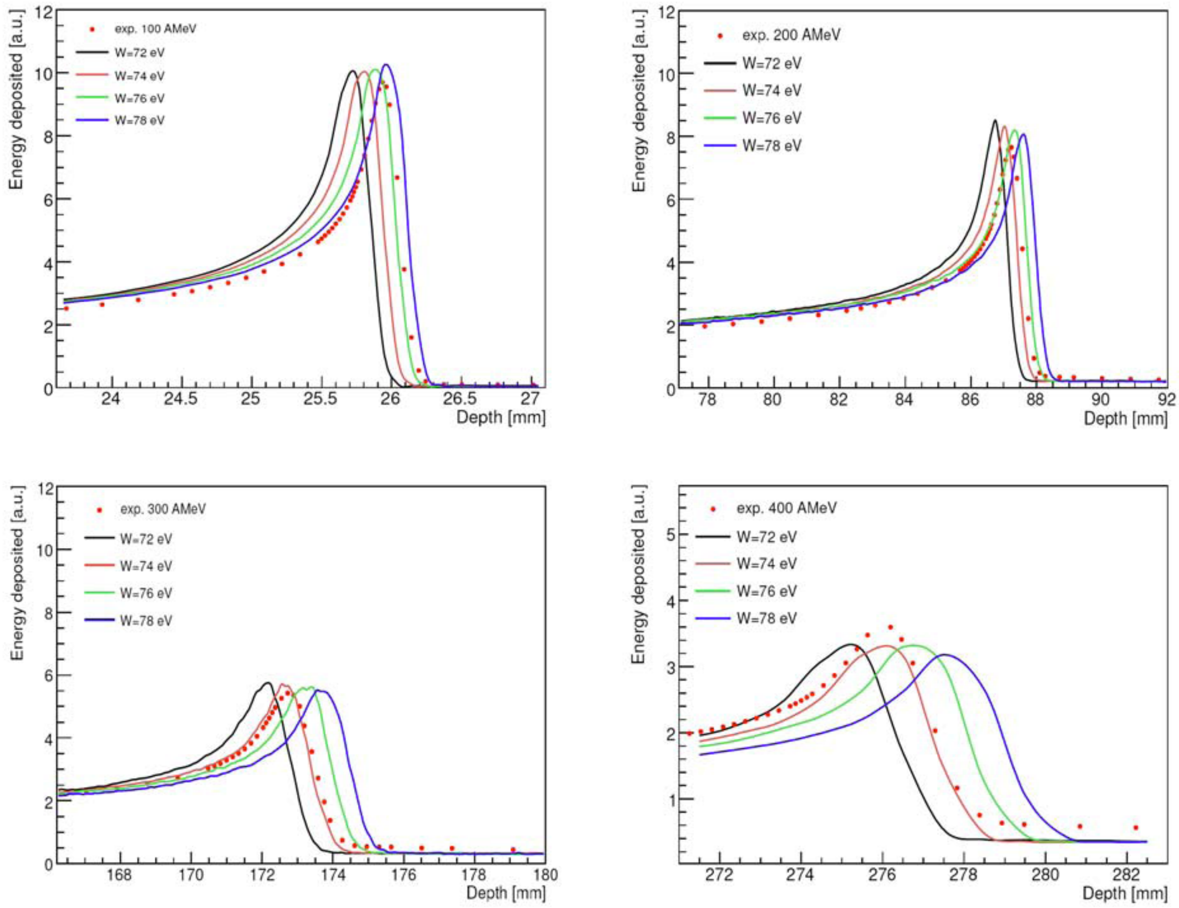

Figure 2.8 *Comparison of simulated Bragg curves with experimental data for different ionization potential.*

To further assess the correctness of the chosen *W* value, and not only by means of an integral estimator (i.e. the maximum of the Bragg curve), the single track range distribution was calculated for different values of the ionization potential. The positions where the carbon ions came to rest was fitted by means of a Gaussian and the mean value was assumed as the range at a given *W* value and primary energy. Fig. 2.9 shows the distributions at 400 MeV/u carbon ions.

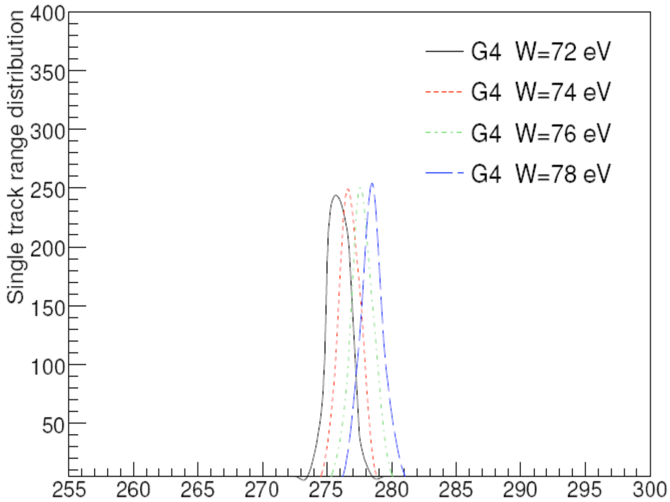

Figure 2.9 *Distributions of the single track range in water of 400 MeV/u carbon ions at different W values.*

The difference between the calculated differential ranges and the experimental ones are presented in Fig. 2.10. It is seen that the difference increases with increasing ionization potential. The optimal value is *W*=72 eV.

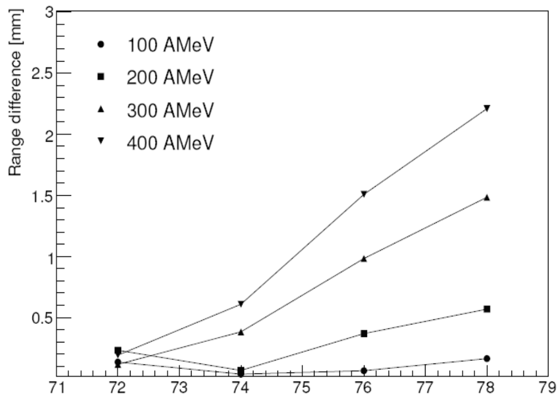

Figure 2.10 *Difference of the single track range with respect to the maxima of the experimental Bragg curves.*

The result slightly differs from the one previously obtained but since it refers to the comparison between the calculated differential and the experimental integral ranges, some deviations are acceptable. The difference with *W*=74 eV is less than 1 mm, so that this was kept as the optimum value of the ionization potential.

The overall agreement with experimental data is shown in Fig. 2.11. All the Bragg curves have been normalized to the energy deposited in the first slice, in order to have a common point.

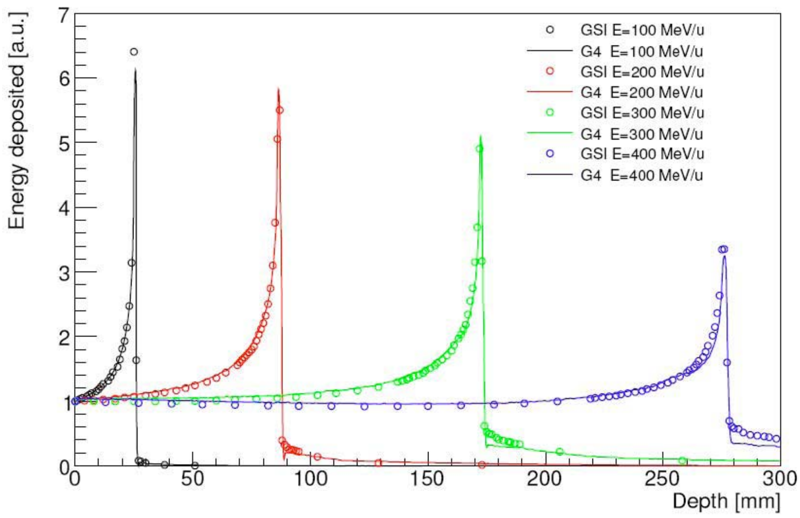

Figure 2.11 *Comparison of simulated carbon ion Bragg curves with experimental data at different energies in water.*

The agreement with experimental data is satisfactory in the entrance part of the curve, but at higher energies, when the fragmentation processes become increasingly relevant, the energy deposited in the tail is underestimated. The underestimation can be due either to an incorrect energy deposition by secondary fragments or to a lower fragment production yield. This point will be further investigated in the next Section.

Polymethyl methacrylate (PMMA, ρ = 1.18 g/cm) is a material that will be used in the next Sections for hadronic physics validation. Since it is important to verify the correctness of the coded electromagnetic processes in this medium, the Bragg curve was simulated and compared to the data published in Ref. [38]. In the experiment the primary carbon ion was 279.23 MeV/u. The value of the ionization potential used in the simulation is 68.5 eV, the Geant4 default value.

Since the calculation is performed in PMMA while the experimental data are given in water equivalent depth, a rescaling factor was applied to the curve. By taking the values at different carbon ion energies of the Stopping Power (SP) in liquid water and PMMA from ICRU73 [39], the ratio of the two SPs has been computed. For a wide interval of energies, down to few MeV, the ratio is nearly constant with an average value of 0.97. Considering the densities of water and PMMA, it comes out that 1 mm of Water is equivalent to 1.14 mm of PMMA which means that the same dose is deposited in 1.14 mm of water or in 1 mm of PMMA. As shown in Fig. 2.12, the agreement is good.

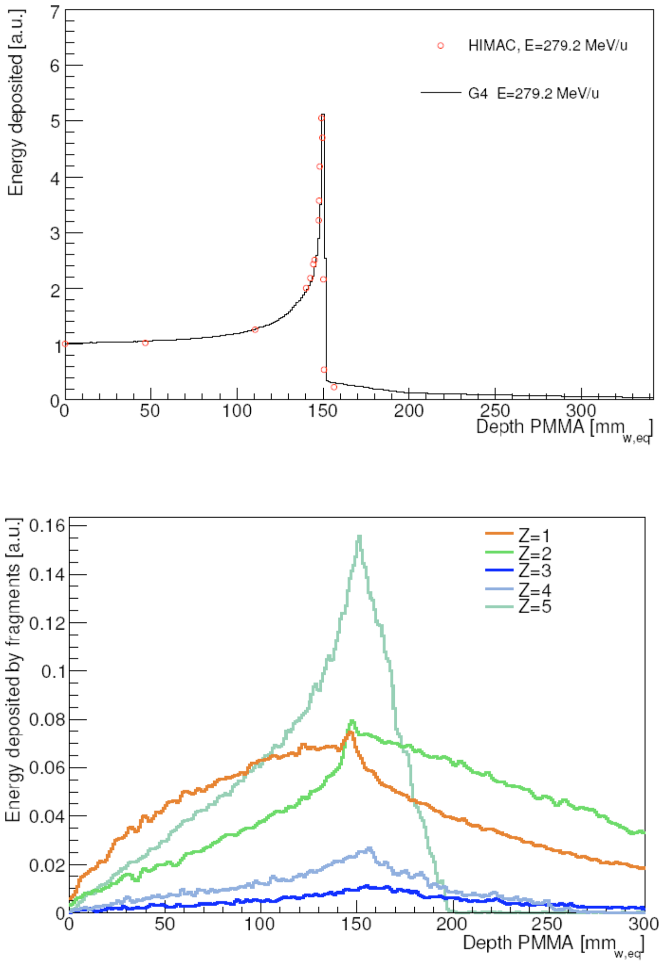

Figure 2.12 *Top panel: comparison of simulated Bragg curve with experimental data in PMMA for a 279.23 MeV/u carbon ion energy. Bottom panel: contribution to the dose due to secondary fragments.*

In the bottom panel of the same figure, the contribution of the secondary fragments to the energy deposited is shown. The larger contribution to the dose, in the region before the Bragg peak, is given by Z=5 fragments. In the distal region instead, the larger contribution is due to Z =1 and Z =2 fragments.

[38] Matsufuji N. et al., "Influence of fragment reaction of relativistic heavy charged particles on heavy-ion radiotherapy", Phys. Med. Biol 48 (2003) 1605-1623.
[39] "Stopping of Ions Heavier that Helium", Journal of the ICRU Report 73 5 (2005)

2.6 Physics validation of the hadronic processes

The production of projectile nuclear fragments is a most important but not yet well understood problem in the use of light ions for radiotherapy since the fragments - produced inside the patient body - reach a region beyond the range of the primary particles.

To compute their effect one has to take into account that the biological effectiveness of charged particles depends on the particle specie.

The fragment fluence, energy and LET distributions of each particle species, are often globally called "beam quality". The knowledge of the beam quality as a function of the depth is necessary for the precise estimation of the clinical effects of any therapeutic beam. Unfortunately hadronic interactions cannot be accurately simulated, because of the scarcity of good experimental data, and a model of high predictive capability has to be used.

The validation presented in the following is based on measurements performed at the GSI facility by E. Haettner [40] and by K. G. Marx [41] Both experiments were realized at the heavy ion synchrotron SIS18, accelerating ^{12}C ions between 80 MeV/u and 430 MeV/u. This energy interval corresponds to water ranges 2 - 30 cm.

In the study performed by E. Haettner, nuclear reactions have been studied in a water phantom with adjustable water thickness. The target was a 60x50x50 cm^3 box, with 2 mm thick plexiglass windows at the entrance and at the exit of the beam. A 5 cm diameter air filled tube entered the target and could be moved back and forth, so that the water thickness could be adjusted. A step motor controlled the movements of the tube with high precision and reproduced positions with an accuracy of 8μm. The number of incoming ions that hit the target were counted by means of a 1.5 mm thin plastic scintillator. The signal from this detector was also used to start the time-of-flight measurements and, for this reason, it was also called "Start detector". The detector area was 10x10 cm^2 and was always positioned in front of the target, few cm from the beam exit window.

In order to recognize the fragments exiting the target two approaches were applied.
The first technique was based on a thin scintillator used in dual mode: to measure the energy loss ΔE of the particle and the time-of-flight. The ΔE of a particle of charge Z and speed v is given by

$$\Delta E \propto Z^2 / v^2, \tag{2.8}$$

while the time-of-flight t is related to the kinetic energy of the particle as follows

$$E_{kin} = \frac{1}{\sqrt{1-(\frac{l}{t \cdot c})^2}} \cdot m_0 c^2, \tag{2.9}$$

where l is the distance travelled by the particle.

The second technique employed two detectors: a thin detector to measure the energy loss ΔE and a thicker detector, capable of stopping all the particles, to obtain the total energy E. The typical outputs of the two different measurements are shown in Fig. 2.13.

Even if the apparatus was intended to measure carbon ions, the telescope was capable of detecting secondary boron nuclei as well.

---

[40] Haettner E., "Experimental study on carbon ion fragmentation in water using GSI therapy beams", Master thesis, Kungliga tekniska hogskolan, Sweden (2006)

[41] Gunzert Marx K., "Nachweis leichter Fragmente aus Schwerionenreaktionen mit einem BaF_2 Teleskop-Detektor", PhD thesis Darmstadt University of Technology, Germany (2004)

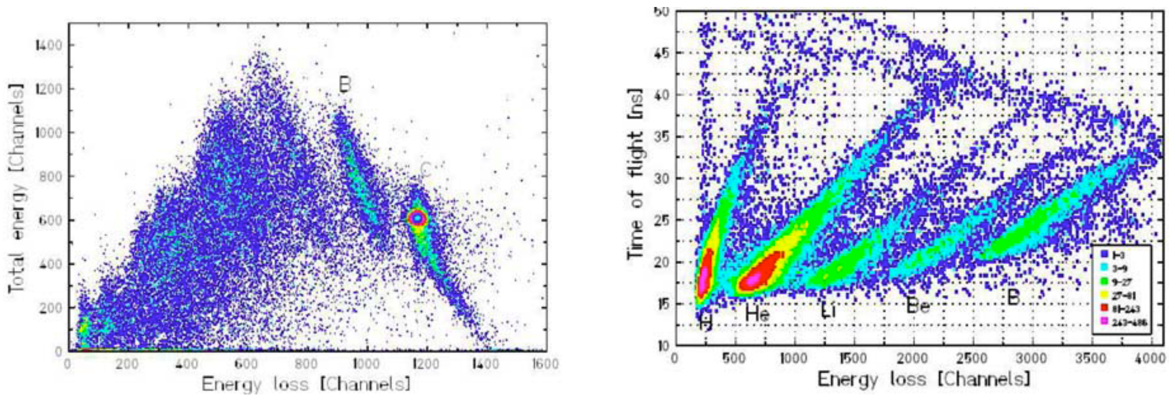

Figure 2.13 *Left panel: two dimensional representation showing E versus ΔE. Boron and carbon can be recognized easily, whereas particle with $1 \leq Z \leq 4$ cannot be distinguished. Data originate from 400 MeV/u carbon beam passing through a 23 cm thick water target. Right panel: two dimensional representation showing TOF versus ΔE. The data were obtained by Haettner with a 400 MeV/u carbon beam fully stopped in a 28.8 cm water target.*

The figure shows the capability of the telescope to identify and resolve carbon and boron nuclei.

Primary beam characterization

The paper by E. Haettner presents two studies. The first one is centred on the characterization of the primary beam. For this purpose the ΔE-E telescope was used and the electronic chain optimized for carbon signals. The attenuation of carbon and boron ions has been computed by means of Geant4. Fig. 2.14 shows the comparison with the data obtained at 200 MeV/u and 400 MeV/u with beams having a FWHM of 5 and 7 mm respectively.

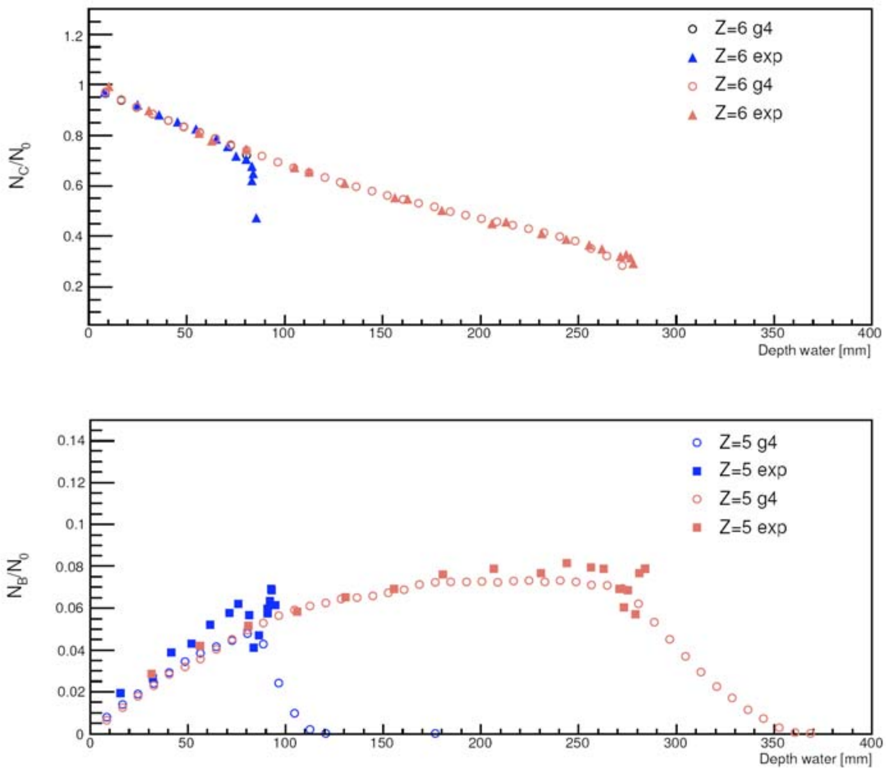

Figure 2.14 *Top panel: attenuation of carbon ions in water of 200 MeV/u (blue) and 400 MeV/u (red). Bottom panel: fluence of boron fragments in water produced by 200 MeV/u (blue) and 400 MeV/u (red) primary beam.*

To obtain the Geant4 points (indicated as g4 in the figure) the experimental set-up has been reproduced in the simulation. The 40 cm water phantom was divided into 8 mm thick layers and the ion fluxes were recorded at each layer interface, saving the properties of each fragment: *A*, *Z*, energy, position and momentum.

The attenuation of carbon ions is well described by an exponential, up to few centimetres before the Bragg peak, where the number of ions drops rapidly. The value of the attenuation length λ computed at 400 MeV/u from the simulation is 257 mm, to be compared to the value 259±5 mm reported by E. Haettner. Overall, both the simulated carbon and boron fluences are in excellent agreement with the experimental data.

Another interesting property is the evolution of the lateral distribution of carbon nuclei after traversing various water thicknesses. Experimentally, the lateral distribution of the particles was measured by means of a MWPC. From the simulation point of view, since the position of each ion is recorded at each slice interface, a Gaussian fit has been applied and the FWHM of the lateral distribution computed. The results of the calculation are compared with the experimental data in Fig. 2.15 for the same 200 and 400 MeV/u primary beams.

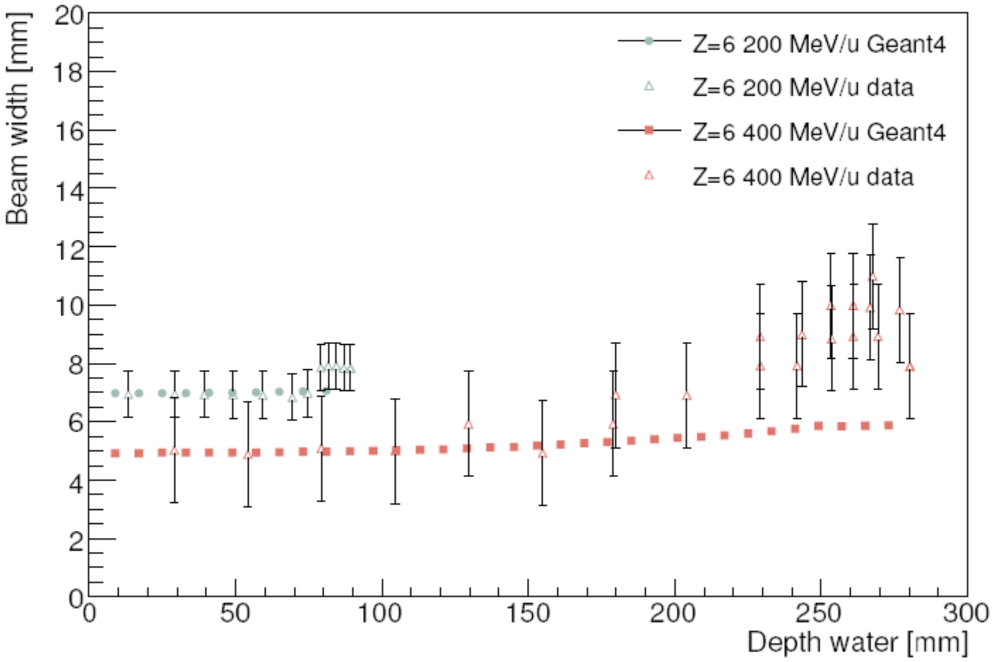

Figure 2.15 *FWHM of the transverse distribution of carbon nuclei at different water depths for 200 MeV/u (blue point) and 400 MeV/u (red point) primary beams.*

The distribution of carbon ions for the 200 MeV/u beam is in the error bars of the data acquired at GSI. At the higher energy the FWHM of the carbon beam is underestimated by Geant4. This happens in the last 10 cm before the Bragg peak, probably because the small angle approximation of the Monte Carlo simulation fails.

Fragment fluences and spatial distributions

The second study by E. Haettner aims to investigate the build up of fragments of different *Z* due to the interaction of 400 MeV/u carbon ions in water, whose range is 27 cm. Particles were identified with the time-of-flight technique. The angular spectra of the fragments were acquired at different angular positions between 0 and 10 degrees, with respect to the primary beam direction, and for seven depths of the water target, ranging between 5.9 and 34.7 cm. The angular distribution of each fragment was fitted with the equation:

$$f(\theta) = \begin{cases} f_g = \dfrac{A}{\sqrt{2\pi}\sigma} \cdot exp(\dfrac{-\theta^2}{2\sigma^2}) & \theta < \bar{\theta} \\ f_e = a \cdot exp(-b \cdot \theta) & \theta > \bar{\theta} \end{cases}, \tag{2.10}$$

where A, σ, a, b and θ are the parameters of the fit, depending on the nuclear specie and on the water thickness.

The fragment fluences at each depth in the water target were computed by integrating Eq. 2.10 between 0 and 10 degrees. Since the angular distributions of the Z=1 and Z=2 fragments extends to angles larger than 10 degrees, the experimental fluences of these two species are not the total one.

From the simulation point of view, the fluences are given by the number of particles passing through each interface between slices; no angular cut is applied. Since Li, Be and B fragments have a maximum angular aperture that does not exceed 10 degrees, the computed and simulated data can be compared directly.

In order to correct lower Z nuclei fluences, the angular distribution of fragments exiting a 15.9 cm water target was computed, and the results are compared with experimental data in Fig. 2.16.

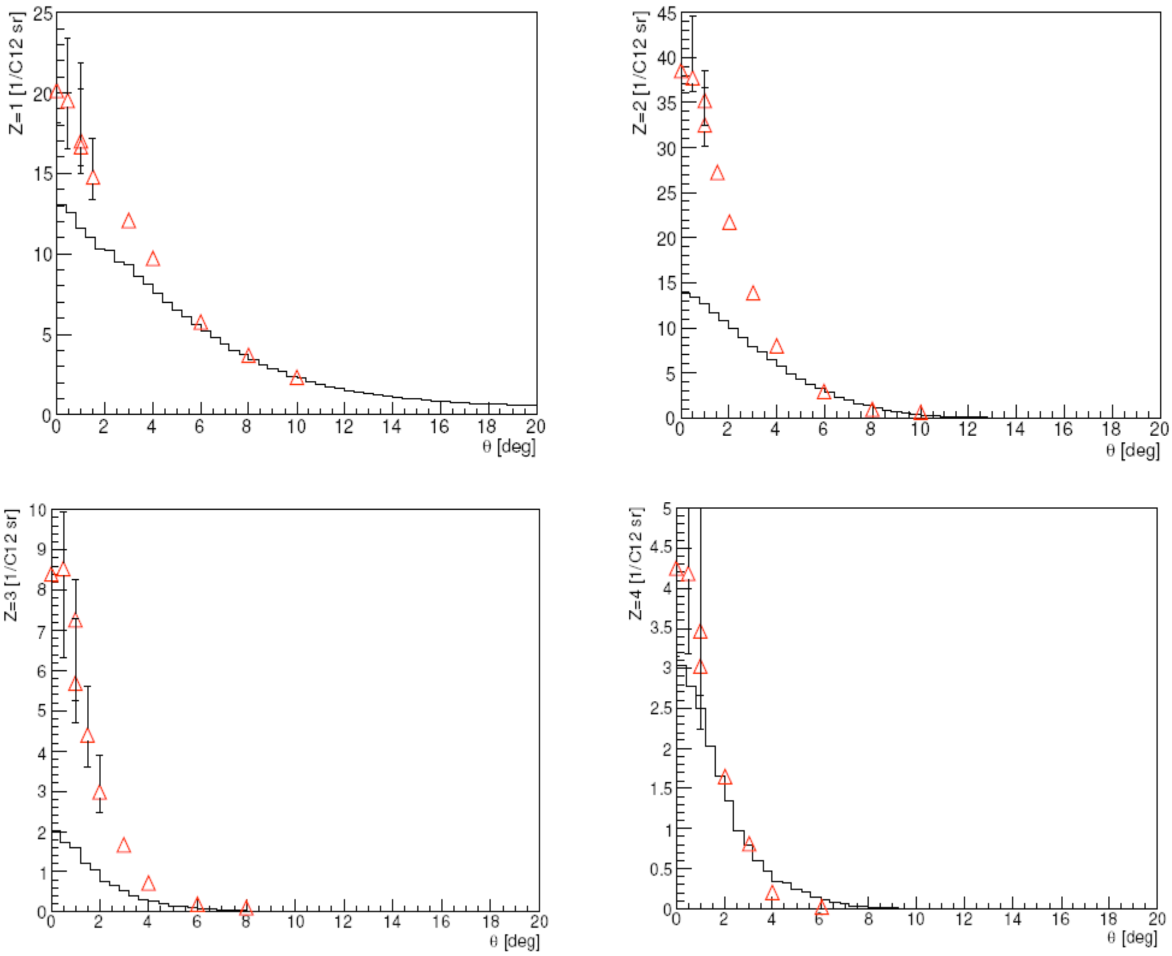

Figure 2.16 *The angular distributions of Z=1 (top left), Z =2 (top right), Z =3 (bottom left) and Z=4 (bottom right) computed by means of Geant4 (black solid line) are compared to experimental data (red triangles). The fragments, produced by a 400 MeV/u carbon beam, are detected 3 m downstream from a 15.9 cm thick water target.*

At the studied water thickness, the computed fractions of *Z*=1 and *Z*=2 fragments within 10 degrees are, respectively, 35% and 95% of the total. Experimental measurements pointed out that the shape of the angular distribution of every fragment does not change significantly by changing the water thickness, for the same energy of the primary beam.

By using this argument, the correcting factors calculated at 15.9 cm were applied to the computed fluences at all depths.

The simulated fluences are compared with the experimental data in Fig. 2.17. It is seen that both *Z*=1 and *Z*=2 fragments are underestimated by a factor 2. Beryllium and boron fragments are instead well reproduced, while lithium fragments are underestimated.

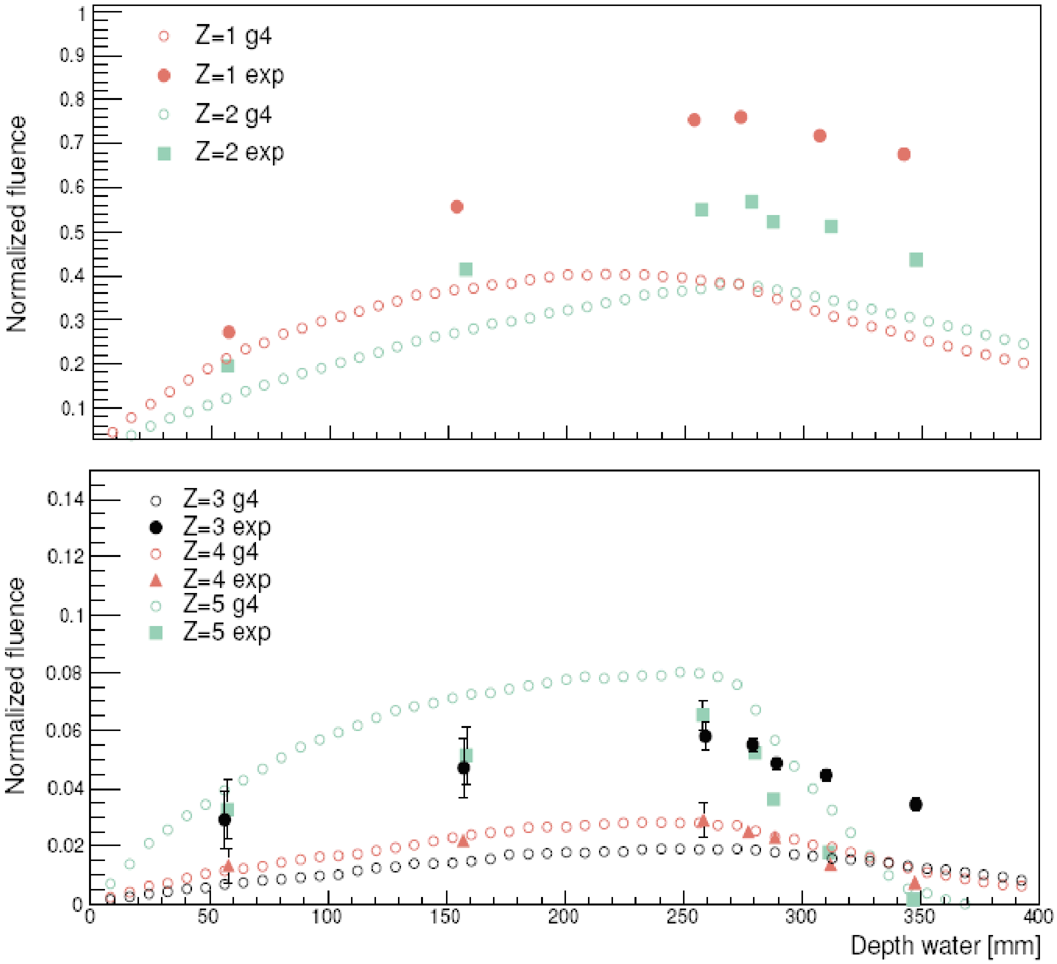

Figure 2.17 *Top panel: fluence per incident carbon in water of Z=1 and Z=2 ions for angles 0≤θ≤10°, at 400 MeV/u. Bottom panel: fluence of Z=3, Z=4 and Z=5 ions in the same condition as in the top panel. In both panels, open circles are experimental data and filled circles are computed results.*

In the study of C.G. Marx, a 200 MeV/u carbon ion beam is stopped in 8.5 cm in a 13 cm long water target. The ΔE-E telescope was placed 3 m downstream. The detector system was moved from -2 to 30 degrees, to collect fragment energy spectra at different angles. The time-of-flight spectra of the neutrons were converted into energy spectra according to the relation given in Eq. 2.2.

The fragment yields at different angles calculated with Geant4 and the ones experimentally measured are given in Table 2.2.

Table 2.2 *Fragment yields in various angular angular ranges with respect to the beam direction for a 200 MeV/u carbon beam fully stopped in 13 cm water.*

	$0-10$ **degrees**		$0-20$ **degrees**	
Fragment	**G4**	**exp.**	**G4**	**exp.**
n	0.098	0.109 ± 0.022	0.255	0.243 ± 0.049
p	0.070	0.076 ± 0.011	0.154	0.147 ± 0.022
d	0.024	0.038 ± 0.006	0.041	0.068 ± 0.010
t	0.008	0.016 ± 0.002	0.014	0.026 ± 0.004
^{3}He	0.008	0.028 ± 0.004	0.013	0.032 ± 0.005
^{4}He	0.075	0.086 ± 0.013	0.107	0.092 ± 0.014
	$0-45$ **degrees**		$0-90$ **degrees**	
Fragment	**G4**	**exp.**	**G4**	**exp.**
n	0.534	0.462 ± 0.092	0.751	0.541 ± 0.108
p	0.229	0.194 ± 0.029	0.256	0.198 ± 0.030
d	0.046	0.081 ± 0.012	0.046	0.082 ± 0.012
t	0.016	0.029 ± 0.004	0.016	0.029 ± 0.004
^{3}He	0.014	0.032 ± 0.004	0.014	0.032 ± 0.004
^{4}He	0.108	0.093 ± 0.014	0.108	0.093 ± 0.014

The yields of neutrons, protons and alfa particles are in good agreement with the experimental data over a wide angular range. In the simulated total production yield deuterons, tritons and He-3 fragments are underestimated by about a factor 2.

In Table 2.3 the Geant4 and the experimental results are compared with simulation results obtained by means of the FLUKA code [42].

Table 2.3 *Fragment yield fin the angular range $0 \le \theta \le 10°$ for a 200 MeV/u carbon beam.*

Fragment	**G4**	**FLUKA**	**exp.**
p	0.070	0.088	0.076 ± 0.011
d	0.024	0.039	0.038 ± 0.006
t	0.008	0.023	0.016 ± 0.002
^{3}He	0.008	0.016	0.028 ± 0.004
^{4}He	0.075	0.143	0.086 ± 0.013

FLUKA exhibits, compared to Geant4, an opposite trend since it overestimates all fragments, in particular alfa particles.

The energy spectra of neutrons, protons and alphas are compared to the experimental data in Figs. 2.18 and 2.19.

[42] Sommerer F.et al., "Investigating the accuracy of the FLUKA code for transport of therapeutic ion beams in matter", Phys. Med. Biol. 51 (2006) 4385-4398.

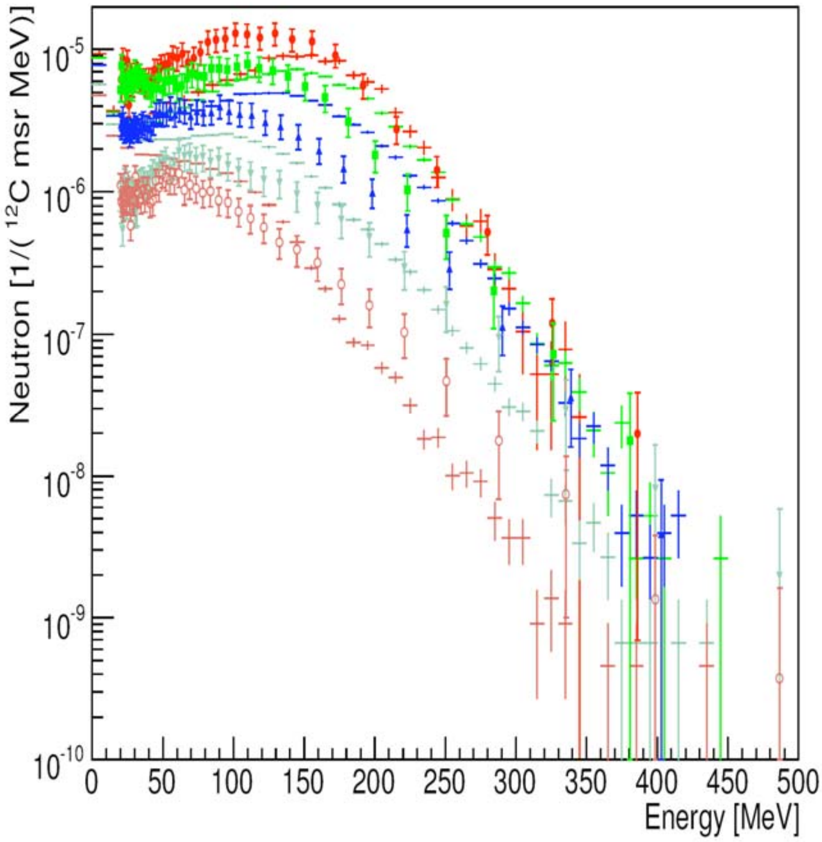

Figure 2.18 *Neutron energy spectra at 0, 5, 10, 20 and 30 degrees. Spectra are cut below 20 MeV because of the high inefficiency of the detector (data: bars; simulation: crosses).*

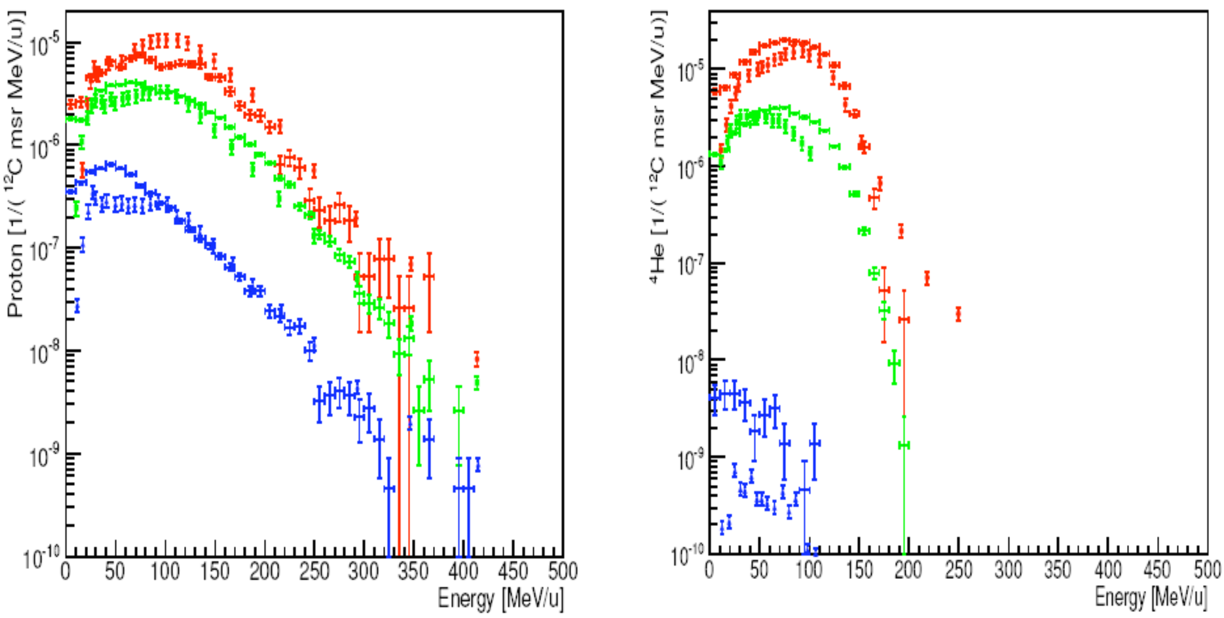

Figure 2.19 *Energy spectra of protons (left) and alfas (right) at 0° (data: red circles, simulation: red bars), at 10° (data: green squares, simulation: green bars) and at 30 (data: blue triangles, simulation: blue bars).*

The overall agreement is reasonable. Some deviations from measurements emerge for the fragments of Fig. 2.19 in the low energy part of the spectra, while the high energy components of the proton and neutron spectra are well reproduced.

The 0 degrees spectra are peaked around 130 MeV/u and the peaks move towards lower energies with increasing angular aperture. Neutron and proton spectra are rather wide. If we consider the abrasion-ablation model described in Section 2.2 as reference model, the energy distribution can be better understood.

The projectile nucleus, after the interaction with a target nucleus, can be left in an excited state. Therefore it de-excites emitting nucleons, with energy much higher than the mean primary beam energy per nucleon, also because of the Fermi momentum. These nucleons contribute to the high energy part of the spectrum. At intermediate energies, the spectrum is dominated by nucleons produced by the fireball break-up. Instead, the low energy component is mainly due to nucleons emitted by excited target nuclei. Heavier fragments, like deuteron, triton and alphas, come uniquely from the break-up of the fireball into small complexes.

2.7 Positron-emitters distribution in tissue-like media

In preparation of the work to be done for the definition of the in-beam-PET detector, this last Section is devoted to the comparison with experimental data of the yields of positron emitting nuclei computed with Geant4.

Among all fragments produced by carbon ion interactions, positron emitters are also produced. Since the initial energy per nucleon is the same and the momenta are nearly parallel, a clear correlation exists between the ranges of the primary ions and of the projectile β^+-emitter fragments. This correlation is the key point on which in-beam PET is based. The present study aims to test the capability of Geant4 to correctly reproduce the production yields and the spatial distribution of positron emitters produced by carbon ions. The experimental data used are taken from the very complete study reported in [43].

The measurements have been realized at GSI. Incident primary beams of different energies are considered. The target was made of PMMA instead of water, since the stochiometry ($C_5O_2H_8$) is much closer to that of human tissue due to the presence of carbon. The target dimensions were $300 \times 90 \times 90$ cm^3 box. The positron emitting nuclei considered in this study were ^{11}C, ^{10}C and ^{15}O. The first two species are produced by projectile as well as by target fragmentations. ^{15}O is instead only due to target nuclei break-up. Other positron emitters like ^{12}N and ^{8}B have lower production yields and shorter time-lives and tare not considered here.

In the experiment the targets were irradiated for an average time of 10 minutes. The activity induced was measured for 10-20 minutes after stopping the irradiation by means of the in-beam PET detector present at the GSI irradiation site. The relative amount of the isotope ℓ, N_ℓ, present at the end of the irradiation, was deduced by means of a fit of the activity measured for several minutes after the end of the irradiation. Since only monoenergetic beams have been used, the isotope production rate in each beam was supposed to be constant. Therefore it is possible to use a recursive formula to extrapolate the production rate of the isotope of interest, with the condition that the final amount at the end of the beam extraction must be equal to N_ℓ.

The measurements were repeated for several primary beam energies. In order to extrapolate an absolute isotope production rate, the measured activity must be corrected for the geometrical efficiency of the scanner and the gamma attenuation in the target. From the

[43] Parodi K., "On the feasibility of dose quantificaion with in-beam PET data in radiotherapy with ^{12}C and proton beams", PhD thesis,Technischen Universitat Dresden, Germany (2004)

simulation point of view, β^+-emitters have been identified and registered in the position where they decay.

In Tab. 2.4 the comparison of the calculated isotope yields with the experimental data is reported. Data for the energy of 337.50 MeV/u are taken from [44]..

Table 2.4 *Positron-emitter yields produced in PMMA for different carbon ion energies.*

Energy ^{12}C [MeV/u]	**$N_{^{11}C}/N_0$ [%]**		**$N_{^{15}O}/N_0$ [%]**		**$N_{^{10}C}/N_0$ [%]**	
	G4	exp.	G4	exp.	G4	exp.
212.12	10.2	10.5 ± 1.0	2.1	2.1 ± 0.2	1.9	0.8 ± 0.3
259.50	14.3	14.6 ± 1.5	3.1	3.1 ± 0.3	2.5	1.1 ± 0.2
337.50	18.9	22.0 ± 2.2	5.2	5.0 ± 0.5	3.4	1.6 ± 0.2
343.46	19.4	19.9 ± 2.0	5.4	5.1 ± 0.3	3.6	1.5 ± 0.3

The agreement with experimental data is very good for ^{11}C and ^{15}O yields. Instead, the few ^{10}C nuclei are overestimated by Geant4 by a factor two. The computed results for 259.5 MeV/u are compared in Tab. 2.5 with the production rates computed by the POSGEN code[45].

Table 2.5 *Comparison between the Geant4 and the POSGEN β^+-emitter yields in PMMA .*

Source	**Energy** [MeV/u]	**$N_{^{11}C}/N_0$** [%]	**$N_{^{15}O}/N_0$** [%]	**$N_{^{10}C}/N_0$** [%]
Data	259.50	14.6 ± 1.5	3.1 ± 0.3	1.1 ± 0.2
Geant4	259.50	14.3	3.1	2.5
POSGEN	270.55	26.7	10.0	2.0

For the lowest and the highest energies, the spatial distribution of β^+-emitters is shown in Fig. 2.20. It is seen that ^{11}C isotopes have a distribution characterized by a pronounced peak, since they are mainly produced by projectile fragmentations. In the same picture, the distribution of the annihilation points of e^+ is also shown: due to the low positron end-point energy of the considered isotopes, the mean path is rather low and the correlation to the real isotope distribution is very good. In the distal part of the Bragg peak, the long tail is made of isotopes mainly produced by proton induced fragmentation. ^{11}C has the same Z of carbon ions, but a lower A leading to a shorter range. But since the mass is lower, it experiences a higher multiple scattering, with a resulting broader spatial distribution, as shown in the bottom panel of the figure.

---

[44] Fiedler F. et al., "The Feasibility of In-Beam PET for Therapeutic Beams of ^{3}He", IEEE Trans. Nucl. Sci. 53 (2006) 2252-2259.
[45] Ponisch F. et al., "The modelling of positron emitter production and PET imaging during carbon ion therapy", Phys. Med. Biol. 49 (2004) 5217-5232.

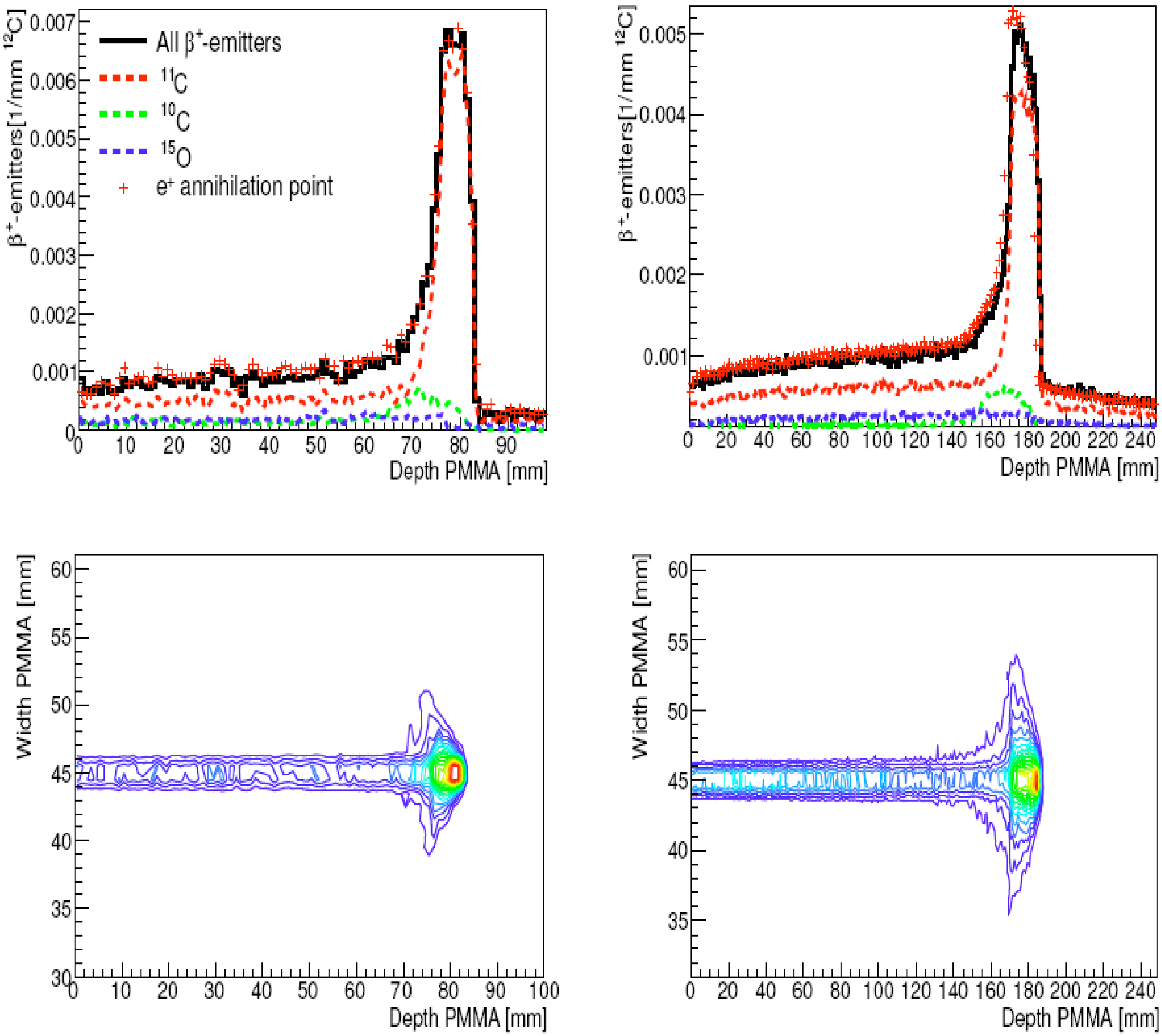

Figure 2.20 *Top panel: depth isotope distribution from 212.12 MeV/u (left) and 343.46 MeV/u (right) ^{12}C. Bottom panel: 2-D spatial distribution of all isotopes produced by 212.12 MeV/u (left) and 343.46 MeV/u (right) ^{12}C.*

The computed isotope distribution has been compared to experimental data reported by Ponisch F. et al.

The primary beam energy was 337.5 MeV/u and the target material was PMMA. Only coincidences coming from a well defined region of the target (slices of 5 mm each) have been acquired and, for each acquisition, the activity has been recorded at different times in short time window. The evolution of the activity with time should carry out information concerning the different radioisotope concentrations, since each one contributes inversely with respect to its time-life. Every isotope distribution has been normalized to the total number of isotopes produced (experimentally and computationally).

The result are given in Fig. 2.21. The agreement is excellent for ^{11}C and rather good for ^{15}O. ^{10}C is, as expected, overestimated. It can be seen that few centimeters before the Bragg peak region, ^{10}C distribution has a quite pronounced peak. This could signify that the high production rate of ^{10}C is due to the too high projectile fragmentation in Geant4.

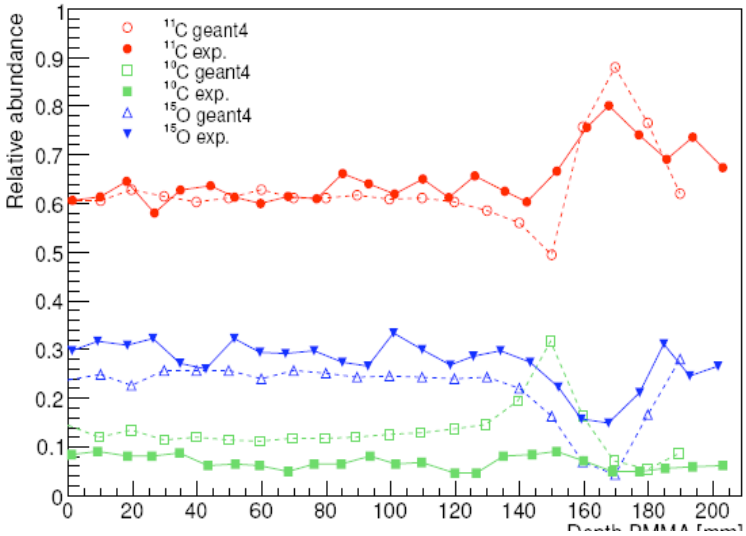

Figure 2.21 *Relative abundance of isotopes as a function of the depth in PMMA produced by a 337.5 MeV/u carbon beam.*

2.8 Discussion of the results

The Geant4 capability to reproduce the interactions of carbon ions in tissue equivalent material was tested with respect to both electromagnetic and hadronic physics.

Concerning electromagnetic physics, the Bragg curves in water and PMMA phantoms for different primary beam energies have been compared to experimental data. In order to achieve a sub-millimetric agreement with respect to the localization of the peak, a fine tuning of the ionization potential value of water has been operated. The optimum value is 74 eV, with which the entrance part and the peak position are correctly calculated.

At higher energies, when nuclear reactions play an important role, the energy released in the distal part of the curve is underestimated. This can be due to the low production yield of secondary fragments as well as to the incorrect energy deposited by lower Z fragments (mainly $Z=1$ and $Z=2$). This last hypothesis is less probable since the Low Energy Ionization model based on ICRU49 was chosen because of the good agreement with experimental data, with respect to protons and alphas, reported in several works. It has to be underlined that the calculated optimum value of the ionization potential ($W=74$ eV) reported in the present study has to be considered as relative. In fact, an improvement of the secondary fragment production and therefore of the energy deposited would require a new estimation of the W value.

Carbon ions attenuation in water is instead very well reproduced by the code and a mean value of the attenuation length $\lambda=257$ mm is obtained, to be compared to the experimental value $\lambda=259\pm5$ mm. Also the build up of boron fragments is in good agreement with experimental data .

While $Z\geq4$ fragments are well reproduced, the production yields of $Z=1$ and $Z=2$ fragments are underestimated by 50% and 30% respectively (Fig. 30) at 400 MeV/u carbon beam, whereas at 200 MeV/u the production yields of protons and alphas are in good agreement with measurements. Therefore with increasing the energy of the projectile the discrepancies are more pronounced, suggesting that some charge-changing cross sections are underestimated leading to an effect that increases with increasing the range and hence with the energy.

Since the attenuation of the primary carbon ions agrees with data and hence its total charge changing cross section, one can suppose that the low production yield can be due to an underestimation of the reactions induced by secondary fragments. This hypothesis needs further investigation and direct comparison with experimental data.

In the last release of Geant4 (9.0) new nucleon-nucleus reaction cross sections have been implemented, based on experimental data. A comparison was performed between the results obtained with the previous release (8.2) and the new one (9.0). Fig. 2.22 shows the comparison of the $Z=1$ and $Z=2$ fluences calculated by means of the last Geant4 release and the measured ones.

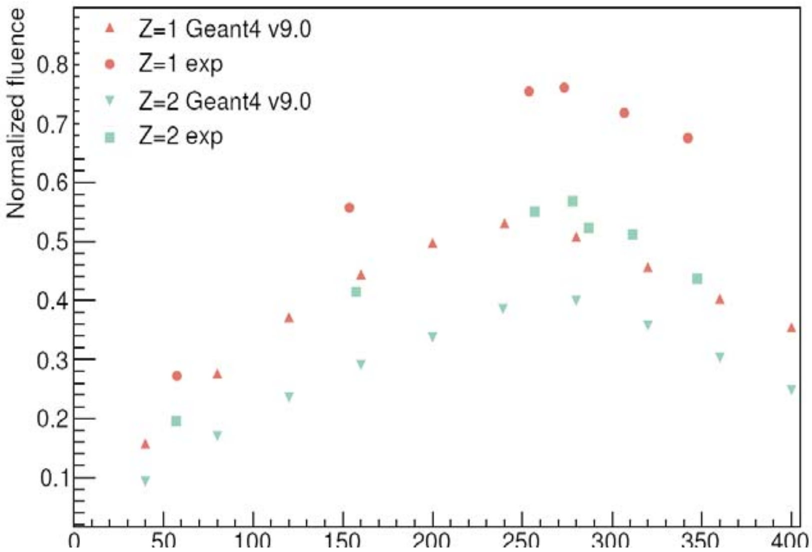

Figure 2.22 *Comparison of the fluences of $Z=1$ and $Z=2$ fragments originated by 400 MeV/u carbon beam in 30 cm thick water target obtained experimentally and by means of the new release 9.0 of Geant4.*

An increase of the $Z=1$ production yield has been obtained, with a 30% difference between calculated and experimental fluences to be compared to the 50% value obtained by the previous release.

The capability of Geant4 to correctly simulate the production of positron emitters and their distribution in tissue equivalent material has been also investigated. The isotopes analyzed are ^{11}C, ^{10}C and ^{15}O and a good agreement with experimental data was obtained leading to the conclusion that neutron emission is correctly reproduced by the code.

The overall agreement of the Geant4 based code described in the present Chapter is not completely satisfactory, at least with respect to the present physics choice. The most critical part concerns the fragmentation processes. The few experimental data available, in particular concerning partial charge-changing cross sections in the energy range of interest for hadrontherapy, make any more detailed validation extremely difficult.

3. INTERACTION VERTEX IMAGING AND NUCLEAR SCATTERING TOMOGRAPHY

3.1 Introduction

Together with the creation of isotopes exploited for on-beam PET imaging, charged and neutral particles are copiously produced by the projectile-target interactions, and constitute a severe source of background. However it is possible to exploit these secondary tracks produced by the beam to measure on-line the profile and the penetration depth of the beamd.

In the present proposal, only the ejected protons are considered, but the study can be extended to other charged particles (deuterons, alphas) that being more massive suffer less the dispersive effects of multiple Coulomb scattering in the target. Gammas could also be used, because they do not scatter on the way out. In this respect, neutrons would also be a good probe of the interaction vertex; but, while ways to detect neutrons and determine the direction of flight do exist, they are probably not efficient and accurate enough for imaging purposes.

Protons are produced in a wide angular and momentum range, both as direct result of nuclear interaction between the projectile and the target molecules, or indirectly from the interactions or decays of nuclei created in the primary interactions. The high momentum fraction of these particles emerges from the target with a direction that, while dispersed by multiple scattering in the body, retains information on the point of emission. A reconstruction of the outgoing protons tracks, intersected with the (known) direction of the carbon ion pencil beam, can thus provide information on the interaction vertex density distribution in the target.

The first part of this chapter addresses the power and limitations of a novel beam diagnostic method, thereafter named *Interaction Vertex Imaging* (IVI), based on the detection of emitted protons. In the second part, we will describe a method for obtaining 3-dimensional density distributions from the reconstruction of interaction vertices of high-energy protons with the target, named *Nuclear Scattering Tomography* (NST).

The two methods differ in two fundamental aspects: while IVI has to be made during the patient treatment and can serve as assurance of the treatment plan, NST needs a higher beam energy (above 600 MeV) and requires therefore a dedicated, medium exposure run. With the selection of elastic scatters, as discussed in Section 3.3, NST provides a first level of chemical analysis, imaging the hydrogen content in the target.

3.2 Interaction Vertex Imaging (IVI)

Fig. 3.1 gives a graphical representation of about twenty random ^{12}C interactions in the PMMA phantom, generated using the simulation tools described in Chapter 2.

Fig. 3.2 shows the Geant4 simulated distribution of proton emission vertices for a narrow beam of 400 MeV/u ^{12}C ions stopping in the standard PMMA phantom. While the secondary vertices generate a diffuse, forward-peaked halo, one can clearly see that the core of the distribution corresponds well to the position and range of incoming beam particles.

A scatter plot of the correlation between emission angle θ_x and kinetic energy, for several slices of penetration depth (Fig. 3.3), reveals as expected, that high momentum tracks tend to be emitted at shallow angles, and the density of those tracks diminishes with the penetration.

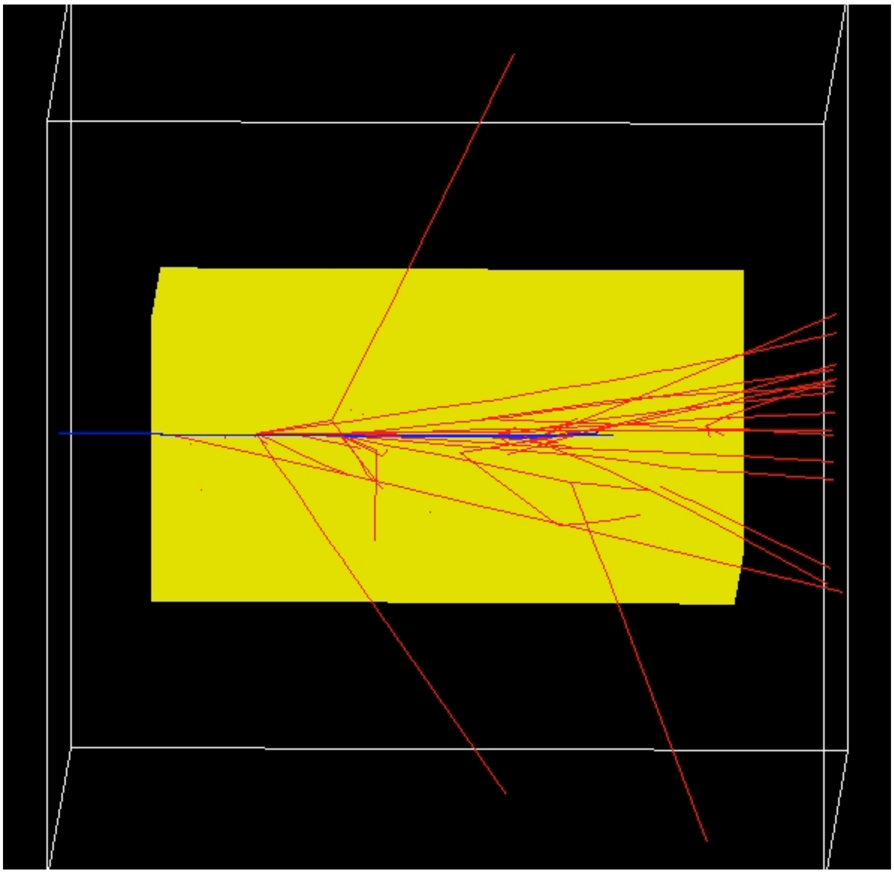

Figure 3.1 *Visualization by OPENGL of the PMMA target (yellow box) and carbon ions at 400 MeV/u (blue lines) stopping in the target. The red lines represent secondary protons produced mainly by primary beam reactions.*

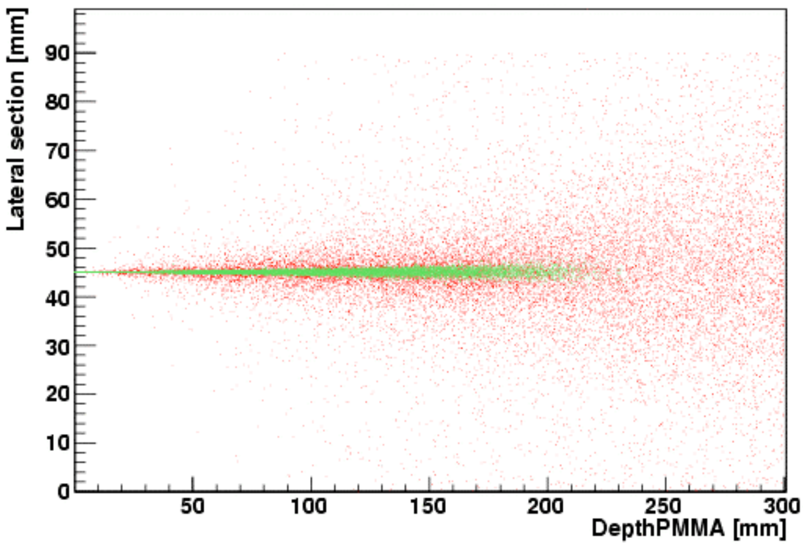

Figure 3.2 *Protons produced directly by primary beam (green points) and exiting from the target are grouped around the primary tracks penetrating 220 mm. The red points are secondary vertices produced by the fragments of the primary interactions.*

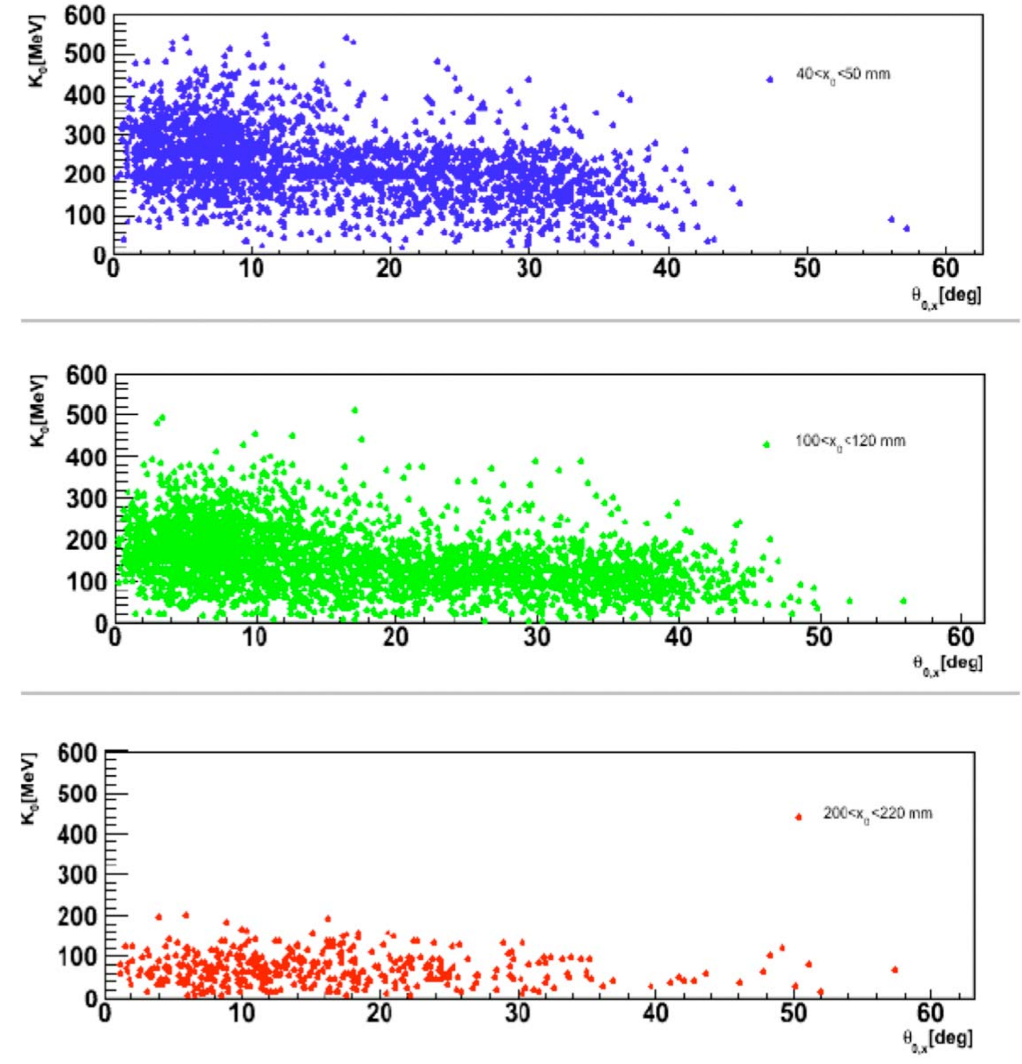

Figure 3.3 *Scatter plot of kinetic energy versus emission angle for different depth slices: 40-50 mm (top), 100-120 mm (centre) and 200-220 mm (bottom); θ_x is the angle of the track with respect to the incident beam direction.*

In Fig. 3.4, the differential energy loss distribution due to 50,000 carbon ions at 400 MeV/u, is superimposed to the computed density of the primary, secondary and total ion-proton vertices for all outgoing protons (top red curve), and with a selection of proton tracks above 100 MeV and 25º of emission angle (bottom green curve). The incident ions have a 22 cm range in PMMA, as shown by the full line histogram, The angular and energy cuts, while depleting the useful events, remove the tracks having excessive multiple scattering and/or a shallow crossing angle with the beam which imply a large vertex reconstruction error.

The production of protons increases along the depth in the target due to the increasing inelastic cross section with decreasing energy. However, lower energy protons produced near the end of the range are more attenuated even if the residual path to get out from the target is shorter. These effects combine resulting in a number of primary vertices monotonically decreasing to reach zero almost at the end of the range. Note that the energy loss distribution has a considerable tail after the Bragg peak as a consequence of the production of secondary long-range ions, but this does not contribute to the density of the proton interaction vertices. In both case, the overall distributions, which can be measured experimentally show a well characterized change of slope at a depth corresponding to the end of the range.

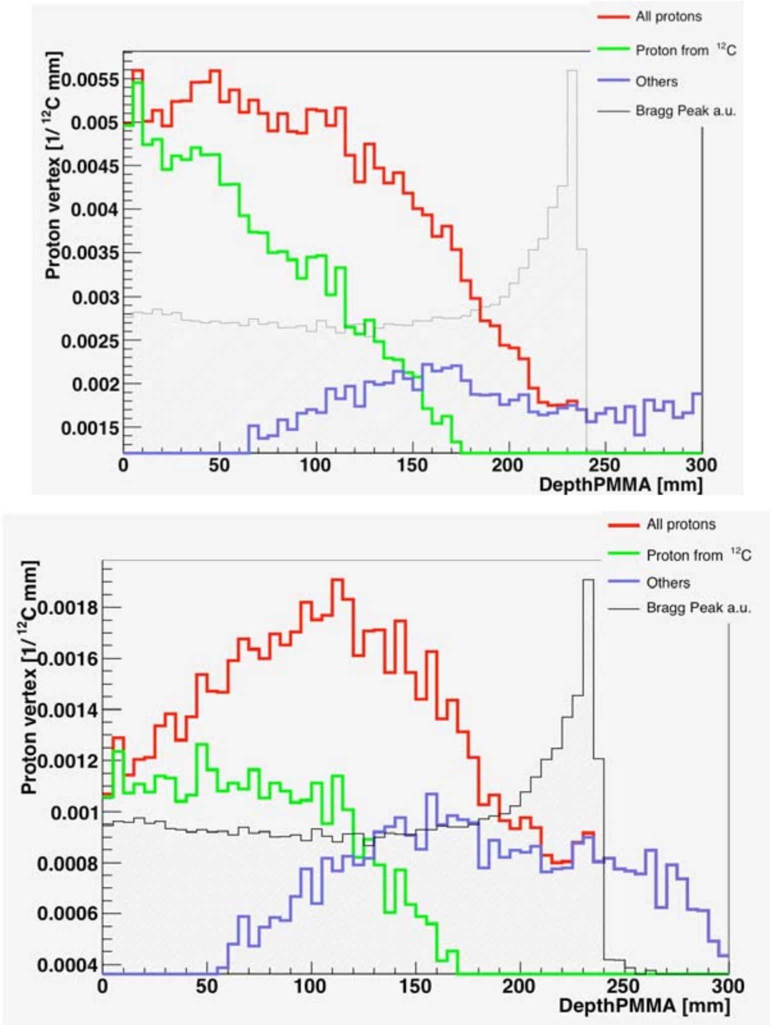

Figure 3.4 *Vertex distributions along the PMMA target of primary, secondary and total protons created by 400 MeV/u carbon ions and exiting the phantom. The calculated Bragg peak, due to not fragmented ^{12}C ions, is superimposed in order to make evident the correlation between the vertex distribution and the LET curve. Top: all events; bottom: selected events above 100 MeV and 25º.*

Due to the dispersive effects of multiple Coulomb scattering, the reconstructed proton track can differ significantly from the primary one, particularly at the lower energies. However, in view of the statistical distribution of the scattering, the average value of the measured tracks corresponds to the original emission direction.

For this first study of IVI, it has been assumed that incoming the proton tracks are localized with infinite accuracy in a set of detectors in front of the target because the intrinsic position accuracy of modern tracking devices is at least one order of magnitude better than the possible beam localization, limited by multiple scattering.

In the simulation, for each event the segment of minimum distance between the (known) beam track and the measured outgoing track has been computed. Assuming that the best estimate of the vertex is the middle point of the minimum distance segment, the differences between real and reconstructed vertices in the three projections have been obtained. Fig. 3.5 shows a scatter plot of the correlation between known and reconstructed vertex in the direction of the beam (the x coordinate), for outgoing tracks selected in energy and angle (E>100 MeV and cos θ_x<0.90).

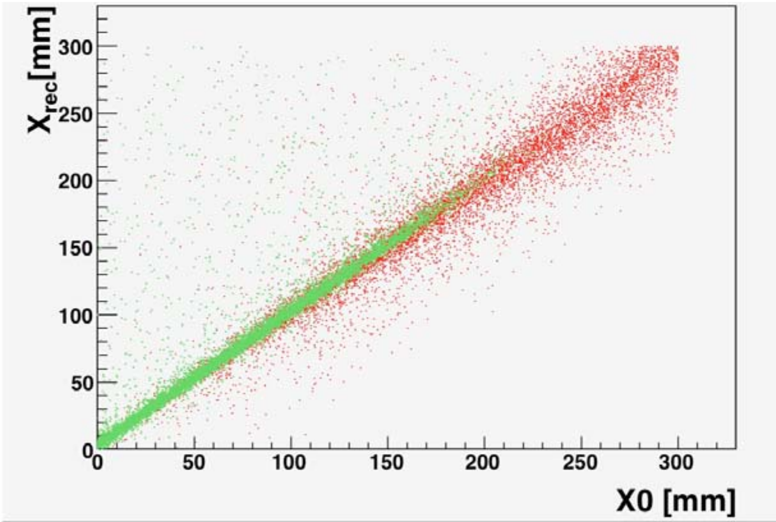

Figure 3.5 *Correlation plot between real and reconstructed vertex coordinates along the beam direction for primary (green) and secondary vertices (red). Tracks selection: E>100 MeV, cos θ_x<0.90.*

While dispersed by multiple scattering, the correlation is linear. The integrated density along the beam direction corresponds to the lower plot in Fig. 3.4. The difference between real and reconstructed events is shown in Fig. 3.6; Fig. 3.7 provides the distribution of the differences in the Y-Z plane, perpendicular to the beam.

A projection of the last plot on one axis (Fig. 3.8) shows that the data can be fitted by the sum of two Gaussians, a narrow one with a FWHM of about 6 mm, representing the reconstruction accuracy of the beam position, ad a wider one (FWHM ~ 30 mm) given by the background of secondary vertices.

The results of the simulation presented above, while preliminary, confirm the possibility of a determination of the range and transverse distribution of the beam from the measurement of the ejected protons. Further analysis is needed to ascertain the optimum strategy of angular and energy selections on the tracks to improve the quality of the results.

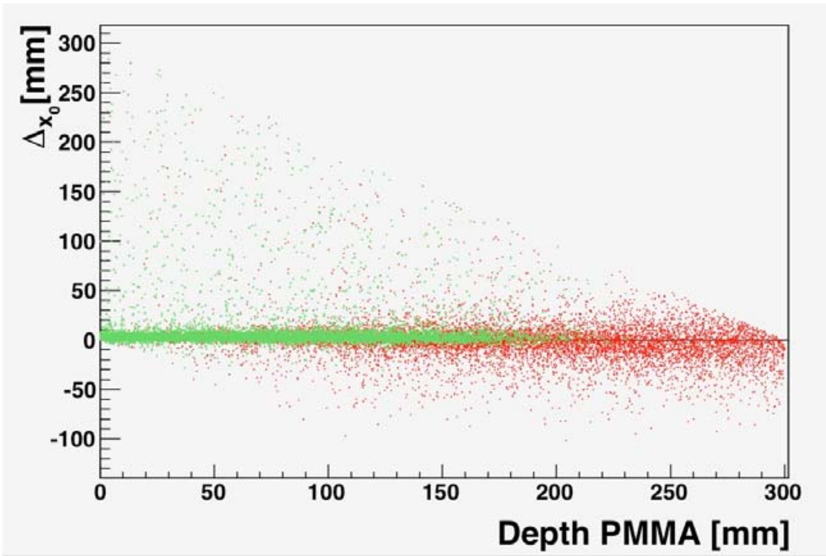

Figure 3.6 *Difference plot between real and reconstructed vertex coordinates along the beam direction for primary (green) and secondary vertices (red). Tracks selection: E>100 MeV, cos θ_x<0.90.*

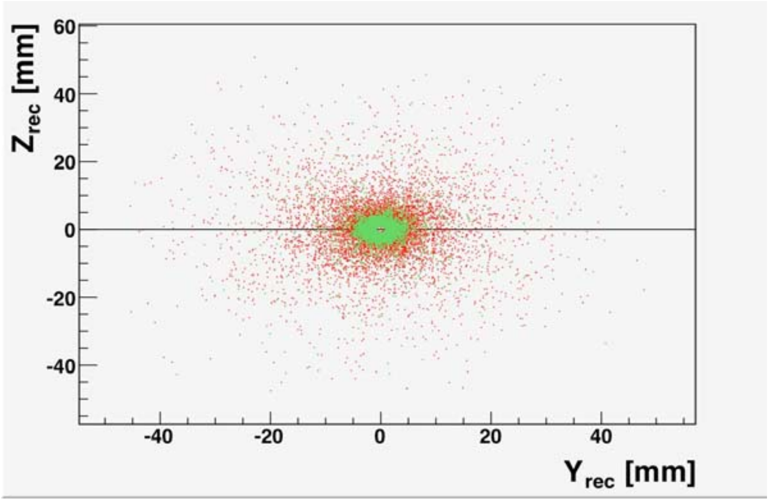

Figure 3.7 *Correlation plot between real and reconstructed vertex coordinates in the plane perpendicular to the beam direction for primary (green) and secondary vertices (red). Tracks selection: E>100 MeV, cos* θ_x*<0.9.*

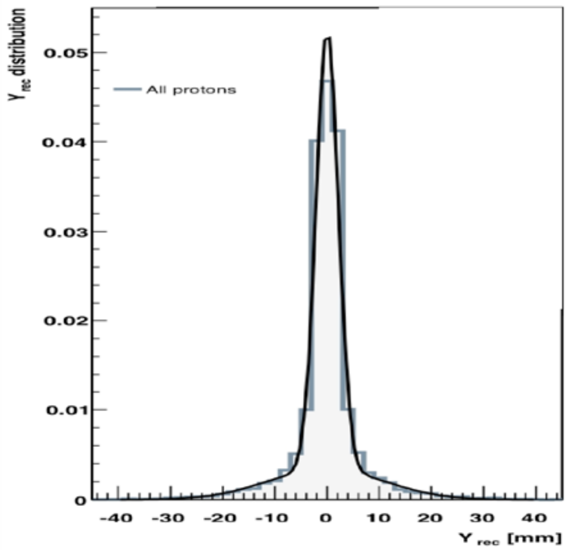

Figure 3.8 *Transverse distribution projected on one axis. The main Gaussian, representing the primary vertices, has a FWHM of 4 mm.*

3.3 Nuclear Scattering Tomography (NST)

The IVI method is similar to the so-called *Nuclear Scattering Tomography* developed long ago by the Charpak group[46], which allows the reconstruction of the three-dimensional density distribution in bodies by measuring the scattering angles of charged prongs produced by the interaction of high energy protons. Identification of the elastic p-p component permitted even to map the density of hydrogen in the body, a first level of elemental analysis. Successful from the imaging point of view, the method required the use of a high-energy particle accelerator, and remained a curiosity. Recently, a tomographic imaging method making use of the protons diffused by the target in proton therapy has been studied [47]. Due to the large

---

[46] Duchazeaubeneix J. C. et al, J.Computer Assisted Tomography 4 (1980) 803.
[47] Heimann J., Johnson L., Satogata T. and Williams D.C., IEEE Nucl. Sci. Symp. Conf. Rec. Vol. 5 (2003) 3663.

multiple scattering and absorption in the body of the protons a sophisticated data analysis is required to reconstruct the images[48]

At CNAO these techniques are applicable because the 400 MeV/u synchrotron can accelerate protons up to about 1200 MeV. One can thus imagine a short irradiation with a scanned beam of 600-800 MeV protons (so to remain below the threshold for pion production) before a treatment session which would give an *in situ* image of the patient body and of the organs to be then irradiated with the carbon ion beam. Gas chambers and plastic scintillators are the simple instruments needed for such in-beam mapping of the irradiated regions in the target.

The original setup (Fig. 3.9) included a set of Multiwire Proportional Chambers to record the coordinates of the incoming beam particle as well as of the scattered particles, and also several scintillation counters for geometrical selection of the events. After track reconstruction, and for events with two outgoing tracks, a coplanarity and angular selection permitted to identify the events due to elastic proton-hydrogen scattering.

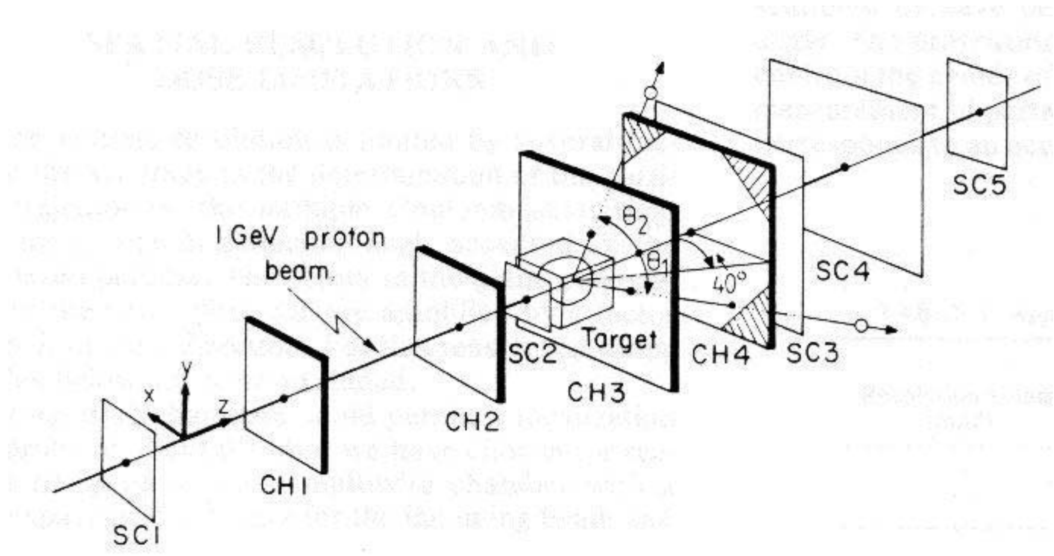

Figure 3.9 *Schematics of the proton scattering radiography setup.*

Fig. 3.10 shows the values of total and elastic cross sections for protons as a function of their momentum; one can see that the maximum is reached around 1200 MeV/c, corresponding to an energy of about 600 MeV. At this energy, about ½ of the collisions are elastic.

High-energy protons undergo several dispersive processes when traversing dense materials:

- Slowing down by to energy loss due to electromagnetic interactions, leading to ionizations and excitations along the trajectory. Fig 3.11 [49] shows the differential energy loss (stopping power) for protons in water, as a function of energy; above 5-600 MeV, protons are close to minimum ionizing and lose ~ 2 MeV cm^{-1}; in a 30 cm water-equivalent target, they lose about 10% of their energy.

- Multiple Coulomb scattering in the electromagnetic field of the nuclei; with a consequent modification of the trajectory. A 1 GeV proton scatters by about 10 mrad after traversing 20 cm of human-equivalent target.

- Elastic scattering by nuclear interaction on nuclei without breaking them: this process is limited to a very narrow range of forward angles.

48 Li T., Liang Z., Mueller K. et al, , IEEE Nucl. Sci. Symp. C. R. Vol. 4 (2003) 2767.

49 http://physics.nist.gov/PhysRefData/Star/Text/contents.html

- Quasi-elastic scattering on nucleons, either free in hydrogen atoms or weakly bound in other molecules; as the binding energy of nucleons is a few MeV, the collision has most of the characteristics of elastic scattering.

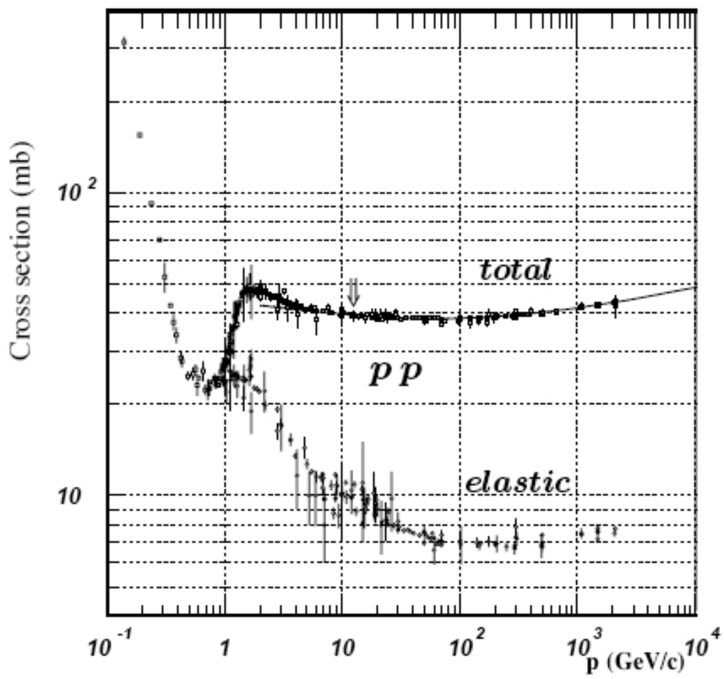

Figure 3.10 *Elastic and total proton-proton cross sections as a function of momentum.*

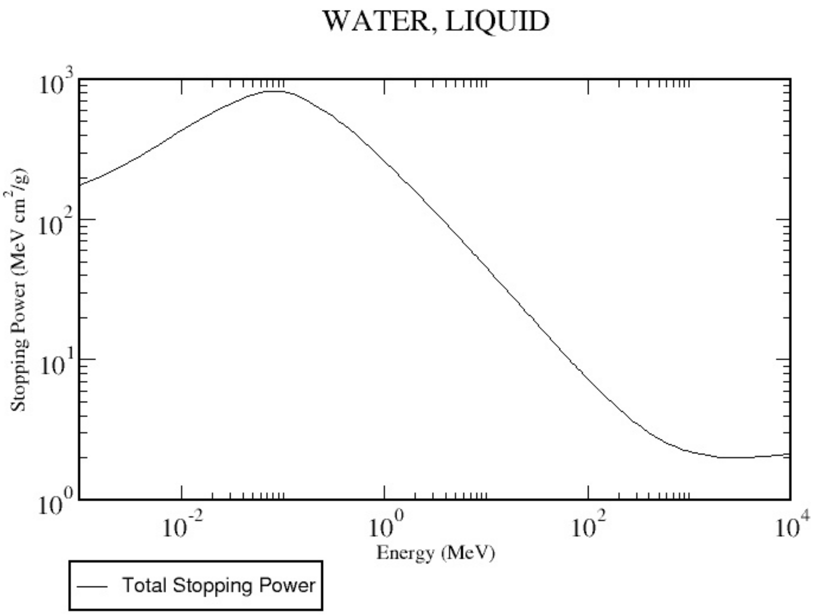

Figure 3.11 *Stopping power for protons in water.*

In the nuclear collision, the proton scatters at an angle and transfers momentum to the hit nucleon; if this is a neutron, it goes undetected and the vertex of the interaction is deduced only from the geometry of the incident and outgoing tracks. If the target particle is a proton, the two outgoing tracks are not distinguishable but emerge from the same vertex.

Fig. 3.12 provides the correlation between the outgoing angles in the laboratory frame for elastic proton-proton scattering. The angular coverage of the detector defines then the region of acceptance of elastic scatters (see the next section).

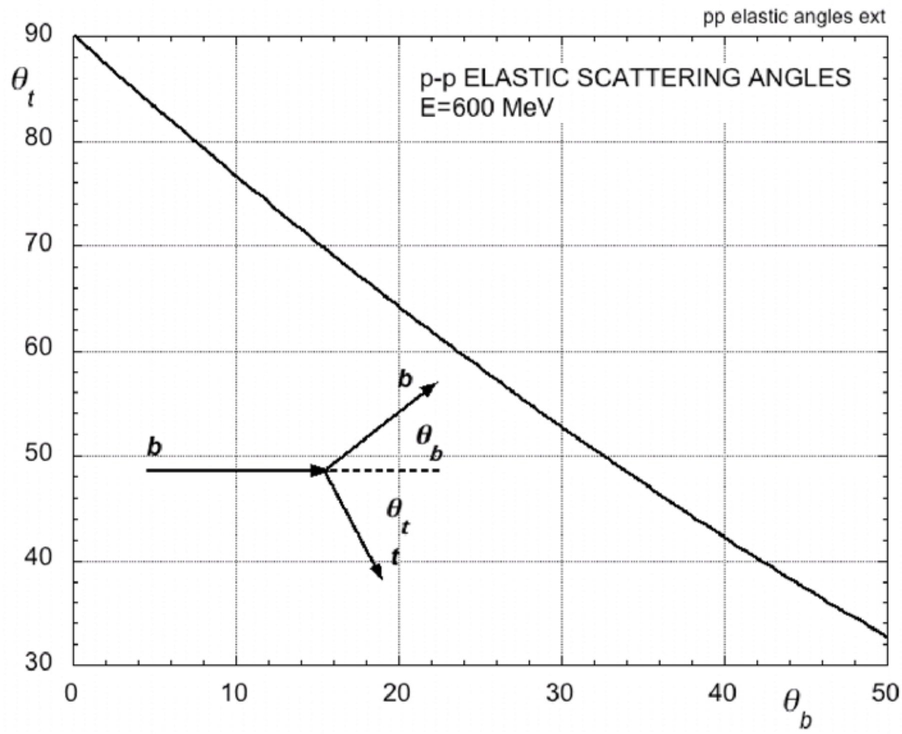

Fig. 3.12 *Angular correlation between scattered and target proton at 600 MeV.*

The kinematical correlation between scattering angles and a coplanarity check between the tracks can be used to select elastic scatters on (quasi) free hydrogen. Fig. 3.13 shows the distribution of the coplanarity angle measured by Charpak and collaborators with 1 GeV protons on quasi-free protons (water) and bound protons (carbon); Fig. 3.14 gives the distribution of the angle between the two outgoing tracks. One can see that a combined cut on the data a few mrad wide on the opening angle and on the coplanarity sorts out the majority of elastic events, permitting a hydrogen density measurement.

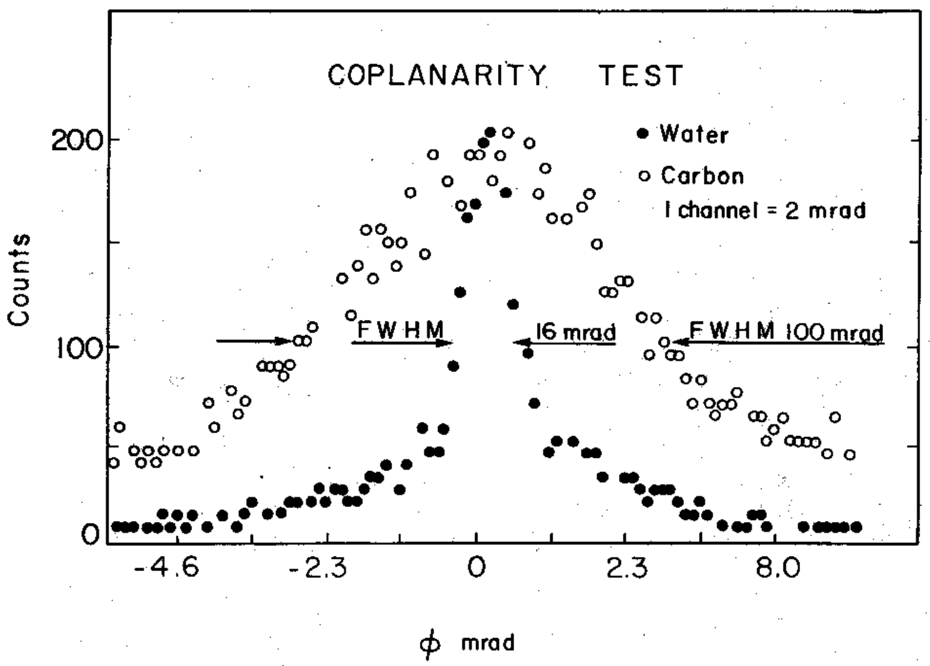

Figure 3.13 *Opening angle between two charged prongs measured for water (full dots) and carbon targets (open dots).*

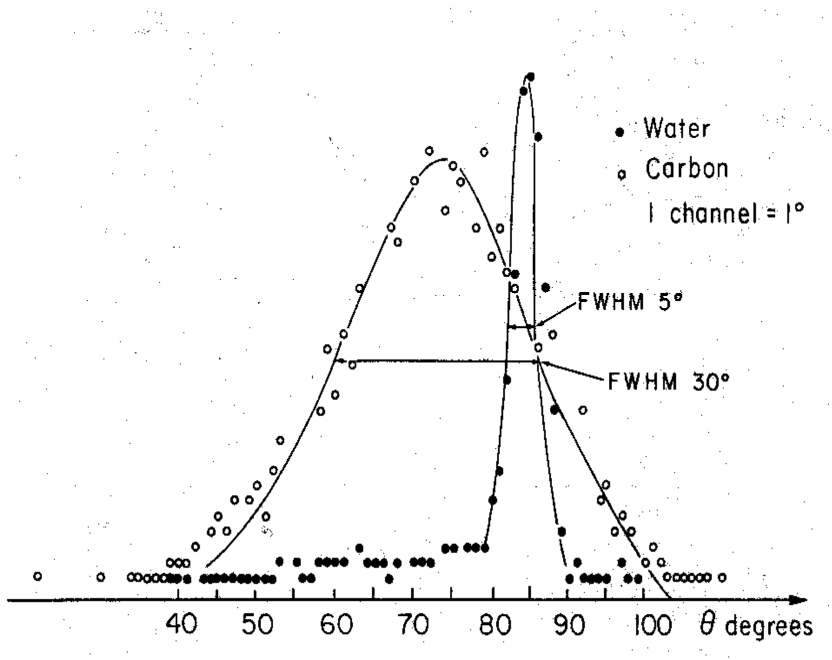

Figure 3.14 *Angle between the planes containing the incoming particle and each of the two outgoing tracks, for water and carbon target.*

The basic performances of NST have been assessed long ago by Charpak and collaborators. Seriously rate-limited by the technologies available at the time, Multiwire Proportional Chambers with events storage on magnetic tape, the initial experiments using an in-vitro target (a human head preserved in formol) confirmed the space resolution and three-dimensional imaging powers of the method.

With a volume resolution (voxel) of 5 mm^3, the authors could obtain a 5% density resolution with an exposure dose of about 5 mGy; with a typical data acquisition rate of 1000 events/s, and due to the use of a low duty cycle beam, obtaining full 3-D tomography required several days.

Examples of the density distribution in successive slices, 3 mm thick, through a human head are shown in Fig. 3.15 for the sagittal, transverse and frontal projections. The last pane shows a comparison of tomographic slices with one scattered track (top row) and selected elastic p-p events (bottom row). As clearly visible, the elastic selection completely eliminates the skull's bones from the image.

The system can be largely improved today using fast detectors and electronics, as well as improved reconstruction algorithms.

Using for diagnostics a beam scan strategy, as in the therapy exposure but at much reduced rate, the position of the beam for each scan is known within the required voxel size, and need not be measured. Making use of a pair of fast tracking detectors, such as the Gas Electron Multiplier with presently available electronics, one can achieve a data acquisition rate approaching 100 kHz. For a beam cross section of 5x5 mm^2 and voxels 5 mm deep, a 10x10x30 cm^3 target has 24,000 voxels. To obtain a 3% statistical accuracy, 2,4 10^7 events need to be recorded; a full field 3-D image could then be obtained in less than 3 minutes, delivering about one milligray. Perspectives of reducing the exposure time are discusses in the next section.

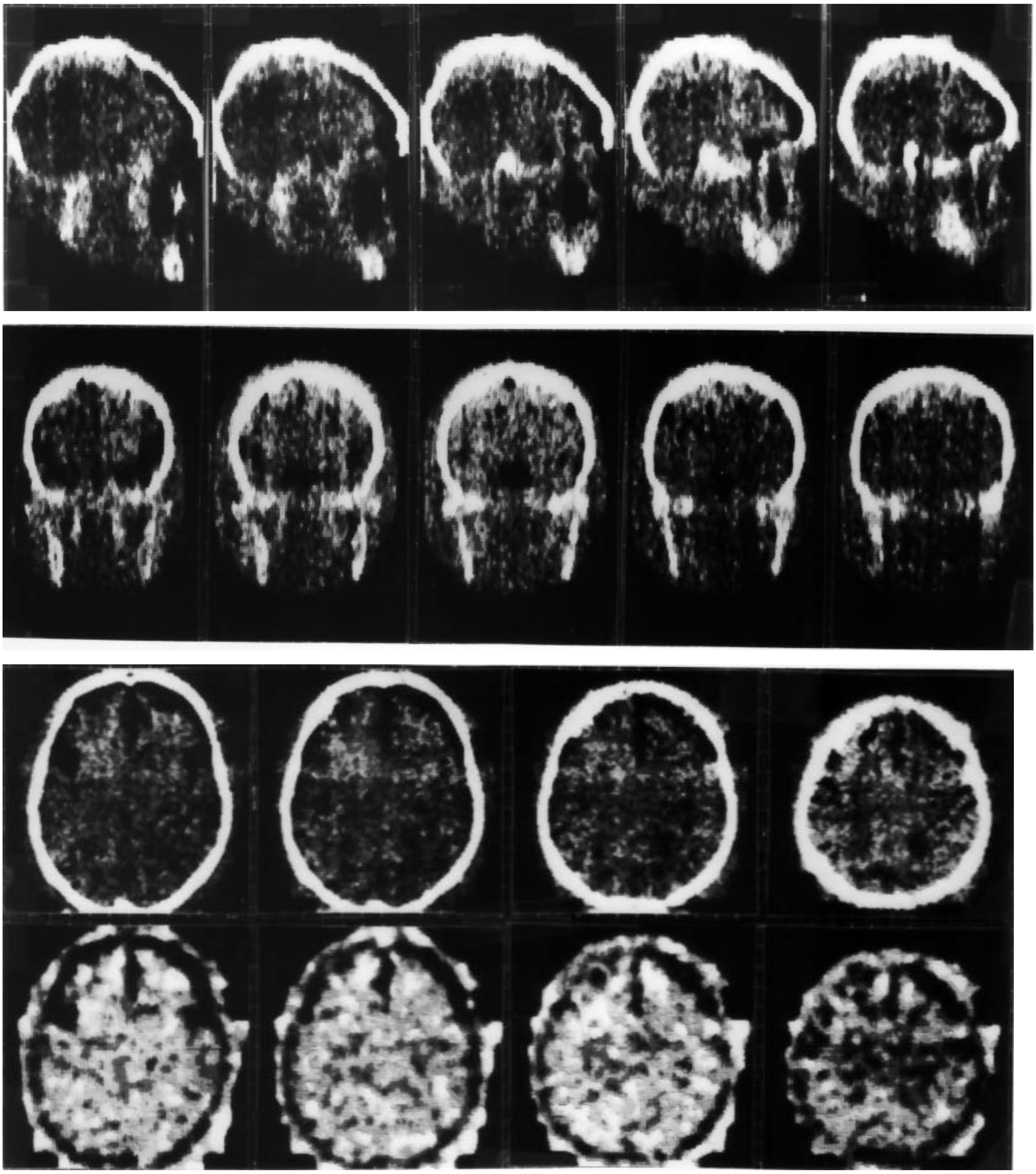

Figure 3.15 *Sagittal, frontal and transverse 3-D density distribution in successive slices through a human head, measured with the Nuclear Scattering Radiography method. In the last pane, the top set corresponds to events with one scattered track and the bottom set only to the fraction of elastic p-p scatterings.*

3.4 Detectors for proton tracking

A variety of devices, developed for the needs of high-energy particle physics, can be used for the proton tracking needed in both NST and IVI. Generally named "Micro-Pattern Detectors", they permit to measure the coordinates of charged tracks traversing a plane of detection at high rates and with sub-millimetre accuracies. Due to the rather large detection area needed, and to maintain reasonable costs, preference is given in this project to devices based on the already described Gas Electron Multipliers[50]. Robust and flexible in shape, they can be designed to match the optimal geometry and to cover a large solid angle. A further advantage of GEM-based detectors is that they are completely insensitive to radiation with the operating voltage turned off while most solid state devices would be damaged by long-term exposure to high radiation levels.

GEM detectors are widely used in particle physics for tracking of charged particles at high rates. Fig. 3.16 shows one of the modules used in the COMPASS experiment at CERN[51]; with an active area of around 1000 cm^2, they have a projective two-dimensional readout recording the charge collected on perpendicular sets of strips. In the experiment, the central circular region (visible in the picture) can be activated or made insensitive by external voltage control, possibly a useful feature for the present project (see below). With the analogue charge recording circuitry used in the experiment, one can achieve routinely localization accuracies around 60 µm rms. However, in view of the unavoidable dispersions due by multiple scattering of the tracks, discussed before, a simpler, less accurate but faster digital recording of the hit strips seems to be better suited. With a strip pitch of 400 µm and a digital pulse-over-threshold recording, the localization accuracy is ~ 150 µm rms, well below the multiple scattering dispersion.

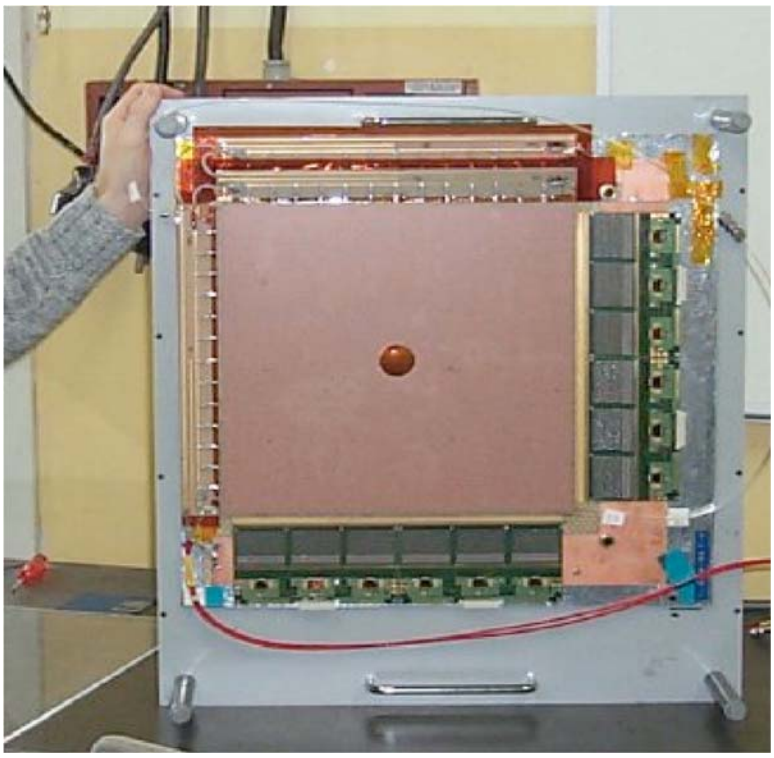

Figure 3.16 *GEM detector module used for the COMPASS experiment at CERN.*

A digital readout system based on the VFAT chip has been developed for the TOTEM experiment at CERN; to cope with the experimental requirements, the GEM detectors have been "tailored" with a semi-circular shape, as shown in Fig. 3.17. One of the built-in functions of the circuit, a fast grouped OR pulse, can be used to select events satisfying external geometrical constraint, as for example a coincidence between aligned planes of detection, thus avoiding the need of using large-area scintillation counters as in the early setups.

[50] Sauli F., Nucl. Instr. and Meth. A386 (1997) 531.
[51] Ketzer B. et al, Nucl. Instr. and Meth. A535 (2004) 314.

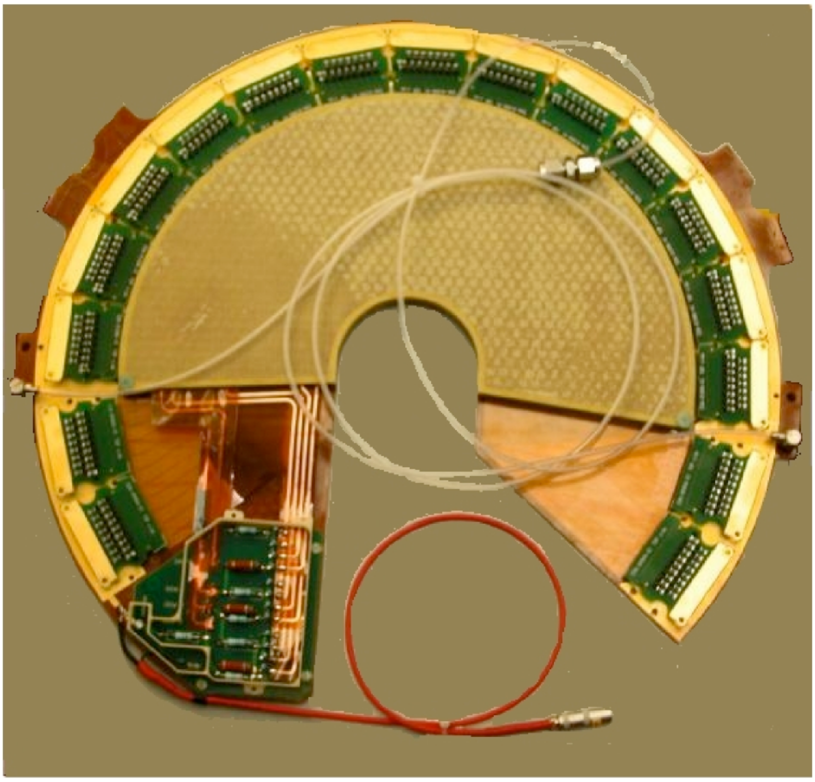

Figure 3.17 *A semi-circular GEM detector module for the TOTEM experiment.*

While for the time being we have adopted for our development the simpler square-shape devices, given the radial symmetry of the scattering process a circular shape for the detectors can be considered in the future.

Made with very light material (typically a 0.5 % of a radiation length) they are almost insensitive to gamma and neutron backgrounds.

A possible setup of the Interaction Vertex Imaging is shown schematically in Fig. 3.18. It is made of three GEM detectors, placed downstream of the ion beam, covering an angular region of 20º around the beam axis. An absorber between the first and second chamber stops protons having energy smaller than 50 MeV. The last chamber is sandwiched between a “dE/dx” scintillator and a “E” scintillator, used to tag the type and energy of the detected particle. The pulse from the counters are recorded as flags to mark the computed vertex, allowing to select off-line a populated, more dispersed distribution, due to the multiple scattering in the body of the ejected protons, or a more accurate set of data with less events. An on-line analysis is also possible.

In each detector, a bi-dimensional projective readout is used to record the crossing proton coordinates and reconstruct the tracks. Placing the first plane of detection 35 cm from the centre of the target, and the second 10 cm farther, the active area of each detector is close to the one of the devices shown in Figs. 3.16 and 3.17. A simple and fast algorithm can be implemented to reconstruct, event by event, the angles of emission of the protons, as well as the vector of minimum distance between the track and the known beam direction. Suitable cuts to the absolute values of this vector allow reconstructing a three-dimensional density distribution in the target of the primary interaction vertices, from which, as discussed Section 3.2, one can deduce the incident beam range distributions.

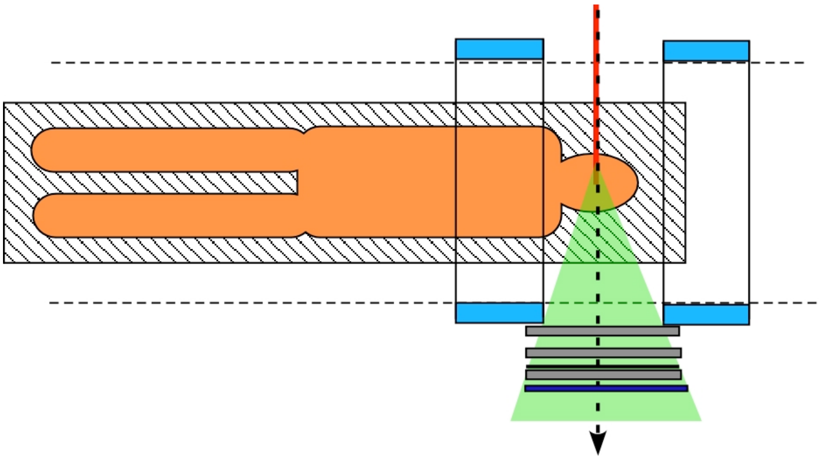

Figure 3.18 *Possible set-up of a dual closed ring PET scanner with a GEM detector for Interaction Vertex Imaging (IVI). With a somewhat larger coverage the same counters can be use, in conjunction with a high energy proton beam, to reconstruct the spatial position of the patient organs (NSR technique)*

If, as suggested by the simulation analysis, the vertex resolution is improved selecting tracks at larger angles, the setup can be modified mounting the detectors above and below the central plane, as schematically shown in Fig. 3.19. In this case, the event rate is reduced by a factor two or three, as compared to a full coverage.

With the proposed designs, that avoid detection in the central core of the charged ejects, the Interaction Vertex Imaging could in principle be operated during the therapy exposure, typically using ion fluxes of 10^8 per second. However, this choice suffers from two major drawbacks: on one hand, the system of data acquisition and rendering should be able to operate at the same rates, and on the other hand any mismatch between the treatment plan and the actual irradiation would only be discovered after exposure of the patient.

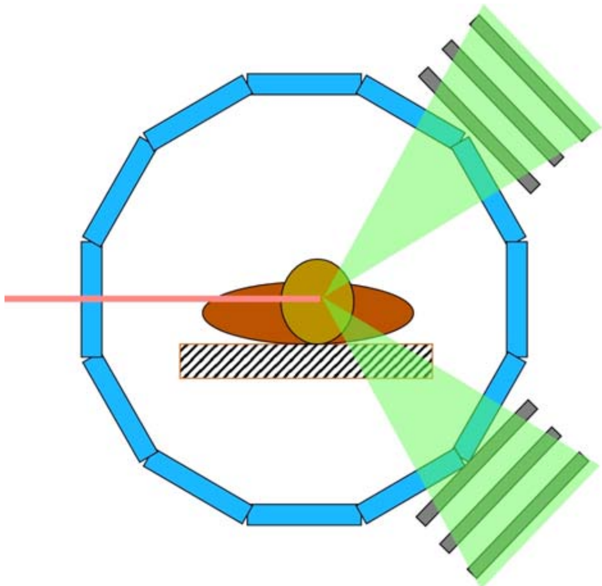

Figure 3.19 *Alternative tracking setup to cover a larger angle region (20º to 50º) for both IVI and NSR.*

A better strategy would be to precede the actual therapy with a short diagnostic exposure, in identical conditions but at much lower beam rates. For example, for a diagnostic beam flux of 10^6 ions per second (two orders of magnitude less than for therapy) given to the distal layer of the tumour target, making use of the previous data one can estimate that in one second about 170,000 "useful" proton tracks are generated within the sensitive area of the detector; assuming an overall Vertex reconstruction efficiency of 50%, this gives about 70,000 reconstructed vertices per exposure of which 1% from the last 2 cm range region.

The region of solid angle covered is determined by the maximum size and distance of the detectors; assuming position accuracies in each detector of 0.5 mm, a 10 cm distance ensures an angular resolution on the outgoing tracks close to the dispersion due to multiple scattering. At present, the GEM manufacturing technology is limited to active areas around 40x40 cm^2, but a large collaborative effort is on the way to increase this limit to a square meter or more[52]. Alternatively, several smaller size detectors can be assembled to cover the desired area. The efficiency in the central part of the detector, in-line with the incident beam, can be easily inhibited with a method used for example in the COMPASS experiment at CERN (the so-called beam killer).

For the initial assessment of the diagnostic method, we are assembling a smaller NST system making use of available detectors and readout electronics. A schematic of the demonstrator, which should be tested by the end of 2008, is shown in Fig. 3.20. Two small (10x10 cm^2) GEM detectors, identical to those already described for the Proton Range Radiography are used to record the incoming beam track, and two COMPASS-type GEM chambers, 31x31 cm^2 active are placed in the forward direction to cover an angle between 15º and 45º in respect to the centre of the target.

As already discussed, GEM detectors are capable of operating at very high rates, above 10^5 tracks per mm^2, largely exceeding present days electronics capability. The two circuits made available to the project, based on the VFAT and GP5 128-channels chips, have intrinsically a very wide bandwidth, but having been developed for LHC experiments, relying on a very sophisticated event selection, are limited in the readout to about 100 kHz data transfers. In principle, a re-design of the same basic circuits and a dedicated sparsified readout (transferring only valid hits) should increase the data transfer rate by one or two orders of magnitude We have therefore initiated, in collaboration with an electronics group at Rutherford Labs, a research program for the design of faster readout electronics, the goal being to reach several tens of MHz of data transfer rates. If this progress is successful, we expect the on-line fast 3-D imaging system with hydrogen content selection to add to the range of diagnostic tools for hadrotherapy.

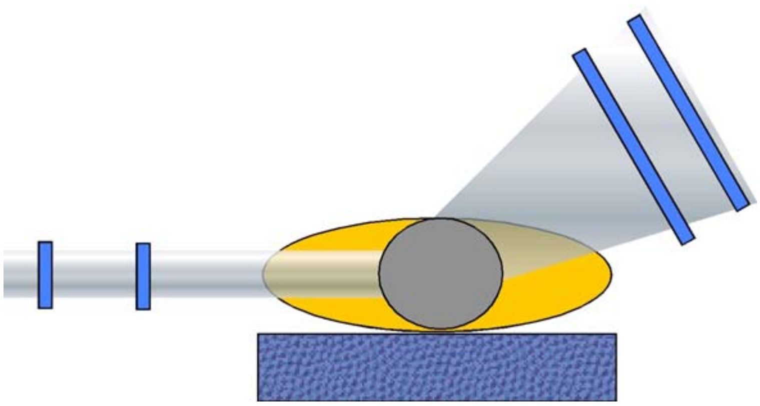

Figure 3.20 *A smaller NST demonstrator setup. presently in construction using existing detectors and readout electronics. The angular coverage for scattered protons is between 15º and 45º.*

[52] CERN Research Program RD-51.

4. GEOMETRY AND UTILIZATION OF AN IN-BEAM-PET SYSTEM FOR CNAO

4.1 Introduction

In-beam PET is a non standard application of PET imaging and it has specific requirements to be fulfilled. The positive experience of PET monitoring of carbon treatments at GSI yields a new line of research of scanners suitable for in-beam PET. These investigations must be facility dedicated, since each centre has some special features that may determine the final detector choice. Among these, the beam field size, the patient bed volume and mobility, the nozzle location, the time structure of the beam and the beam delivery technique are the most relevant ones.

In the present Chapter, the study of a suitable scanner for the CNAO hadrontherapy centre is carried out taking into account the specifications of the facility. On the bases of these results a final design of the tomograph is proposed, consisting in two arcs separated by an angular aperture. The width of the two gaps has been optimized by considering the extension of the fragments exiting the patient downstream.

Because of the low activity induced in the treated patient, the sensitivity of the PET detector is an important point. It has been estimated and compared to the sensitivity of a high performance PET (HiRez from Siemens) used in nuclear imaging.

The studied in-beam PET scanner has been eventually used in the simulation of an in-beam acquisition, in order to estimate the number of coincidences available during the treatment and study possible optimization of the acquisition scheme.

The studies performed in the present Chapter put some light on the feasibility are the starting point for the final detector unit choice.

4.2 Requirements for an in-beam PET for CNAO

The final scanner geometry must be optimized to fulfill the following conditions:

1. no collisions with any component: patient, patient bed and beam nozzle;
2. no obstructions to the primary beam and minimum overlap with the exiting fragments from the patient;
3. easy access to the patient if an intervention is required.

These are the major limitations in the choice of the geometry. Other issues related to the detector choice are treated in Chapter 5. Furthermore, the detector solution will be influenced by the geometrical design of the scanner, since a lower geometrical coverage has to be compensated by higher detection efficiency. At the same time, a compact detector helps in increasing the mobility of the scanner.

The two possible scanner geometries are a full cylindrical scanner and a double-head scanner, i.e. a cylindrical detector with two apertures (Fig. 4.1). A third solution considered in the first analysis was a double-ring scanner, i.e. two ring detectors placed at a fixed distance. This solution has been rejected because, first of all the Field of View (FOV i.e. the maximum axial extent) of each ring does not contain the source, resulting in a lower global sensitivity. Secondly, the access to the patient is more limited.

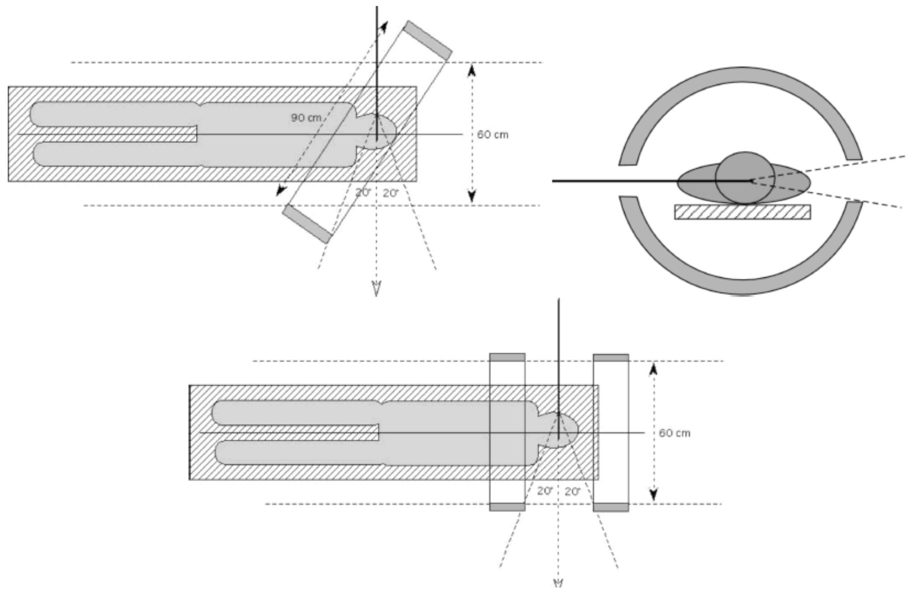

Figure 4.1. *Three geometries considered for the CNAO PET scanner: standard full ring cylindrical geometry with a rotation angle respect to the primary beam direction (left panel), double-head scanner (right panel) and double-ring scanner (lower panel).*

4.3 Optimization of the in-beam PET geometry for CNAO

In Phase 1 the CNAO facility features three treatment rooms, each one equipped with an horizontal beam line; one of these has also a vertical line. The study has been performed for this room, with both vertical and horizontal lines, since this choice puts more limitations to the geometry. The following discussion is based on the present design of the treatment room, but some parameters are still under discussion.

The isocentre height is 1200 mm. Both vertical and horizontal beam lines before reaching the patient pass through the two monitoring devices, i.e. two nozzles. The two detector systems have been developed by a group of Turin University and INFN Section [53].

An almost cylindrical vertical system supports the beam diagnostic and the CT devices. The end face of the support is at 50 cm from the isocentre. The horizontal line nozzle ends 50 cm from the isocentre, hence the free space for the scanner is very limited with respect to both the vertical and the horizontal detectors. The sensitive area of the beam detectors is 24×24 cm^2 in order to cover the 20×20 cm^2 maximum field with a certain margin. The patient bed, mounted on a precision robot, has all 6 translational and rotational degrees of freedom.

The optimization of the scanner geometry for CNAO is studied in two steps: the first one is centred on the limitations imposed by the nozzle location with respect to the isocentre and by the patient size, while the second one takes into account further constraints coming from the spatial distribution of the fragments exiting the patient.

In-beam-PET collision study

When considering the full ring scanner, its horizontal axis, passing through the isocentre, must be rotated with respect to the primary beam direction to avoid any overlap with the incoming beam (condition 2). The minimum rotation angle is obtained by imposing that at

[53] Pecka A. et al., "The beam monitor system for the Centro Nazionale di Adroterapia Oncologica", Nuovo Cimento 121 (2006) 869-877.

least the 24×24 cm^2 sensitive area of the nozzle detector is not covered by any component of the scanner. By rotating the scanner, the distance between the detector and the patient is shorter, when the bed is perpendicular to the beam direction (Fig. 4.2).

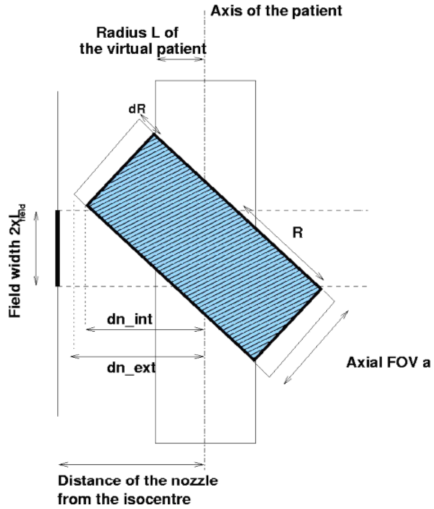

Figure 4.2 *Schematic drawing of the configuration used to carry out the study of the collision of the in-beam PET scanner with the patient and with the nozzle. The set-up corresponds to the minimum rotation angle of the scanner to avoid any overlap between the scanner and the maximum field of the incoming particles.*

Note that this is the geometry that puts the strongest limitation on the internal radius R of the scanner. Such distance depends on the internal radius R and on the axial FOV a of the tomograph. By imposing a minimum rotation angle, it is possible to study the dependence of the collision-free area of the patient (i.e. a virtual cylinder of radius L) on the geometry of the scanner. Fig. 4.3 shows a schematic drawing of the bed and the patient to explain the arguments to be considered when the virtual cylinder radius is chosen.

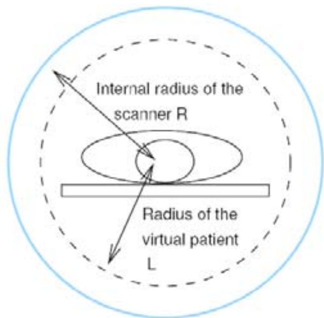

Figure 4.3 *Positioning of the patient in the centre of the scanner. The radius L has to take into account the mean size of the patient and possible displacement of the target with respect to the isocentre, plus a certain margin to leave a reasonable comfort to the patient.*

The radius L of the virtual cylinder around the patient is related to the scanner geometry and to the size of the field of the incoming primary particles by the following equation:

$$L = d_{n,int} - \arcsin[\arctan(\frac{L_{field}}{d_{n,int}}) + \arctan(\frac{a}{2R})] \tag{4.1}$$

where $d_{n,int}$ is the transaxial extent of the scanner from the isocentre with respect to its internal radius R and L_{field} is the half-size of the primary particle field. The equation assumes that the nozzle surface has a large extension, as shown in Fig. 4.2. For the calculation L_{field} was fixed at 12 cm, corresponding to the minimum rotation angle configuration, as shown in Fig. 4.2, and to the maximum constraint to the geometry. The parameter $d_{n,int}$ is given by the first term of the following equation:

$$d_{n,ext} = \sqrt{(a/2)^2 + R^2}\cos[\arcsin(\frac{L_{field}}{\sqrt{(a/2)^2 + R^2}})] + dR \cdot cos\theta_{L_{field}}(a, R), \qquad (4.2)$$

that gives the relation between the external maximum transaxial extent of the scanner given by the sum of $d_{n,int}$ and the radial depth dR of the scanner, depending on the rotation angle $\theta_{L_{field}}(a, R)$ of the axis of the tomograph with respect to the beam direction.

Fig. 4.4 shows the dependence of the radius L of the collision-free volume around the virtual patient as a function of the axial FOV of the scanner, for different values of the internal radius R of the tomograph. For the minimum size the value L =25 cm was chosen, values of the radius of the virtual patient smaller than this are represented in Fig. 4.2 by the red dashed area.

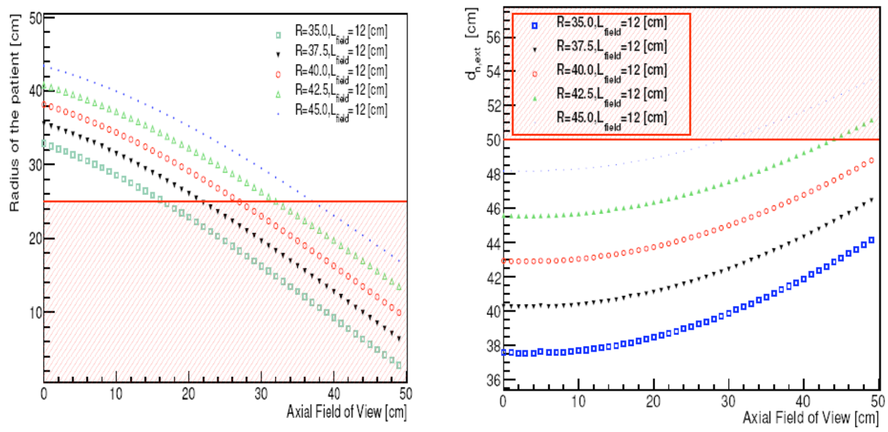

Figure 4.4 *Left panel: behaviour of the collision-free radius of the virtual patient as a function of the axial FOV of the scanner, for different values of the internal radius of the tomograph. Right panel: maximum transaxial extent of the scanner asa function of the axial FOV for different internal radius. The red dashed area cover the forbidden region: the patient radius cannot be shorter than 25 cm and the transaxial extent of the scanner cannot by larger than 50 cm. In both pictures the scanner is in the minimum rotation angle configuration, i.e.* L_{field} *is 12 cm.*

The external transaxial extent of the scanner $d_{n,ext}$ is useful to evaluate the collision with the nozzle by changing the geometry of the scanner. In this study the value of L_{field} is 12 cm as in the previous one. The right panel of Fig. 4.2 shows the dependence of $d_{n,ext}$ on the size of the axial length of the scanner, for different values of the internal radius R. In the plotted curves the radial depth dR was set equal to 5 cm, assuming an extremely compact detector. The value of $d_{n,ext}$ cannot be larger than 50 cm, i.e. than the distance from the nozzle to the isocentre, and the excluded region is represented in Fig. 37 by the red dashed area.

If one considers a value of L of 35 cm, that gives a reasonable comfort to the patient, the maximum axial FOV of a 40 cm radius scanner is 10 cm whereas a 45 cm radius tomograph cannot have an axial length larger than 20 cm. This last solution is interesting, but the right panel of Fig. 39 shows that the distance to the nozzle is few cm. This poses important constraints on possible detector choices requiring a very compact unit detector solution, as the one investigated for the Heidelberg facility [54].

[54] Crespo P. et al., " First in-beam PET imaging with LSO/APD-array detecters", IEEE Trans. Nucl. Sci. 51 (2004) 1389-1395.

Another possibility is represented by the double-head scanner. In this case, the angular gaps between the two arcs must fulfill the second condition. The two angular apertures make possible to keep the axis of the scanner always parallel to the axis of the patient. Therefore in the case of a double-head tomograph, there are no geometrical constraints imposed by the collision with the patient, while the problem of the distance to the nozzle still remains even if less strict.

The absence of constraints on the internal radius and on the axial length imposed by the patient makes possible to choose R=40 cm and a=30 cm, with few cm still remaining between the scanner and the nozzle. It has also to be underlined that due to the presence of the two gaps, the length of the projection of the scanner diameter in the horizontal plane is again reduced, depending on the external radius and on the angular aperture.

When considering vertical treatments, since the distance of the nozzle to the isocentre is equal to the horizontal line, the geometrical constraints are the same. To allow the vertical beam to reach the patient, the full ring scanner would be able to rotate with respect to the vertical plane. For the same reason, the double-head device must be free to rotate by $\pi/2$ in the ring plane, in order to move the two gaps in front of the vertical nozzle. To guarantee different angle positioning of the patient bed, the scanner needs to be rotated with respect to the vertical axis. A schematic drawing of a possible location of the double-head scanner in the treatment room is presented in Fig.4.5.

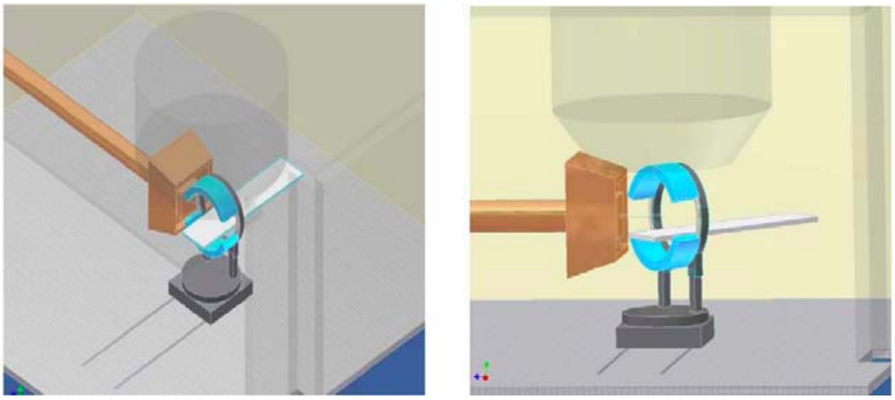

Figure 4.5 *Location of a dual-head scanner in the treatment room of CNAO, in different set-ups. The horizontal and vertical nozzles are also drawn. The mechanical support is schematically shown to underline the required degrees of freedom of the tomograph.*

In conclusion a full ring scanner seems feasible, but with strong geometrical constraints on the external radius, on the axial FOV and on the radial depth of the device. A dual-head scanner is much more attractive due to the weaker limitations.

It is interesting to estimate the solid angle covered by the three scanners, according to what previously discussed. A simple formula valuable in case of point source located in the centre of the tomograph is:

$$\varepsilon = \frac{\pi - \alpha}{\pi} \cos[\arctan(\frac{R}{a/2})], \tag{4.3}$$

where α is the angular width between the two arcs (0 in case of a full ring scanner). The geometrical sensitivity amounts to 0.11, 0.23 and 0.27 respectively for two full ring scanners with R=40 cm and a=9 cm, R=45 cm and a=20 cm, and for a double-head scanner of 40 cm radius, 30 cm width and 40 degrees gap. The geometrical sensitivities are comparable in the last two cases and the surface covered by the double-head scanner is only 3% larger than the one of the second full ring scanner considered.

One of the major problems in case of a double-head scanner is the degradation of the PET image due to the loss of events in the two gaps, as discussed in Ref. [55]. This problem can be partially overcome by the development of dedicated reconstruction tools, as well as by a clever acquisition method, as discussed in the last Section.

In-beam PET acquisition: Heidelberg facility versus CNAO

The very low activity induced in the patient, and hence the low number of useful coincidence events available, asks for improvements not only in the detector performance but also in new acquisition protocol. At the GSI pilot-project, in-beam PET data have been collected during the off-time, due to the ramping-down and ramping-up of the synchrotron. This reduces the number of acquired events typically by a factor 3.

For the Heidelberg facility, an intra-spill acquisition has been proposed to increase the number of detected events. For a synchrotron having circumference L, a carbon ion beam of energy E has a revolution period T_r given by the ratio between L and the speed of the ion βc. The radiofrequency (RF) period T_{RF} is equal to T_r / h, where h is an integer named the "harmonic number", equal to 1 for CNAO. Hence, we have:

$$T_{RF} = \frac{L}{c} \cdot \frac{E}{\sqrt{E^2 - (m_0 c^2)^2}}. \tag{4.4}$$

The elapsed time between two bunches is therefore given by T_{RF} divided by the number of concomitant bunches within the same period.

For the GSI SIS, T_{RF} ranges between 480 and 250 ns by increasing the energy from 88.83 MeV/u up to 430.10 MeV/u[56]. The prompt gamma background is strictly correlated to the spill time microstructure. Therefore, any standard method for random coincidences subtraction (i.e. delayed window) fails because of the time structure of the signal (Fig. 4.6).

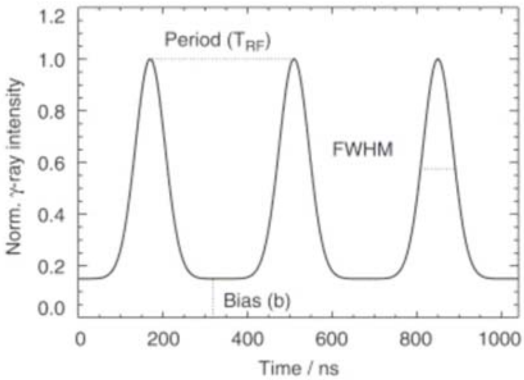

***Figure 4.6** Model of the time dependence of the background of un-correlated gammas due to carbon ion beam microstructure* [57].

Two methods have been proposed to acquire coincidences during the macropulses, between consecutive micropulses, both related to the synchronization of the gamma coincidences with the time microstructure of the beam either by using the RF-signal from the accelerator or of a fast particle detector located in front of the target. With these approaches the gain in image

[55] Crespo P. et al., " First in-beam PET imaging with LSO/APD-array detectors", IEEE Trans. Nucl. Sci. 51 (2004) 1389-1395.

[56] Crespo P., "Optimization of In-Beam Positron Emission Tomography for Monitoring Heavy Ion Tumor Therapy", PhD thesis, Technischen Universitat Dresden, Germany (2005)

[57] Parodi K. et al., "Random coincidences during in-beam PET measurements at micro-bunched therapeutic ion beams", Nucl. Instrum. Meth. A 545 (2005) 446-458.

statistics lies between 70% and 90%, for the GSI 40% accelerator duty factor (the ratio between the macropulse duration and the synchrotron acceleration cycle) [58].

The impact of inter-spill acquisitions is more important for machines with smaller duty factors.

At CNAO a slow beam extraction is performed by means of a betatron core. The use of a betatron core to drive the resonant extraction enables to control very accurately both the length and the intensity of the spill, but does not allow intra-spill acquisition.

4.4 Background particles in a in-beam PET system

A non negligible amount of fragments are forward directed with respect to the primary beam direction, as shown in Fig. 4.7.

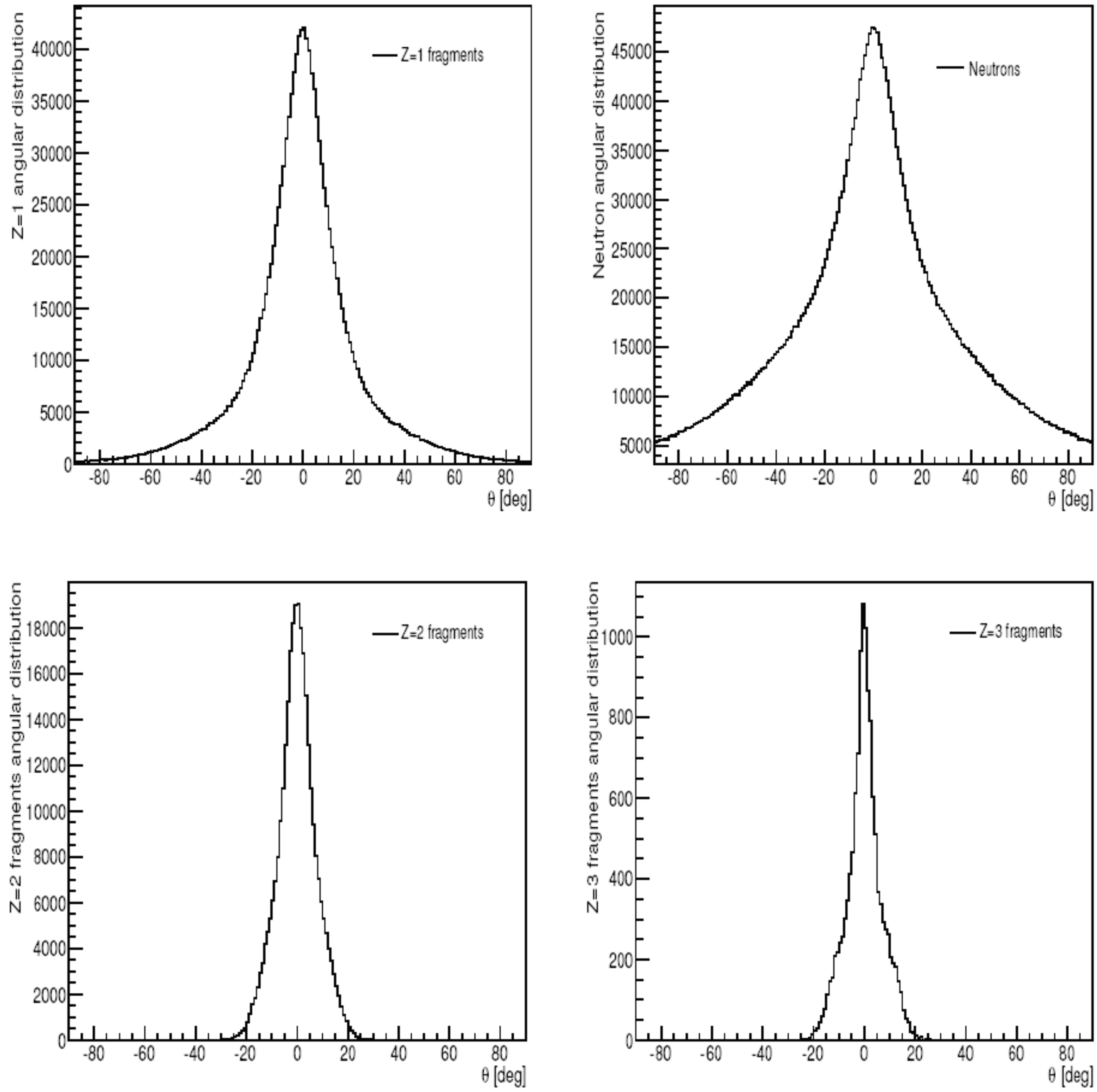

Figure 4.7 *Angular distribution of neutrons, Z =1, Z =2 and Z =3 fragments, generated by a 400 MeV/u carbon ion beam stopped in a 30 cm long PMMA target, on a 40 cm radius scanner with 30 cm axial length. The distributions are computed with 500000 carbon ions.*

[58] Crespo P., PhD thesis (2005)

To reduce the background rate, the treatment field (20×20 cm^2) imposes an angular aperture, between the two arcs of a 40 cm radius double-head scanner, of about 30°.

As shown in the figure, the background consists of low Z particles, neutrons and gammas, and has to be kept into account in the final choice of the detector material: even if the scintillating material is radiation hard, the flux of particles interacting in the crystal must be as low as possible, to avoid material activation as well as tertiary fragment production.

For this purpose, the angular distributions of all relevant particles exiting the patient have been computed by means of Geant4. The phantom is a $30\times25\times25$ cm^3 PMMA box. The primary beam energy is the maximum achievable i.e. 400 MeV/u. Carbon ions enter perpendicular to the target with a position ranging between -10 cm and +10 cm, in both the lateral and transversal dimensions.

Around the target, and centred on it, a 40 cm radius scanner is located, spanning an angle φ between $-\pi/2$ and $+\pi/2$, with an axial length of 30 cm. The distribution of particles has been calculated as a function of φ. For the considered double-head scanner of 40 cm radius and 30 cm axial length, by considering a high intensity spill of $1\cdot10^8$ s^{-1}, the rate of fragments on the detector at different angles can be computed. The results are shown in Fig. 4.8 for neutrons, $Z=1$, $Z=2$ and $Z=3$ fragments. The contribution of heavier nuclei is negligible.

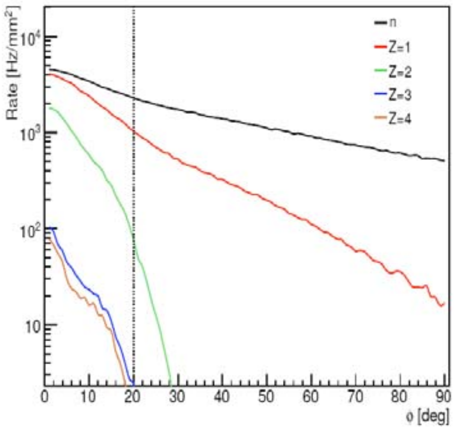

Figure 4.8 *Average rate of fragments on the in-beam PET detector, at different angles φ with respect to the primary beam direction. The rates are computed by considering a spill of $1\cdot10^8 s^{-1}$ carbon ions. The dotted line indicates the proposed half-angle of the gap.*

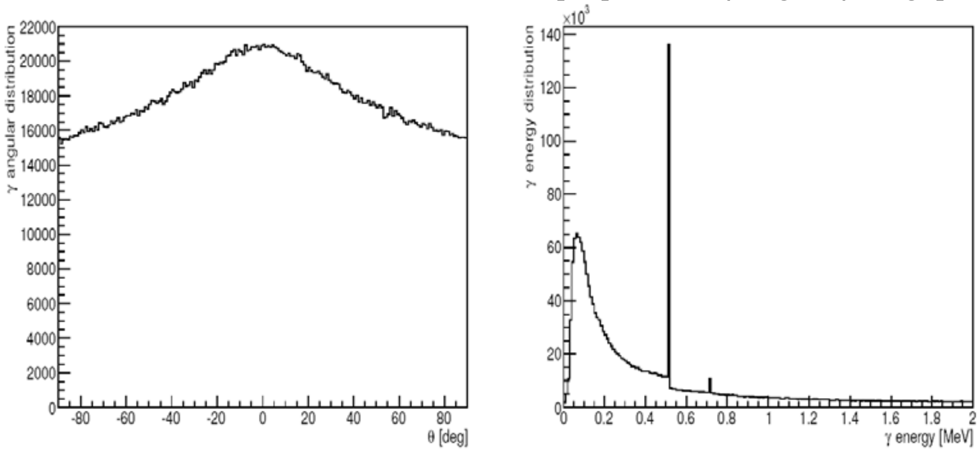

Figure 4.9 *Left panel: angular distribution of γ generated by a 400 MeV/u carbon ion beam, on a 40 cm radius scanner. Right panel: energy distribution of all the gammas.*

By considering a 40 degree angular aperture, the rate of protons and neutrons in the proximity of the gap is about 2000 Hz mm^{-2} each. The final rate of protons is obtained by combining the calculation results of Fig. 4.7 with the correcting factor (about 2) estimated in the Chapter 2 by comparing Geant4 with experimental data.

Figs. 4.7 and 4.8 show that fragments with Z higher than 2 do not constitute a major problem, since they are all confined within ± 20 degrees. The rate of alfa particles is peaked and, at 20°, is about 5% of the proton one. Instead the gammas of Fig. 4.9 have a flat distribution. High energy gammas, above 511 keV, derive from nuclear de-excitations and they are prompt, hence emitted within a short time window from the parent production. The 511 keV gammas come mainly from the annihilations of e^+ produced by high energy gammas.

4.5 Materials and methods for sensitivity assessment

The impossibility to acquire β^+-decays during the beam extraction limits the number of coincidences during a treatment. Hence it is fundamental to assess and maximize the sensitivity of the scanner. In this non-standard application of PET, and for pure inter-spill or post-treatment acquisition, the performances of the scanner are not very difficult to obtain. For instance, good random coincidence suppression and subtraction represents a major goal in many scanners; in this case it is not important since the activity in the patient is rather low (about 200 Bq $\text{cm}^{-3}\,\text{Gy}^{-1}$).

The spatial resolution of the scanner is another important issue for standard PET application, and it is mainly improved by using small pixellated detectors and high light yield crystals. For an in-beam acquisition a high spatial resolution is not fundamental: 4-5 mm are sufficient due to both the very low statistics (which anyway limits the precision) and because in hadrontherapy treatment monitoring the aim is to compare the reconstructed image with the simulated one.

The sensitivity is a more general parameter, which is mainly influenced by the scanner geometry and the detector material properties (density and detection efficiency). Therefore it is possible to estimate the sensitivity of a system without actually choosing the unit block detector read-out. Timing performance and spatial resolution are of course important in the final image quality, but do not affect the sensitivity of the device.

Geant4 application to tomographic emission

GATE is a simulation toolkit dedicated to PET and SPECT applications [59] [60]. It is based on Geant4 general purpose classes, involved in the construction of the geometry, the interaction physics, the event generator and the visualization management. All these classes are defined in the core layer. Here some additional classes specific to GATE are also defined, such as that dedicated to time management. In order to make GATE a suitable computational instrument also in clinical environment, all the functionalities provided by the classes are available to the user through script commands.

The general simulation architecture is structured as following:

- definition of the scanner geometry,

[59] Fiedler F. et al., "The Feasibility of In-Beam PET for Therapeutic Beams of ^{3}He", IEEE Trans. Nucl. Sci. 53 (2006) 2252-2259.

[60] Jan S. et al., "GATE: a simulation toolkit for PET and SPECT", Phys. Med. Biol 49 (2004) 4543-4561.

- definition of the phantom geometry,
- choice of the physics processes,
- initialization of the simulation,
- definition of the detector model,
- definition of the source,
- specification of the data output format,
- start of the acquisition.

In GATE there are different systems available (template of predefined geometries), compatible with different data output formats. Currently there are five systems implemented in GATE: one for SPECT, three for PET, and a generic system appropriate to model novel tomographs. Once the system geometry and the phantom are set, the physics can be turned on. It consists of radioactive decay (performed by the Geant4 radioactive decay module) and electromagnetic physics. As in Geant4, GATE can use two different packages: the standard and the low energy electromagnetic physics.

The most important part of the simulation is the description of the digitizer chain. It simulates the electronics read out of a detector within the scanner. Once a portion of the scanner is defined as sensitive, the interactions of the particles within this region are recorded. Each detected event carries information about its history like vertex position, interactions in the phantom (if it is defined as sensitive volume) and source type. The digitizer is organized as a chain of modules that begins with the *hit* and ends with the *single*, which represents the physical observable seen by the detector. The user can define several modules of the digitizer chain to reproduce the behaviour of a real scanner, i.e. energy resolution, energy window, spatial resolution, time resolution and dead time. Once the *single* is produced, GATE sorts the coincidences, according to the user defined coincidence time window and multiple coincidence policy.

Detector parameters: the NEMA NU-2 2001 protocol

The NEMA NU-2 2001 protocol has been used to evaluate the performance of a PET scanner with the geometry, previously described, optimized for hadrontherapy in-beam acquisition [61]. The report specifies standardized measurements, in order to make different PET scanner performances comparable. The protocol aims to quantify relevant parameters of a PET detector: scatter fraction, random fraction, spatial resolution, Noise Equivalent Count Rate (NECR), image quality, and sensitivity. The present study is centred on the estimation of the sensitivity, that is expressed as the rate of true coincidences detected for a given source strength. A 700 mm tube of 4.8 mm diameter is filled of water mixed with the source of activity A_{cal}. It is placed parallel to the scanner axis, in the centre of the detector. The line source is surrounded by different metal sleeves. This ensures the annihilation of all emitted β^+, but at the same time increases the attenuation of the gammas. Several acquisitions with different metal thicknesses are required so to extrapolate the count rate value to zero thickness. The position of the line source can also be moved from the central axis, to estimate the sensitivity as a function of the radial position of the source. The source activity must guarantee a number of random coincidences less than 5% of the true detected coincidences. The aluminium sleeves have the dimension reported in Table 4.1.

Table 4.1 *Metal sleeves of the sensitivity measurement, according to NEMA NU-2 2001 protocol.*

[61] National Electrical Manufacturers Association, "Performance measurements of Positron Emission Tomographs", NEMA Standards Publication NU-2 2001 (2001)

Total number	Inside diameter [mm]	Outside diameter [mm]	Length [mm]
1	3.9	6.4	700
2	7.0	9.5	700
3	10.2	12.7	700
4	13.4	15.9	700
5	16.6	19.1	700

At each acquisition j the count rate of true coincidences is given by:

$$R_j = R_0 \cdot exp(-\mu_M 2X_j), \tag{4.5}$$

where X_j is the metal thickness, and the two unknowns are μ_M and R_0, respectively the metal attenuation length and the count rate with no attenuation, to be fitted on measurements (calculation) results. The system sensitivity is $S_{TOT} = R_0 / A_{cal}$.

Scanner geometry and acquisition

For this work, the first scanner system simulated was the HIREZ scanner (Siemens Medical Solutions). Its main technical characteristics are summarized in Table 4.2.

Table 4.2 *Technical characteristics of the HIREZ scanner and of the in-beam double-head scanner.*

Parameter	HIREZ	Double-head
Detector ring diameter	830 mm	800 mm
Detector material	LSO	LSO
No. of detector rings	39	65
Slice number	81	142
Crystal size	$4 \times 4 \times 20$ mm ^{3}	$4 \times 4 \times 30$ mm ^{3}
Crystal array/block	13×13	13×13
Face of crystal block	52×52 mm ^{2}	52×52 mm ^{2}
No. of detector blocks	144	170
Avial FOV	162 mm	284 mm
Coincidence window	4.5 ns	4.5 ns
Energy window	425-650 keV	425-650 keV
Gap angle α	0 deg.	40 deg.

The unit block detector is based on an array of 13×13 LSO crystals of $4 \times 4 \times 20$ mm^3. The scanner ring diameter is of 830 mm, with 3 blocks arranged along the axial direction in a spherical orientation, for a total number of 39 rings. The number of blocks per ring is 48 and the scanner extends axially for 162 mm. Each block is read out by 4 PMTs, in an electronic scheme that achieves 500 ps coincidence time resolution. The coincidence time window is set to 4.5 ns. The energy resolution of the crystals has been set 15%. Fig. 4.10 shows the simulated HIREZ system.

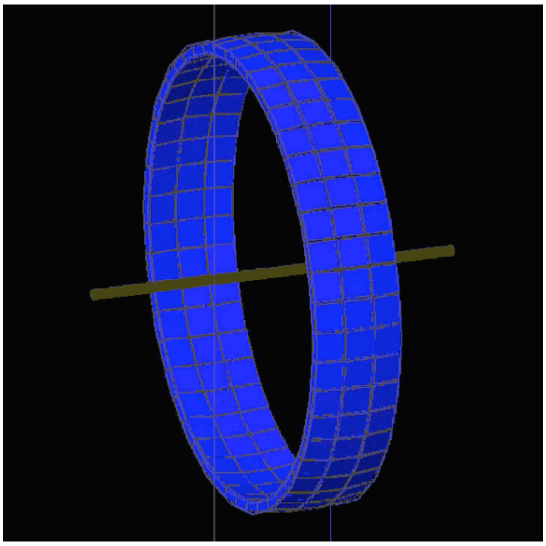

Figure 4.10 *Simulation of a 3 rings HIREZ PET scanner, with the 700 mm line source placed in the centre of the transaxial FOV.*

The geometry of the in-beam dual-head scanner is based on the HIREZ unit block detector. The length of the crystal is increased to 30 mm, to compensate the foreseen geometrical sensitivity loss. According to the geometrical constraints discussed in the first Section, the HIREZ detector design has been modified to match the in-beam PET requirements. The angular gaps are 40 degrees and the detector ring diameter is reduced to 800 mm, therefore the number of blocks per ring is reduced from 48 to 34. The number of blocks along the axial direction has been increased to 5, with 274 mm axial FOV. The coincidence and energy windows are kept equal to the standard HIREZ detector. The energy resolution of the crystals is assumed to be 10%. In both systems, the *takeWinnerOfGoods* coincidence policy has been adopted i.e. in a multiple coincidence event, only the two hits with the higher energy are considered. The simulated double-head scanner is shown in Fig. 4.11.

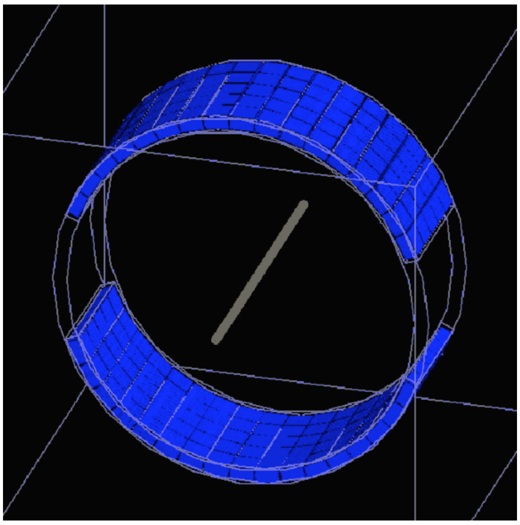

Figure 4.11 *Simulation of a 5 ring HIREZ scanner, arranged into a double-head geometry with 40 degree gaps on opposite sides. The 700 mm line source is also drawn.*

For the sensitivity assessment of the two systems, the line source was simulated as a water filled tube with a homogeneous distribution of ^{18}F within it, that isotropically emits β^+. The sleeves surrounding the source were made of aluminium. Once the acquisition is started, the single and coincidences events detected are stored in ROOT format.

4.6 Validation for the HiRez system

The estimation of the sensitivity has been performed following the NEMA NU-2 2001 protocol previously described. Two acquisitions have been performed, with the line source in the centre and at 10 cm radial offset from the centre of the transaxial FOV. The activity in the line source was of 100 kBq, for 500 s long acquisitions.

The digitizer chain of the HIREZ scanner is not still optimally implemented in GATE, giving some disagreements with respect to the count rate performance at high activity concentrations. Since the activity used for our calculations is rather low, the present results are reliable.

The calculated relative sensitivity for 5 aluminium thicknesses is given in Fig. 4.12, with the regression fit line also plotted. The extrapolated absolute sensitivity at zero thickness is of 6.65 cps/kBq. If a certain span and ring difference (RD) in the coincidences selection is introduces, we obtain a much more flat distribution in the central region of the scanner. For the 27 RD implemented in HIREZ systems, the correction factor of the total sensitivity is 0.67 according to Ref. [62], giving a new value of the absolute sensitivity of 4.46 cps/kBq, in good agreement with the experimental value given in Ref. [63]: 4.87 cps/kBq.

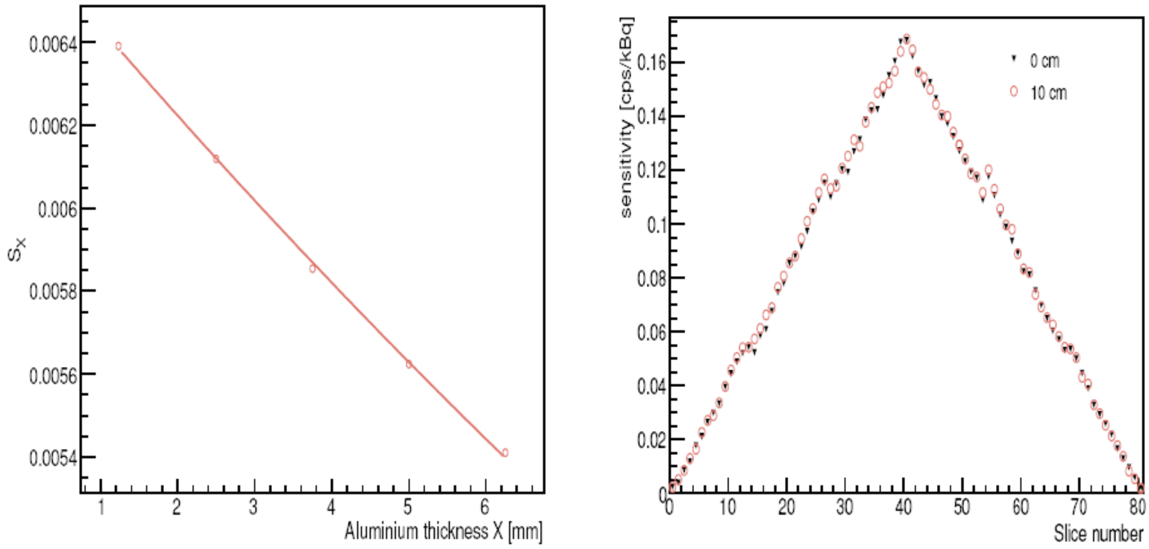

Figure 4.12 *Left panel: calculated count rate of the HiRez scanner as a function of the aluminium thickness. The red line represents the regression fit given by Eq. 20. Right panel: sensitivity profile of the HIREZ scanner, without span and RD. The line source is placed in the centre (black triangle) and 10 cm apart (red circle) of the transaxial FOV.*

Moving by 10 cm the source from the centre of the transaxial FOV, the sensitivity increases by 2%, as also reported in the last Reference. The central and 10 cm away axial sensitivities (without span or RD correction) for each slice are given in the right panel of Fig. 47. The sensitivity of the HIREZ scanner is in reasonable agreement (10%) with experimental data.

The difference between the two results (4.46 cps/kBq and 4.87 cps/kBq) can arise from some features of the scanner not properly reproduced in the GATE geometry, like the packing

[62] Eriksson L. et al., "Potential for a fifth generation PET scanner for oncology", IEEE Nucl. Sci. Symp. Conference Record (2005)

[63] Brambilla M. et al., "Performance Characteristics Obtained for a New 3-Dimensional Lutetium Oxyorthosilicate-Based Whole-Body PET/CT Scanner with the National Electrical Manufacturers Association NU 2-2001 Standard", J. Nuc. Med. 46 (2005) 2083-2091.

fraction of the unit block detectors. Anyway, the agreement is good and certainly sufficient for the aims of the present work.

Sensitivity of a dual-head scanner

For the dual-head system the same procedure of the HIREZ scanner has been followed.

The calculated absolute sensitivity, extrapolated from the regression fit of Fig. 4.13, is 8.0 cps/kBq, 20% higher than the HIREZ system.

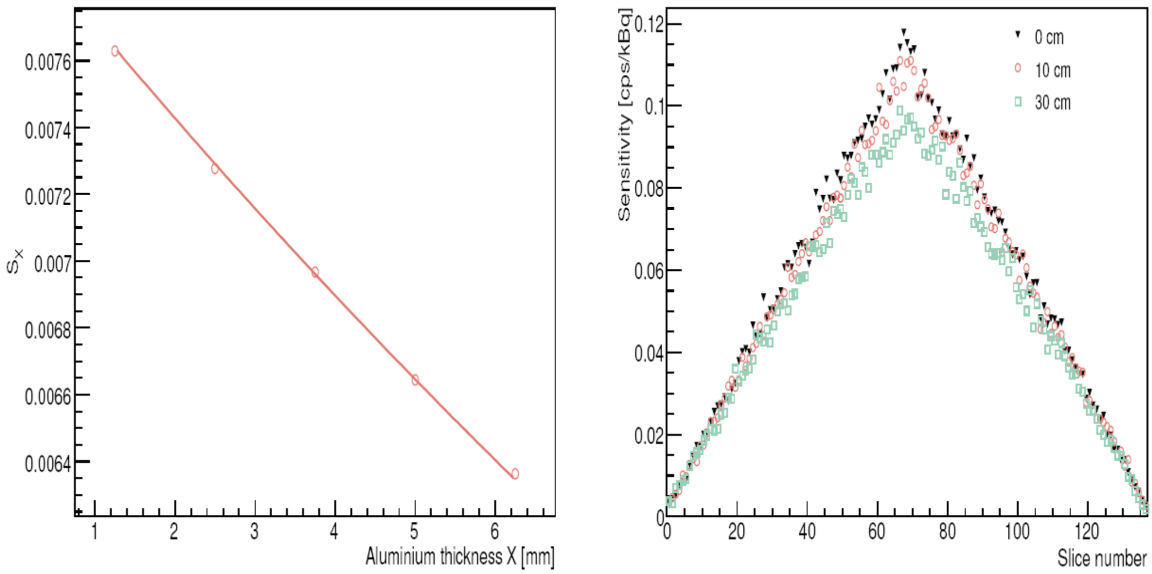

Figure 4.13 *Left panel: calculated count rate of the dual-head scanner as a function of the aluminium thickness. The red line represents the regression fit given by Eq. 20. Right panel: sensitivity profile of the dual-head scanner, without span and RD. The line source is placed in the centre (black triangle), 10 cm apart (red circle) and 30 cm apart (green square) of the transaxial FOV.*

Moving the line source 10 cm and 30 cm from the centre of the transaxial FOV, the sensitivity decreases by 3% and 12% respectively (see the right panel of Fig. 4.13).

The higher sensitivity can be attributed partially to the wider axial FOV, but also to the increased crystal length. The scintillator sensitivity of an LSO block can be expressed, according to [64], as:

$$\eta_{scint}(s) = -0.05877 + 1.0754 \cdot [1 - exp(-s \cdot 0.5963)], \tag{4.6}$$

which gives the sensitivity for 511 keV gammas for different LSO thicknesses s, in the energy window 0.425 and 0.650 MeV.

The computed value of the sensitivity of a 3 cm long crystal is 0.837, to be compared to 0.690 for a 2 cm long crystal. The increase in sensitivity is of about 47% if the coincidence events are considered.

Thus the scanner studied satisfies the demand of increased sensitivity, despite the detector block is still not optimized for an in-beam acquisition.

[64] Eriksson L. et al., "Future Instrumentation in positron emission tomography", IEEE Nucl. Sci. Symp. Conference Record (2006)

4.7 Simulation of the hadrontherapy treatment acquisition

The number of in-beam recorded coincidences foreseen for CNAO will be relatively low with respect to other facilities with a beam microstructure that allows an intra-spill acquisition. It is thus even surly essential to quantify the number of coincidences in a standard treatment.

A carbon ion treatment planning has been simulated by means of Geant4, described and validated in Chapter 2.

A realistic treatment has been calculated by using the analytical code (ANCOD) implemented in the C++ object oriented environment [65] (courtesy of F. Bourhaleb). This code is based on the technique of inverse planning, that allows to estimate the best parameterizations and the optimal treatment. ANCOD is implemented in the frame of the voxel scan technique with pencil beams. Considering as input a CT and the target volume definition, ANCOD provides for each field and for each elementary voxel the energy and the fluence of the pencil beam.

The simulated volume, made of PMMA (ρ =1.19 g/cm^3), was divided into $128\times128\times51$ voxels, of $1.96\times1.96\times3.0$ mm^3. The target was confined within this volume. A virtual source was located 4 m far away from the treated volume. The pencil beam considered had $FWHM$ =4 mm, in both transverse directions.

The optimal values of fluence, energy and beam direction computed by ANCOD were given as input to Geant4. The outputs of the simulation were stored in ROOT format. The stored data were the dose delivered to each voxel of the volume and the isotopes produced (type and decay position) with an additional flag for the voxel during whose treatment the isotope has been produced.

The output data have been re-processed to reproduce the time delivery scheme of the treatment.

The initial carbon ion fluences have been divided into spills 2 s long, each delivering $7\cdot10^6$ carbon ions, resulting into 30 spills to release the reference dose of 2 Gy. The carbon energies decrease when moving the scanned beam from the distal layer of the target to the closer one. The intensity of the beam is lower than the nominal value for CNAO (10^8 s^{-1}) due to the small size of the tumor (despite no protocol has still been defined for small tumor treatments at CNAO) [66].

The time structure of the incoming beam was assigned to the created isotopes by using the recorded voxel flag. For each spill, three voxellized isotope maps have been created and written in an ASCII data format compatible with GATE: they refer to ^{11}C, ^{10}C and ^{15}O, the three isotopes whose production yields have been validated against experimental data.

An inter-spill pause of 2 s was assumed, resulting in a 50% duty factor (see Fig. 4.14).

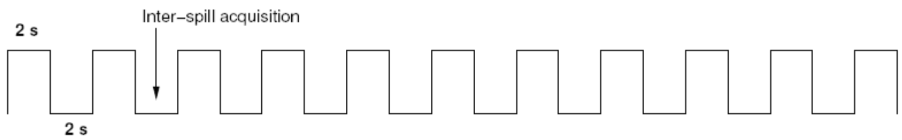

Figure 4.14 *Schematic drawing of the time structure of the simulated treatment. The dose is delivered in 30 spills, with 2 s long macropulse and 2 s pause between each beam extraction. The coincidence acquisition is performed during the inter-spill pauses.*

[65] Berga S. et al., "A code for hadrontherapy treatment planning with voxelscan method", Comp. Bio. Med. 30 (2000) 311-327.
[66] Pullia M., private communication

After each beam extraction, a 2 s long acquisition is started by means of GATE with the double-head detector geometry described above (see Fig. 4.15).

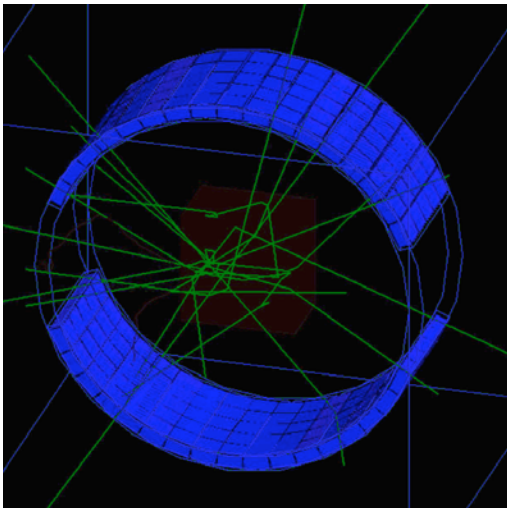

Figure 4.15 *Dual-head scanner for an in-beam acquisition simulation. The treated volume is located in the centre of the FOV of the scanner (red box).*

At each acquisition the isotope voxellized map, located in the scanner FOV, was given by the sum of the activities induced in the last spill and in the previous ones, with a weighting factor to take into account the time elapsed between the production spill and the acquisition time. The full simulation scheme is depicted in Fig. 4.16.

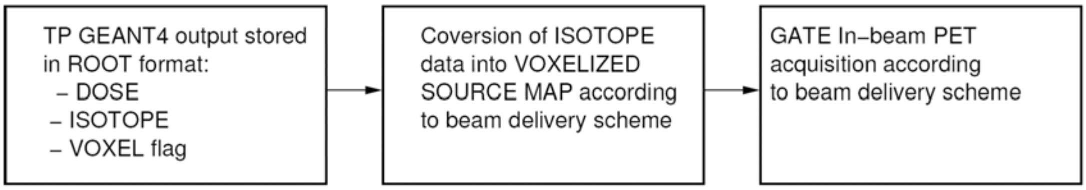

Figure 4.16 *Scheme of the simulation code.*

The first acquisition has been performed during the beam extraction pauses with 5 additional minutes after the end of the treatment. The scanner configuration is presented in Fig. 50, with in the centre of the scanner the volume treated. The coincidences are selected with a narrow energy window (0.425-0.650 keV as before) and a short coincidence time (4.5 ns). Fig. 4.17 shows the detected coincidences during the spill pauses.

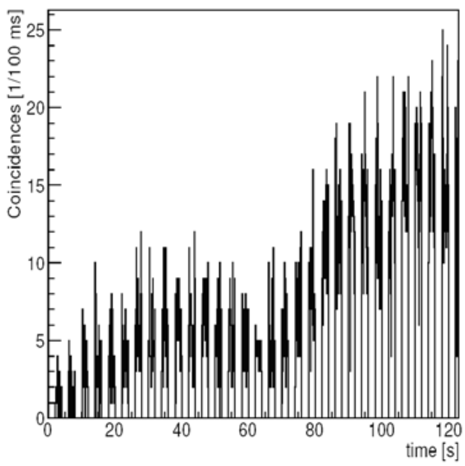

Figure 4.17 *Time distribution of the detected coincidences during the inter-spill acquisition.*

The sensitivity of the system calculated in Section 4.4 is 8.0 cps/kBq. In the last 2 s, at the end of the irradiation, the number of coincidences detected within the indicated energy window is 300. By dividing by the absolute sensitivity of the scanner (8.0 cps/kBq), the acquisition period (about 2 s), the target volume (about 45 cm^3) and by the 2 Gy delivered, the activity concentration in the volume is about 200 Bq $cm^{-3} Gy^{-1}$, close to the value measured at GSI [67].

In the five post-treatment minutes the number of detected coincidences decreases as the sum of three exponentials, with the three decay time constants equal to that of the three considered isotopes. The amplitudes of the three exponentials (see Fig. 4.18, red line) are related to the coincidence rate of ^{11}C, ^{10}C and ^{15}O, that - after the last beam spill - contribute to the total activity by 17%, 60% and 23% respectively. After five minutes, the number of coincidences is 5 times lower than at the peak.

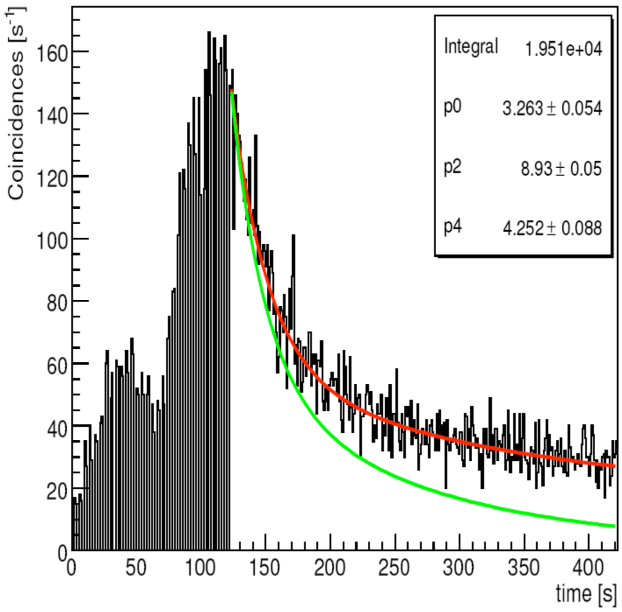

Figure 4.18 *Time distribution of detected coincidences without energy selection. The post-treatment acquired events are fitted by means of the sum of 3 exponential functions, one for each isotope considered (red line). The green line represents the convolution of the fit function with the exponential decay due to the biological wash-out whose life time is 4 minutes.*

To compensate the loss of coincidences during the beam extraction, it is reasonable to acquire for few minutes after the end of the treatment. This is particularly recommended in case of small tumors, as in this discussed case, because of the low activity induced and the short duration of the treatment. But the duration of the post-treatment acquisition must be defined taking into account the wash-out due to tissue metabolism. The wash-out can be modelled by means of an exponential decay with a time life, T_{biol}, of about 4 minutes [68]. In Fig. 4.18 the number of coincidences detected after the irradiation are multiplied by the biological decay, represented by the green curve. The main problem introduced by the biological wash-out is the lower contrast in image reconstruction. In fact, the isotopes are moving far from the target

[67] Parodi K., "On the feasibility of dose quantificaion with in-beam PET data in radiotherapy with ^{12}C and proton beams", PhD thesis, Technischen Universitat Dresden, Germany (2004)

[68] Fiedler F. et al., "In-beam PET measurements of biological half-lives of ^{12}C irradiation induced β^+ -activity", GSI Report.

volume creating a diffuse background. The diffusion rate depends on the individual and on the tumor treated, but it poses an upper limit to the duration of the post-treatment acquisition.

Even if the sensitivity of the chosen scanner is compatible (and even higher) than the one of standard scanners, the presence of the two gaps limits the quality of the reconstructed image introducing some deformations and artifacts. The in-beam scanner studied, at least for treatment room equipped with both vertical and horizontal lines, must be able to rotate around its horizontal axis in order to leave a free entrance window for the vertical beam (see Fig. 4.19). Therefore, to compensate for the loss of events by the two gaps, it is possible to perform a complementary post-treatment acquisition with the scanner rotated by $\pi/2$ with respect to the inter-spill acquisition, when the position of the scanner is limited by the irradiation set-up.

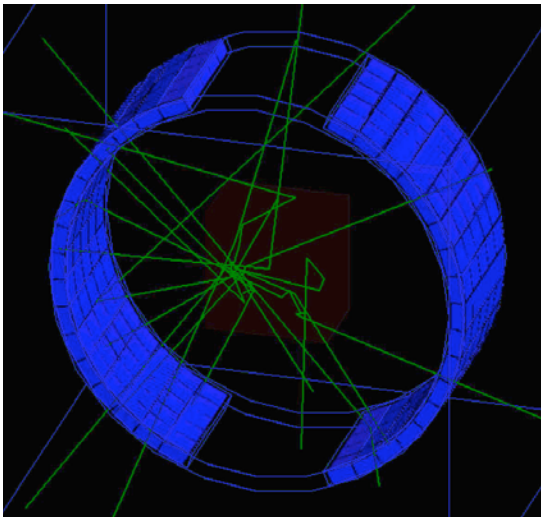

Figure 4.19 *Dual-head scanner for an in-beam post-treatment acquisition, rotated of* $\pi/2$. *The treated volume is located in the centre of the FOV of the scanner (red box).*

In Fig. 4.20 the sinograms of two different acquisitions are presented. In the first one (left panel) the scanner gaps are kept in the same position during and after the treatment.

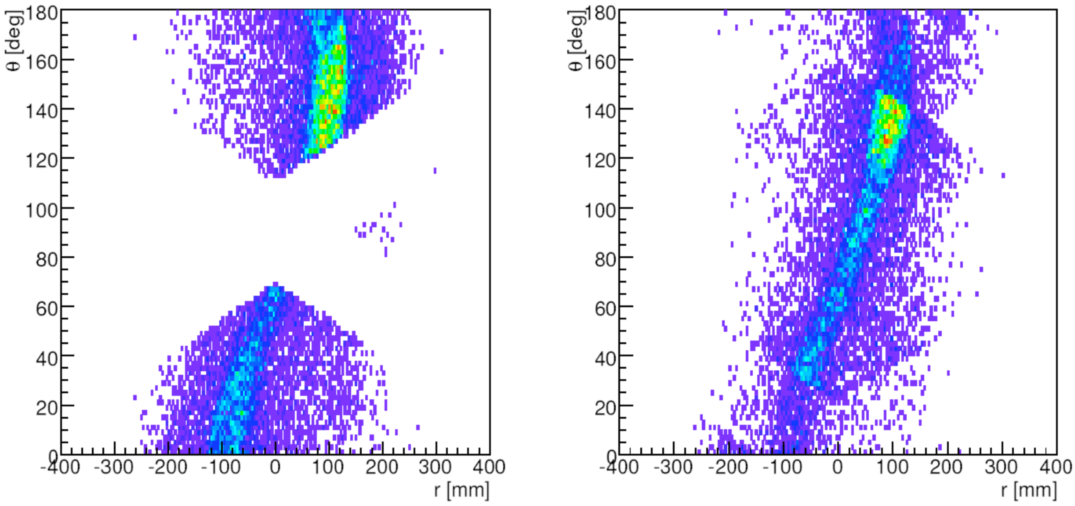

Figure 4.20 *Sinograms reconstructed for two different acquisition scheme. Left panel: the position of the two gaps in fixed during the inter-spill and post-treatment acquisition. Right panel: the two gaps are rotated of* $\pi/2$ *between the inter-spill and post-treatment acquisition.*

The sinogram of the left panel is empty in the angular interval where the angular coverage is missing. In the second case, after the inter-spill acquisition, the scanner is rotated by $\pi / 2$ for the5 minutes long post-irradiation acquisition. The area in the middle of the sinogram of the right panel is now covered.

By combining events acquired in the two scanner positions, the final reconstructed image is expected to be less affected by artifacts and therefore the monitoring of the treatment is more accurate. The rotation angle can be optimized to obtain the higher sensitivity over the full treated area, depending on the size of the treated tumor and its location with respect to the centre of the tomograph.

The optimal way to implement this acquisition scheme needs a more detailed study concerning the effective gain on the quality of the reconstructed image. To perform this study a dedicated reconstruction algorithm is required.

4.8 Discussion of the results

The possible geometries of the in-beam PET scanner for the CNAO are a full ring and a double-head scanner. In the first considered design, the geometrical constraints i.e. the limitations on the internal radius and on the axial length of the tomograph, are imposed by the size of the virtual patient, by the distance of the external surface of the nozzle to the isocentre and by the extent of the incoming beam field and of the fragments exiting the patient. Whereas when considering a double-head scanner, the two gaps make possible to keep the axis of the scanner parallel to the patient axis, with weaker constraints on the geometry.

The limitations to the geometry of a full ring scanner have been extensively discussed leading to a feasible geometry having R =45 cm and a =30 cm. Such a geometry would require an extremely compact block detector in order to avoid any collision with the nozzle. In the case of a double-head scanner, because of the absence of constraints with respect to the patient, the chosen parameter values of the geometry are R =40 cm, a =30 cm and 40 degrees gap. This solution puts less strict constraints on the size of the final detector and mainly for this reason it is the geometry of choice.

Due to the low activity induced in the patient, the performance of the in-beam PET needs to be first estimated with respect to the sensitivity i.e. the true coincidences count rate detection capability. In order to estimate the sensitivity of the chosen PET in a rigorous way, the NEMA NU-2 2001 standard protocol was used. The study was performed by means of GATE, a Monte Carlo application to emission tomography. The sensitivity of the considered scanner obtained by the calculations was 8.0 cps/kBq, to be compared to the computed value of 4.46 cps/kBq for the HiRez PET from Siemens. The obtained sensitivity is high enough to guarantee an efficient detection of the few coincidences available during an in-beam acquisition.

The reliability of a treatment monitoring is affected by the quality of the acquired activity map as well as by the proper simulation of the calculated one. The computed isotope distribution map has to be convoluted with the scanner response and an accurate simulation of the full acquisition can reduce computational artifacts in the simulated activity profile. For this purpose, a full in-beam acquisition was simulated with the described double-head scanner. A carbon ion treatment of a rather small (about 45 cm^3) tumor was simulated by means of Geant4 and the distribution of radioisotopes produced in the target was computed. An inter-spill acquisition was simulated supposing 50% duty factor with 2 s long pause between beam macro-pulses. The number of calculated coincidences at the end of the treatment, within the energy window 425-650 keV, was 300 that, by considering the sensitivy of the scanner leads to a value of 200 Bq cm^{-3} Gy^{-1}, in agreement with the value provided by GSI.

The main disadvantage of a double-head scanner is the possible presence of artifacts and distortions of the reconstructed image, due to the lack of a full angular coverage. To overcome this problem, a few minutes post-treatment acquisition has been suggested with the scanner rotated in order to guarantee a more uniform coverage of the treated volume.

5. IN-BEAM-PET WITH CRYSTALS

5.1 Introduction

PET is a well-known diagnostic technique to interrogate cancer and cardiac biology and serves as a critical component of molecular imaging. The continuous developments in detector and computing reflecting the growth of High Energy Particle Physics experiments, contribute to increase the performances of such devices.

Proton-rich isotopes may decay via positron emission, in which a proton in the nucleus decays to a neutron, a positron and a neutrino. As positrons travel through human tissue they give up their kinetic energy principally by Coulomb interactions with electrons. When the positrons reach thermal energy, they start interacting with electrons either by annihilation, which produces two 511 keV photons, anti-parallel in the positron frame, or by formation of a hydrogen-like orbiting couple called positronium.

In its ground state, positronium has two forms: ortho-positronium, where the spins of the electron and positron are parallel, and para-positronium, where the spins are anti-parallel. Para-positronium again decays by self-annihilation, generating two anti-parallel 511 keV photons. Ortho-positronium self-annihilates by emission of three photons. Both forms are susceptible to the pick-off process, where the positron annihilates with another electron. Free annihilation and the pick-off process are responsible for over the 80 % of the decay events.

Variations in the momentum of the interacting particles involved in free annihilation and pick-off process result in an angular uncertainty in the direction of the 511 keV photons around 4 mrad in the laboratory frame of reference. In a PET camera of 1 m diameter and an active transaxial Field Of View (FOV) of 0.6 m this results in a positional inaccuracy of 2-3 mm.

The two 511-keV annihilation photons have a mean attenuation length of 10.4 cm in water. The human head and chest have dimensions of the order of 20 cm; this means that in whole-body PET only 15 % of photon pairs have no interaction in biological tissue. In most cases, one or both photons will be either absorbed or Compton scattered. In PET scanners, each detector generates a timed pulse when it registers an incident photon. These pulses are then combined in coincidence circuitry, and if the pulses fall within a short time window, they are deemed to be coincident. A coincidence event is assigned to a line of response (LOR) joining the two relevant detectors. In this way, positional information is gained from the detected radiation without the need for a physical collimation (*septa*). This is known as *electronic collimation* and it has two major advantages over physical collimation: the improved sensitivity and the improved uniformity of the point source response function (*psrf*).[69]

5.2 Scintillators and detectors

Inorganic scintillator crystals are the most commonly used detectors for PET. Annihilation photons interact within the scintillator through Rayleigh, Compton and photoelectric effects. Only the latter two release energy to the detector, making the photons “detectable”. The absorbed energy causes the crystal lattice to make a transition to higher energy state, from which it may undergo decay after a characteristic time by emitting lower energy photons.

[69] http://depts.washington.edu/nucmed/IRL/pet_intro/toc.html

Inorganic crystals are used for gamma detection and in the last years there has been a positive trend towards the development of faster, more luminous and denser scintillating materials (Table 5.1).

Table 5.1 *Comparison of scintillator properties that have already been used for PET and newly developed scintillating materials* [70]*. R_E is the energy resolution and L_{att} is the attenuation length.*

Scintillator	**Luminosity** $[N_{ph}/MeV]$	**Decay time** $[ns]$	**Initial rate** $[N_{ph}/ns/MeV]$	$\mathbf{R}_E$ $[\%]$	$\mathbf{L}_{att}$ $[cm]$
BGO ($Bi_4Ge_3O_12$)	700	60	12	12	1.1
	7500	600	25		
Total	8200		37		
BaF_2	1800	0.8	2250	10	2.3
	10000	630	16		
Total	11.800		2260		
CsF	2500	2.9	862	20	2.7
GSO (Gd_2SiO_5:Ce)	10000	43 fall	232	9	1.5
		14.4 rise			
LSO (Lu_2SiO_5:Ce)	25000	37	676	10	1.2
LuAP ($LuAlO_3$:Ce)	5800	11	524	8	1.1
	2500	28	104		
	1200	835	1		
Total	9500		629		
LuYAP ($Lu_{0.7}Y_{0.3}AlO_3$:Ce)	12500	25 + 250		8	1.3
$LaCl_3$:Ce	50000	20	2500	3	2.9
$LaBr_3$:Ce (5%)	60000	15	4000	3	2.2
$LaBr_3$:Ce (10%)	56000	16	3500	3	2.2
$LaBr_3$:Ce (20%)	55000	17	3235	3	2.2
$LaBr_3$:Ce (30%)	55000	18	3056	3	2.2
$CeBr_3$	68000	17	4000	3	2.2
$LaCl_3$:Ce	100000	23	4348	4	1.8

[70] Moses W., "Recent advances and future advances in time-of-flight PET", Nucl. Instr. and Meth. A in press (2007)

The luminescence processes occurring in inorganic scintillators are of two types, according to the time scale in which light emission takes place: fluorescence, if the time constant is shorter than 10^{-8} s, and phosphorescence or afterglow, with emission time larger than 10^{-8} s and for some materials as large as several hours. The majority of inorganic crystals are impurity-activated, as alkali halides activated by heavy metals like Thallium (CsI:Tl), or oxides doped with rare earth ions as Cerium (LSO:Ce). Other scintillators are self-activated, like BGO or BaF_2, by an excess of one of the constituents.

Gamma interactions

Gammas interact with matter by different processes: coherent scattering, Compton scattering, photoelectric effect and pair production. The total absorption coefficient is the sum of the coefficient of each process and is given by:

$$\mu = \sigma_{coherent} + \tau_{photoelectric} + \sigma_{compton} + \kappa_{pair}. \tag{5.1}$$

The resulting μ is called the linear attenuation coefficient.

Among all the possible gamma interactions, for detection purposes the most effective process is the photoelectric one, since all the energy of the incoming gamma is transferred to a single electron. The photoelectric process is enhanced for absorbers with high atomic number Z, and this is the reason for which the tendency in scintillators is towards the development of higher Z materials. No single analytic expression is valid for the probability of photoelectric absorption per atom over all ranges of the gamma energy E_γ and Z. A good approximation is given by the following equation:

$$\tau \propto \frac{Z^n}{E_\gamma^{\ 3.5}}, \tag{5.2}$$

where n varies between 4 and 5.

Mechanisms in inorganic scintillators

The efficiency η of a scintillator to convert the energy of the incident gamma into light depends mainly on three parameters:

$$\eta = \beta \cdot S \cdot Q, \tag{5.3}$$

where β, S and Q are the conversion, transfer and luminescence efficiencies respectively[71]. At the very beginning of the interaction process, the ionization event creates an inner shell hole and an energetic primary electron is freed with subsequent radiative or non-radiative decay, and inelastic electron-electron scattering. This first stage occurs in the first 10^{-15}-10^{-13} s and it is related to the parameter β that describes the efficiency of the conversion process. The energy E_e of the electron, set in motion by the gamma, generally allows to produce a large number of electron-hole (e^--h) pairs. If the energy required to produce an e^--h pair is ξ=kE_g, where E_g is the band gap energy and k ranges between 2 and 7, the achievable number of pairs of charge carriers is E_e/kE_g.

When the electron energy becomes lower than the ionization threshold, it (or the hole) can thermalize by means of intraband transitions and energy loss to phonons. The charge carriers can remain as a diffuse band states, become trapped on defects and impurities, become self-

[71] Lempicki A.et al., "Fundamental limits of scintillator performance", Nucl. Instr. and Meth. A333 (1993) 304-311.

trapped by the crystal lattice, or form free and impurity-bound excitons. During this second stage luminescent centres can be excited by impact with hot electrons or sequential electron-hole capture. The energy transfer process, related to the parameter S, ranges from less than 10^{-12} to more than 10^{-8} s, and it is responsible of the rise time of the scintillation light. Hence S is related to the efficiency of e^--h and excitons to migrate and transfer their energy to luminescence centres.

In the third stage, the excited luminescent sites return to their ground state by non-radiative quenching processes or by emitting photons. The radiative process can last 10^{-9} s for e^--h recombination or can take several minutes for highly forbidden transitions. At this stage, many processes can limit the luminescence efficiency Q, like non-radiative transitions or processes related to energy transfer [72]. For example, for NaI:Tl, typical values for β, Q and S are 0.88, 1.0 and 0.59, leading to a total efficiency η of 0.52. At the end of the three stages, the number of photons produced is given by:

$$n_p = n_{e-h} \cdot S \cdot Q = \frac{E_e}{kE_g} \cdot \beta \cdot S \cdot Q. \tag{5.4}$$

A typical value for NaI:Tl is 75,000 n_{e-h}, to be compared with 38,000 N_{ph}/MeV.

From Eq. 5.4 it is clear that the lower is the band gap energy the higher will be the light output, but in this extreme case of small E_g the probability that an optical photon is reabsorbed by the gap is high and this consequently reduces the light output [73].

Energy resolution

In order to resolve the energies of the incoming gammas, a good energy resolution is an important requirement. The average amount of charge Q_0 delivered by a Photomultiplier Tube (PMT) is:

$$Q_0 = \bar{N} \cdot \bar{p} \cdot \bar{M}, \tag{5.5}$$

where $\bar{N}$ is the average number of optical photons produced by the scintillator after a gamma interaction, $\bar{p}$ is the average transfer efficiency of light from the crystal to the first dynode of the PMT (i.e. the probability that a photon from the scintillator results in the arrival of a photoelectron at the first dynode) and $\bar{M}$ is the mean electron multiplication factor of the PMT [74].

The energy resolution R is a feature of the gamma energy E and is defined as the ratio between the $FWHM$ of the peak and its maximum. The variance $\upsilon(Q_0)$ is calculated as:

$$R = \left(\frac{\Delta E}{E}\right)_{FWHM} = 2.36\sqrt{\upsilon(Q_0)}. \tag{5.6}$$

The variance can be approximated as:

$$\upsilon(Q_0) \approx \left[\upsilon(N) - \frac{1}{\bar{N}}\right] + \upsilon(p) + \frac{1+\upsilon(M)}{\bar{N}\bar{p}}. \tag{5.7}$$

---

[72] Lecoq P. et al., "Inorganic scintillators for Detector Systems- Physical Principles and Crystal Engineering", Berlin Heidelberg, Springer-Verlag (2006)

[73] Derenzo S. E. et al., "The quest for the ideal inorganic scintillator", Nucl. Instr. and Meth. A 505 (2003) 111-117.

[74] Dorenbos P., et al. "Non-proportionality in the scintillation response and the energy resolution obtainable with scintillation crystals",IEEE Trans. Nucl. Sci. 42 (1995) 2190-2202.

The term in brackets in Eq. 5.7 refers to fluctuations in the number N of photons which are not due to pure Poisson statistics. The second term $\upsilon(p)$ is the fluctuation in the photon transfer and the last term is the photomultiplier variance, mainly due to gain fluctuations. From Eqs. 5.6 and 5.7, the energy resolution can be written as:

$$R^2 = R_i^2 + R_p^2 + R_M^2, \tag{5.8}$$

where R_i is the intrinsic resolution of the scintillator, dominated by non linearities of the light output for different gamma energies and by the presence of impurities or dishomogeneities in the crystal. In modern PMTs R_p can be neglected, while R_M is proportional to the square root of the last term of Eq. 5.7, i.e. is inversely proportional to the number of electrons hitting the first dynode.

Light detectors

The light collected in crystals is converted into measurable electrical voltage pulse in commercial PET scanners usually by photomultiplier tubes (PMTs). These devices convert the scintillation light into a very weak electrical signal at the photocathode, which is then amplified through an efficient low noise avalanche cascade process. This process repeats until amplifications of the initial voltage pulse of > 10^5 are achieved. The high gain, stability and low noise of PMTs have rendered these devices the standard ones used in PET scanners. The most common detector configuration used in commercial scanners couples each detector block to four PMTs with light sharing, providing the position of the conversion with an accuracy of a few mm or better.

The development of multi-anode position-sensitive photomultiplier tubes (PSPMTs) of square shape allows accurate positional and energy information to be derived from the PMT itself. These devices utilize the positional information of the electron ejection site from the photocathode, which are steered into different compartments within the PMT tube.

The spatial resolution of typical PET scanners is limited by the scintillator PMT block design and the low quantum efficiency of PMTs. To achieve a higher spatial resolution, a higher segmentation of scintillators is required with the ability to readout each segment independently.

Solid-state photodiodes, in contrast to PMTs, are small, operate at much smaller voltage and exhibit higher quantum efficiencies. This allows the possibility of easy read-out patterns of the sensitive area, especially through the introduction of monolithic pixilated photo-detectors. The most important silicon planar photo-detectors are silicon p-i-n photodiodes (PDs), avalanche photodiodes (APDs) and silicon drift photo-detectors. A recent development, the silicon photomultiplier (SiPM) is receiving a lot of attention for PET imaging applications, due to its high gain and promising low cost; at the present time however it is not yet commercially available in sizes and quantities suited for a PET project.

5.3 Specification of the in-beam-PET device

The basic detector technologies used for in-beam-PET imager are similar to those used for standard systems. However the results of the simulation discussed in the previous Chapter indicate some major differences in the requirements and thus in the design:

1. The true counting rates, defined as the total number of 511 keV collinear photons due to positron-emitting isotopes, are of the order of 200 Bq Gye^{-1} cm^{-3} and are smaller by at least two orders of magnitude than in normal PET diagnostics;

2. The relatively long range of the emitted positrons, mainly due to ^{11}C and ^{15}O, is larger than the one of ^{18}F used in standard PET examinations, and limits the achievable image resolution;
3. The large background of charged and neutral particles emitted during a treatment with carbon ions, peaked in the forward direction but conspicuous over the full solid angle, implies large singles rates in each detector element and masks the true coincidence signal;
4. The large flux of secondary particles may cause radiation-induced aging problems in the detector elements close to the forward direction;
5. The short decay time of the beta-emitting isotopes implies that data have to be collected during and immediately after the irradiation, i.e. during the ramping down and up of the synchrotron magnets and, if necessary, for a few minutes before the patient leaves the irradiation position.

Points 1 and 2, in particular, suggest a detector design which is very different from the ones developed and constructed by many groups for the so called "animal PETs". In the former case millimetre accuracies combine with enormous counting rate and, thus, not very large solid angles are sufficient. For a PET-on-beam device the statistical error on the number of positron annihilations is important and resolution is not a major issue.

Point 3 and 4 require that no detector be placed "forward", i.e. close to the direction of the incoming beam which at CNAO covers a 20x20 cm^2 surface.

The remarks above suggest a device design with the following main properties:

- Detector thickness between two and three absorption lengths, to provide efficient detection;
- Fast detector elements with, if possible, a good energy resolution, to optimize the signal-to-noise ratio, or NEC (Noise Equivalent Count);
- Short intrinsic time of the detector elements, permitting a coincidence width of ten nanoseconds or shorter, in order to improve the effective count rate in presence of a large non-correlated background;
- Detector elements in the forward cone which are robust to radiation damage, due in particular to high gamma and neutron fluxes, so that the system can stand the high background during treatments;
- Data recording taking place only in the time intervals between spills;
- Methods for coarse determination of the depth of interaction, which may be needed for some geometry, in order to reduce the parallax error.

A scintillator solution based on LSO (Lanthanum Orthosilicate) as scintillator satisfies the above requirements at best, and is commercially available in large quantities, being the material of choice for the present generation of PET/SPECT scanners.

For the scintillation photon detectors, the choice is wider, from conventional photomultipliers to solid-state devices. However, the requirement of a coarse determination of the depth of interaction, considerations of cost and commercial availability indicate a preference for the readout of multi-anode photomultipliers (MAPM) or Avalanche Photodiodes (APD) arrays.

The already mentioned recently developed Silicon Photomultipliers (SiPM) have also to be considered, owing to their large gain, which eliminates the need of using channel amplifiers. In the long term, this would be a better choice, but for the time being SiPM are not commercially available in the sizes needed for a PET scanner.

In general, for in-beam-PET, the most important quantity to be mapped is the beam penetration or range in the body. The detector geometry has therefore to be optimized for the measurement of the positron-emitting nuclei density in the direction of the beam while leaving an opening for the entry port of the beam with its halo, and the most intense part of the forward secondary radiation.

5.4 Review of in-beam-PET systems

The first attempts at operating an in-beam positron tomography at Lawrence Berkeley National Laboratory had to be abandoned due to detector activation arising most probably from the flux of secondary particles caused by passive beam shaping techniques. To avoid this problem, a dual-head positron camera was installed at GSI. This was done after careful investigations of imaging capabilities of the selected tomograph[75]. The In-beam-PET acquisition was synchronized with the time structure of particle extraction.

The BASTEI detector (Beta Activity Measurements at the Therapy with Energetic Ions), installed at GSI, consists of two heads having a 42x21 cm^2 front area each. Each sphere, forming a calotte of 41.5 cm radius, was built from block detectors of the ECAT EXACT tomograph from CTI PET Systems Inc. The block units of this detector are made of inorganic scintillator BGO crystals coupled to photomultiplier tubes (PMT). Each block is subdivided into 8x8 BGO with 6.75x6.75 mm^2 front surface each and 20 mm depth and is read by four PMT. Each head consists of 8x4 block detectors. This detector arrangement consists of about 4.2 million lines of response (LOR) crossing the field of view (FOV) of the scanner. For the limited-angle tomograph described, a dedicated, attenuation correcting, maximum likelihood expectation maximization (MLEM) algorithm was developed[76].

The positive clinical impact of the GSI tumour therapy pilot project triggered the construction of a hospital-based hadron therapy facility HIT in Heidelberg, with in-beam PET expected to monitor more delicate radio-therapeutic situations.

In order to improve In-beam-PET by optimizing the detector arrangement, both a closed ring and a dual-head scanner have been considered. From simulations performed, both dual-head tomograph studied (φ=46 deg. and φ=100 deg.) clearly show reconstructed image degradation although the FOV completely covers the irradiated volume.

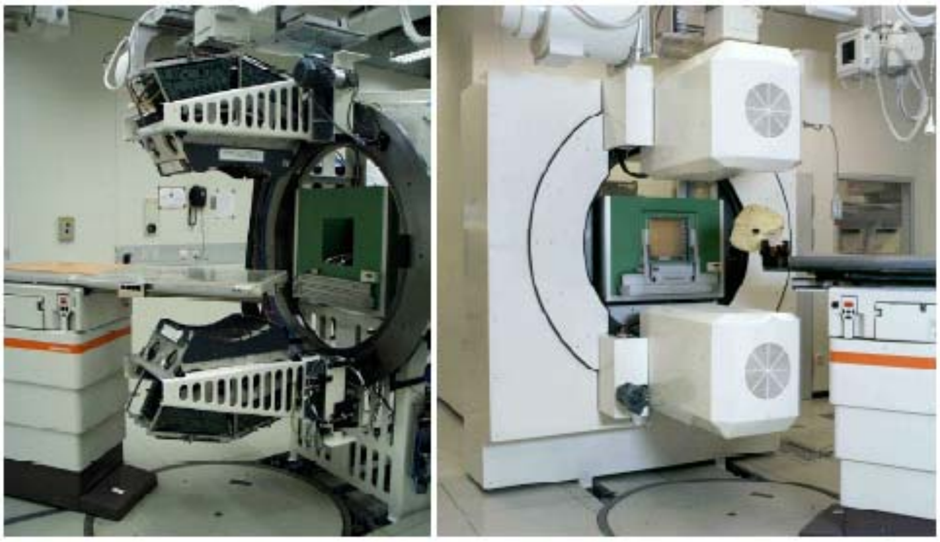

Figure 5.1 *The PET scanner installed at GSI without (left) and with (right) its housing.*

[75] Pawelke J. et al, Phys. Med. Biol. 41 (1996) 279.
[76] Crespo P., Shakirin G. and Enghardt W., Phys. Med. Biol. 51 (2006) 2143.

This result is due to less information arising from the gap between the detector heads. The benefits of a closed-ring tomograph are evident especially in case of a larger volume treated. The main problem occurring in the latter case concerns the constraints on the geometry of the tomograph due to the patient couch dimensions and the beam width, with a maximum window deliverable of 20x20 cm^2. Evaluating different combinations, some optimal configurations seem to be realizable although a very compact scanner is required with a limited radial depth including detectors, front-end electronics, cabling and support structure. To satisfy this requisite a LSO/APD array as possible detector for in-beam-PET has been proposed and studied[77]. The prototype consists of 32 LSO crystals coupled to the 4x8 pixels of a Hamamatsu S8550 avalanche photodiode array. The dimensions of a crystal after manual polishing are 2.34 ± 0.14 x 2.30 ± 0.15 x 15 ± 1 mm^3. Each crystal had all faces but one wrapped with Teflon tape, with the non-covered face coupled by silicon glue to each pixel pf the array (see Fig. 6.3). The Hamamatsu APD array shows good performance but a low internal gain (<80) and as a consequence a low signal-to-noise ratio, that can be improved by means of low noise preamplifiers[78].

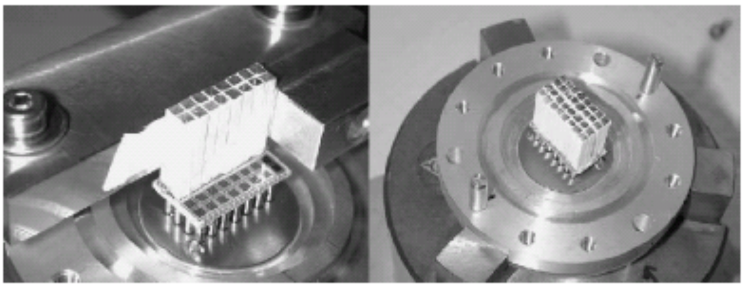

Figure 5.2 *Detector block made of 32 LSO crystal wrapped by Teflon and coupled one by one to an APD pixilated matrix.*

A first aspect analyzed concerns the check of the stability of the detectors and the influence of the beam on their performance since the imaging capabilities of these detectors are expected to be mostly influenced by the particle and photon flux generated by nuclear reactions. Two blocks as described above were developed and a ^{68}Ge line γ-source positioned between them. Imaging of this line source was performed before, during and after irradiating phantoms (9x9x20 cm^3) of PMMA. A pencil-like beam of 341 MeV/u carbon ions was used. The phantoms were positioned outside the FOV of the LSO/APD detectors. The mean energy resolution obtained on the photo-peak is 15.5 ± 0.4 % FWHM, while the measured coincidence time resolution is 6.2 ± 0.2 ns FWHM. An image of the depth distribution of β+ decaying radionuclides created in a phantom stopping the high-energy carbon ion beam was successfully performed. This was a major achievement since it demonstrated: 1) the in-beam capability of this detector type and 2) the sufficient radiation hardness of such detectors to be operated at a radiotherapy treatment site.

5.5 Description of the chosen device and motivations

The results obtained in the previous Chapters underline the key requirements that an in-beam-PET unit detector has to satisfy. Of course a good spatial resolution is desirable, but first of all a high detection capability is necessary due to the low counting rate. This requirement implies a high scanner sensitivity, which reduces the geometrical loss. In this Chapter the

[77] M. Kapusta et al, IEEE Trans. Nucl. Sci. 51 (2004) 1389.
[78] P. Crespo, M. Kapusta, J. Pawelke, M. Moszynski and Enghardt W., IEEE Trans. Nucl. Sci. NS51 (2004) 2654.

prototype of a new unit block detector is described. A preliminary study of the device has been carried out by means of an optical transport Monte Carlo code, LITRANI. Some preliminary experimental results are described in the last Sections.

Conventional PET cameras are a convenient starting point. Since long time the favored solution has been to couple a segmented block of BGO with 4 PMTs (see Fig. 5.3).

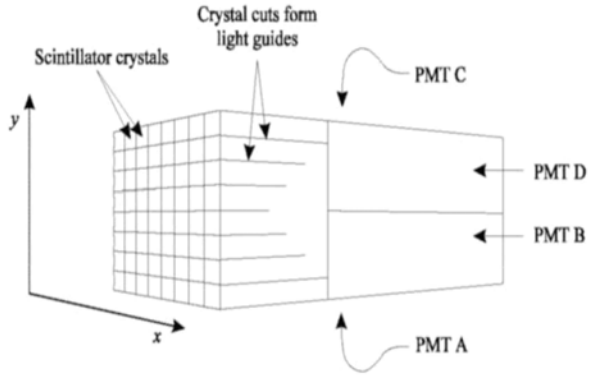

Figure 5.3 *Anger logic scheme read-out for a BGO block detector coupled to four PMTs* [79].

The crystals are obtained from a unique scintillator block and several grooves of variable lengths in the BGO act as light guides that improve the position accuracy of the four-PMT position logic [80]. The X and Y coordinates of the hit crystal are calculated with the Anger logic, according to the following equations:

$$X = \frac{A+C-B-D}{A+B+C+D} \qquad Y = \frac{A+B-C-D}{A+B+C+D}, \tag{5.9}$$

where A, B, C and D are the outputs of the four PMTs. The main drawbacks of these detectors are the uncertainty in the determination of the interaction point (the spatial resolution provided is of 5-6 mm), the limited counting rate and the difficulty in distinguishing Compton scattering events [81].. In fact, the total energy of the gamma can be deposited in a single photoelectric event or in multiple Compton and photoelectric interactions. In this last case, the Anger logic fails to localize the interaction point since the signal is more spread among PMTs than in a single energy deposition.

The modern trend in PET detector development is to use 2D-arrays of small crystals individually coupled to pixellated photodetectors. In this way a higher spatial resolution is easily achieved, because uncertainties in the identification of the hit crystal are avoided.

Another important issue, that triggered new detector research, is the capability of the device to determine the Depth Of Interaction (DOI), in order to improve the image quality at the periphery of the Field Of View (FOV). Many approaches have been studied like the phoswich detector, that exploits the pulse shape layer discrimination technique, and double-end read-out schemes, that compare the signal amplitudes arriving to the two end of each detector [[82]. This last technology has the drawback of a substantial increase in cost.

[79] Unversity of Washington Web page: http://depts.washington.edu/nucmed/IRL/pet _ intro/, "Introduction to nuclear physics".
[80] Phelps M., "Molecular Imaging with Positron Emission Tomography", Annu. Rev. Nucl. Part. Sci52 (2002) 303-338.
[81] Korzhik M. et al., "Development of scintillation materials for PET scanners", Nucl. Instr. and Meth.. A 571 (2007) 122-125.
[82] Auffray E. et al., "The ClearPET project", Nucl. Instr. and Meth. A527(2004)171-174

In this work a different detector solution was studied, based on a continuous scintillating material coupled to a position sensitive photodetector. This simple device, requires indeed sophisticated signal processing to localize the interaction point (X, Y, Z) and achieve a spatial resolution good enough for in-beam-PET.

To reduce the parallax error for off-normal incidence photons, a coarse measurement of the depth of interaction is needed, particularly for the proposed double ring solution. Several methods have been used for measuring the DOI:

- Dividing thick crystals in shorter elements with individual readout;
- Using the “phoswitch” scheme, where two or more crystals having different signal decay time are glued together on the same sensor, the DOI being estimated from a measurement of the pulse width or rise time;
- Measuring the light signal sharing on long crystals, read from both sides.

For the CNAO in-beam-PET it has been proposed an improved version of the last solution, made possible by the availability of multi-anode photomultipliers, avalanche photodiode and silicon photomultiplier matrices.

The basic idea is to use large crystals read out on one wide face with a multi-pad sensor, recording for each event the full profile of the collected light. To avoid the spread due to internal reflections, all faces of the crystal except the one read out can be either blackened or de-polished. For a localized flash of light within the crystal, produced by a photon conversion, the centre of gravity of the distribution, recorded on the sensor’s pads, provides the position of the conversion in the x-y projection, while its relative width increases with the distance from the sensor, or DOI.

One can start by considering a typical light yield of about 15,000 photons emitted at the conversion point by a 511 KeV gamma. An estimate of the expected signal, taking into account the solid angle seen by the wide face (10 to 50%, depending on the DOI), the quantum efficiency of the PM (20%) and the DOI-dependent sharing between pads gives between a few tens and a few hundreds photoelectrons collected by one pads, well above the PM noise.

Fig. 5.4 shows schematically the setup used for the simulation studies and the experimental measurements to be discussed in the following.

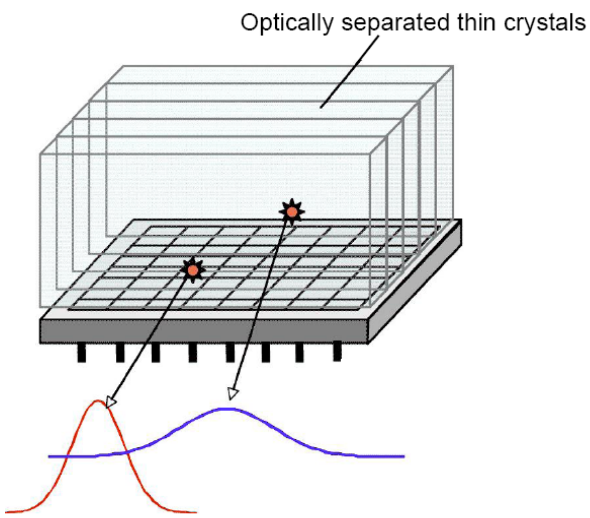

Figure 5.4 *Scheme of a PET detector module, made of many thin crystals mounted over a multi-pad detector. The photon distribution determines the longitudinal and depth coordinate of the scintillation point.*

The scintillation material choice has been led by several considerations. First of all the material has to be dense. Moreover, the material has to be fast, to keep small the integration time of the signal. Last, but not least, the crystal has to have a large scintillation yield.

The bromides $LaBr_3$ is attractive: this crystal has an excellent light yield and a fast decay time (15 ns), but unfortunately it is hygroscopic, very expensive and it has a small attenuation length (2.2 cm). Other two interesting materials are LuAP and LuYAP. They are fast and dense, relatively bright and they have a high light absorption. Another possibility is LYSO, which has been actually chosen not only because of the high light output and the fast decay time, but also because these crystals present a high level of transparency and homogeneity.

Concerning the photodetector, several devices have been considered among all technologies presently available (Table 5.2).

Table 5.2 *Photon detectors properties [84]. PDE is the photon detection efficiency.*

	Solid-state technology		Vacuum technology		
	APD	**SiPM**	**HPD**	**MA-PMT**	**MCP-PMT**
PDE Blue	50%	-	20%	20%	20%
PDE Green-Yellow	60-70%	-	40%	40%	40%
PDE Red	80%	-	<6%	<6%	<6%
Timing/10 ph.e.	few ns	tens ps	100 ps	100 ps	10 ps
Gain	1000	10^5-10^6	$3\text{-}8\times10^3$	10^6-10^7	10^6-10^7
Operation voltage	100-500 V	<100 V	20 kV	1 kV	3 kV
Operation in B	Yes	Yes	axial B 4 T	$<10^{-3}$ T	axial B 2 T
Sensitivity/ph.e.	10	1	1	1	1

An Avalanche PhotoDiode (APD) combines the advantages of a PIN photodiode (small, cheap, high QE, insensitivity to magnetic field) and those of a photomultiplier (gain and speed). Photons create electron-hole pair in the thin p-doped silicon layer of an APD. The electrons drift to the high field region at the p-n junction where they start, by ionization, an electron avalanche. The gain, that can be 1000 or more, is very sensitive to the stability of the applied voltage and to temperature fluctuations

The Silicon Photomultiplier (SiPM) of Fig. 5.5 would be a good candidate.

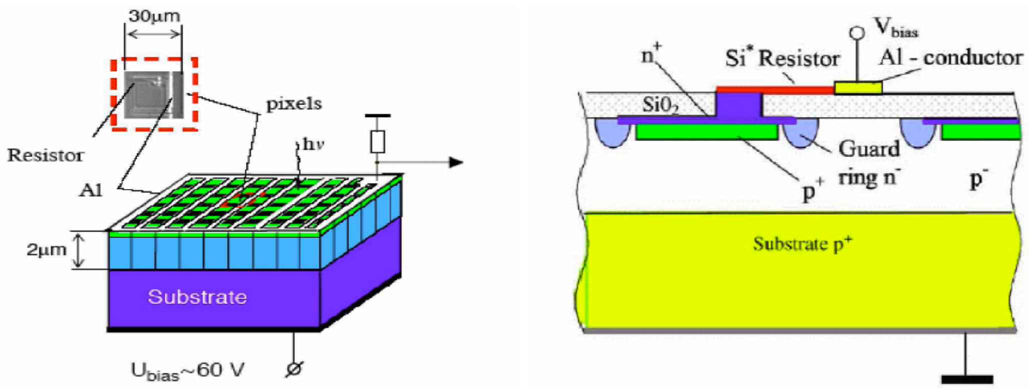

Figure 5.5 *Schematic drawing of a SiPM made of 30x30 μm^2 cells.*

It is a densely packed matrix of small, Geiger-mode avalanche photodiode (GAPD) of 30-50 μm side, with individual quenching resistances for each cell. It results in a compact device with a fast timing (50 ps), high gain (10^5-10^6), single photoelectron resolution and low noise [83]. But, even if SiPM would be a better choice, for the time being they are not commercially available in the sizes needed for a PET scanner. Instead Hybrid Photon Detectors (HPD) are available and combine the sensitivity of a vacuum PMT with the excellent spatial and energy resolutions of a silicon sensor. A single photoelectron ejected from the photocathode is accelerated through a potential difference of 20 kV before it impinges on the silicon anode. Since the gain is achieved in a single step one can expects to have an excellent resolution. HPDs can be segmented down to 50 μm. A prototype with 208 anode pixels, designed for an axial PET, is currently under construction at CERN [84].

Other two devices have been considered: the Multi-Anode PMT (MA-PMT) from Hamamatsu [85] and the Micro Channel Plate PMT (MCP-PMT) from Burle [86]. The MA-PMT is a position sensitive detector, which behaves like multiple PMTs within a single housing. The electron multiplication section consists of nine dynode stages. The spatial integrity of photoelectrons, which comes from the particular location (x, y) on the photocathode facing each anode, is preserved. The MA-PMT developed by Hamamatsu has a good time resolution for single photoelectrons of 140 ps [87].

The MCP-PMT consists of a microchannel-plate electron multiplier with a proximity focused cathode on one side and an anode at the other. The electron multiplication takes place in each single microchannel: one electron at the input can give rise to as many as 10^8 electrons at the output. The MCP-PMT shows in particular an excellent time resolution and it's considered as one of the candidates for the Ring Cherenkov (RICH) detector in the forward region of the upgraded Belle spectrometer. A single photon time resolution of 75 ps has been measured [88].

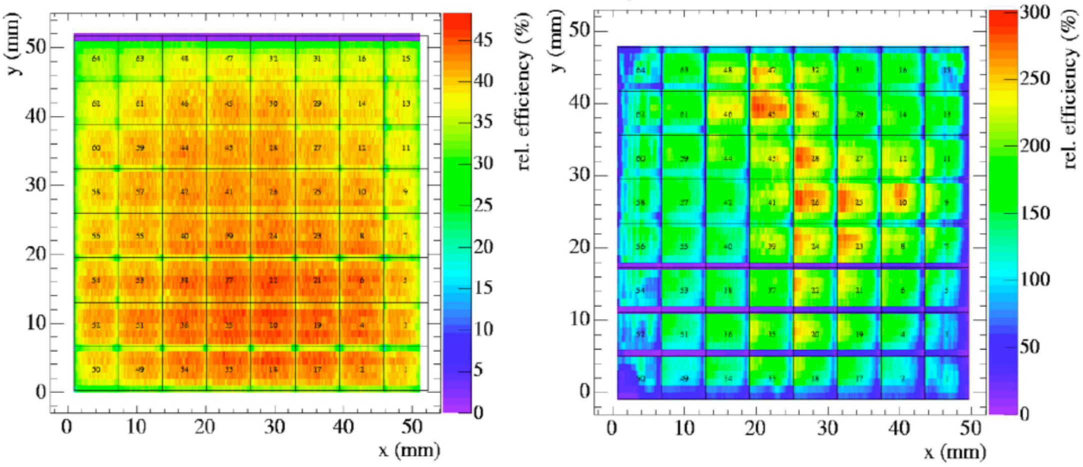

Figure 5.6 *Response of a MCP-PMT from Burle (left) and a MA-PMT from Hamamatsu (right) to a uniform illumination.*

---

83 Saveliev V. and Golovin V., "Silicon avalanche photodiodes on the base of metal-resistor-semiconductor (MRS) structures", Nucl. Instr. and Meth. A 442 (2000) 223-229.

84 Braem A. et al., "Design, fabrication and performance of the 10-in. TOM HPD", Nucl. Instr. and Meth. A518 (2004) 574-578.

85 Hamamatsu Web page: http://www.hamamatsu.com/

86 Burle Web page: http://www.burle.com/

87 Field C. et al., "Timing and Detection Efficiency Properties of Multi-Anode PMTs for a Focusing DIRC", IEEE Trans. Nucl. Sci. (2004) 1518-1521.

88 Bertovic I. et al., "Timing and Cross-Talk studies of BURLE 85011 MCP PMT", Nucl. Instr. and Meth. A (2007) 408-409.

As shown in Fig. 5.6, a MCP-PMT presents also a higher uniformity in response than a MA-PMT, and this is a critical property for the position reconstruction accuracy.

For its high uniformity and its excellent time resolution, the MCP-PMT has been chosen for the continuous crystal read-out. The MCP-PMT has some limitations in the counting rate and continuous operation at maximum rates may result in unreliable performances. In fact, due to the large total surface of the microchannel plate, it is difficult to outgas the channels completely. Internal electron bombardment therefore generates ions that hit the cathode and quickly reduce its sensitivity. However this is not a major problem because of the inter-spill acquisition foreseen at CNAO. It will be of course required to control the high voltage supply, turning it off quickly during the beam spills.

An additional problem is related to secondary fragments (mainly protons and neutrons) bombarding the detector. Fragments could damage the photocathode, reducing its quantum efficiency, even if the voltage is not applied. This issue will require further investigations.

The MCP-PMT model received from Burle is the prototype XP85013 501. The total surface is $59\times59\ \mathrm{cm}^2$, with 80% active area. The microchannels have a diameter of 25 μm. The active face is divided in 8×8 anodes, of 5.9 mm size and 6.5 mm pitch. The maximum sensitivity is at 400 nm, that matches the maximum of the LYSO emission spectrum. The nominal QE is 24% and the average anode uniformity is 50%.

In the proposed device the area of the MCP-PMT is covered by 5 $60\times12\times30\ \mathrm{mm}^3$ LYSO crystals, each one with the $60\times12\ \mathrm{mm}^2$ face optically coupled to the PMT window as shown in Fig. 5.7.

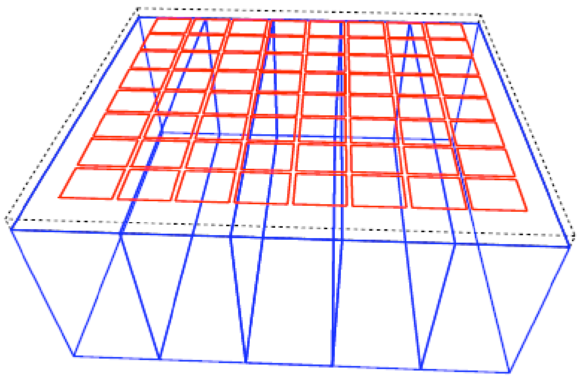

Figure 5.7 *The central crystal of a prototype detector block (made by five 12x30x60 mm^3 crystals) was viewed by 16 central anodes of a MCP-PMT.*

5.6 Optical properties of five LYSO crystals

The crystals used are PreLude^{TM} 420 from St. Gobain [89]. PreLude^{TM} 420 ($Lu_{1.8}Y_{0.2}SiO_5$:Ce) is a Cerium doped scintillating material.

Besides the crystal intrinsic properties, the response of a scintillator depends on the size of the crystal and on the absorption phenomena occurring inside the scintillator, the surface state (polished level) and the wrapper properties. Moreover the photodetector properties like the light transmission of the entrance window, the quantum efficiency (QE) of the photocathode and the photoelectron collection efficiency must be considered.

[89] St. Gobain Web page: http://www.detectors.saint-gobain.com, PreLude^{TM} 420 Product Data Sheet

The light yield and the energy resolution of the LYSO crystals of the sample have been measured with the apparatus of the Crystal Clear Collaboration (CCC – CERN). The experimental system, schematically presented in Fig. 5.8, consists of a XP2020Q photomultiplier, with an applied voltage of 2200 V.

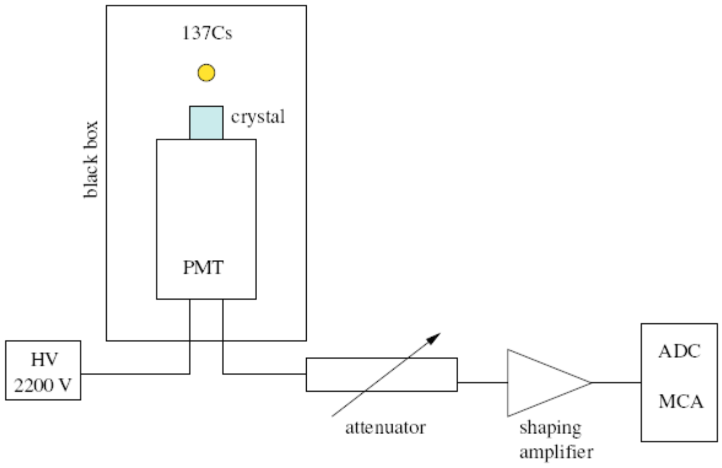

Figure 5.8 *Scheme of the CCC set-up used to measure the crystal horizontal light yield at CERN.*

Each crystal has been measured in the vertical position, with the $30 \times 12\ \mathrm{mm}^2$ face optically coupled by silicon grease to the PMT window. All the other crystal faces were wrapped with Teflon tape. Teflon is a reflective material that improves the light collection. The crystal was tucked into a Teflon cylinder with an appropriate hole and one of the crystal small end faces is coupled by silicon grease to the PMT. All measurements were performed at least three times.

The 5 LYSO crystal sizes provided by the producer are summarized in Tab. 5.3.

Table 5.3 Properties of 5 PreLude^{TM} 420 crystals produced by St. Gobain

Name	Thickness [mm]	Width [mm]	Length [mm]
27 LYS 108-1	12.11	30.12	60.10
27 LYS 108-2	12.12	30.06	60.10
27 LYS 108-3	12.10	30.13	60.09
27 LYS 108-4	12.11	30.10	60.09
27 LYS 108-5	12.15	30.14	60.14

LYSO crystals have an intrinsic radioactivity due to the presence of the Lutetium isotope ^{176}Lu, a naturally occurring β^--emitter. ^{176}Lu beta decays 99.66 % of the times to the 597 keV excited state of ^{176}Hf. This state decays with a 3 gamma rays in cascade which have 88, 202 and 307 keV. The intrinsic background due to this spontaneous emission has been measured from a first acquisition without source. The amount of radioactivity in the crystal has been obtained by integrating the area of the acquired spectrum: the measured radioactivity is 6kBq, in agreement with the manufacturer reference value of 39 Bq/g.

For the light yield measurements a ^{60}Co source has been used instead of the usual ^{137}Cs.. It emits two gammas of 1.173 and 1.333 MeV respectively. The resolution of the apparatus allows to resolve completely the two photoelectric peaks from the radioactivity background of the crystal. An example of an acquired spectrum is given in Fig. 5.9.

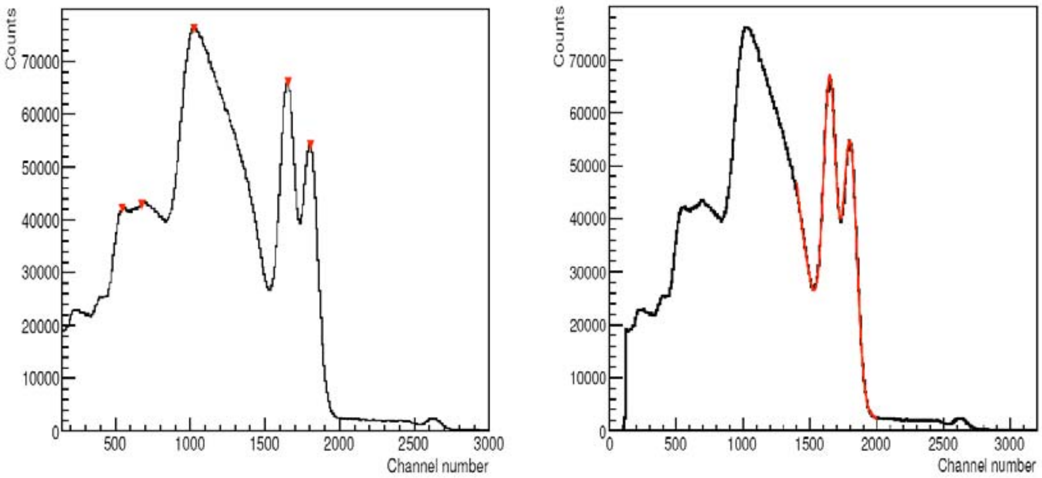

Figure 5.9 *Left panel: energy spectrum of PreLude^{TM} 420 crystal ($60\times12\times30$ mm^3) acquired in vertical position and irradiated with a ^{60}Co source. The red triangles at the left point to the peaks coming from the radioactivity background due to the isotope ^{176}Lu: 700 keV, 400 keV and 300 keV (from right to left). Right panel: the same spectrum as in the left panel, with the fit superposed (red line).*

The red triangles point to the most pronounced peaks in the spectrum. The two peaks on the right are clearly the two photoelectric peaks from ^{60}Co. Moving to the left, the following peak is the 700 keV peak coming from the contemporary detection of the two gammas of 88 and 202 keV from ^{176}Hf de-excitation with the β^- from ^{176}Lu decay. In fact, the emitted β^- has a continuous energy spectrum with a maximum at around 400 keV. The two lower peaks on the left are the 88+202keV and the 88+307 keV peaks, as confirmed by the calibration of the channels.

The calculation of the light yield and of the energy resolution of the three crystals was performed by fitting the acquired energy spectra by means of a double Gaussian fit superposed to an exponential, as shown in the right panel of Fig. 5.8. Each crystal light yield measurement has been repeated three times and the results of each acquisition of each crystal are given in Fig. 5.10.

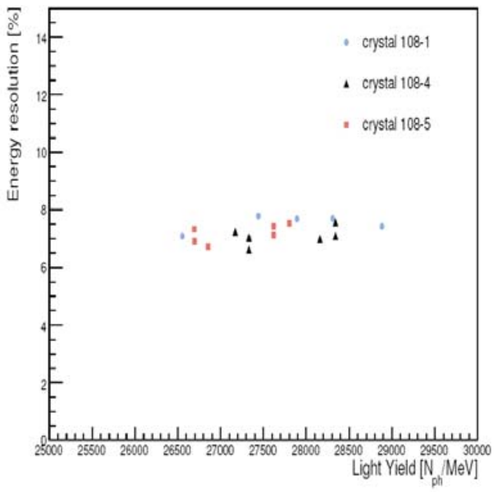

Figure 5.10 *Measured energy resolution as a function of the light yield of three of the LYSO sample. The 6 points of each crystal represent the results of the two ^{60}Co photopeaks calculated in three consecutive measurements.*

The average value of the light yield of the three samples studied is 27,500 ph/MeV with 7% energy resolution.

All measured light yields lie within 5% of the mean value, demonstrating the homogeneity in response of the measured crystals, in spite of their large size.

Another critical optical property that needs to be investigated for large size crystals is the transmission. With the same apparatus the five crystals have been measured in two configurations, with the light traveling in the middle axis along the 6 cm and along the 3 cm directions. The two average transmission curves obtained are given in Fig. 5.11.

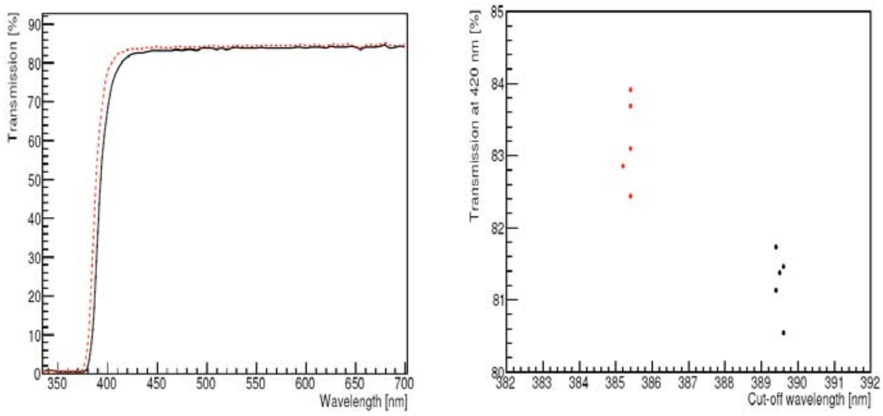

Figure 5.11 *Left panel: average transmission curves for 5 LYSO crystals with light traveling through the 6 cm (black solid line) and 3 cm (red dotted line) long directions. Right panel: transmission of 5 LYSO crystals with light traveling through the 6 cm (black circles) and 3 cm (red circles) long axis measured at 420 nm as a function of the cut-off wavelength.*

The maximum transmission in the high wavelength region is the same in the two cases, since it is due to the optical properties at the interface air-crystal (Fresnel reflection). The cut-off value moves to higher wavelengths passing from the 3 cm long side to the 6 cm one. This red-shift indicates that a higher absorption is experienced by light, but the small change observed confirms the high transparency of LYSO.

Thanks to the small light absorption occurring in LYSO, the crystals exhibit an excellent light yield, not far from the intrinsic nominal value of 32,000 ph/MeV. In fact, light traveling through a large size crystal experiences a number of reflections on crystal faces lower than in small size crystals. Since at each reflection, depending on the incident angle, a photon can escape, the light transfer efficiency for a transparent large size crystal is higher.

5.7 Monte Carlo study of the MCP-PMT/LYSO continuous crystal detector

The performance of the proposed detector block has been first investigated by means of a Monte Carlo optical transport code: LITRANI. In the present Section the working principles of LITRANI are briefly explained, the simulation set-up is described and the reconstruction algorithm of the interaction position is discussed[90].

LITRANI: an optical transport dedicated Monte Carlo

LITRANI is a Monte Carlo program intended to simulate emission, collection and detection of light in optical materials [91] [92]. It is an object-oriented application written in C++ and built upon ROOT.

[90] Solevi P., PhD thesis, Università di Milano Bicocca, 2007.

[91] Gentit F., "Litrani: a general purpose Monte Carlo program simulationg light propagation in isotropic and anisotropic media", Nucl. Instr. and Meth. A 486 (2002) 35-39.

Many physical quantities concerning the optical behaviour of each material used in the simulation set-up can be modelled by the user. Those that depend on a variable parameter (e.g. wavelength) can be described by means of fits or interpolations between experimentally measured values. The simulation is structured as follows:

- definition of the optical materials used in the simulation with associated properties: index of refraction or dielectric constant or tensor, isotropic or anisotropic absorption length, diffusion length, magnetic permeability, fluorescent spectrum and sensitivity (so that the material can be or not be a detector);
- definition of the volumes through which LITRANI has to follow the light propagation;
- definition of the faces of the shapes, i.e. polished level, wrapping material and type (painted or not painted);
- definition of contacts between volumes;
- definition of the detector: general surface and volume detectors, phototubes with associated quantum efficiency as a function of the wavelength;
- definition of the source of light: energy/wavelength and angular distribution of the photons or of the particles (in this last case the dE/dx of the particle in a specific material has to be given as a function of energy).

LITRANI is a fast Monte Carlo and an extremely useful tool to optimize the geometry and the wrapping of the crystal. It is also very helpful in driving the choice of the materials.

Description of the simulation

The "mother volume" (where all volumes are located) was filled with Air, having an isotropic index of refraction equal to 1. The emission spectrum of LYSO was simulated (see Fig. 5.12) according to Ref. [93].

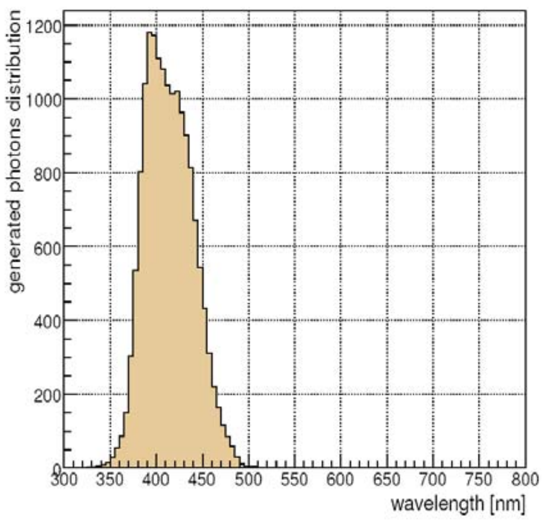

Figure 5.12 *Distribution of emitted optical photons as a function of the wavelength.*

One LYSO crystal was simulated having the size of the sample provided by St. Gobain. The LYSO optical material was modelled as isotropic, with a refraction index of 1.82. The decay time had only the fast component set equal to 40 ns. One Gaussian is centred at 390 nm, with a σ =10 nm and a weight of 20%. The second component, contributing 80%, is given by a gaussian of mean 420 nm and σ =25 nm.

---

[92] LITRANI Web page: http://gentit.home.cern.ch/gentit/litrani/
[93] Kronberger M., private communication.

The absorption length has been calculated as a function of the light wavelength λ from the transmission measurements described in the previous Section. In fact, as reported in [95], the behaviour of electromagnetic waves generated in a crystal depends on the boundaries and on the refractive index (N) of the crystal. For isotropic scintillators, N is a complex number ($N = n + ik$) depending only on λ . The real part n mainly affects the reflectance of light at the air-crystal interface, while the imaginary part k determines the attenuation inside the crystal. The absorption coefficient α is given by:

$$\alpha = \frac{4\pi k}{\lambda}, \tag{5.10}$$

and the absorption length L is the inverse of the absorption coefficient. At normal incidence at the air-crystal interface, supposing $n_{air} = 1$ and $k << n$, the transmittance and the reflectance of a plane wave are:

$$r = \left| \frac{n-1}{n+1} \right|^2 \quad t = 1 - r. \tag{5.11}$$

The overall transmittance T, that takes into account both end crystal interfaces, is given by:

$$T = \frac{t^2 e^{-\alpha d}}{1 + r^2 e^{-2\alpha d}}. \tag{5.12}$$

The α parameter has been fitted to the experimentally measured transmittance along the 6 cm long side, and the absorption length in the crystal was calculated, as shown in Fig. 5.13. When L was larger than 100 cm, its value was set to this maximum value.

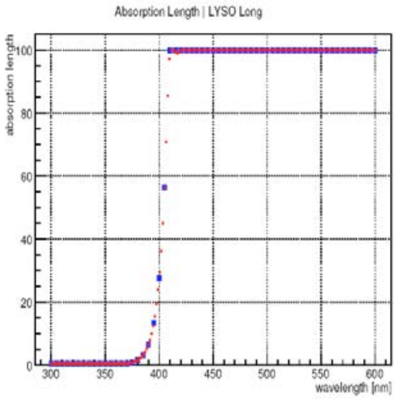

Figure 5.13 *Absorption length (in cm) of LYSO crystal as a function of the wavelength, calculated from experimental data.*

Each crystal was wrapped by Tyvek, whose optical properties are already available in LITRANI, and coupled by a 250 μm layer of meltmount glue to the MCP-PMT window. A thin air slice was left between the wrapper and the crystal in order to maximize thelight collection (not painted surface).

The simulated MCP-PMT window was 60×60 mm^2, 2 mm thick layer and it was made of Sodocal. The pixellated detector was placed on the window face opposite to the one in contact with the crystal, in order to reproduce the Bialkali photocathode deposited on the inner face on the entrance window. Each pixel was 5.9×5.9 mm^2 and it was modelled in the simulation like a surface detector, i.e. once a photon reaches the surface of the detector, it was considered detected with a probability proportional to the quantum efficiency estimated as 25%. In the simulated set-up the crystal was therefore read-out by 16 anode pixels (Fig. 5.14)

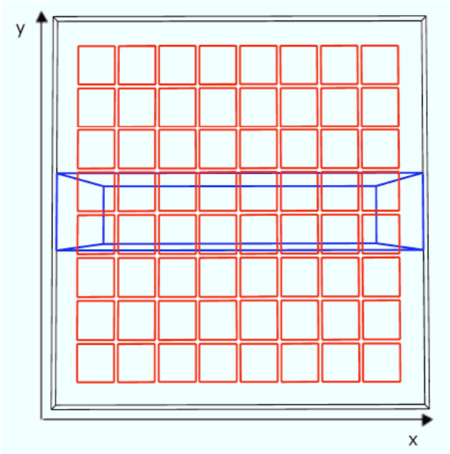

Figure 5.14 *Schematic drawing of the detector system simulated in LITRANI. The blue box is the LYSO crystal located in the centre of the anode matrix (red squares) of the MCP-PMT. The MCP-PMT window is delimited by the black line. The axis X and Y areindicated. The perpendicular Z axis is such that Z=0 is far from the detector surface.*

A number of photons equal to the measured LYSO light yield (when a 511 keV photon produces a photoelectric effect) were isotropically generated inside the crystal, once given the interaction point. The photons seen by the anode were considered detected if they reached the pixel surface within 130 ns (integration time usually adopted in L(Y)SO based PET scanners). The properties of the detected photons (arrival time, wavelength, distance traveled, anode number) were recorded in ROOT format.

5.8 Performances simulated with LITRANI

Several position reconstruction methods are possible in continuous crystal read-out by pixellated detectors and in the following the most important are briefly summarized following the review by S. Tavernier [94].

- **Centre of gravity**: a threshold is applied to the amplitude of the signal in each pixel, and pixels below this threshold are not included in the calculation. The position of interaction of the gamma is assumed to be the centre of gravity of the signal amplitudes.
- **Least squares**: the response of the interaction at an unknown position is compared to a set of reference events of known position. For each beam position the signal amplitude of each pixel is calculated. To determine the X position, the signal of all pixels in Y direction is integrated and the opposite for the Y determination. For each event of unknown position, the difference in amplitude for each pixel with respect to reference data sets is calculated. The position of the reference data that minimizes the difference is assumed as the best estimate of the position of interaction.
- **Chi-square**: the method is very similar to the least squares one. For each beam position, the signal amplitude of each pixel with an associated r.m.s. error is calculated. Also in this technique the amplitude in X and Y are integrated. The difference between the measured amplitude of the unknown position and the reference data sets of each pixel are calculated, weighted with the error of the reference data. Also in this case the interaction position is assumed to be the one that minimizes the χ^2 value.

[94] Tavernier S. et al., "A high-resolution PET detector based on continuous scintillators", Nucl. Instr. and Meth. A 537 (2005) 321-325.

The Depth Of Interaction (DOI) of the gamma in the crystal is related to the spread of signal among pixels [96]. In fact, if the gamma interacts close to the detector surface, the light would be shared among pixels very close to the (X,Y) interaction position. Instead, if the gamma interacts far from the detector surface the number of involved pixels is larger.

Determination of the X coordinate of photoelectric events

In the previously described set-up, within the LYSO crystal, 2,000 events have been generated with a scintillation point (X_0, Y_0, Z_0) randomly chosen. With this data set the spatial resolution in the two main directions X and Z, respectively parallel to 6 cm long side and the 3 cm depth, has been first investigated.

Concerning the X direction, the signal on each pixel has been integrated in the Y direction, for each scintillation position, summing the number of photoelectrons in the two Y-contiguous pads. The centre of gravity X_{CG} of the obtained distributionwas is

$$X_{CG} = \frac{\sum N_{pe,i} x_i}{\sum N_{pe,i}}. \tag{5.13}$$

It was expected that the reconstruction procedure applied would depend on the depth of interaction Z_0 ranging between 0 cm (far) and 3 cm (close to the detector window). Therefore, to perform the X-study, the simulated events were divided into three samples, according to the depth of interaction: Z_0 smaller than 1 cm (first layer), within 1 cm and 2 cm (second layer) and between 2 cm and 3 cm (third layer) respectively.

According to [96], the reflection on the edges of the crystal influences the final achievable spatial resolution. In order to investigate more deeply these border effects, a second simulation was performed with the set-up identical to the previous one but with the two 12×30 mm^2 end faces of the crystal painted in black so that each optical photon hitting one of these two faces undergoes a total absorption. This was expected to at least reduce the distortions of the X reconstruction due to the reflection on the borders, but with the drawback of a loss of the photon collection efficiency (see Fig. 5.15). The total number of events simulated was again 2,000 and they have been divided into three samples as performed for the previous data set.

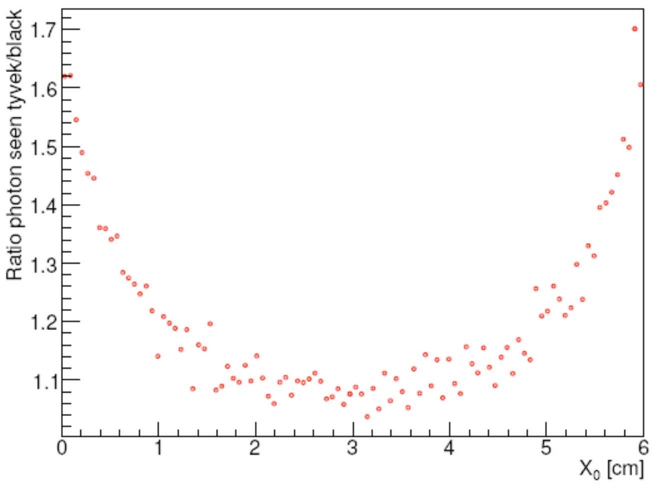

Figure 5.15 *Ratio of the average number of optical photons seen by each anode in the two simulation set-ups (Tyvek wrapping on all faces and Tyvek wrapping of 4 faces plus two end faces black painted) as a function of* X_0. *At the borders the overall light collection reduces by about 60%.*

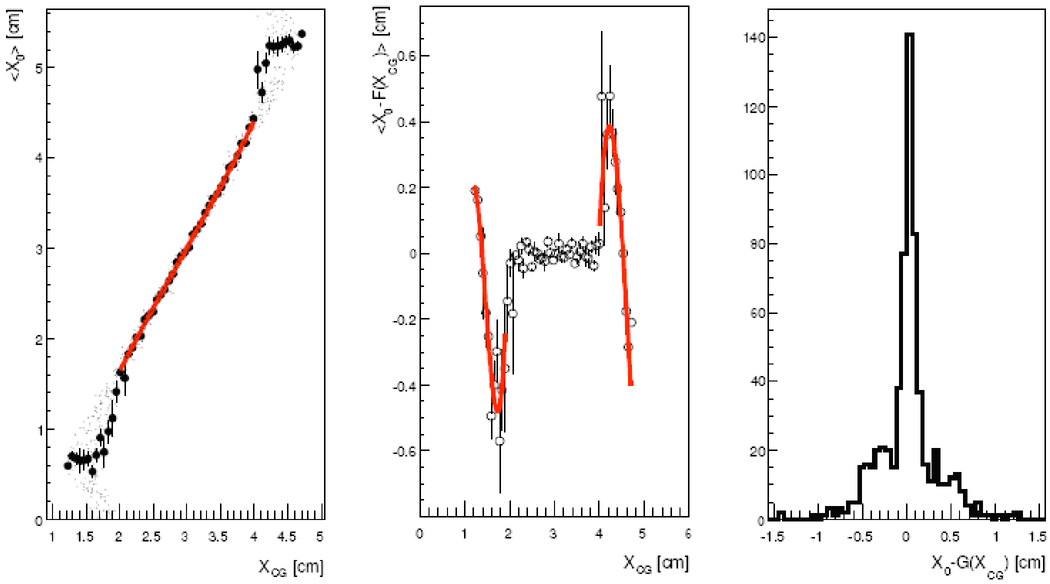

Figure 5.16 *The three panels show the sequence of the reconstruction procedure applied to events generated in the third layer (i.e. between 2 cm and 3 cm, close to the detector surface) of a black painted crystal. Left panel: the distribution of the coordinate* X_0 *of the real position of the interaction as a function of a set of reconstructed position* X_{CG} *is calculated and the shown average of their distributions is fitted by means of a polynomial function* F *(red line). Middle panel: the average of the distribution of the differences between* X_0 *and the expected real position* $F(X_{CG})$ *for each set of values* X_{CG} *is computed and fitted by means of a correcting function* Δ *(red line). Right panel: the overall Monte Carlo spatial resolution is obtained with a Gaussian fit of the distribution of the differences between* X_0 *and the corrected expected position* $G(X_{CG})$*.*

To each sample, the following procedure has been applied:

- the X_{CG} range was divided into bins, the distributions of X_0 for each value of X_{CG} were averaged to obtain a set of data points $< X_0 >$ and the pairs ($X_{CG}, < X_0 >$) were fitted in a restricted range by means of a polynomial function F (Fig. 5.16, left panel);
- the distribution of $< X_0 - F(X_{CG}) >$ as a function of X_{CG} was fitted by a polynomial function Δ mainly to correct the deviations of the reconstructed X from the real position of interaction dominating at the edges of the crystal (Fig. 5.16, middle panel);
- the spatial resolution was computed from the r.m.s of the distribution of the differences between X_0 and $G(X_{CG})$, where G is equal to $F + \Delta$ (Fig. 5.16, right panel).

The reconstructed position of interaction X_{CG} is well correlated to the true one in the central region of the crystal. When X_0 is closer to the edges, the estimated centre of gravity is distorted. In fact, since the anode pad finishes, the signal collected on one side of the maximum is not balanced on the opposite side and moreover, in case of Tyvek wrapped crystal, the reflection of the signal at the crystal borders increases the signal in far pixels. For this reason the procedure of Fig. 5.16 was repeated for each layer of interaction.

The described reconstruction technique was applied to reconstruct events simulated in both set-ups and the results are illustrated in Figs. 5.17 and 5.18.

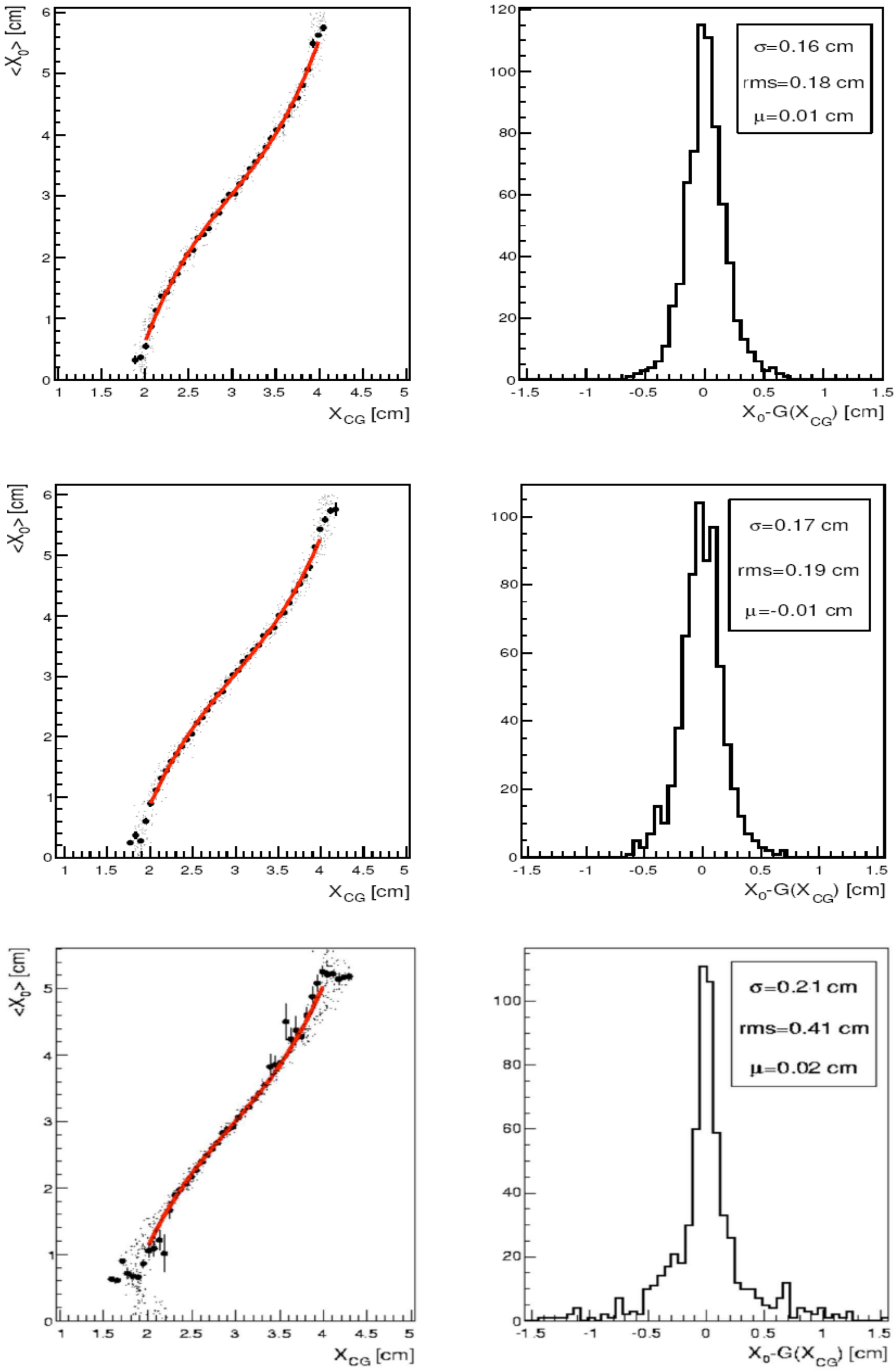

Figure 5.17 *Left panels: the profile of the average* $< X_0 >$ *of the true coordinate of the position of the interaction as a function of the reconstructed* X_{CG} *is fitted by a polynomial function (red line). Right panel: the distribution of the deviations of all the* X_0 *from the reconstructed position* $G(X_{CG})$ *is shown. The analyzed events, simulated with a Tyvek wrapped crystal, are divided into three samples according to their DOI: 0-1 cm (i.e. far from the detector, top panels), 1-2 cm (middle panels) and 2-3 cm (i.e. close to the detector, bottom panels).*

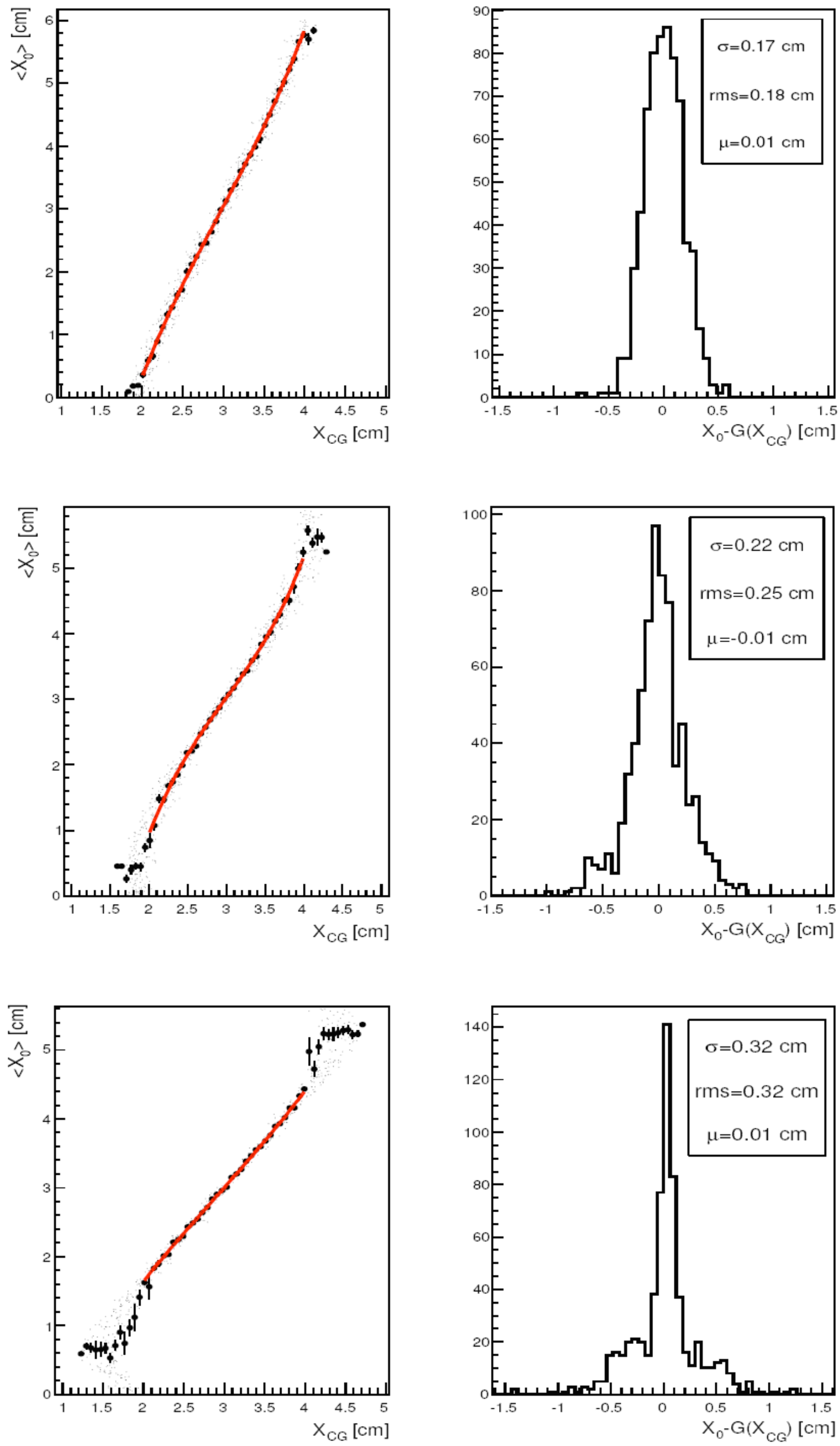

Figure 5.18 *Left panels: the profile of the average $< X_0 >$ of the true coordinate of the position of the interaction as a function of the reconstructed X_{CG} is fitted by a polynomial function (red line). Right panel: the distribution of the deviations of all the X_0 from the reconstructed position $G(X_{CG})$ is shown. The analyzed events, simulated with a Tyvek wrapped crystal with two end faces black painted, are divided into three samples according to their DOI: 0-1 cm (i.e. far from the detector, top panels), 1-2 cm (middle panels) and 2-3 cm (i.e. close to the detector, bottom panels).*

It can be noted that the evolution of the distributions of the deviations between the real and the reconstructed X is coherent in the two simulations. By increasing the depth of interaction (i.e. coming closer to the detector pad) the well defined Gaussian distribution splits into two components (Figs. 5.17 and 5.18 bottom panels): a narrow Gaussian distribution, to which events in the central region of the crystal contribute, and a spread distribution due to events close to the edges.

To estimate the evolution of the distribution with the depth of interaction three parameters have been considered: the r.m.s, the FWHM and the FWTM of the full distribution. The first is an indicator of the the quality of the full distribution and therefore is an estimate of the spatial resolution. The FWHM estimates the properly reconstructed events in the central region of the crystal and the FWTM takes into account the worsening of the spatial distribution due to the tail. The results are shown in Table 15 where the efficiency, named ε, is the ratio between the number of events whose deviation is smaller than 5 mm and the total number of events in eachsample. For each sample of events and for both simulations the parameters are summarized in Table 5.4.

Table 5.4 Calculated values of r.m.s, FWHM, FWTM and ε for the totally reflective crystal (refl.) and for the one with two black painted faces (black).

Z_0 **[cm]**	**r.m.s [mm]**		***FWHM* [mm]**		***FWHM* [mm]**		ε **($\lvert X_0 - X_{CG} \rvert < 5$ mm) [%]**	
	refl.	black	refl.	black	refl.	black	refl.	black
0-1 cm	1.8	1.8	2.5	4.0	10.0	8.0	96	99
1-2 cm	1.9	2.5	3.0	3.0	9.0	9.0	93	98
2-3 cm	4.1	3.2	3.0	1.8	14.0	10.2	93	93

Firstly, it has to be remarked that all the obtained resolutions in the coordinate X fulfill the requirement of an in-beam-PET. Secondly, it is interesting to note that with increasing depths of interaction (i.e. getting close to the detector), the r.m.s becomes worst because of the non-Gaussian form of the distribution. Thirdly the black painted crystal exhibits the best performance in the last layer i.e. close to the detector surface. This improvement can be explained by looking at Fig.5.15. When the interaction occurs close to the detector surface, the absence of uncorrelated optical photons coming from reflections on the edges of the crystal increases the linearity in the central region.

It has also to be noted that when a gamma interacts within a crystal, the probability of interaction follows an exponential with the decay constant given by the attenuation length of the scintillating material (e.g. 1.1 cm for LYSO). Therefore the number of photons interacting in the first centimeter is larger than in the rest of the crystal. This underlines the importance to achieve a fair spatial resolution in particular in the first layer, condition that the studied device (at least from the simulation point of view) satisfies. In fact, looking at the efficiencies reported in Table 15, almost all events are reconstructed with a deviation smaller than 5 mm in the first two depth layers and only a small loss is present in the last one. From this point of view, the black painted crystal seems to be preferable, also because the distributions of Fig. 5.18 are more Gaussian (for $Z_0 \leq 2$ cm) than the ones of Fig. 5.17.

Determination of the depth of interaction of photoelectric events

To determine the depth of interaction, appropriate indicators and their correlation with Z_0 have been studied in detail.

The first estimator is the σ (named σ_{fit}) obtained from a Gaussian fit of the distribution of the signal $N_{pe,i}$ on the anode array. In fact it is expected that the closer is Z_0 to the detector surface the more peaked is the signal distribution. Hence the σ_{fit} value is expected to decrease with increasing depth of interaction. ALSO in this case the border effects are a source of error in the reconstruction. In fact the signal distribution of events whose X_0 is close to the crystal edges is flattened by photon reflections, resulting in an unreliable correlation of σ_{fit} with Z_0.

By exploiting the good linear correlation existing between X_0 and the reconstructed X_{CG}, cuts were applied to study separately the reconstruction of Z in the central and in the lateral region of the crystal. The events were divided into two samples: one with $2.2 < X_{CG} < 3.8$ cm and the other with $X_{CG} \leq 2.2$ and $X_{CG} \geq 3.8$ cm.

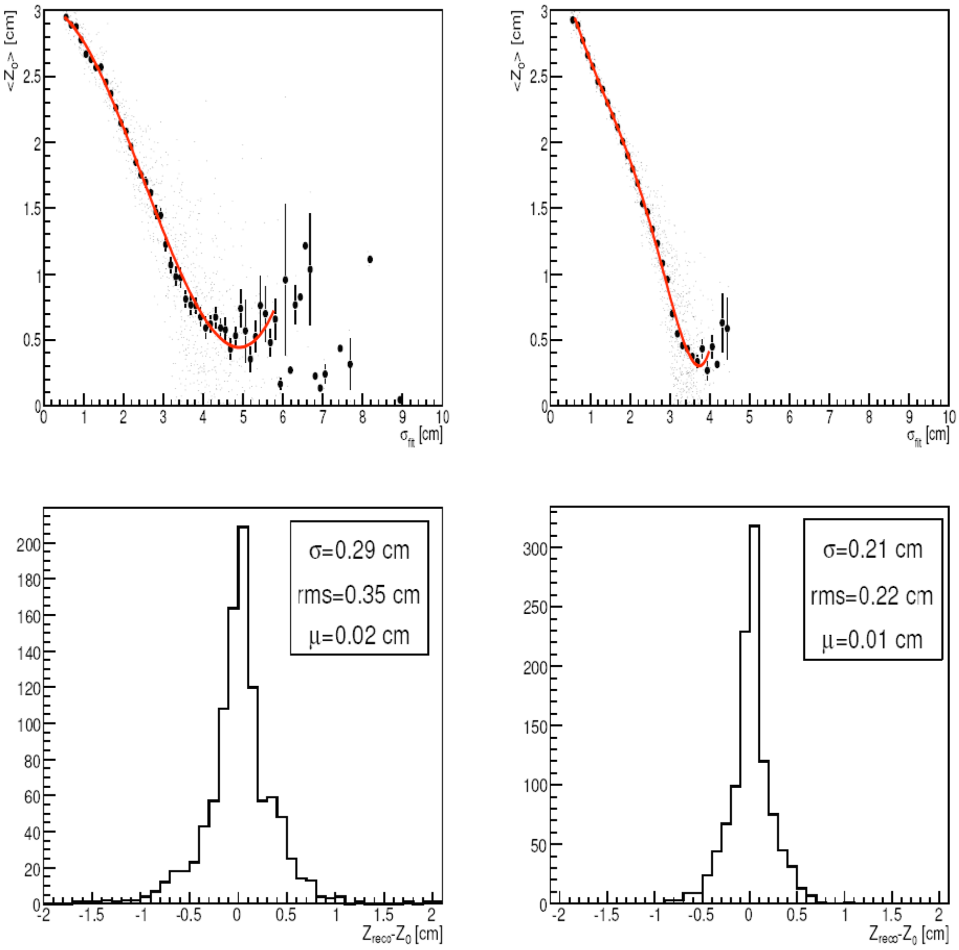

Figure 5.19 *Events in the lateral region of the crystal: $2.2 < X_{CG} < 3.8$ cm. Top panels: average $< Z_0 >$ as a function of σ_{fit} with the fitted curve superimposed (red line). Bottom panels: distribution of the deviations between Z_0 and Z_{reco}, which is the position reconstructed by means of the fit function illustrated in the top panels. The left panels refer to Tyvek wrapped crystal while the right panels give the results for the crystal with two black painted end faces.*

For the first sample (i.e. central events), the range of σ_{fit} was divided in bins and in each bin the average value $< Z_0 >$ of the true origin of the events was computed. Fig. 5.19 shows the distribution of of $< Z_0 >$ as a function of σ_{fit}, for both simulations. The functions obtained by fitting the previous distributions were used to compute the expected reconstructed depth of interaction Z_{reco} and the differences between the real and the reconstructed Z. The results are given in the lower panels of Fig. 5.19. The r.m.s of the last distributions was estimated. The results are summarized in Table 5.5.

Table 5.5 *Calculated values of r.m.s for the totally reflective crystal (refl.) and for the one with two black painted faces (black). The efficiency ε is the ratio between the number of events whose deviation is smaller than 1 cm and the total number of events of the sample.*

X_{CG} **[cm]**	**r.m.s [mm]**		ε **($\lvert Z_0 - Z_{reco} \rvert$< 10 mm) [%]**	
	refl.	black	refl.	black
2.2-3.8	3.5	2.2	87	99

The spatial resolution achieved in the central region of the crystal is, in both cases, excellent. In particular, the r.m.s value of the black painted crystal is 40% smaller than the one of the reflective crystal, that has also a smaller efficiency.

When selecting events close to crystal edges, the correlation between σ_{fit} and $< Z_0 >$ is partially lost. To overcome this problem, a second indicator has been introduced.

Since the quality and the stability of the fit results depend on the bin to bin fluctuations, the second estimator is related to the flatness of the signal distribution on the anode array which was named "smoothness". In fact, when the interaction takes place close to the anode pad, the variations of the signal from pixel to pixel are expected to be higher than when the interaction occurs far from the detector surface. At the same time the Gaussian fit hardly describes the photon counting pattern for events whose Z_0 is small (i.e. far from the detector surface).

The smoothness is defined as:

$$S = \frac{\sum(\bar{N}_{pe} - N_{pe,i})^2}{\bar{N}_{pe}^{\,2}}, \tag{5.14}$$

where $\bar{N}_{pe}$ is the average signal amplitude on the anode array and $N_{pe,i}$ is the amplitude of the signal on the i-th anode, with i ranging between 1 and 8.

Fig. 5.20 shows the distributions of $< Z_0 >$ as a function of σ_{fit}. A fair correlation is maintained between the two variables for relatively small values of σ_{fit} and the distribution, after reaching a minimum at σ_{cut} (equal to 3 cm and 3.5 cm for reflective and black painted crystals respectively), increases with relatively wide fluctuations. The smoothness was computed for two intervals of σ_{fit}: smaller than σ_{cut} and larger than σ_{cut}. The two average distributions of Z_0 versus the smoothness were fitted and the obtained functions were alternatively used to reconstruct the Z depth according to the calculated value of σ_{fit}.

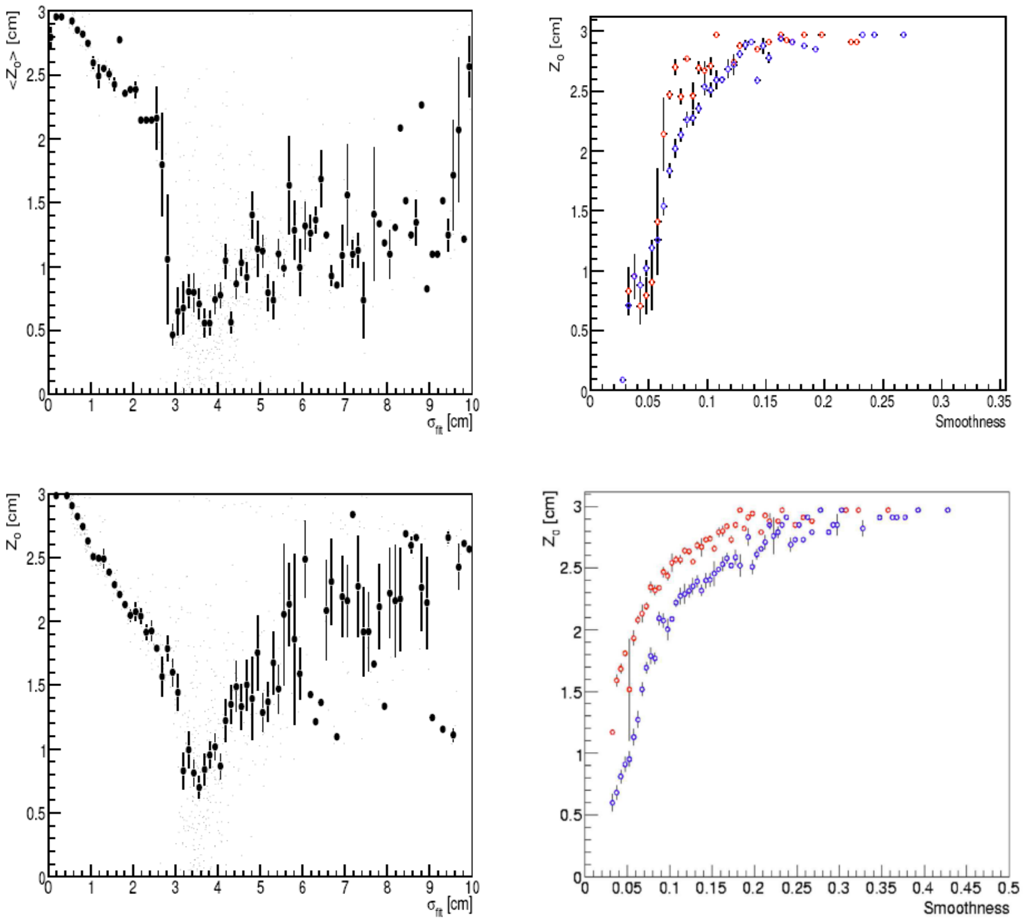

Figure 5.20 *The figure refers to events which are in the lateral region of the crystal:* $X_{CG} \le 2.2$ *cm and* $X_{CG} \ge 3.8$ *cm. Left panels: distribution of* $< Z_0 >$ *as a function of* σ_{fit}*. Right panel: average distribution of the* Z_0 *as a function of the smoothness for* $\sigma_{FIT} < \sigma_{cut}$ *(red points) and for* $\sigma_{fit} > \sigma_{cut}$ *(blue points) with* $\sigma_{cut} = 3.0$ *cm and 3.5 cm respectively. Top panels refer to Tyvek wrapped crystal while bottom panels give the results for the crystal with two end faces black painted.*

The distribution of the deviations between the reconstructed and the real depth of interaction are illustrated in Fig. 5.21.

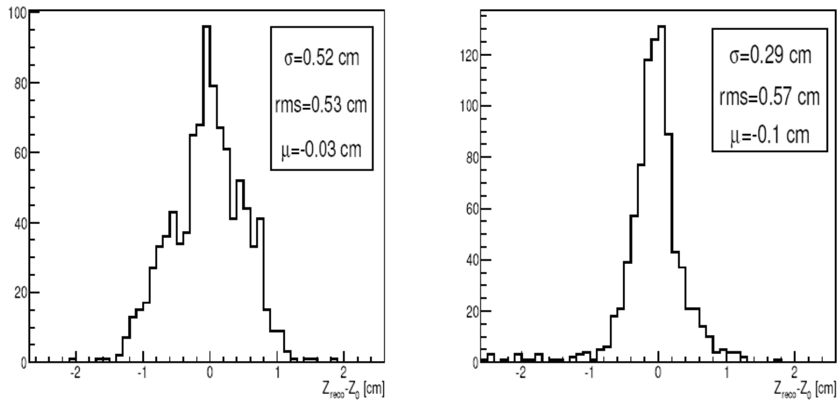

Figure 5.21 *Distribution of the deviations between the real and the reconstructed Z coordinate for reflective crystal (left panel) and black painted crystal (right panel).*

The estimated spatial resolutions summarized in Table 5.6

Table 5.6 *Calculated values of r.m.s for the totally reflective crystal (refl.) and for the one with two black painted faces (black). The efficiency* ε *is the ratio between the number of events whose deviation is smaller than 1 cm and the total number of events of the sample.*

X_{CG} **[cm]**	**r.m.s [mm]**		ε **(** $\lvert Z_0 - Z_{reco} \rvert$ **< 10 mm) [%]**	
	refl.	black	refl.	black
0-2.2 and 3.8-6.0	5.3	5.7	83	93

The figures and the table show that the black painted crystal is superior in the measurement of DOI both in the central and in the lateral regions. Moreover the two distributions are nearly Gaussian in shape and their sigma values are not very different: 2.1 and 2.9 mm respectively. By combining with the results obtained for the X coordinate, the black painted crystal has to be preferred.

Summary of the Monte Carlo results on the spatial resolution

The spatial resolution, both in X and Z, obtained by applying the reconstruction techniques described in the previous Section are within the limitations required for an in-beam-PET. Both reflective and black painted crystals exhibit good performances but the black painted crystal has to be preferred. On the whole crystal the average spatial resolution in the X direction can be computed by combining the results summarized in Fig. 85 and taking into account that, due to the 1.1 cm interaction length of 511 keV gammas in LYSO, the three layers see 67%, 22% and 11% of the events. The overall distribution is shown in Fig. 5.22 and the overall resolution is 2.0 mm.

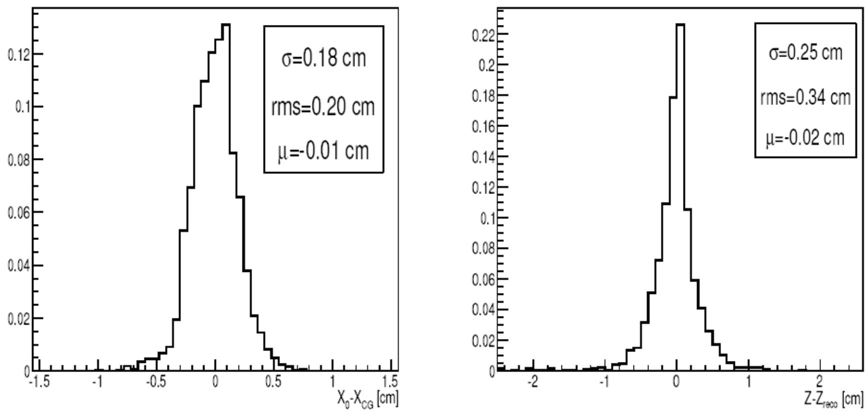

Figure 5.22 *Left panel: distribution of the deviations between the true and the reconstructed* X *coordinate for black painted crystal on the whole volume. The distribution is obtained by weighting the distribution calculated for each layer by a factor proportional to the number of 511 keV gammas interacting at each depth. Right panel: distribution of the deviations between the true and the reconstructed* Z *coordinate on the whole volume for the black painted crystal.*

Concerning the Z reconstruction, an excellent resolution is obtained in the central region of the crystal, where the correlation between the signal distribution on the anode pad and the interaction point is very pronounced. In this region, the spatial resolution is 2.2 mm, practically equal to the X-resolution. Such a resolution is competitive with respect to the one achieved by means of device optimized for DOI reconstruction. A degradation of the spatial resolution is obtained when selecting events close to the crystal edges. In this region the spatial resolution is 5.7 mm for the black painted crystal. The right panel of Fig. 5.22 shows the distribution of the deviations between the true and the reconstructed Z coordinates, averaged over the whole volume. The obtained overall spatial resolution is 3.4 mm. It has to be noted that the worsening of the resolution close to the crystal edges is partially due to the smaller active area of the detector with respect to the crystal length. Actually Burle is working on a new MCP-PMT prototype having a higher active area that is expected to improve the performance of the detector unit studied.

The techniques applied to reconstruct the X and Z coordinates are very sensitive to the bin to bin fluctuations in the signal distribution on the pixel matrix, therefore it would be required a very accurate calibration of the anode response in the experimental part.

It has to be underlined that one of the drawbacks of the studied device is foreseen to be the poor Compton events resolution, as observed in Anger logic based device, but this issue needs still to be investigated. In all circumstances Monte Carlo results are always more favorable than experimental ones, but even if there would be in practice a loss in resolution by a factor 2, the requirements of in-beam-PET would be satisfied.

5.9 Experimental results

Anode calibration

The gamma interaction point in a continuous crystal read-out configuration is obtained by means of a reconstruction technique based on the interpolation and fit of the signal distribution on the anode pad, as described in the previous Section. Even if the homogeneity of the MCP-PMT from Burle is higher than the one of other photodetectors, the average level of uniformity on the anode pad is quoted by the producer to be about 1:1.5, with a maximum value of about 1:2.5. Such a difference would significantly affect the achievable accuracy in the reconstruction of the interaction point within the crystal. Therefore at first a calibration of the anode signal is recommended.

The monochromatic light used was a 3 mm diameter UV LED (LED3-UV-400-30) which emits 400 nm photons (close to the maximum of the emission spectrum of LYSO). To focus the light on the PMT window plane the LED was tucked into a plastic cylinder with an appropriate hole and the holder was located in the eyepiece of a microscope (see Fig. 5.23). The LED was powered with a 30 ns square pulse at 1 kHz.

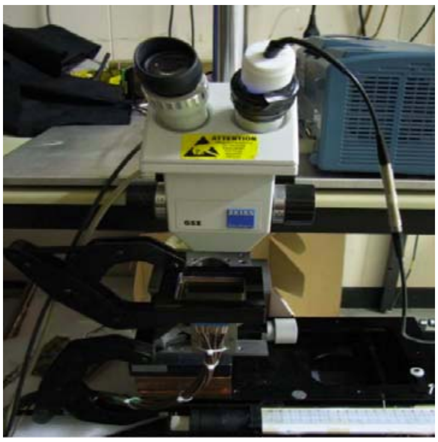

Figure 5.23 *Picture of the experimental set-up for the anode calibration of the MCP-PMT anodes. In one of the eyepieces of the microscope a LED tucked into a plastic cylinder is located and the 400 nm light emitted is focused on the PMT window plane.*

The LED light was partially collimated by means of the plastic cylinder and focused on the PMT window. The size of the spot was about 2 mm diameter.

The microscope was equipped with a mechanical support on which the MCP-PMT was fixed. The PMT window could be moved in the microscope focusing plane and its position could be arranged in both transversal directions (X and Y) with a precision of 0.3 mm.

The equipment was located in dark environment in order to suppress any backgrounds.

The electronic read-out chain used is schematically represented in Fig. 5.24.

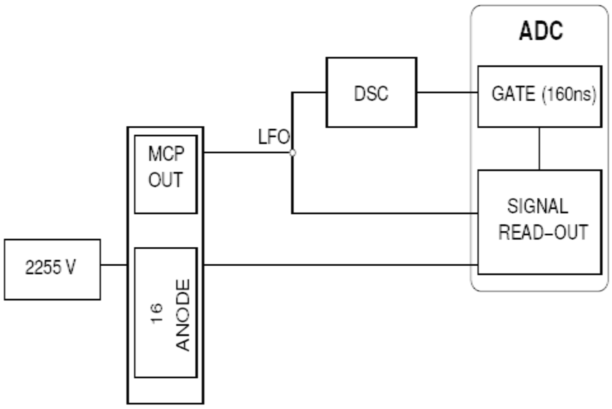

Figure 5.24 *Schematic drawing of the electronic read-out chain used in the anode calibration measurement.*

The MCP-PMT has one output giving the integrated signal over all anodes and a single read-out for each anode. The MCP-PMT output was sent by a linear Fan Out (LeCroy 428F) to the discriminator (LeCroy 821CL). A threshold is applied on the discriminator and the width of the output NIM pulse set to 160 ns and fed to ADC (LeCroy 2249A) to trigger the acquisition to the MCP-PMT output. The electronics was interfaced to the PC by a CAMAC Wiener CC-USB. For each acquisition, 5000 events were recorded. For every anode and acquisition, the pedestal was estimated and subtracted from the acquired signal.

The location of the read-out anodes with respect to the PMT window is represented in Fig. 5.25.

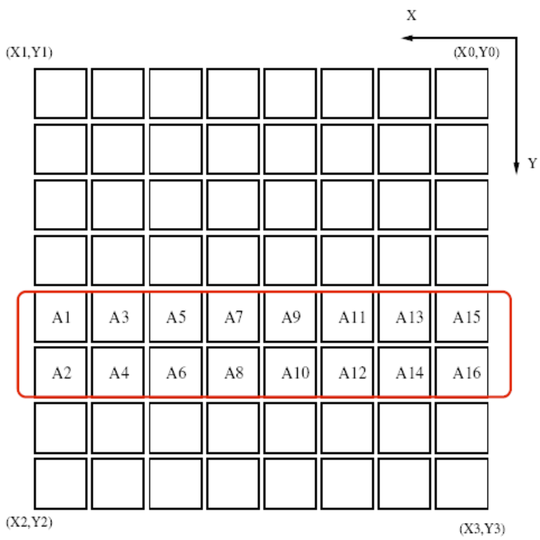

Figure 5.25 *Schematic drawing of the 8×8 anode matrix of the MCP-PMT from Burle. In the red square the 16 read-out anodes are grouped.*

Only the 16 anodes of interest were calibrated.

With the calibration setup we have measured the overall relative sensitivity of the MCP, shown in Fig. 5.26. The red squares provide the maximum signal on each of 8 aligned anode pads, while the black squares are the amplitude measured on the MCP output. One can see that the maximum variation of the anode pad response is about 7%; this is not far from the tolerance required for the position reconstruction, and can be corrected with a proper calibration. Near the edge of the tube the amplitude drops, due to the geometry of the tube and the finite size of the light spot used for the measurement.

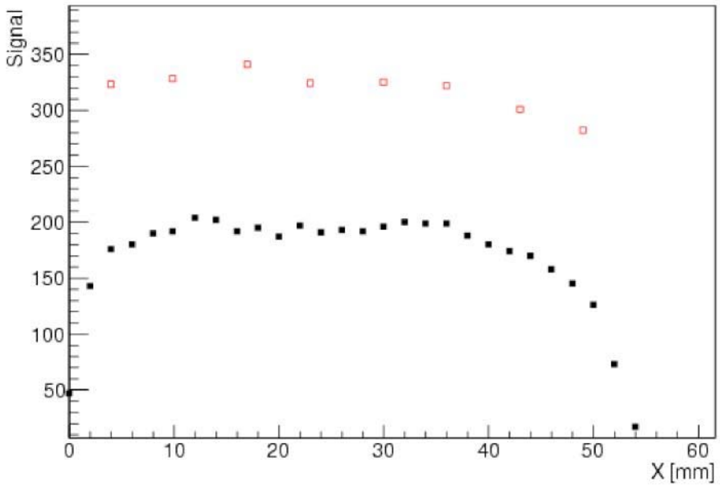

Figure 5.26 *Relative signal amplitude measured with a collimated UV light beam. Red squares correspond to the amplitude measured in the centre of eight adjacent anode pads; black squares correspond to the measured amplitude on the MCP output..*

Even when the light spot was focused on the centre of an anode, a non negligible signal (about 10 % of the reference anode) was measured in the neighbouring anodes. This signal can arise from the non perfect collimation of the light spot as well as from optical photon reflections within the PMT window and between the photocathode and the MCP surface. The last contribution is a function of the angle of incidence of light on the PMT window.

LYSO crystal measurement

The Multi-Anode tube, shown in Fig. 5.27, was calibrated and then used in the measurements described in this Subsection.

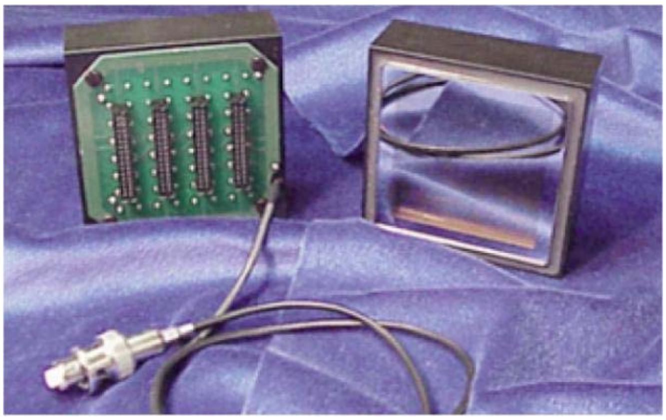

Figure 5.27*The Multi-Anode Photomultiplier used for the measurements.*

For the study of position and DOI localization according to the method discussed in the previous section we have used the laboratory setup shown in Fig. 5.28.

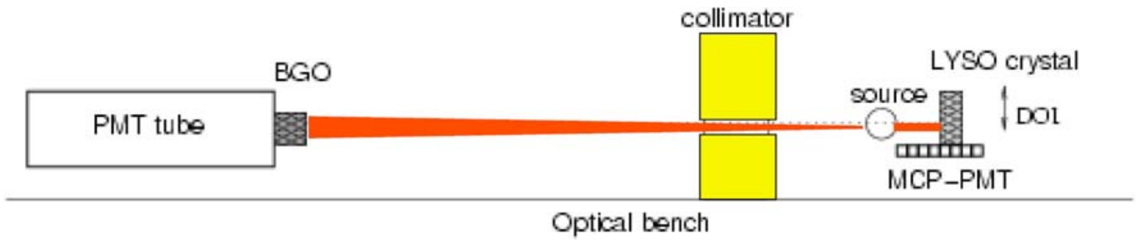

Figure 5.28 *Experimental setup for studying localization properties.*

The main detector consists of a LYSO crystal, 60x12x30 mm^3, mounted with the long side perpendicular and in optical contact with the Multi-Anode Photomultiplier. The crystal was Teflon wrapped and coupled through the $12 \times 60\ mm^2$ face (by means of Silicon grease) to the MCP-PMT window in front of the 16 central read-outs. The crystal and the MCP-PMT were placed on a metal support in order to maintain the crystal position fixed during all measurements and to avoid any misalignment of the crystal with respect to the 16 anodes.

A smaller crystal, mounted on a standard Photomultiplier tube (PMT) allows to select events corresponding to a 511 photon conversion. A lead collimator 5 cm thick with a 5 mm diameter hole was located on the optical bench, with the ^{22}Na source placed between the MCP and the lead collimator. The distances between the collimator and the PMT and between the collimator and the source were adjusted in order to obtain a ~2 mm diameter spot focused on the LYSO crystal. The optical bench was adjusted in order to centre the gamma spot at different distances with respect to the anode surface (i.e. at different Z).

The electronic chain used to perform all the measurements hereafter described is provided in Fig. 5.29

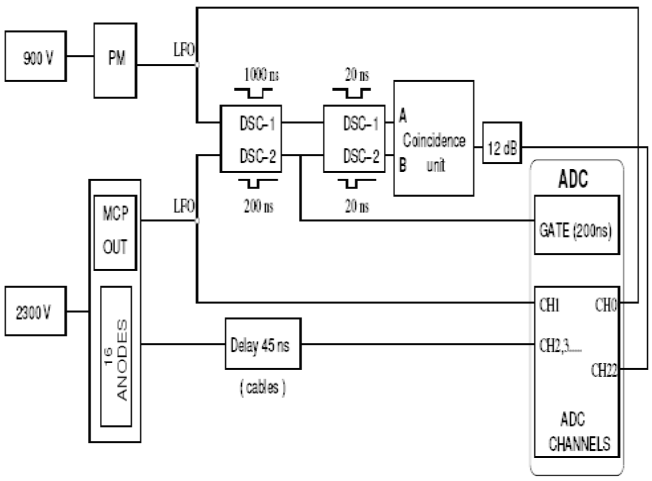

Figure 5.29 *Schematic drawing of the electronic read-out used to perform experimental measurements.*

The 12 mm thick crystal was positioned cantered between two anode pads rows, so that the light flash generated by a gamma conversion was recorded on two rows of anodes. The 16 pads were connected via miniature cables to CAMAC-based multi-ADC modules[95]; two more channels were used to record the signals from the MCP and from the coincidence PMT. Because of the rather long delay of the PMT, its signal could not be used directly for the selection of coincidence two-gammas events; instead, we have used the MCP output to

95 LECROY Type 2249A 12-channels ADC

initiate the readout, and selected the events having a signal in the PMT within the energy window corresponding to the 511 keV photopeak.

A LABVIEW-based system and a desktop PC were used for data acquisition and analysis.

Fig. 5.30 shows the pulse height spectra recorded on the MCP, for events in coincidence with the PMT; the lower peak (green histogram) recorded on common MCP output, while the higher distribution corresponds to the sum of pulse heights over 16 anodes, after correction taking into account the response calibration. The energy resolution for the 511 keV photopeak is 18.7%, adequate for position determination.

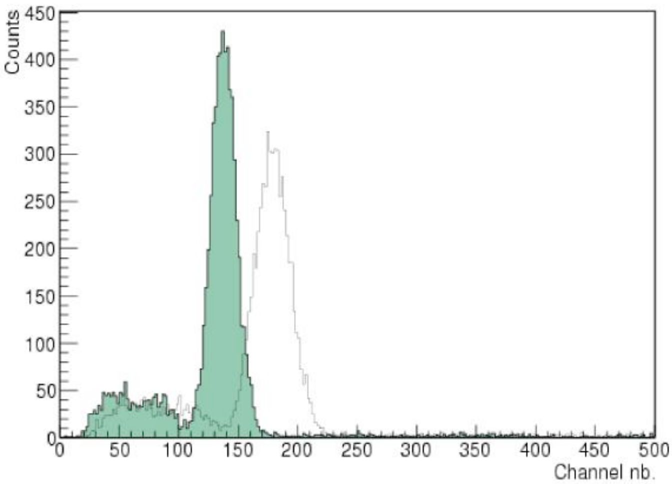

Fig. 5.30 *Coincidence pulse height spectra on the MCP output (green) and sum of 16 anodes.*

Measurements were performed for two values of DOI at 5 mm from the centre of the crystal: Z=27 mm (close to the detector surface) and Z=2 mm (far from the detector surface); the distributions of the signal amplitudes recorded for the two cases on the 16 anodes and integrated in the Y dimension are shown in Fig. 5.31

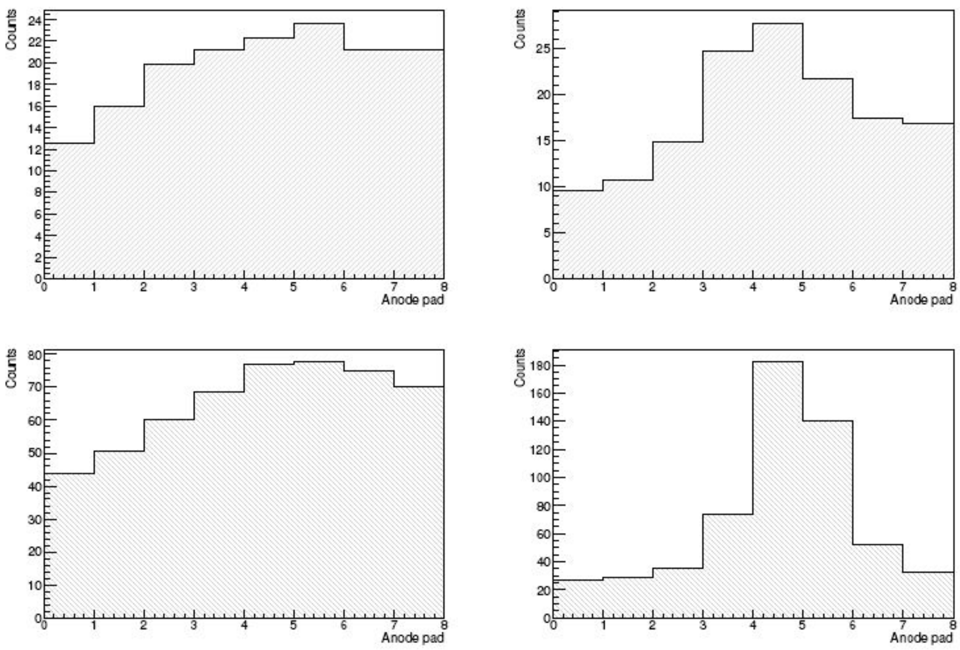

Figure 5.31 *Distribution of the signal on the anode pads far (left) and close (right) to the detector surface. Top; measured distributions; bottom: simulated distributions in the same conditions.*

The measured distributions (Fig 5.31, top) are compared to the average distributions computed by means of LITRANI with the (X, Z) coordinates of scintillation points set as the experimental values (Fig. 5.31, bottom). When the DOI is far from the detector surface the two distributions agree well, while in the second measurement the signal has a diffused background.

Three processes that were not considered in the simulation and require further investigations can explain the difference:

- Multiple energy depositions, causing a spread of the signal distribution on the anode pad; this effect is expected to worsen the spatial resolution both in X and Z directions.
- Optical cross talk between anodes can further broaden the signal distribution.
- Difficulties encountered to properly model the optical materials in the simulation, in particular the wrapping, can be an additional source of disagreement.

The localization accuracy for the different position of exposure has been estimated using a simple center-of gravity calculation algorithm.

Fig. 5.32 provides the distribution of the reconstructed coordinate for a position near the center of the crystal, both in the direction of its long face (X=40 mm) and in the DOI direction (Z=19 mm). The distribution has a quasi-Gaussian shape, with 2.4 mm rms; the small tail is probably due to the contribution of double-Compton events.

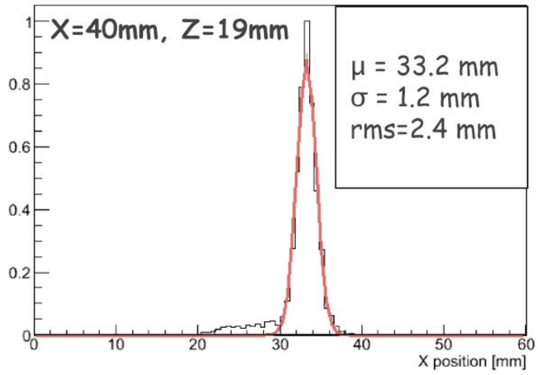

Figure 5.32 *Distribution of the centre of gravity of the recorded signal profiles on anode rows for an exposed region 40 mm from one edge of the crystal and 19 mm from the sensor.*

Fig. 5.33 summarizes the measurements correlating the real coordinate of the collimated spot and the one deduced by the centre-of gravity calculation.

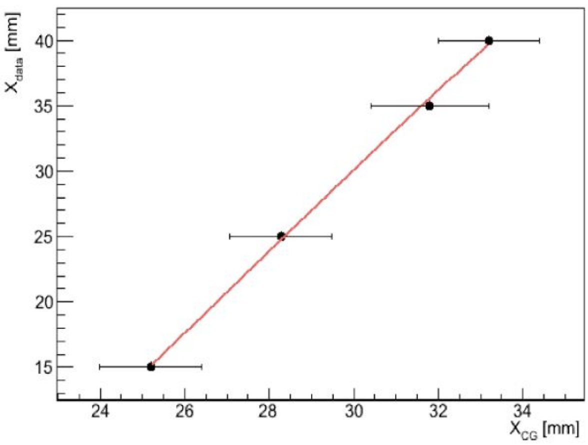

Figure 5.33 *Correlation between computed centre of gravity and real coordinate of the exposed spot.*

In the figure the error bars correspond to the standard deviation of the respective distributions. One can see that, although the correlation is almost linear, the scale of the reconstructed coordinates is compressed by the edge effects discussed previously. Taking into account the finite size of the collimated photon source, the results indicate a localization accuracy in the direction of the anode pad rows around 2 mm rms.

The localization accuracy along the direction perpendicular to the MCP (the DOI) has been determined moving the collimated spot, at fixed X coordinate, in three positions 27, 18 and 5 mm from the top surface of the crystal (the entry face for the gammas). The Z coordinate is then estimated, as discussed in the previous section, from the width of the detected scintillation light distribution on the anode pads.

As shown in Fig. 5.34, the distribution is the narrowest for the largest DOI (27 mm, corresponding to conversions 3 mm from the MCP readout), and spreads with asymmetric tails for events far from the anodes.

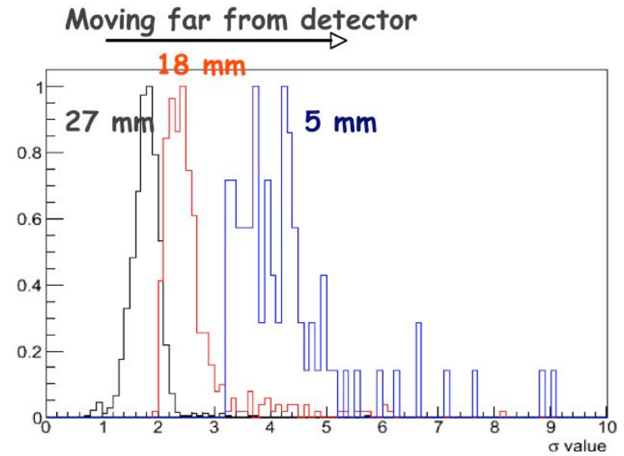

Figure 5.34 *RMS of the signal distribution on anode pad rows for three positions of the collimated source.*

Fig. 5.35 summarizes the results of the measurements, providing the correlation between real DOI (Z_{data}) and average width of the distributions (<σ>). Error bars indicate the rms of the width distributions.

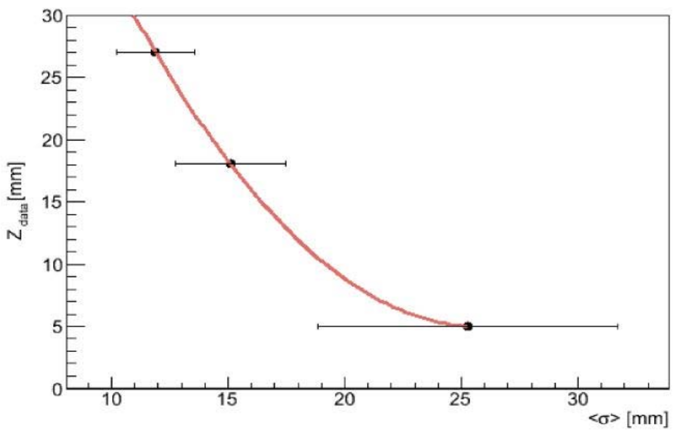

Figure 5.35 *Average width and error of the signal distribution for the three DOI positions.*

As expected, the precision in the DOI determination depends on the penetration depth, and permits to resolve events about 10 mm apart, corresponding to one third of the crystal thickness.

5.10 Summary of the results and future work

The described simulation work and the preliminary experimental data obtained with a reduced setup, confirm that proper analysis of the signal distribution on segmented light sensors permits to reconstruct the coordinates of the conversion of 511 keV gammas in crystals with a position accuracy around 2 mm rms in the plane perpendicular to the photon direction, and a determination of the Depth of Interaction within the crystal with an accuracy around 5 mm rms. An even coarse determination of the DOI permits the use of thicker and more efficient crystals without suffering from parallax errors, an essential advantage for PET-on-beam applications in view of the low activity and short lifetime of the positron-emitting isotopes.

To continue investigating this promising approach to PET imaging, we are preparing an improved setup:

- Two Multi-anode PM, of the model already used, will be procured and operated in coincidence, thus largely increasing the event rates, presently limited by the small sensitive area of the crystal-PMT used in coincidence;
- An electronic system is under development, making use of fast Analogue-to-Digital Converters (ADC) directly mounted on the MCP sensors, and a dedicated read-out interface to transfer the data to a desktop PC;
- The centre of gravity and distribution width reconstruction algorithms will be optimized, combining experimental and simulation results, and implemented as on-line analysis of the data; the aim is to obtain X-Y localization and DOI coordinates in real time.

6. IN-BEAM-PET WITH GAS DETECTORS

6.1 Introduction

While most commercial PET scanners make use of scintillating crystal detectors, the superior localization properties and lower cost of gas-filled proportional counters have since long attracted dedicated research. Able to amplify, detect and localize the charge released in the gas by ionizing tracks, proportional counters have however a negligible efficiency in detecting high-energy photons. However the efficiency can be enhanced with internal converters, thin foils of high-Z materials used as electrodes or inserted in the gas volume.

Because of the requirement for the electron (Compton or photoelectric) produced in the interaction to emerge from the converter into the gas, there is an optimum thickness for the converter foil. For 511 keV photons and tungsten, this is typically around 100 μm. To obtain a reasonable efficiency, one needs several tens of converter foils in a stack of independent detectors. A pioneering device of this kind was developed long ago at the Rutherford Laboratory, assembling together twenty wire chambers planes with thin lead cathodes, each with a two-dimensional electronic readout on thin cathode strips[96]. A double arm detector had typically 10% efficiency in coincidence and 3 mm resolution, and was successfully used for years in clinical investigations[97].

In a more advanced device, the Heavy Drift Chamber, a composite converter is made of a stack of metallic grids, alternating with insulators, with through holes; application of a graded potential allows to drift the ionization electrons, resulting from the photon interaction in the stack, to a single multi-wire proportional chamber for detection and localization[98]. Named HIDAC, the device has been extensively tested in hospital environment, and for years was the highest accuracy PET scanner available[99].

Despite the lack of energy resolution, due to the partial absorption of the ejected electron in the converter, these devices have good space resolution and low cost. However wire chambers are difficult to manufacture and are rather fragile. More recent devices as RPC and GEM are sturdier and present less mechanical problems. In this Chapter the applications of such devices to PET systems are presented.

6.2 Optimization of the gamma detection efficiency in gas detectors

The optimization of the detection efficiency of 511 keV photons of gas detectors involves several aspects. Many of these are peculiar to the gas detector considered. In the present Section a detailed study of the optimization of a lead converter foil is carried out by means of a pure Monte Carlo approach.

The Livermore Low Energy electromagnetic physics package of the Geant4 toolkit (see Chapter 2) was used to simulate a point-like beam of 511 keV photons hitting perpendicularly a thin slice of lead of $10 \times 10\ \text{cm}^2$.

The 511 keV photons interact in the converter by photoelectric and Compton interactions. Both result in the production of a lower energy electron that can ionize the gas gap and

---

[96] Bateman J. E. et al, Nucl. Instr. and Meth. A176 (1980) 83.
[97] Ott R. J. et al, Nucl. Instr. and Meth. A269 (1988) 436.
[98] Jeavons A. et al, Nucl. Instr. and Meth. 124 (1975) 491.
[99] Townsend D. et al, J.Nucl. Med, (1988)

consequently be detected by means of the multiplication of the freed electrons in the GEM foil or in the RPC gap.

The probability that a 511 keV photon interacts in the converter increases with its thickness, while - by increasing the thickness - the probability to extract a secondary electron (that is the detectable particle) is lower. Therefore two efficiencies can be defined: one is given by the fraction of primary gammas absorbed in the converter ($\varepsilon_{\gamma,abs}$) and the other is the electron extraction probability from the converter ($\varepsilon_{e-,ext}$). They can be expressed as following:

$$\varepsilon_{\gamma,abs} = \frac{N_{\gamma,abs}}{N_{\gamma,inc}} \qquad \varepsilon_{e-,ext} = \frac{N_{e-,ext}}{N_{\gamma,abs}}, \tag{6.1}$$

resulting in an overall efficiency given by:

$$\varepsilon = \varepsilon_{\gamma,abs} \cdot \varepsilon_{e-,ext} = \frac{N_{e-,ext}}{N_{\gamma,inc}}. \tag{6.2}$$

In a single layer detector, the aim would be to maximize the number of produced electrons over the number of incident primaries. When considering a multi-layer multi-converter detector, it is necessary to evaluate the number of lost gammas (i.e. absorbed with no consequent electron emission) per layer, since once an event is lost in a converter it cannot be detected in any following layers. Moreover the converter thickness has to be chosen in order to have reasonably high detection efficiency in a limited number of layers, to reduce the radial depth of the tomograph (supposing to arrange the gas chambers on a cylindrical geometry).

The present study is focused on transmitted electrons, i.e. forward directed with respect to the incident gamma beam.

In case of GEM backscattered electrons, even if not negligible, do not contribute to the final efficiency. In fact, secondary electrons freed in the gas gap above the converter foil by backscattered electrons do not undergo any multiplication and are stopped by the converter itself.

On the other hand, secondaries produced by backscattered electrons created by the interaction of gammas in the GEM foil (Cu+Kapton) can undergo an avalanche in the same GEM were they have been generated. Since the GEM foil does not attenuate a significant number of gammas, this effect has been therefore neglected in the present study.

Considering multi-stack not independent RPCs (as discussed later) besides the contribution of electrons directed in the forward direction, backscattered electrons can contribute as well to the total efficiency. Since they are peculiar to a particular set-up they are not treated in detail here.

The overall efficiency ε and the electron yield $\varepsilon_{e-,ext}$ have been evaluated for different thicknesses of the converter (Fig. 6.1). At rather low values of the thickness, the overall efficiency curve exhibits a build-up region and reaches a plateau at high thicknesses. In fact, by increasing the thickness a larger number of gammas interacts within the converter while a smaller number of electrons exits the foil. This is clearer from the right panel of the figure. For a thin converter $\varepsilon_{e-,ext}$ approaches unity since the few gammas that interact yield electrons capable to exit the converter, while for thick converter, for instance of 180 μm, the electron yield efficiency drops to 20%. Therefore from these distributions we deduce that the optimum thickness of the lead converter is around 80 μm.

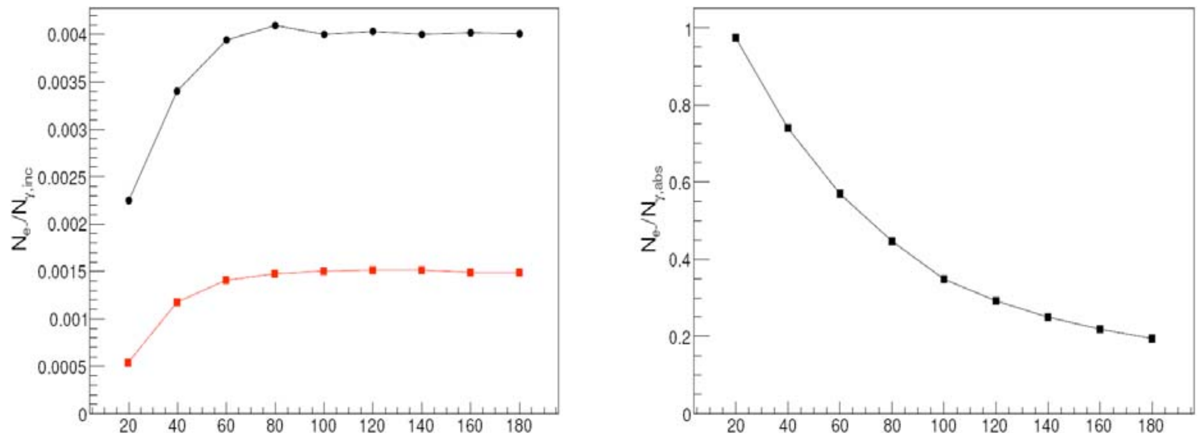

Figure 6.1 *Dependence of ε (left, black circles) and of the electron yield $\varepsilon_{e-,ext}$ (right) as a function of thickness of a single lead converter. In the left panel, the efficiency of backscattered events (red squares) is also shown.*

In Fig. 6.2 the overall efficiency as a function of the number of layers is plotted for two selected thicknesses of lead: 50 μm and 80 μm. Up to 20 layers, the difference between the two curves is rather small. At 50 layers (indicated in the figure by the black dashed line) ε is about 20% and about 17% for the 50 μm and 80 μm thick slice respectively.

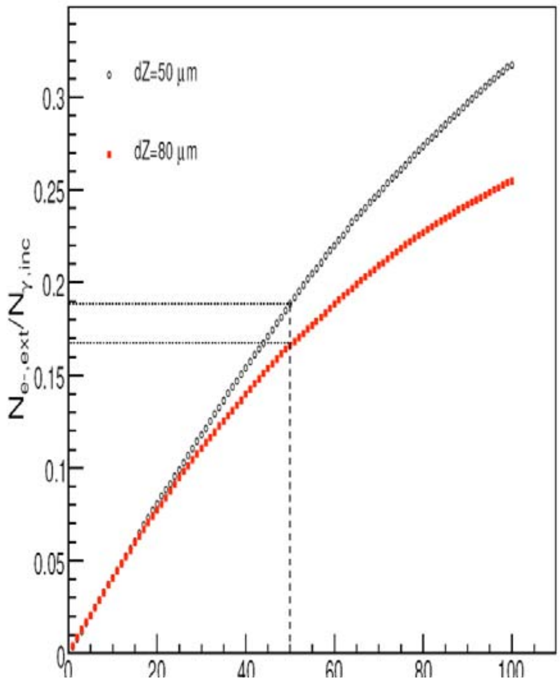

Figure 6.2 *Dependence of the efficiency ε as a function of the number of lead converters (spaced by 3 mm gas) for two different thicknesses: 50 μm (black circles) and 80 μm (red squares).*

Another factor that has to be considered is the energy resolution.

In standard PET applications the energy resolution has to be good enough to discriminate against events arising from photons scattered within the object by rejecting those with low measured energy. Gas detectors with internal converters have no energy resolution. It appears however that a converter sheet has an efficiency decreasing with the photon energy, resulting in a physical threshold for rejection of low energy photons.

This is shown in Fig. 6.3, providing the overall efficiency and the electron yield are plotted for 50 μm and 80 μm thick lead converter respectively as a function of the incident gamma energy.

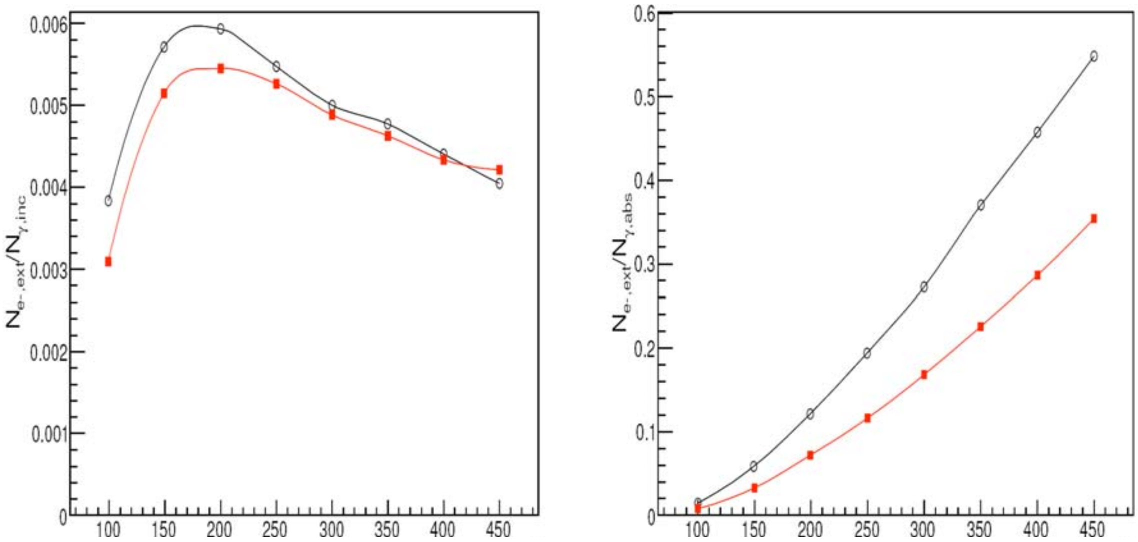

Figure 6.3 *The efficiency ε (left) and the electron yield $\varepsilon_{e-,ext}$ (right) for different energies of gammas incident on a 50 μm (black circles) and 80 μm (red squares) thick lead layers.*

As expected, the electron yield increases with the increase of the energy of the incident gammas, as a consequence of the higher energy of secondary electrons. Besides, the overall efficiency is peaked around 200 keV, and at higher energies it becomes higher for the thicker converter with respect to the thinner one. Lower Z material, having a higher Compton cross-section, can improve the efficiency at higher energies but with the drawbacks of a lower gamma attenuation and a smaller angular correlation with the incident gamma direction.

In a gas detector, the detection efficiency is limited by the number of primary ionizations generated in the gas gap by the primary particle. Therefore it is important to estimate the total energy deposited by the electrons exiting the converter in a standard gas mixture. Fig. 6.4 shows the energy distributions of transmitted and backscattered electrons produced by 511 keV gammas interacting in 50 μm thick lead converter.

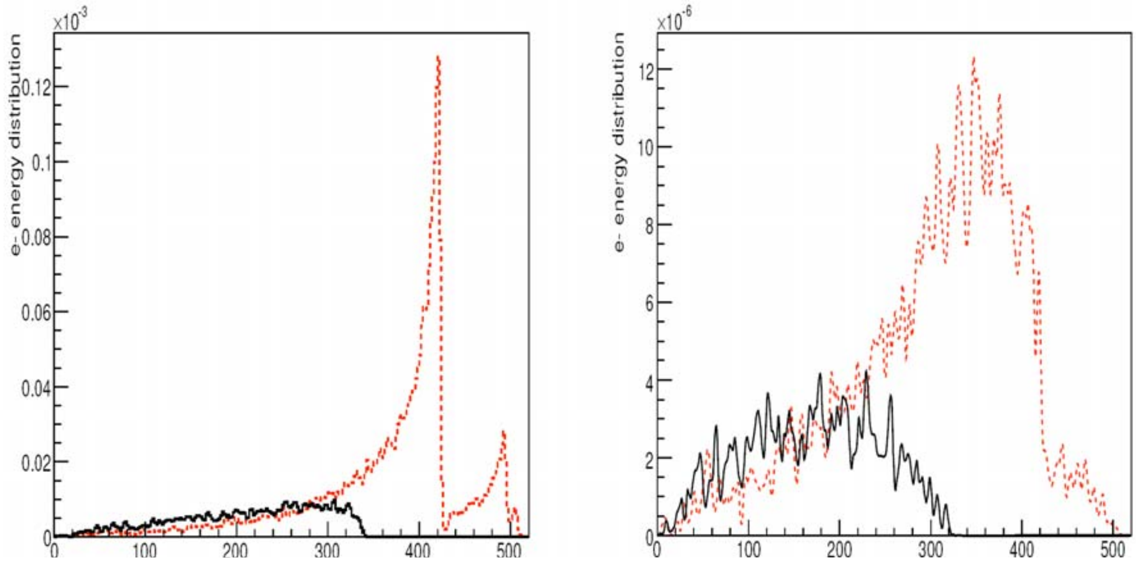

Figure 6.4 *Energy of the electrons produced by 511 keV gammas in a 50 μm Pb foil.*

The distributions plotted in the figure refer to transmitted (left panel) and backscattered (right panel) electrons, produced by Compton (black solid line) and photoelectric (red dashed line) interactions.

Electrons produced by Compton and photoelectric interactions are indicated with different colors.

The maximum energy of a Compton electron from 511 keV is about 340 keV. In the transmitted electron energy spectrum the shell structure of lead is clearly visible, with a pronounced peak at about 400 keV corresponding to photoelectrons freed from the K-shell, whose binding energy is 88 keV.

The total energy deposited by these photoelectrons in a 3 mm gas gap - filled with a Ar+CO_2 (70%-30%) mixture - is shown in Fig. 6.5.

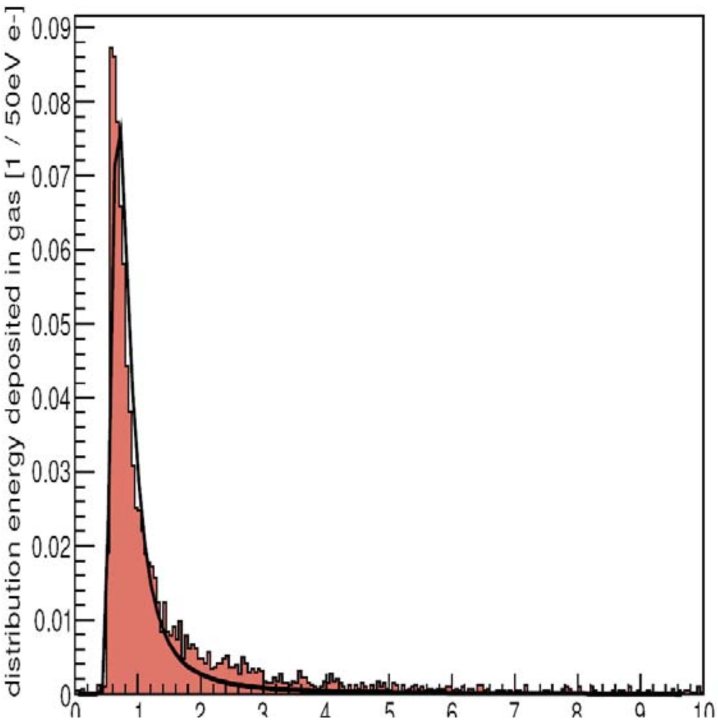

Figure 6.5 *Total energy deposited per detected event in 3 mm gap filled with Ar 70% and CO_2 30%.*

The total energy deposited was fitted by a Landau function, resulting in 0.71 keV mean value. The mean energy deposit in Argon to produce an electron-ion pair is 26.3 eV, therefore the average number of primary ionizations is about 27 (assuming a pure Argon gas). This implies a practically 100%detection efficiency.

To estimate the achievale space resolution, the spatial distribution of the energy deposited in the 3 mm Ar-CO_2 was computed.

Fig. 6.6 shows that the energy is deposited in a cone around the primary beam direction - i.e. perpendicular to the converter foil - with is less than two millimetres wide. This reflects the fact that the secondary electrons are mainly produced in the forward direction.

The spatial distribution of the energy deposition projected in one of the transverse directions has a low diffuse background with a sharp peak superimposed. The distribution was fitted by the sum of two Gaussians of different widths. They are shown in the right panel of Fig. 6.6

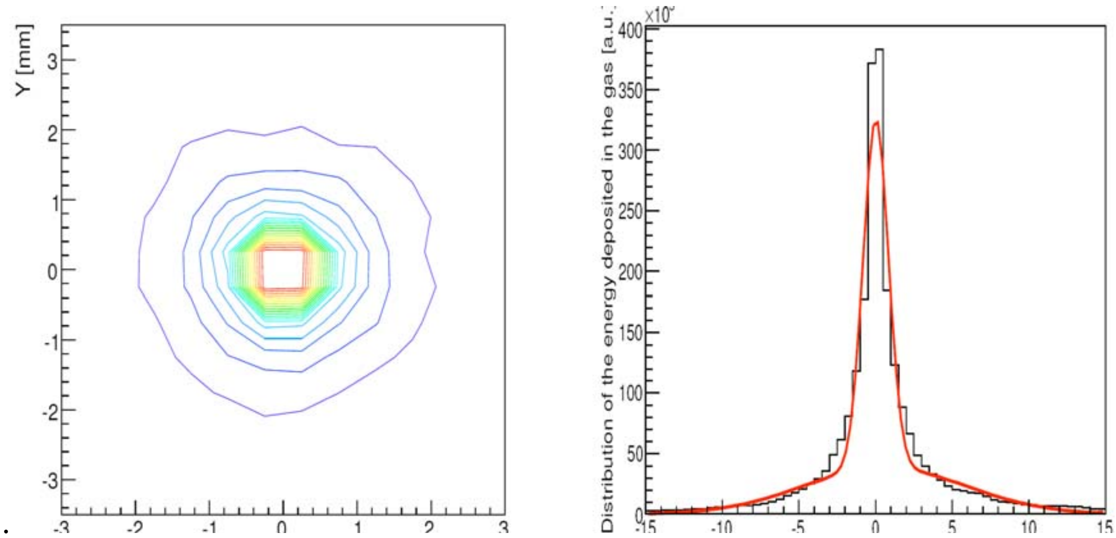

Figure 6.6 *Projected spatial distribution of the energy deposited by electrons in 3 mm gap filled with a mixture Ar 70% and* CO_2 *30%. In the left panel the distribution is projected on the plane of the lead converter layer and in the right panel it is further projected in one dimension.*

The standard deviation of the sharper Gaussian is of particular interest since it is a direct estimation of the difference between the reconstructed position of interaction of the gamma (i.e. exploiting the signal distribution on the read-out plane) and the real interaction point of the gamma in the converter layer since all gammas hit the converter in (x,y)=(0,0). The calculated deviation is 80 μm.

By taking into account all the factors discussed above, as an optimum a 50 μm lead converter has been chosen to perform first experimental estimations of the detection efficiency of 511 keV gammas emitted by a ^{22}Na source.

A simple set-up consisting of the lead converter and a standard GEM foil, with 3 mm gas gap (Ar-CO_2) has been designed and built. The events will be acquired in coincidence with a standard PMT-crystal detector. The measured efficiency will be the overall detection efficiency, i.e. including gamma absorption, electron extraction and gas ionization by the extracted electron.

6.3 Resistive Plate Chambers (RPC)

A new line of search has appeared based on the use of a sturdier device, the Parallel Plate Avalanche Chamber sometimes called simply PPC (Parallel Plate Chamber). Constituted by two conducting electrodes separated by a thin gas layer, PPACs are cheap, robust and simple to build.

In the present proposal, the major drawback of conventional parallel plate counters, the tendency to discharge when operated at large gains, is solved making one or both electrodes with a high-resistivity material, having the property of quenching discharges by a local voltage drop. Using high-resistivity glass as electrodes, high gas pressures and narrow gaps (100 μm or less) to reduce the statistical fluctuations in the avalanche formation, the so-called Pestov or spark counters can achieve few tens of ps time resolutions[100], a very attractive feature for PET systems.

[100] Pestov Yu., Nucl. Instr. and Meth. 196 (1982) 45.

In a popular model, with Bakelite electrodes, wide gaps operated at atmospheric pressures Resistive Plate Chambers (RPC)[101] have mm localization properties and time resolutions of a few ns, and are widely used in particle physics to cover large detection areas[102].

More performing RPCs, in particular for what concerns the timing properties without the need of using inconveniently high gas pressures, have been recently developed. The statistical dispersion intrinsic in the energy loss process is reduced by the use of narrow gaps, and, to compensate for the low efficiency, multi-gap structures are assembled in the same detector, with signals or-ed together as shown in Fig. 6.7[103].

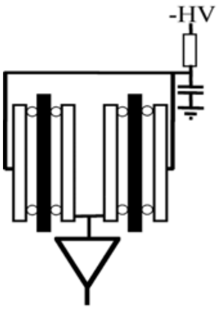

Figure 6.7 *Thin-gap RPCs or-ed together for fast response and good efficiency.*

Alternatively, a composite detector can be made with a stack of independent RPCs[104] (Fig. 6.8). To reduce the complexity of the electronics, the position information can be obtained not individually in each layer, but from a hardware wiring in columns of the readout electrodes. A fast pulse, recorded from an electrode in each layer, provides the timing and DOI information.

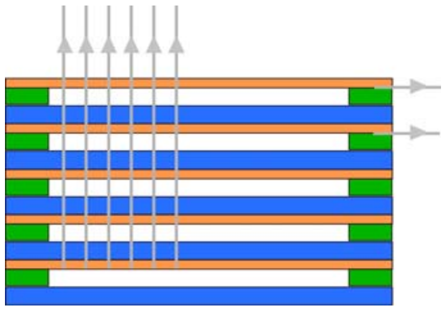

Figure 6.8 *A stack of 6 independent RPC gaps with internal conversion layers; readout strips in each layer are connected in columns to reduce the complexity of the electronics.*

An elegant way to achieve the best timing properties of narrow gaps, preserving efficiency without the need of readout electronics on each gap, is to assembly in the same detector, between two active electrodes, several thin insulating electrodes (usually made of glass), left floating, get the appropriate potential by electrostatic equilibrium[105] as shown in Fig. 6.9. Used in CERN's ALICE detector, Multigap RPCs can achieve full efficiency for minimum ionizing tracks with 50 ps time resolution and are used to identify particles from a measurement of Time of Flight [106].

---

[101] Cardarelli R. et al, Nucl. Instr. and Meth. 333 (1993) 399.
[102] Proc. Int. Workshop on Resistive Plate Chambers, Nucl. Instr. and Meth. A533 (2004)
[103] Blanco A. et al, Nucl. Instr. and Meth. A533 (2004) 139.
[104] Anulli F. et al, A Hybrid Parallel Plate gas Counter for Medical Imaging, Proceedings of the International Symposium On Detector Development For Particle, Astroparticle and Synchrotron Radiation Experiments (SNIC 2006), SLAC, April 2006, in print.
[105] Cerron Zeballos E. et al, Nucl. Instr. and Meth. 374 (1996) 132.
[106] Akindinov A. N. et al, Nucl. Instr. and Meth. A533 (2004) 74.

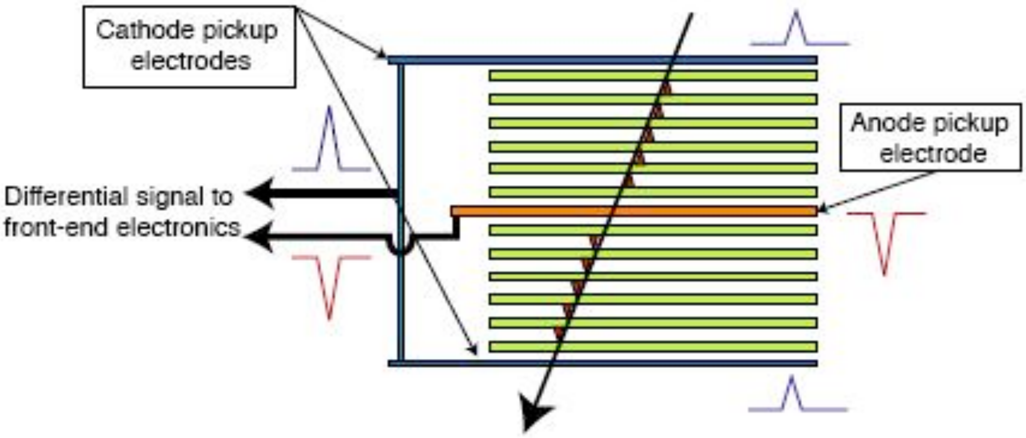

Figure 6.9 *Schematics of the Multi-Gap RPC. The operating voltage is applied between the outer cathodes and the central anode; intermediate resistive electrodes obtain the appropriate voltage by electrostatic equilibrium.*

The described detectors, when used in a PET device, provide mm position information, correction of the parallax error and sub-ns time resolution. Despite their performances, however, the described RPC devices have a drawback for the use as detectors of high energy photons: most high-Z materials, needed to improve the conversion efficiency, are metallic, and therefore can at best be used for one electrode, the second being a high-resistivity material. This implies that in a multi-stack device each layer has to be read-out individually, with a heavy electronic overhead. Use of floating lead-glass glass plates both as converters and floating electrodes with the Multigap geometry permits to increase the efficiency of a stack with a single readout plane; this is the solution proposed by the authors of Ref. 19. A recent Monte Carlo simulation by the group shows than using borosilicate or lead-loaded glass one can reach 30-40% detection efficiency for 500 keV photons with a stack of 50 plates, 300 μm thick each for borosilicate glass and 100 μm for lead glass (Fig. 6.10)[107].

Based on experience acquired during the development of Micro-Strip Chambers manufactured on thin glass substrates, however, doubts can be raised on the stability of such a detector at high radiation fluxes. Boro-silicate glass can be procured with the required thickness and high resistivity (10^{10}-10^{11} Ω cm^{-3}), but its electrical properties depend on the migration of ions, inevitably resulting in long-term polarization, modifying electrical characteristics[108]. Glass with electronic conductivity exists, and was in fact used in the original Pestov Counters, but it is very expensive and not available in large sizes.

For CNAO a better solution is proposed which is based on the work done on Micro-strip chambers. A thin controlled-resistivity diamond-like layer is deposited on glass by Carbon Vapor Deposition, appropriate to avoid charging up and polarization problems can be easily obtained by a standard low cost industrial method[109]. Fig. 6.11 shows several glass converter plates stacked with a common electronic readout on each side of the stack. For the converters, a borosilicate floated glass available in large sizes and 300 μm thickness, will be used[110. 111].

[107] Fonte P., Nucl. Instr. and Meth. A580 (2007) 915.
[108] Alunni L. et al, Nucl. Instr. and Meth. A348 (1994) 344.
[109] Bouclier R. et al, Nucl. Instr. and Meth. A369 (1996) 328.
[110] DESAG D-263, made by Deutsche Spezialglas AG, Griinenplan.
[111] SURMET Co, Burlington MA, USA.

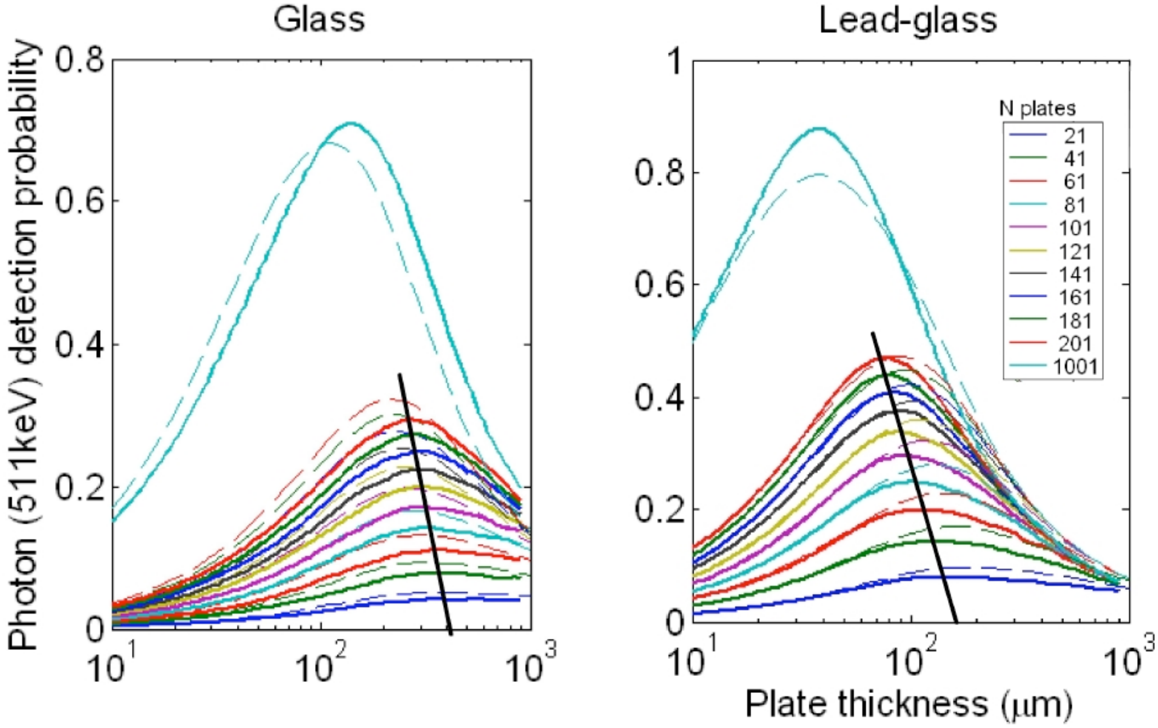

Figure 6.10 *Computed efficiency of a multi-gap RPC for 511 keV photons as a function of plate thickness and number, for borosilicate glass (left) and lead-glass (right).*

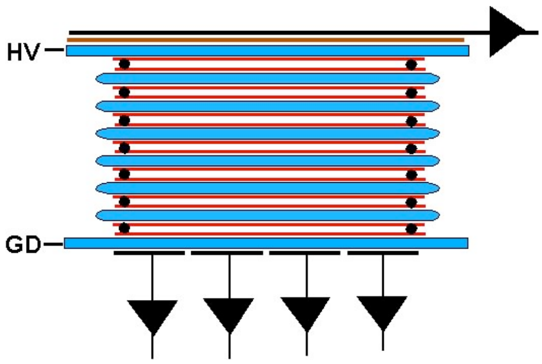

Figure 6.11 *Multi-gap RPC with the internal floating electrodes made of glass with high-resistivity coating, for improved stability of operation.*

In the figure, five floating electrodes are assembled in a single detector, with 100 μm gaps; thin insulating rods help preserving the gap thickness. In the floating electrode configuration of the Multigap RPC, only the two outer electrodes are powered, the other plates setting at the equilibrium value of voltage. However, having well defined high-resistivity electrodes, a more stable operation, particularly at high radiation rates, would be to apply the appropriate potential to each electrode through a simple resistor chain, connected to ground and HV at the two ends.

An artist's view of a module assembly, currently on design by TERA is shown in Fig. 6.12 and 6.13. The converter electrodes, resistive-coated glass plates, 300 μm thick, are inserted in grooves cut in two thin ceramic plates (Fig. 6.6); a front and a back plate then close the structure; the topmost glass sheet is covered by a conductive layer (graphite) and connected to the high voltage; similarly, on the bottom side, the two-dimensional strip readout circuit is placed in contact but mechanically independent to the lower face of the first glass plate at ground potential (Fig. 6.7). For the preliminary tests, the module will be assembled without the front and back ceramic plates, and mounted inside a gas envelope; future plans however call for a sealed assembly, filled during manufacturing with the preferred gas mixture.

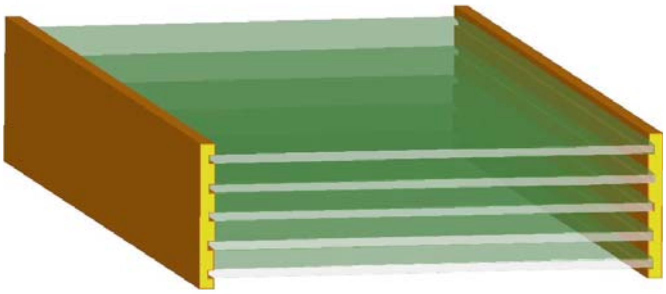

Fig. 6.12 *Five glass foil module assembly between grooved ceramic plates.*

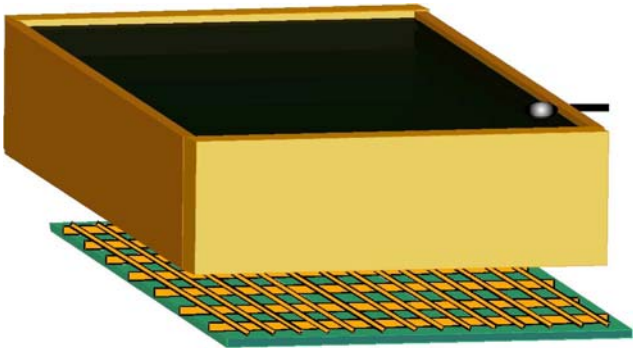

Fig. 6.13 *A complete module with top HV connection and bottom 2-D readout circuit.*

Depending on the detector geometry and photon angular range, the number of plates within one module can be increased, reducing the cost of the readout. To reach the desired efficiency, several modules have to be stacked as in Fig. 6.14.

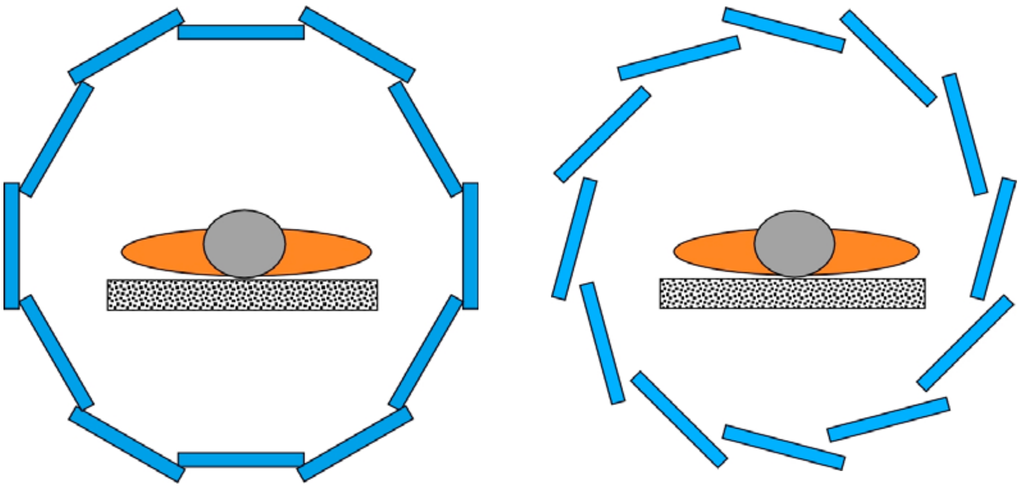

Figure 6.14 *Schematic representation of a PET system using two possible assemblies of RPC modules, partly overlapping.*

The figure shows a possible assembly scheme of a full ring PET scanner making use of the described RPC detectors: individual modules have a size of 10 cm radially and are 30 cm long. To avoid the efficiency loss at the edges, the modules can be assembled alternatively at a different radius, or slightly rotated with a partial overlap as shown in the figures.

6.4 Gas Electron Multiplier (GEM)

Owing to their excellent position resolution and high rate capability, Gas Electron Multiplier (GEM) detectors are widely used for tracking of charged particles in high-energy physics[112]. Applications in other fields have also been developed, in particular for neutron and high-energy X-ray detection, adding appropriate converter sheets in front of the GEM electrodes used for charge amplification; thicker electrodes on the multipliers themselves can act as converters. To compensate for the low efficiency of a single element, multi-layer structures are made, with stacks of converter-GEM pairs; ionization released by a photon conversion anywhere in the stack is transported through the structure into a terminal position-sensitive GEM detector.

A fundamental problem hinders however the use of the technology, when its performances are confronted to crystal-based detectors. In a multi-layer GEM-converted stack, one has to ensure that the amount charge transported to the final multiplier does not depend on the conversion depth; this implies that each layer has to have unitary effective gain. The thickness of each layer, typically several mm, adds then an (unknown) delay to the final charge collection, implying a poor time resolution; for ten layers, this is of several hundred ns, seriously restricting the use of the device. For thick detectors and off-normal angles of incidence of the photons, there is also a large parallax error in the coordinate determination.

In collaboration with the Gas Detectors Development group at CERN we have studied a structure that permits to overcome this limitation[113]. The basic concept is to design each element in a multi-layer GEM-converter stack with high gain, to allow local detection of the event, but very low charge transmission to the following elements; if G is the effective gain of a foil, the goal of unitary gain for each layer is achieved if its the transmission is 1/G. We demonstrated that this can be obtained using a converter foil with narrow holes and optimized values of electric fields with the single-cell prototype detector shown in Fig. 6.15:

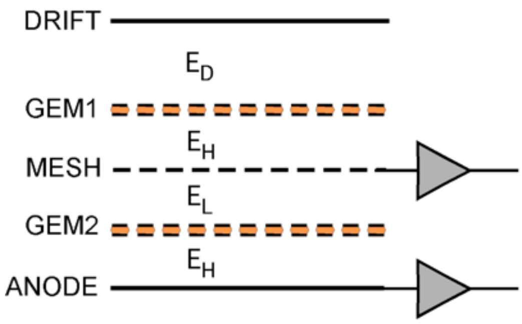

Fig. 6.15 *Single-cell GEM-converter prototype.*

Charge released in the drift space by a source is injected into GEM1 and amplified; choice of a high field E_H followed by a low optical transparency mesh and a low field E_L allow to collect most of the avalanche charge on the mesh, with only a small transfer into the following cell.

We recorded the charge on the mesh and on the anode as a function of GEM voltages and electric fields above and below the mesh (E_H and E_L respectively); a summary of the results is shown in Fig. 6.16, giving the ratio of mesh and anode charge as a function of GEM effective gain, for two choices of fields. Owing to the different charge collection efficiency, the unitary ratio is reached at different gains.

[112] Sauli F., Nucl. Instr. and Meth. A522 (2004) 93.

[113] Croci G., Ropelewski L., Sauli F. and Solevi P., "Depth of interaction determination in GEM-based multi-layer PET detectors", Nucl. Instr. and Meth. A582 (2007) 693.

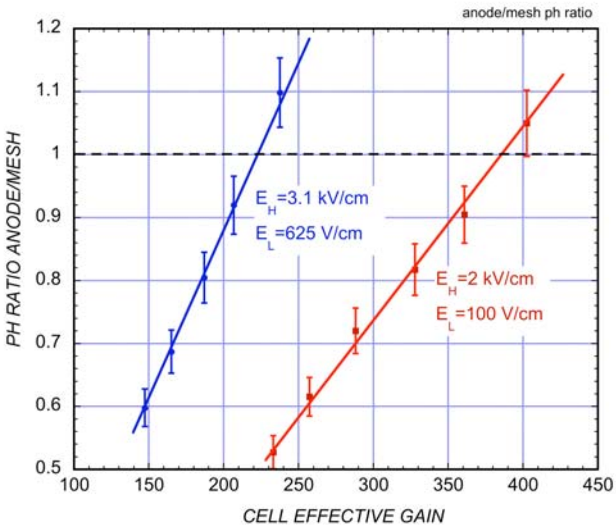

Fig. 6.16 *Ratio of charge collected on the last anode and on the mesh, as a function of GEM1 gain.*

The results show that proper choice of geometry and field conditions permit operation of a GEM-converter pair at a large enough gain to allow direct detection of gamma ray conversions in a layer, with a transmitted gain close to unity in each cell. This opens the way to the construction of a multi-layer stack, detection of a pulse on one of the meshes will indicate the depth of interaction, while positional information is obtained from an end-cap multiplier using standard readout methods with projective strips or pads. Work is on the way to optimize the structure, and in particular the geometry of the mesh to have large conversion efficiency for 511 keV photons but very low charge transparency.

6.5 Overview and future work

Gas detectors are an attractive solution for a PET scanner because of the low cost, the high spatial resolution and - in some cases - the excellent time resolution. On the other hand they exhibit a low efficiency in detecting 511 keV gammas and for this reason multi-layer chambers are necessary, with alternated converter slices or by using electrodes themselves as converters. Recently, the two types of gas detectors discussed in this Chapter have been studied in detail by several research groups for their application in the medical field: RPCs and GEMs.

Resistive Plate Chamber based PET detector has been successfully tested for small-animal imaging at LIP Coimbra (Portugal) [114]. In this case the converter is the resistive glass plate of the chamber itself. The computed detection efficiency approaches 17 % for 100 plates. The efficiency can be further enhanced by using lead-glass but this technology is still not available. Considering a RPC unit detector with 300 μm of gas gap and an optimal thickness of the glass converter equal to 400 μm, each cell is about 1 mm thick, therefore 100 plates would give about 10 cm radial depth. This is still an acceptable volume for a PET tomograph.

Gas Electron Multipliers have also been recently considered for application to PET. The optimization of the multi-layer multi-converter detector geometry is under study by the Gas

[114] Blanco A. et al., "An RPC-PET prototype with high spatial resolution", Nucl. Instr. and Meth. A 533 (2004) 139-143.

Detector Group at CERN [115]. Such a geometry has been chosen in order to control the cost of the full device, dominated by the electronic required that increases with the number of layers. According to the study described in this Chapter, a lead converter with thickness ranging between 50 and 80 μm is required and an experimental measurement of the detection efficiency of a 50 μm lead converter combined with a GEM foil with 3 mm gas gap is in progress.

These technologies show some differences that need a more detailed discussion.

The final total efficiency of a GEM based device for a 511 keV photon detection has to take into account the probability that an electron produced by the gamma interaction in the converter creates a certain number of primary ionizations (N_p). The lower is the energy of the exiting electrons the higher is N_p, that depends on the gas gap thickness as well. In case of RPCs, working at higher applied field, an electron that produces a few ionizations in the "effective" gap (generally the first half of the gas gap) is detected. This component of the detection efficiency limits the thickness of the gas gap in GEM chambers, which cannot therefore be too small. Hence, a GEM based detector would be thicker than a RPC based one by a factor three.

Moreover, in in-beam-PET applications, were the rate is low, the detection efficiency is important because determines the sensitivity of the scanner. The sensitivity is determined by other components as the geometrical coverage of the tomograph. With the lower cost of gas detectors, large volumes can be easily fabricated.

Another important factor is the sensitivity possible with a good measurement of the Time Of Flight (TOF). A good time resolution makes possible to confine the source position in the FOV of the scanner by measuring the difference of the arrival times of the two events detected in coincidence. The sensitivity gain is given by the formula:

$$g_{TOF} = \frac{2d}{\Delta t(c/2)},$$

where d is the average radius of the scanned object, Δt the time resolution and c the speed of light. By assuming d=5 cm and Δt=300 ps, the gain is about 2 for RPCs. For a GEM based detector, due to the lower timing performance, there is no gain in using the TOF information.

It is clear that, even if converter materials with higher efficiency would be found, the geometrical occupancy of a gas detector based scanner will be higher than the one based on crystals. The lower sensitivity can be compensated by increasing the geometrical coverage of the scanner that, on the other hand, would complicate the location of a large device with respect to the patient and the other components of the treatment system.

In conclusion, for the smaller size and the higher timing performance, RPCs are a more attractive solution with respect to GEMs. A first prototype for human RPC PET is at present under production at the University LIP of Coimbra and will be ready and tested by the end of 2007. It is a 30×30 cm^2 head, which assures 3D measurement of the interaction point. A similar development is being planned by the TERA Foundation, so to have a definite device to compare, in performances and cost, with the crystal solution discussed in the previous Chapter.

[115] Croci G., Ropelewski L., Sauli F. and Solevi P., "Depth of interaction determination in GEM-based multi-layer PET detectors", Nucl. Instr. and Meth. A582 (2007) 693.